Vibroacoustics modelling using the Finite Difference Time Domain method: Incorporating porous materials and mechanically excited plates

Thesis submitted in accordance with the requirements of the University of Liverpool for the degree of Doctor in Philosophy

by

Nuno M. G. Ferreira

March 2019

Major comments

1) Justification of the use of the MFM model. As currently presented, the model seems to include both a 3D model of the interior of the porous material, as well as a lumped model. Though experimental results are good, the theory is not, as yet, internally consistent. One way to test this would be to check results under the presence/absence of one or both of these modeling features in the code. The two effects should be the same, leading to a potential doubling of the correction in the LF range.

Response:

The opportunity has been taken to try and clarify the text in current section 2.11.2 on the implementation of the Moving Frame Model (MFM). In Chapter 5 Figures 5.2 and 5.3, and Figures 5.4 and 5.5 show the FDTD result with and without the MFM model from which the difference can be seen; the comparison of measurements against FDTD with and without the MFM model provides evidence that there is no 'double counting'. In the description of the Rayleigh model, a new diagram (current Figure 2.10) has been added to show the representation of the porous material as a set of parallel narrow channels. In addition, current section 2.11.2 clarifies that the interior of the porous material was not included in the 3D model since the density used for this medium was that of air, and also that the pressure inside the porous material is updated using the equation of continuity for the Rayleigh model (equation 2.79) with the density of air. An additional clarification was added to text in section 5.2.5: "As mentioned in section 2.11.2, the value of density used to model the porous material was that of air.".

The calculation of the lump mass motion of the porous panel was also clarified in the text indicating that the pressure gradient Δp is calculated from the two pressure nodes that are adjacent to opposite sides of the panel. Once the pressure gradient is known, Equation 2.78 is used to calculate the frame velocity v_F. Once the frame velocity is known, the velocity of the air particles inside the air channel is calculated using equation 2.79. The MFM calculation procedure is illustrated in a flow diagram – see Figure 2.13.

2) Definitions of efficiency. Claims regarding superior performance of the scaling approach need to be back up by a solid definition of computational efficiency which is informed by the low-frequency character of the problem, as well as bandwidth and dispersion characteristics of the scheme. i.e. For a given bandwidth f Hz and maximal wave speed error y%, efficiency could be defined as the number of floating point operations needed to carry out the simulation per second

Response:

A precise mathematical derivation of the numerical dispersion characteristics of the FDTD scheme upon which the scaling approach is based is now flagged as potential future work in section 7.1 "Suggestions for future work":

“The mathematical derivation of the numerical dispersion characteristics of the vibroacoustic FDTD scheme [68] upon which the scaling approach is based could also be carried out in future work.“.

The meaning of efficiency has been clarified in the text of current section 3.13 “Scaling of vibroacoustic fields”: “In this thesis, an alternative formulation is proposed for the vibroacoustic problem to yield much faster results, in the sense of requiring less calculations to obtain a vibroacoustic prediction, than using only a non-parallelized standard FDTD approach, based on the work of Toyoda et al [68]”

The reduction in bandwidth associated with increased time step used is now addressed in current section 3.14:

“Both the 'scaling' approach and 'simplified boundary' approach lead to a significant increase in the time step that is required to run the simulations. This leads to a reduction in the maximum possible frequency for the analysis relating to the Nyquist frequency. However, this is not problematic for the low-frequency applications that are considered in this thesis, such as building acoustics.”

3) Use of the scaling approach: limit of validity of the approach, given the use of separate models for the scaling factor and resulting FDTD method needs to be shown in a definitive way. It is highly advised to perform simulations for the standard Kirchhoff plate model for the sake of comparison.

Response:

This has been carried out by adding a new appendix (Appendix II - Comparison of isolated aluminium plate mode shapes obtained via NMM and FDTD) which contains an assessment of the validity of the general three-dimensional FDTD method for simulating thin plate bending wave motion. It compares the results obtained for the isolated aluminium plate using FDTD and analytical bending wave theory for thin plates. The correlation pattern obtained between FDTD and the analytical model is similar to that which exists when the analytical model is compared with itself. This confirms that the results obtained using the general three-dimensional FDTD method are equivalent to those of the analytical model which describes thin plate bending wave motion.

Specific comments

Chapter 2

p. 7 Acoustic impedance of a surface requires both pressure and velocity to be readily expressed: not in velocity potential form.

Response:

The correction is current section 2.4.1 “Field variables” :

Added text - “(…) requiring the implementation of digital filters. For the sake of simplicity, a formulation based on both pressure and particle velocity was chosen as the method used for this thesis, based on the work of Yokota et al [16].”

Removed text: “ (…) since, in its basic form, the acoustic impedance of a surface requires both pressure and velocity to be readily expressed. Hence in this thesis both pressure and velocity are used to allow detailed modelling of the boundary conditions.”

p. 7 It must represent curved boundaries using staircase geometry. Many techniques such as finite volume method can be used.

Response:

Section 2.4.2 “Grid geometry”: Added the following text: “In addition to the use of non-Cartesian coordinate systems and non-regular grids, another closely related method to FDTD, the finite volume method [32,33] can also be used to accurately represent curved surfaces.”

Added Reference [33] W. M. Henk Kaarle Versteeg, An introduction to computational fluid dynamics - The finite volume method. Essex: Pearson Prentice Hall, second ed., 2007.

p.8 No definition of grids…Eq. 2.1 etc.: what dimension are we in? What is p? System under study has not been defined yet.

Response:

Major restructuring of the text has been carried out: The Euler equations are now introduced (current section 2.2) before the literature review (current section 2.4)..

In response to “*what dimension are we in?*”, Equation 2.1 refers to one-dimensional space (as mentioned in text above the equation “taking the x-direction as an example”).

In response to “*What is p?*”, p indicates pressure. In the current version of the text, this is defined in section 2.2 – Sound propagation in acoustic media.

p. 8: Eq. 2.2; not fourth order as written (where is expansion point?) Not centered.

Response:

Equation 2.38 (which corresponds to previous 2.2) has been corrected. Corresponding bibliographic reference have also been updated.

p. 9: ‘This class of methods can be made *very efficient* due to FFT and IFFT routines….’ Relative to what? High frequency behaviour? Accuracy remains second order in time.

Response:

Section 2.4.4 “Approximation of space derivatives”: The phrase “made very efficient” has been reworded to say “...can be implemented with widely-available, validated FFT and IFFT routines...”.

p. 9: sources. No model problem defined here yet. What are the sources driving it?

Response:

Restructuring of the text has been carried out so that the acoustics problem is now introduced in current section 2.2 before the literature review (current section 2.4).

p. 10: Figure 1.2 shows simulation results without system descriptions – restructuring is required. What problem is being solved? What is the driving function? Use proper axis scalings.

Response:

In response to *“Figure 1.2 shows simulation results without system descriptions – restructuring is required”*, Restructuring of the text has been carried out: The acoustics problem is now introduced (current section 2.2) before the first simulation results, which have been moved into section 2.4

In response to *“What problem is being solved?“*, the problem of the acoustic wave propagation is now defined in section 2.2.

In response to **“***What is the driving function? “*, a Gaussian function – please see the text of in Section 2.4.5 - Types of sound sources which says states “A visualization of two hard FDTD pressure sources can be seen in Figure 2.4, where two Gaussian pulses are *positioned close to one another“*.

In response to “Use proper axis scalings”, the colorbar axis of figure 2.4 (corresponds to former 2.1) is now bounded between -1.5 and 1.5. In addition, the source code that generated this figure is included in Appendix III.

p. 10: staggering to prevent instabilities…how so? – reference [33] is missing. What about solving 2D wave equation on non-staggered grid (which is equivalent)?

Response:

A reference to R. Janaswamy and Y. Liu, “An unstaggered colocated finite-difference scheme for solving time-domain Maxwell’s equations in curvilinear coordinates,” IEEE Transactions on Antennas and Propagation, vol. 45, no. 11, pp. 1584–1591,1997, was added to the statement: “The main reason for the offset of field variables is to reduce discretization error and prevent instabilities [41].”

p. 11: Use bold notation for vectors v. v_{i} conflicts with notation for grid indices.

Response:

This has been corrected. The notation is now consistent throughout the thesis: The subscripts that appear after the variable indicate the Cartesian coordinate directions (x,y,z, i^{th}direction). The subscripts that appear after the vertical bar "|" indicate a position index in the grid.

p. 12 Figure 22; Systems were not defined yet – define systems (1D, 2D, and 3D) in advance.

Response:

Restructuring of the text has been carried out. Before the literature review (which is now current section 2.4), the acoustics problem is now introduced (current section 2.2) and 1D, 2D and 3D systems are defined in current section 2.3.

p. 13: Section 2.4 should be first. Need to define system up front. No definition, explanation of sigma

Response:

Sections 2.1 to 2.5 have been re-ordered and are now presented as:

2.1 Introduction

2.2 Sound propagation in acoustic media

2.3 Implementation of FDTD equations

2.4 Literature Review of the FDTD model

p. 14: Clarify that stress tensor is defined for Chapter 6 on vibroacoustics.

Response:

Section 2.2.1 "Euler equation of motion": Added "The use of the stress tensor components is especially important when defining vibroacoustic problems, discussed in chapters 3 and 6 of this thesis."

p. 15: Define density

Response:

Density is defined in section 2.2.1.

p. 15: Are we in 3D now? You have already shown grids for 1D and 2D.

Response:

Restructuring of the text has been carried out and the problem of the acoustic wave propagation is now defined in current section 2.2 for a 3D space. Note that dimensionality of the field variables is discussed in current section 2.3.1 “Field variables in acoustics”.

p. 16: now in 2D?

Response:

Justification for the jump from 3D to 2D is now in the text of current section 2.3.4: “To gain insight into the implementation of the FDTD three-dimensional update equations, it is convenient to consider the two-dimensional version of the discrete field equations.”

p. 17: Very awkward notation in 2.21-2.26. Use subequations env’t.

Response:

The mathematical notation is now as follows:

$p|_{i,j}$ for positional indices;

$p_{i,j,}$ for cartesian coordinates

p. 17: v_{x} conflicts with v_{i}, etc.

Response:

The notation is now consistent throughout the thesis: The subscripts that appear right after the variable indicate Cartesian coordinate directions (x,y,z, i^{th}direction) and the subscripts that appear after the vertical bar “|” indicate a position index in the grid.

p. 17-20: Section 2.5.1: probably unnecessary, and quite poorly explained. These can be simplified or a piece of code can be shown in appendix.

Response:

A suitable piece of code has been included in Appendix IV.

p. 20: Error in Eq. 2.37, extra minus sign.

Response:

Extra sign was deleted.

p. 21: Highest phase velocity: reference should be mentioned. Courant condition is a heuristic only. What system are we talking about now? One with a variable phase velocity? Like what? Such systems do not appear in this work - it would be true in the case of the plate, but you do not invoke the plate equation in this thesis.

Response:

In response to *"Highest phase velocity: reference should be mentioned."*, a reference was added in the text following the Courant Condition equation 2.41 to "F. Zheng and Z. Chen, "A finite-difference time-domain method without the courant stability conditions," IEEE Microwave and Guided Wave Letters, vol. 9, no. 11, pp. 441–443, 1999."

In response to *"Courant condition is a heuristic only. What system are we talking about now? One with a variable phase velocity? Like what? Such systems do not appear in this work - it would be true in the case of the plate, but you do not invoke the plate equation in this thesis. "*, to make it clearer that dispersive systems are not being discussed, the text in current section 2.5 has been clarified to say "where C is the highest phase velocity of any wave motion within the frequency range of source excitation [47]".

p. 21: Clarify what dh is?

Response:

Δh is defined as the distance between two source and receiver cells.

p. 22: dt must always be checked for the time period…do you mean stability depends on the duration of the simulation? What is time period?

Response:

Sometimes a simulation only shows the effects of instability (unbounded growth) after some particular time duration, and therefore it is still possible to obtain useful information from the period before this point. Such examples can be found in the literature, for example see Figure 4.54 below from section 4.8 of Electromagnetic Simulation Techniques Based on the FDTD Method by W. Yu, John Wiley & Sons 2009:

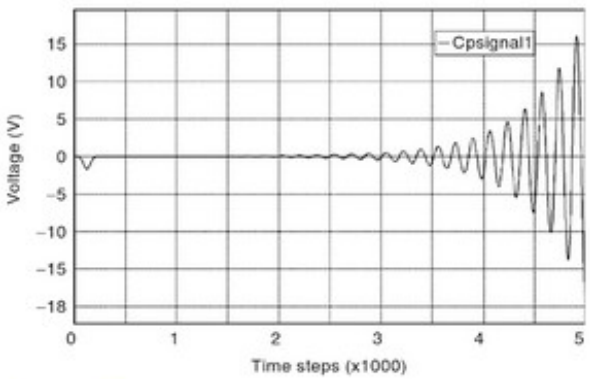

Figure 4.54 Unstable signal using a first-order Mur boundary to truncate the open cavity.

p. 23: k should be replaced with kx.

Response:

Done.

p. 24: Describe that ‘dt ->0, dx ->0…’ is for holing Courant condition.

Response:

Done.

p. 25: already stated on p. 23 –

Response:

Only kx seems to be on this page.

p. 25: v_{o}: a scalar? Another notation conflict.

Response:

To avoid confusion with the variable velocity v, v_{o} was renamed to s_{o}.

p. 26: eq. 2.46: hard source? Soft source?

Response:

This is general acoustics theory and as it does not describe an FDTD source, the ‘hard’ or ‘soft’ terminology is not used.

p. 26: S is not total area, but a defining surface

Response:

Changed text from “total area” to “defining surface area”.

p. 27: eq. 2.48: v(t). Is this v_{o}(t)? v is already used for velocity.

Response:

Replaced v(t) by v_{z}(t), as the source function consists of a velocity node that points in the vertical z-direction.

p. 28: what is v_{z}? Is this for 3D field?

Response:

as stated in the text in current section 2.8 “FDTD acoustic sources”, “vz indicates the vertical z-component of the velocity that was used to implement the source (figure 2.9)“

p. 29: what is sigma? = sigma_{o}?

Response:

Changed caption of Figures 2.7 and 2.8 from “sigma” to sigma_{o}.

p. 30: Frequency dependent impedance introduced but not used - confusing.

Response:

Section 2.10 was simplified and no longer introduces frequency-dependent boundaries as they are not used.

p. 31: no equivalent in the time domain. Rational forms for Z? large literature on this as well.

Response:

Statement was removed from the text.

p. 31: do you actually use frequency-dependent impedances in this work?

Response:

Section 2.10 was simplified and no longer includes frequency-dependent boundaries as they are not used.

p. 32: how to estimate phase from 2.58? This information and reference are required.

Response:

Equation 2.58 was not essential so it has been deleted and the corresponding section (2.10.1) has been restructured and merged with part of section 2.10.2, to form what is now section 2.9.1.

p. 32: modal expressions given without any justification/definition. Or 2.10.2 could be omitted.

Response:

Most of section 2.10.2 has now been omitted and part of it was merged with section 2.10.1, to form what is now section 2.9.1.

p. 33: stability conditions for 2.64?

Response:

Equation 2.64 was omitted due to restricting the text to frequency independent variables.

p. 34: 2.65 to 2.67 are provably unstable. Need centering of variables!

Response:

A reference to these equations has been added in section 2.10: T. Yokota, S. Sakamoto, and H. Tachibana, “Visualization of sound propagation and scattering in rooms,” Acoust. Sci. Tech, vol. 23, no. 1, pp. 40–46, 2002, but no stability issues are mentioned by these authors, and no stability issues have been identified in the models used in this thesis.

p.34: Moving Frame model. No explanation of what the “frame” is, or any diagrams here.

Response:

Section 2.11 “Sound propagation in porous media” - Added explanation “(the solid constituent of a porous material)”

p. 35: parallel narrow channels: desperately needs diagram. What is the coordinate system here?

Response:

This diagram has been added as Figure 2.10.

p. 35: \bar{v}: a constant (i.e., not time dependent?)

Response:

\bar{v} varies with time, and that is implicit in the time derivative. To make it more clear it is a spatial average, the following was added to section 2.11.1 “Rayleigh model”: “where \ bar{v}_{i} is the average air particle velocity developed across each air channel of the porous absorber along the i^{th} direction.”

p. 35: what is \bar{v}_{i}? Same as \bar{v}? If so, why is it time differentiated if it is constant?

Response:

This has been dealt with in the response above.

p. 35: r is a constant? Don’t use “t” here for averaging duration, better to use T.

Response:

In response to “*Don’t use “t” here for averaging duration, better to use T. “*, *t* has been replaced by *T*.

In response to “*r is a constant? “*, *r* is a constant that corresponds to the airflow resistivity. This constant is now introduced in the text of current section 2.11.1 - Rayleigh model: “the airflow resistivity (Pa.s/m^2), *r*, is then given by [64]:”

p. 36: Eq. 2.74: why not use div v? What dimension are we in “if the x direction is considered”: does this mean we are in 1D?

Response:

Changed text in section 2.11.1 “Rayleigh model” to “For example, in one dimension (along the x-direction), the continuity equation reduces to” to make it clearer that the following equation is a 1D example of the 3D continuity equation.

p. 36: validity of 2.75; typical frequencies? Regarding the results on 118, more explanation about frequency rages of Rayleigh is required.

Response:

The validity of equation 2.68 (previously eq. 2.75) has been included in section 5.2.5

p. 37: if the frame is allowed to move: in what direction? Diagram is required.

Response:

Clarification was added in the text (along with a diagram for the Rayleigh model) that the frame of the porous panel is allowed to move along the direction of the narrow air channels (Figure 2.10)

p. 37: which is the variable to be solved for, i.e., which v?

Response:

Additional text has been added to give more clarity in this section.

p. 37: no explanation of v_{F}?

Response:

Added definition of v_{F} as velocity of the frame. Also added equation v_{air|Frame} = v_{air} - v_{F}

p. 37: pressure inside the panel is not introduced but it might have an impact on the results in 3D – it needs clarification.

Response:

Additional text has been added to give more clarity in current section 2.11.2 “Moving Frame Model”.

p. 38: Figure 2.10 does not make sense

Response:

The caption of current figure 2.11 (previously fig. 2.10) now indicates which of the diagrams corresponds to the room volume and to the spring-mass-spring model: “The room volume separated by the porous panel (left) and its equivalent spring-mass-spring model (right)”

p. 38: k1, k2, m: from physical considerations? If so, what are they?

Response:

The definitions of k1 and k2 were added to the text in current section 2.11.2 “Moving Frame Model”.

p. 40: is m_{S} the same as m on page 38?

Response:

The definition of m_{S} was restated: “If the mass per unit area of the panel m_{S} approaches infinity”

p. 40: implemented in such a way that knowledge of k1, k2 is not required…really, it is because you have not included this in your model in 2.77---but how does this relate to the form with stiffness?

Response:

The relation of k1 and k2 with the form with stiffness was added to the text in section 2.11.2:

“where m is the total mass of the panel and k_{1} and k_{2} are the stiffness corresponding to each enclosed volume of air on either side of the porous panel. The stiffness values k_{1} and k_{2} are calculated using\cite{Kinsler+2000}:

$$k=\rho_{o}c^{2}S^{2}/V$$

where V is the volume of air and S is the area of the porous panel.”

The spring-mass-spring resonance, and therefore the constants k1 and k2, is expected to occur when a room volume is completely divided by a porous panel, as indicated in Figure 2.11. It is calculated in order to identify the frequency range where the MFM model is expected to make a difference to the predicted sound field.

Chapter 3

Clarify why 3D model is needed. 2D model is not enough?

Response:

Flexibility of modelling different wave types using a single implementation is the main motivation for not using 2D models. The following text was added to current section 3.3.3 to make this point clearer:

“This thesis primarily concerns the modelling of thin plates using a general three-dimensional FDTD method that, for flexibility, can support all wave types. “

p.46: eq. 3.1 could be simplified.

Response:

It is not clear how the momentum equation 3.1 could be further simplified. It is a tensor equation, so it can be decomposed into several other equations 3.4 – 3.6 as indicated in the text in current section 3.3.1 “Momentum Equation”:

“Equation 3.1, the momentum equation, is a tensor equation. If expanded in Cartesian coordinates, it is equivalent to the following system of first-order partial differential equations (...)”

p. 46: sigma: depends on t only? Why written this way?

Response:

Changed “sigma(t) =” in equation 3.2 to “sigma =”

p. 46: why asymmetry in definition 3.3?

Response:

There was a typo in this equation. The ½ is now multiplied by both terms.

$\varepsilon_{ij} = 1/2 \left(du_j/dx_i + du_i/dx_j\right)$

p. 46; C_{ijkl} need to define explicitly.

Response:

Added the references [71] and [72], now the text reads: “where Cijkl is the stiffness tensor of rank 4 [71][72].”

p. 47: eq. 34-3.6 could be combined.

Response:

Equations 3.4 – 3.6 can be combined into tensor equation 3.1, as mentioned in the text in current section 3.3.1 “Momentum equation”:

“Equation 3.1, the momentum equation, is a tensor equation. If expanded in Cartesian coordinates, it is equivalent to the following system of first-order partial differential equations (...)”

p. 49: plates: have not defined these at all in Section 3.3.3; a plate is not the same as a solid 3D medium. Which plate model? Kirchhoff? Mindlin Reissner?

Response:

In response to *“plates: have not defined these at all in Section 3.3.3;”*, the text has been rephrased as follows and reference [73] to “L. Cremer, M. Henckl, and E. Ungar, Structure-borne sound. Berlin: Springer-Verlag, second ed.,” 1973 has been added:

“This thesis primarily concerns the modelling of thin plates [73] using a general three-dimensional FDTD method that, for flexibility, can support all wave types. There are four types of structure-borne sound waves that occur over the audio frequency range in thin plates: bending, transverse shear, quasi-longitudinal and dilatational waves [73].

For the low-frequency vibroacoustic applications that are considered for engineering structures in this thesis it is often bending waves that are of primary interest. For this reason the validity of the general three-dimensional FDTD method in reproducing thin plate bending wave motion is assessed numerically. A comparison of FDTD and analytical bending wave theory for thin plates [73] is shown in Appendix II through consideration of both mode shapes and eigenfrequencies. These results confirm the validity of the general three-dimensional FDTD method for simulating thin plate bending wave theory."

In response to *"a plate is not the same as a solid 3D medium.", the* Response: text has been rephrased in section 3.3.3 as indicated in the previous response to emphasize that the strategy is to model thin (Kirchhoff) plate dynamics using a 3D FDTD model.

In response to "*Which plate model? Kirchhoff? Mindlin Reissner?",* the term "thin" was added to the title of section 3.3.3 "Elastic waves occurring in thin plates"

p. 49: Third wave speed is introduced in eq. 3.10. This is from thins plate rather than the system in previous pages. Justification is required to show mathematically why this is usable and valid for scaling approach.

Response:

Appendix II - comparison of isolated aluminium plate mode shapes obtained via NMM and FDTD using MTMAC is introduced as evidence that the 3D scaling approach models the dynamic behaviour of thin plates.

In addition, the text in section 3.3.3 has been rephrased as indicated in the previous responses to emphasize that the strategy is to model thin (Kirchhoff) plate dynamics using a 3D FDTD model.

p. 49: definition of \vu
Response:

Added definition here when it appears for the first time (already defined in "List of symbols and abbreviations").

p. 49: expression in 3.10 does not follow from the analysis of a 3D solid directly, which is not dispersive! Are you suggesting using this frequency-dependent expression as Courant condition? It comes from Kirchhoff model, which itself relies on other hypotheses (thin plate, etc.)

Response:

In response to *"expression in 3.10 does not follow from the analysis of a 3D solid directly, which is not dispersive!"*, the strategy in this thesis is to model a thin Kirchhoff plate using a general 3D model. This is achieved with the general 3D solid wave propagation equations

and then defining the appropriate geometry and boundary conditions. For out-of plane excitation and with bending wavelengths that are large relative to the plate thickness this approach is shown to be valid in Appendix II. For clarity, the following text was added to 3.3.3: “This thesis primarily concerns the modelling of thin plates using a general three-dimensional FDTD method that, for flexibility, can support all wave types. There are four types of structure-borne sound waves that occur over the audio frequency range in thin plates: bending, transverse shear, quasi-longitudinal and dilatational waves [73]”

In response to “*Are you suggesting using this frequency-dependent expression as Courant condition? It comes from Kirchhoff model, which itself relies on other hypotheses (thin plate, etc.)*”, clarification was added in current section 3.9: “In this thesis, the mechanical behaviour of thin plates is approximated and therefore the phase velocities mentioned in section 3.3.3.1 need to be considered, within the frequency range of the simulation, for stability analysis.

p. 50: use of a 3D model of losses in the context of thin structure vibration---justification? See, e.g., Lambourg and Chaigne: https://asa.scitation.org/doi/pdf/10.1121/1.1354200. Do you not have to consider the boundary layer effects in the material? How are these modelled in your 3D system?

Response:

In response to *“use of a 3D model of losses in the context of thin structure vibration---justification?“*

The approach used in the thesis is to have the damping constants implemented directly in the three-dimensional momentum and constitutive equations. This produced acceptable results in terms of measured/predicted loss factors, as can be seen in Table 6.4.

In response to *“See, e.g., Lambourg and Chaigne”*, text has been added in section 6.4 - “Driving-point mobility of the aluminium plate”. This notes that although thermoelastic effects are mentioned in the paper by Chaigne and Lambourg [93] indicate how internal damping and radiation damping could be incorporated in time-domain models for three basic mechanisms of damping, which they list as thermoelasticity, viscoelasticity and radiation. This potentially has practical application to lightly damped musical instruments such as a cymbal, but it is of limited use to engineering structures such as buildings, aircraft or marine structures where the total loss factor of plates is determined by the sum of the internal losses, radiation losses, losses due to additional damping layers and structural coupling losses. As the latter two losses tend to dominate the response, the approach of Chaigne and Lambourg was not incorporated, and experimental determination of the damping was used in the model.”

Note that for the aluminium plate with additional damping material that is considered in this thesis, the approach to incorporate damping in the FDTD model gives the required agreement with measurements.

In response to *"Do you not have to consider the boundary layer effects in the material? How are these modelled in your 3D system?"*, the boundary layer is not considered in the modelling as the air is considered to be inviscid (current section 3.12 - "Simplified air/solid boundary conditions") and therefore the no-slip condition (zero velocity of the fluid relative to the boundary) is not implemented.

p. 50: '…damping mechanism…' is required the reference (Toyoda et al [70]) and justification is required to use this equation for this plate.

Response:

This reference was added and justification concerning the use of general 3D viscoelastic equations for thin plates was added to the text in section 3.3.3

p. 51: Define F in eq. 3.13.

Response:

Done.

p. 54: why are both the 2D and 3D systems presented here? It is especially unclear here, given that you will be modelling plates, which system you are planning to use.

Response:

The 2D and 3D systems are presented in section 3.5 "Full form of the viscoelastic field equations" because they are referenced in section 3.7 "FDTD viscoelastic update equations."

p. 58: various new notational problems. Use of 0.5 instead of ½ in index, also use of operators D (these should not be indexed by "i")! Also, why are these being introduced at this stage in the thesis? The place for these is in an introductory chapter on FDTD schemes.

Response:

In response to "Use of 0.5 instead of ½ in index", the whole thesis now complies to this: use of ½ instead of 0.5.

In response to "*also use of operators D (these should not be indexed by "i")*!", there was an error in the text as the index i in the operator D refers to the direction the derivative is taken and so the text was corrected to "where D denotes the forward difference, as defined in appendix I." Having made this correction, the equations in current section 3.7 "FDTD viscoelastic update equations" now show Dx, Dy and Dz depending on the direction the derivative is taken. Thus these equations are consistent with the notation agreed for this thesis (in p.17), e.g. $P|_{i,j}$ for positional indices and $P_{i,j,}$ for Cartesian coordinates.

In response to "*Also, why are these being introduced at this stage in the thesis? The place for these is in an introductory chapter on FDTD schemes.*", the operator D is now defined in Appendix I "Mathematical symbols and operators".

Following from the remarks above, the two-dimensional analysis carried out in current section 3.7 “FDTD viscoelastic update equations” now uses x and y directions instead and y and z. This provides consistency throughout the thesis. Changes to Figure 3.4 have been made accordingly.

p. 62 Is this your model? Or Toyoda’s? Or someone else’s? You claim that the approximation is good, but can you back this up with a plot of reference?

Response:

p.64/65: For clarity, minor text edits have been added along with a new reference [76] (L. Boltzmann). In addition, a new appendix, “Appendix IV - frequency characteristics of the damping coefficients” has been included to show how beta and gamma can be varied to achieve different loss factor frequency profiles.

p. 63; It is not always possible to tell whether waves with the highest phase velocity have been excited…in the context of stability analysis, this is not really an issue, as roundoff error will always lead to the production of such components.

Response:

Removed the text “In addition, it is not always possible to identify whether waves that have the highest phase velocity have actually been excited.” from section 3.9 “Stability of vibroacoustic simulations”.

p. 64; Eq. 3.55: new notation here; use of general grid indices i,j to represent position of a source is not a good idea.

Response: This has been fixed. The notation is now consistent throughout the thesis: The subscripts that appear right after the variable indicate Cartesian coordinate directions (x,y,z, i^{th} direction). The subscripts that appear after the vertical bar “|” indicate a position index in the grid.

p. 65: simply supported conditions; it appears you are now referring back to the Kirchhoff plate model (i.e., from notation “M” for moments). But Kirchhoff is not defined in the thesis. Neither are the “M”. Are you talking about a 2D simulation of Kirchhoff here, or a 3D simulation? If so, in the case of the 3D simulation, how is the ss condition defined? Is there pivoting about the midplane of the slab? Need to be very clear here.

Response:

In response to *“simply supported conditions; it appears you are now referring back to the Kirchhoff plate model (i.e., from notation “M” for moments) Are you talking about a 2D simulation of Kirchhoff here, or a 3D simulation?”*, to make it clear that these conditions refer to thin plate theory, the following italic text was added to section 3.11 “Simply supported boundary conditions”: “*For the edges of the three-dimensional plate, the*

implementation of its simply-supported boundaries aims to approximate the following conditions corresponding to a simply-supported two-dimensional thin plate [79]".

In response to *"If so, in the case of the 3D simulation, how is the ss condition defined? Is there pivoting about the midplane of the slab?"*, clarification in the text in section 3.11 has been made: "This is approximately carried out by assigning a value of zero to the vertical velocities that are located on the mid-plane around the plate edges as shown in Figure 3.7. As shown in the same figure, the lateral velocity components of the plate edges are calculated like the other velocity components of interior of the plate."

p. 66: what is "w"? How does this relate back to vx,vy,vz and stress components? You say that you are assigning a BC at the midplane of the slab, but what are the BCs everywhere else? Have you verified that this is indeed a good approximation to a ss condition in 2D?

Response:

In response to *"what is "w"?"*, text in section 3.11 "Simply supported boundary conditions" has been added: stating "w denotes displacement in the z-direction".

In response to *"How does this relate back to vx,vy,vz and stress components?"*, Figure 3.7 illustrates the connection between the stress and velocity components of a SS condition, as the text on page 66 states "This is approximately carried out by assigning a value of zero to the vertical velocities that are located on the mid-plane around the plate edges as shown in Figure 3.7"

In addition, added the text "As shown in the same figure, the lateral velocity components of the plate edges are calculated like the other velocity components of interior of the plate."

In response to *"You say that you are assigning a BC at the midplane of the slab, but what are the BCs everywhere else?"*, Response: text has been added in the same section 3.11: The boundary conditions defined in this section refer to the plate edges. The solid-air boundary conditions that cover the remainder of the domain are described in the following section 3.12.

In response to *"Have you verified that this is indeed a good approximation to a ss condition in 2D?"*, text has been added to section 3.11: The validity of this approximation is confirmed in the analytical/FDTD eigenfrequency results obtained for a simply supported plate that are shown in Table 6.2.

p. 67; same grid over both solid/fluid regions? Implications for dispersion?

Response:

Added text in section 3.13.6 "Limitations":

"Another important factor that introduces errors when using the scaling approach is numerical dispersion. When using the same space and time grid resolution for the air medium and solid medium additional numerical dispersion is introduced since wave propagation in the air medium occurs further away from the Courant limit than the wave propagation in the

solid medium (which comparatively has a higher phase velocity). In addition, the larger the value used for the scaling factor *s*, the less uniform the rectangular grid will be and the more problematic the numerical dispersion becomes. For the scaling factor value used in this thesis, *s*=6, the experimental validation of the numerical results suggests that the effects of the numerical dispersion are negligible at the low frequency range considered in this thesis (<200Hz).

In order to know exactly by how much the numerical dispersion affects the results when using the vibroacoustics FDTD scheme, it is necessary to mathematically derive the numerical dispersion relation. This derivation is now flagged as future work in section 7.1 "Suggestions for future work":

"The mathematical derivation of the numerical dispersion characteristics of the vibroacoustic FDTD scheme described in this thesis upon which the scaling approach is based could also be carried out in future work."

p. 67: need to specify the boundary condition which is being employed here! All you have is an update.

Response:

The text in current section 3.12.1 - "Theoretical background" was updated with more information about the boundary conditions: "The implementation developed in this thesis considers the update equations for the velocity nodes that lie on the boundaries to have the same form as the other solid medium velocity update equation (Equation 3.37) for which the density equals that of the actual solid and the space steps across the boundaries remain unchanged."

p. 67: to improve computational efficiency: how?

Response:

Modified the text in section 3.12.1 - "Theoretical background" to: "In order to avoid the time step implications required by the standard boundary approach". Also more details were added in the same paragraph.

p. 71: statement about grid coarseness and increased time step is a little naïve…you can always do this, but the cost is of reduced simulation bandwidth.

Response:

In current section 3.14, the following text has been added "Both the 'scaling' approach and 'simplified boundary' approach lead to a significant increase in the time step that is required to run the simulations. This leads to a reduction in the maximum possible frequency for the analysis relating to the Nyquist frequency. However, this is not problematic for low-frequency applications below 250Hz that are primarily considered in this thesis for engineering structures

such as small rooms in buildings, car cabins, or train carriages.”.

p. 72: In contrast to room acoustics simulations…this is backwards. It depends entirely on the frequency range you want to simulate. For a given material, and frequency range, wave speeds are higher in solids, meaning larger grids. What you say about needing high resolution for thin 3D solids implies that you should really be using a 2D model!

Response:

Rephrased text in section 3.13 to “It can be computationally expensive to run a large vibroacoustic model with a fine spatial resolution, especially because wavespeeds (e.g. for quasi-longitudinal waves on structures) are significantly higher in solids than in air.“

p. 73: Are you assuming a synchronous time step for both the acoustic field and the solid? I assume so!

Response:

Yes, the following text was added in section 3.13.1 “Methodology”: ”(…), which in turn results in a synchronous time step delta_t step for both the plate solid medium and the acoustic medium”

p. 73: this scaling assumes the mode frequencies for the Kirchhoff model. And yet you are employing it within a 3D model. What is the validity range of this approximation, particularly when you are scaling the plate dimensions?

Response:

This is addressed in section 3.13.6:

“One limitation concerns the high-frequency limit for pure bending wave theory. If the thin plate frequency limit for the actual plate is (Cremer et al)

$f_B = 0.05 c_L / h$

the limit for the scaled plate f_B' is given by $f_B' = f_B / s^2$ and the error in the simulation results will increase above this limit.”

In addition, the reference to Cremer et al was repositioned in the text above.

p. 73: what is the effect on dispersion/cutoff of the use of different grid spacings? Generally, using different grid spacings leads to very poor dispersion/cutoff behaviour.

Response:

Added text in section 3.13.6 on page 83:

“Another important factor that introduces errors when using the scaling approach is numerical dispersion. When using the same space and time grid resolution for the air medium and solid medium additional numerical dispersion is introduced since wave propagation in

the air medium occurs further away from the Courant limit than the wave propagation in the solid medium (which comparatively has a higher phase velocity). In addition, the larger the value used for the scaling factor *s*, the less uniform the rectangular grid will be and the more problematic the numerical dispersion becomes. For the scaling factor value used in this thesis, *s*=6, the experimental validation of the numerical results suggests that the effects of the numerical dispersion are negligible at the low frequency range considered in this thesis (<200Hz). ”

p. 73: same grid spacings for acoustic field and for plate? But then you are quite far from the Courant limit in one of the two cases.

Response:

Added text in section 3.13.6 as indicated in the response above.

p. 73: ‘…. much faster results than…’: define efficiency and make it clearer along with bandwidth issue.

Response:

Added text on section 3.13 so it says “In this thesis, an alternative formulation is proposed for the vibroacoustic problem to yield much faster results, “In this thesis, an alternative formulation is proposed for the vibroacoustic problem to yield much faster results, in the sense of requiring less calculations to obtain a vibroacoustic prediction, than using only a non-parallelized standard FDTD approach, based on the work of Toyoda et al [68].”. The bandwidth issue is clarified in section 3.14 on page 83.

p. 74: a general notion that operating away from the Courant bond (i.e., with a larger grid spacing) is a good idea…not true!

Response:

The idea is that as the grid resolution gets larger, the corresponding time step given by the Courant condition (Equation 2.41) will also be larger, which in turn allows for reducing the number of iterations necessary to simulate a given time duration.

p. 74: whole technique seems to rely on mode calculations---this seems unnecessary. What you are really doing is coordinate scalings. This can be done, much more simply with the model problem a priori, without resorting to a modal description at all!

Response:

The modal description is considered to be a useful way of ensuring that the scaling factors give the correct sound and vibration response, and is not disproportionately complex.

p. 75: p,q,r in expression for modes?

Response:

Added in current section 3.13.2 - “Scaling of sound fields in rooms” : “(…) where p, q and r are positive integers and correspond to room mode numbers.”

p. 77: modal frequencies for other BCs…this would be obvious if the plate system were scaled a priori. Can remove this section. Typo error in eq. 3.73.

Response:

This section in the thesis is useful as it confirms that for ideal free/clamped boundary conditions, the eigenfrequencies expressions have the same form as that for the simply supported plate. This knowledge is required to prove that the geometric scaling factors remain invariant under any set of ideal free/clamped/simply-supported boundary conditions.

To emphasize this point, text on section 3.13.5 was corrected to: “For plates with boundary conditions other than a combination of ideal free/clamped/simply-supported boundaries, it is only necessary to be able to calculate or estimate the corresponding eigenfrequencies in order to identify the scaling factor for the z-direction.”

In response to “*Typo error in eq. 3.73*”, this has now been corrected.

p. 79. How much dx is larger than dz?

Response:

Equation 3.74 was corrected by adding s to the terms delta_x and delta_y. According to this equation, $s\mathrm{d}x = s^2\mathrm{d}z$ or, equivalently, $\mathrm{d}x = s\mathrm{d}z$.

In addition, the text in the same section 3.13.5 “Numerical efficiency of the scaling approach” was also corrected: “Therefore the time step using the scaling approach is *larger* than that obtained without scaling by a factor of up to s^2.“

p. 80. Limitation of scaling approach should be clearly described.

Response:

Section 3.13.6 has been extended to include the limitations that result from the numerical dispersion. The reduction of the Nyquist frequency that result from the use of an increased time step has also been pointed out in section 3.14.

Chapter 4

Lowest mode for plate here seems to be at about 100 Hz. But your measurement apparatus only works up to 140 Hz. Could use a single mode “lumped” approximation. Are you really testing the method here?

Response:

This comment doesn't seem to be specific to Chapter 4. There are plate modes at approximately 26Hz, 50Hz, 80Hz, 104Hz and 146Hz. Section 4.6 has been changed so that it only describes the experimental procedures with the results moved into Section 6.4.

Chapter 5

p. 110: sufficiently fine. Frequency range of interest here is 140 Hz. But scheme chosen emulates behaviour up to 5000 Hz! Do you really need this resolution/level of accuracy?

Response:

The 10k sampling frequency is dictated by the Courant condition, given both the spatial and time resolutions. The following improvement was made to the text in section 5.2.1 "Numerical resolution" to clarify this point: "the grid spacing was set to $\Delta x=0.0589$m, $\Delta y=0.0574$ m, $\Delta z=0.0578$m . Assuming a speed of sound of 343 m/s, this corresponds to $\Delta t= 9.77\times10^{-5}$s, i.e. a sampling frequency of 10240 Hz."

p. 110: you are not modelling the room boundaries here? I.e., this is a free field simulation?

Response:

This has been clarified through the addition of a new diagram in Figure 5.1.

pl. 111: But now, you are saying that you are indeed emulating the room boundary conditions. Why PMLs then? A diagram is essential here…the reader cannot follow (let alone reproduce) this.

Response:

This has been clarified through the addition of a new diagram in Figure 5.1.

p. 116: you now have k1, k2 appearing…you previously said that these were not used in the calculation. Now it is clear that these represent the total air volumes on either side of the absorber. But you already have FDTD for the room volume. Are you then using both a distributed and lumped representation for the room?

Response:

In order to make it clear that the spring-mass-spring model (and therefore k1 and k2) are only used to estimate the value of the resonance that occurs below the fundamental frequency of the room, the following text in was moved into a new paragraph in section 5.4 "Results - Point responses": "For the configuration of the room that was completely divided by the porous panel, the frequency at which this resonance occurs can be estimated by considering the room as a spring-mass-spring system,"

p. 118: OK matches. But improvement is very limited for MFM to very low frequency range (mass-dominated). Contour plots---some ok, some very poor matches (e.g., p. 140).

Response:

In response to "*OK matches. But improvement is very limited for MFM to very low frequency range (mass-dominated).*", the improvement is significant as indicated by the text in section 5.4 which notes that "When the panel completely divides the room volume the results show that the MFM is essential to correctly predict sound pressure levels near the spring-mass-spring resonance otherwise errors up to 20 dB can be incurred. ".

In response to "Contour plots---some ok, some very poor matches (e.g., p. 140).", those plots with close agreement and those where there is less agreement are indicated in the text.

Chapter 6

p. 148: thickness of plate?

Response:

Thickness of the plate was added to section 6.2 "FDTD implementation of a practical vibroacoustics model"

p. 150: thickness appears.

Response:

Thickness of the plate was added to section 6.2 "FDTD implementation of a practical vibroacoustics model"

p. 150: the simulations stabilise: what is meant here? You are not able to vary C.

Response:

Yes, *C* was fixed at 6000 m/s and the following text was added to section "6.2.6 – Stability of the simulation" : "Therefore the value C=6000 m/s was used in the simulations to calculate the value of dt using equation 2.41."

p. 152: 5% error in wave speed is a lot if you are running at 50 kHz+!

Response:

The frequency range of interest is below 200 Hz, as this is the highest frequency that was measured. This is indicated in section 6.5.2 - "Comparison of measured and predicted contour plots": "The discussion is limited to frequencies below 200 Hz since this corresponds to the highest frequency of the measurements."

p. 152: BCs for plate---are you using free conditions here?

Response:

This is now clear, as the text of section 6.2 - "FDTD implementation of a practical vibroacoustics model" was modified and now reads:

“To assess whether the scaling approach and simplified solid-air boundary conditions described in chapter 3 can be applied to practical vibroacoustic problems, a model of an a simply-supported 5 mm thick aluminium plate inside a small reverberation chamber was created using FDTD”

p. 160: Define HV.

Response:

The “H” and “V” labels in table 6.5 now appear in either red or green, and the meaning of these colours has been added to section 6.5.2: “Where there is a lack of agreement in either the horizontal or the vertical plane for the same mode, a red coloured "H" (horizontal) or "V" (vertical) is used. Conversely, a green "H" or "V" indicates close agreement in the horizontal or the vertical planes, respectively.”

p. 161: Better to show source location in contour plots to easily understand transfer functions.

Response:

The source location has been added to the plots as a black cross in Figures 6.4 – 6.18 a) and b). The text on section 6.5.1 “Comparison of measured and predicted transfer functions” was updated to: “with the outline of the plate indicated using solid black lines and the source location indicated using a black cross.”

General comments

- There is a lack of scientific discussion in Chapters 5 and 6, i.e. criticize their methods, compare their results to previous literature. In particular, advantages of the moving frame model (MFM) and two new modelling approaches (scaling approach and simplified boundary conditions) can be clearly explained.

  Response:

  Changes to Chapter 5:
  Experimental validation of FDTD for a small room that is partially or completely divided by the porous panel has not been published by others in the literature; however, it is possible to compare results with previous literature for the empty room. Hence, in section 5.5.2, a critical comparison with previous literature from Olesen is made in the results obtained for the empty room configuration stating "The level of agreement obtained in the comparison between FDTD results and experimental data for the empty room configuration is a significant improvement on that obtained in the work of Olesen [92] which (a) used a coarser measurement grid (60 cm x 60 cm) to validate the finite difference predictions, (b) was limited to a horizontal grid plane and (c) used 10dB steps in the contour plot which meant that it was not possible to identify the details between nodal and anti-nodal planes.".

  The main advantage of the MFM has been clarified in section 5.6 "Conclusions" stating "The results show that the MFM enabled the FDTD model to estimate the higher response caused by this spring-mass-spring resonance.".

  Cross-correlation coefficients between measured and predicted impulse responses have now been included in Figures 5.6 -5.10. These coefficients are relatively high (range 0.77 – 0.91) so they further confirm the close agreement between measurements and predictions. The values of the cross-correlation coefficients are similar to those obtained by Sakamoto et al, which are in the range 0.8 to 0.87. However, the situations are quite different, Sakamoto's impulse responses were determined in a large concert hall with numerous diffusing elements whereas the impulse responses presented in this work were determined in a small room where the sound field is primarily determined by the modal response.

  Changes to Chapter 6:

  The advantages of the scaling approaches and the simplified boundary approach have been clarified in section 6.6 "Conclusions" stating "It was possible to obtain these numerical results using an ordinary desktop computer due to the computational advantages enabled by the simplified boundary and scaling approaches.".

  A comparison of the accuracy of measured and FDTD predicted eigenfrequencies with those in the work of Toyoda was added in section 6.4 "This difference between measurement and prediction is similar to that obtained in the work by Toyoda et al [69]. Although their geometry and structural supports were different, differences of approximately 10% can be identified in their impedance level diagrams.".

  Discussion of the damping models employed by Chaigne and Lambourg is now included in section 6.4 indicating why these were not used in this thesis, stating that "Chaigne and

Lambourg [92] indicate how internal damping and radiation damping could be incorporated in time-domain models for three basic mechanisms of damping, which they list as thermoelasticity, viscoelasticity and radiation. This potentially has practical application to lightly damped musical instruments such as a cymbal, but it is of limited use to engineering structures such as buildings, aircraft or marine structures where the total loss factor of plates is determined by the sum of the internal losses, radiation losses, losses due to additional damping layers and structural coupling losses. As the latter two losses tend to dominate, the approach of Chaigne and Lambourg was not incorporated, and experimentally-determined values of the damping were incorporated in the model.".

Specific comments

Chapter 3

- Advantages of two new approaches (simplified boundary approach and scaling approach) were described in 3.12.2 and 3.13.6 but they are too brief. In particular, in 3.13.6, descriptions of limitations are longer than those of advantages.
-

  Response:

  The advantages of the simplified boundary and scaling approaches are that they both lead to the use of larger spatial resolutions (which in turn will make the simulations run faster), and in addition, in the case of the scaling approach, fewer cells are required than when using a non-scaled model (which will also make the simulations run faster). In response to "*Advantages of two new approaches (simplified boundary approach and scaling approach) were described in 3.12.2 and 3.13.6 but they are too brief*", the opening paragraphs of Section 3.12.1 "Theoretical background" have now been expanded (partly in response to other comments from the examiners). This has given the opportunity to clarify and expand on the advantages. Both of the advantages described above are given in 3.12.2 and 3.13.6, but it should be noted that the title of section 3.12.2 is "Example application" and the role of this section is to reinforce (through an example) the increase in space step which leads to computational benefits because of the larger FDTD time step; the opening sentence has been changed to reinforce this. Note that it is not possible to further expand on the descriptions of the advantages in the text without repetition.

  In response to *"In particular, in 3.13.6, descriptions of limitations are longer than those of advantages."* it is clear that as other sections in 3.13 gave the advantages it is not appropriate to repeat them; hence this section is now renamed "Limitations" and focuses only on the limitations and has been expanded to give more detailed consideration to the limitation of numerical dispersion.

Chapter 4

- P89: Figure 4.9 should be presented on page 89 along with the descriptions.

  Response:

  Yes, current figure 4.5 "Setup used for the acoustic measurements" (previously 4.9) has been moved to current section 4.4.2 - "Equipment".

Chapter 6

- P158: In Figure 6.5, there were some differences in terms of sound pressure level but it was described that there were close agreements – these differences are reasonable? If not, it would

be better to say there was a close agreement in terms of spatial variation but it is not the case for SPLs.

Response:

Yes, the statement was too general and has been corrected to “At frequencies corresponding to plate modes f_{11} and f_{12} that occur below the lowest room mode f_{010}, the contour plots in Figures 6.5 and 6.6 show agreement between measurements and FDTD in terms of the spatial variation with particularly close agreement in Figure 6.5(a,b)}.”.

- P160: Subjective terms? What is the criteria or value to say it is good or it is H V (?).

  Response:

  In order to clarify what is meant by subjective terms, it is now noted in current section 6.5.2 that “This comparison is primarily carried out in subjective terms as no exact numerical indicator or threshold is used to categorise the level of agreement.”. The caption for Table 6.5 has been changed to “Evaluation of the agreement between measured and predicted mode shapes and transfer function levels”. Using Table 6.5, the cases where the agreement is close in either level or spatial variation are now labelled with “HV” in colour code (red for agreement, green for lack of agreement), where the H stands for horizontal and the V stands for vertical. This is now described in the text of current section 6.5.2 “Comparison of measured and predicted contour plots”.

- P176: No evidence about 63 dB and 66 dB in Figure 6.19. Are they ±3 dB and ±6 dB?

  Response:

  63 dB and 66 dB were a typo and have now been corrected to ±3 dB and ±6 dB.

Chapter 7

- P188: Please define the experimental error.

  Response:

  The statement in section 7 “Conclusions” mistakenly referring to “experimental error” has been rephrased as “The general finding from the comparison of measured and predicted pressure-to-force transfer functions is that FDTD is capable of predicting the spatial variation of sound pressure in close agreement with measured data.”.

Acknowledgements

I am extremely grateful to my supervisor Professor Carl Hopkins for providing insightful guidance for the whole of my PhD. Carl has always managed to motivate me, even at times when the experiments or computations didn't go so well. Without Carl's extraordinary support and understanding, this work would have never happened.

I would also like to thank Dr Gary Seiffert for providing invaluable advice and help in the laboratory activities and measurements.

I am also grateful to Professor Barry Gibbs, for the insightful discussions on physics and precious advice.

I would like to show my sincere gratitude towards Carl, Gary and Barry altogether for trusting me educational roles in the IOA Lab week and in the IOA certificate of competence in environmental noise measurement at the Acoustics Research Unit (ARU) of the University of Liverpool. I have thoroughly enjoyed these most valuable work experiences and I will never forget them.

I would like to thank my colleagues in the ARU, including David Wilson, Xing Wang, Christoph Hoeller, Saul Mate-Sid, Hyoseon Jang, Marios Filippoupolitis, Claire Churchill, Susumu Hirakawa, Yicheng Yu, Xiaoxue Shen and many others for all their support, advice and enjoyable time they have given me.

Last, but not the least, I would like to thank Lauren, my love, for all her incredible patience and motivation and my Family for all their infinite support.

Abstract

Finite Difference Time Domain (FDTD) is a method used to predict field variables related by a wave equation. This thesis focuses on the development and experimental validation of FDTD for low-frequency applications in acoustics and vibroacoustics such as in automotive, aeronautic, marine and building constructions.

For acoustic applications, the thesis focuses on FDTD modelling of porous panels inside an acoustic cavity. This required development of a new modelling approach, the Moving Frame Model (MFM) for porous materials with a non-stationary frame. The MFM assumes lumped mass behaviour of the porous panel which is coupled to the FDTD update equations that incorporate the Rayleigh model. Experimental validation used a small reverberant room when empty, with a porous panel partially dividing the room, and with a porous panel completely dividing the room. For vibroacoustic applications, the thesis focuses on sound radiation from a plate into an acoustic cavity. Two new modelling approaches were developed to significantly reduce the computational cost for FDTD with vibroacoustic problems; a scaling approach to significantly increase the computational efficiency and modelling solid/air boundary conditions to simplify their implementation. Experimental validation used a point excited, thin aluminium plate inside a small reverberant chamber.

Both the acoustics and vibroacoustics FDTD modelling approaches were successfully validated against experimental results. For two spaces completely separated by a porous panel, the MFM accounted for a spring-mass-spring resonance which results in a peak in the response below the fundamental room mode. Close agreement between experimental results and FDTD validates the model as well as implementation of the loudspeaker as a hard velocity source. For the vibroacoustics application, the scaling approach with simplified boundaries resulted in a significant reduction in computation time. Experimental validation confirms the validity of implementing a thin plate undergoing bending wave motion as a three-dimensional solid that can support multiple wave types. Below the lowest room mode, close agreement between FDTD and measurements shows the existence of large variations in sound pressure level. This confirms the importance of validated vibroacoustic models to predict sound fields inside acoustic cavities in the low-frequency range.

List of symbols and abreviations

Abreviations	
1D, 2D, 3D	One, two, three dimensions
B&K	Brüel & Kjær
DFT	Discrete Fourier Transform
FD	Finite-Difference
FDTD	Finite-Difference Time-Domain
FFT	Fast Fourier Transform
FRF	Frequency Response Function
IFFT	Inverse Fast Fourier Transform
IIR	Infinite Impulse Response filter
MFM	Moving Frame Model
NMM	Normal Mode Model
PML	Perfectly Matched Layers

Lower case symbols	
a	Acceleration (m/s^2)
c	Phase velocity of sound in air (m/s)
$\hat{\boldsymbol{e}}_{\boldsymbol{i}}$	Cartesian unit vectors
f	Frequency (Hz)
f_{B}	Thin plate limit for bending waves (Hz)
h	Plate thickness (m)
$\mathbf{i}$	Imaginary unit ($\sqrt{-1}$)
i	Discrete space index used in FDTD
j	Discrete space index used in FDTD
k	Wavenumber (m^{-1})
$\mathbf{n}$	Normal unit vector
n	Discrete time index used in FDTD
p	Sound pressure (N/m^2)
r	Airflow resistivity ($Pa.s/m^2$)
r_{o}	Radius of a pulsating sphere (m)
s_{o}	Surface velocity of a pulsating sphere (m/s)
t	Time (s)
t_{o}	Time offset used in Gaussian pulses (s)
$\overrightarrow{u}$	Displacement (m)
v_{o}	Surface velocity of a pulsating sphere (m/s)
v	Velocity (m/s)
$\tilde{v}_n$	Complex velocity normal to a vibrating surface (m/s)
$\overline{v}$	Average velocity (m/s)

Upper case symbols	
E	Young's modulus (N/m^2)
F	Force (N)
$\mathcal{F}$	Fourier transform
G	Shear modulus (N/m^2)
L	Length (m)
Q	Source strength (m^3/s)
R	Acoustic reflection coefficient (-)
R_s	Specific airflow resistance (Pa.s/m)
S	Surface area (m^2)
T	Temperature (°C)
V	Volume (m^3)
Z_{o}	Characteristic impedance for air (Pa.s/m)
$Z_{\mathrm{a,n}}$	Normal acoustic surface impedance (Pa.s/m)
$Z_{\mathrm{a,s}}$	Specific acoustic impedance (-)

Greek symbols	
δ	Damping constant (s^{-1})
δ_{ij}	Kronecker delta
ϵ	Strain tensor
ε	Rate-of-strain tensor
λ	Wavelength(m), First Lamé constant (N/m^2)
η	Loss factor (-)
μ	Second Lamé constant (N/m^2)
ν	Poisson's ratio (-)
ϕ	Phase angle (rad)
ρ	Density of solid medium (kg/m^3)
ρ_{o}	Density of air medium (kg/m^3)
σ	Stress (N/m^2)
σ_{o}	Gaussian pulse width (s)
ω	Angular frequency (rad/s)

Contents

1 Introduction

1.1 Background

Finite Difference Time Domain (FDTD) is a numerical method that is used to predict the distribution of field variables that are related by a wave equation. The method is primarily based on a calculation cell first proposed by Yee [1], introduced to solve the Maxwell's equations of electromagnetism. However, the use of FDTD has expanded into a variety of other fields and applications. Some examples include:

- Acoustics - With the work of Kunz [2] and Botteldooren [3], FDTD has been used to solve a number of problems in several fields of acoustics, such as room acoustics [4] and environmental acoustics [5, 6];
- Geophysics - The modelling of infrasonic radiation from volcanic eruptions [7], Borehole well prospection [8, 9] and human interaction with landmines [10];
- Medical Sciences - FDTD has been used to model ultrasound propagation within medical contexts [11, 12];
- Seismology: FDTD has been widely used for the study of seismic wave propagation [13] and earthquakes [14, 15].

FDTD is a direct time domain method, where the second-order wave equation or a number of first-order equations of the problem under consideration is solved for a given period of time. As a direct time domain method, it is well suited for the visualization of both 2D and 3D transient sound fields [16, 17].

The FDTD method approximates the solution to the wave equation by replacing its differentials with their finite-difference approximations, forming a system of al-

gebraic equations. It calculates the solution to this system of algebraic equations at a number of points in the domain, usually ordered in a rectangular mesh but many other mesh types have also been used. Depending on the implementation, the number of algeabric equations must be at least one per point in space. Since typically the whole domain of the problem must be included, the computational cost in FDTD increases as the highest frequency limit is raised, since the number of algebraic equations necessary to solve the problem is accordingly higher.

1.2 Motivation

In automotive, aeronautic, marine or building constructions there are small spaces where it is necessary to predict low-frequency sound fields (typically below 250Hz) at the design stage. The aim of this thesis is to develop and experimentally validate the FDTD method for low-frequency applications in acoustics and vibroacoustics that are relevant to these areas of engineering.

For acoustic applications, this thesis focuses on FDTD modelling of porous materials that divide or partially-divide an acoustic space in the low-frequency range. Such situations could be an idealised representation of seats or dividers in car/aircraft/-ship cabins or small rooms with excitation by an acoustic source such as a human speaker or loudspeaker. Experimental work in this thesis showed that resonance peaks can occur below the fundamental frequency of the room which prompted the development of a new Moving Frame Model (MFM) to account for whole-body motion of porous panels.

In most noise control situations it is common for sound to be radiated into an acoustic space by a vibrating plate. However, the application of FDTD to vibroacoustic problems (even with small spaces) is limited by computational demands. Hence a new scaling approach is developed in this thesis to significantly increase the efficiency of FDTD models. In addition, a new approach to model solid/air boundary conditions was developed to simplify the implementation of these type of bound-

aries in FDTD. This thesis considers the vibroacoustic problem for a mechanically point-excited thin aluminium plate radiating into a small acoustic space.

1.3 Outline of the thesis

Chapter 2 reviews the literature for acoustic FDTD and gives the theoretical background for airborne sound propagation and its implementation in FDTD. A Moving Frame Model (MFM) is introduced to model porous panels that partition a space.

Chapter 3 gives the theory of structure-borne sound propagation along with a literature review and a description of vibroacoustic FDTD modelling. Two new modelling approaches are introduced in this chapter, the simplified boundary and scaling approaches.

Chapter 4 describes the experimental work used to validate the FDTD models. The acoustic model considered a small reverberant chamber that was divided or partially-divided by a porous panel and excited by a single loudspeaker. The vibroacoustic model considered the same reverberant chamber with a point-excited plate.

Chapter 5 describes the implementation of the acoustic FDTD model for the experimental validation of the acoustic FDTD model, and presents the comparisons of FDTD and measurements with analysis.

Chapter 6 describes the implementation of the vibroacoustic FDTD model for the experimental validation of the vibroacoustic FDTD model, and presents the comparisons of FDTD and measurements with analysis.

Chapter 8 gives the conclusions and suggestions for future work.

2 Implementation of FDTD for acoustics

2.1 Introduction

For low-frequency problems (typically below 250Hz) in room acoustics, the Finite-Difference Time-Domain method (FDTD) has been shown to have significant potential [18, 16, 19, 20]. This chapter addresses both theoretical and numerical aspects that are required for a full understanding of the implementation of the FDTD method regarding its application in acoustics.

Section 2.2 summarizes the theory used to model sound propagation in air, where the first-order partial differential equations of momentum and continuity equations are introduced.

Section 2.3 details the field variables necessary to describe acoustics problems and the corresponding implementation in FDTD. The FDTD update momentum and continuity equations are also derived and detailed to illustrate their implementation using a computer programming language. These derivations will be carried out in pseudo-code form, in order to remain neutral as far as programming languages are concerned, although source code written in Python is provided in Appendix III.

Section 2.4 contains a literature review, where the connection of the FDTD method to acoustics modelling and the differences between the main approaches to FDTD are discussed.

Sections 2.5 and 2.6 discuss the stability and numerical dispersion of FDTD algorithms.

Sound sources are discussed both from a theoretical point of view in section 2.7 and from a numerical point of view in section 2.8, focussing in particular on the FDTD

modelling of a sub-woofer.

Section 2.9 describes the theoretical aspects of modelling acoustic boundary conditions, that are necessary to understand their FDTD implementation using digital filters, which is described in section 2.10.

Section 2.11 outlines the theoretical background used to describe the acoustic behaviour of porous materials using the Rayleigh model. The theory developed for the implementation of the Moving Frame Model (MFM) is also described in this section. The corresponding FDTD implementation of the Rayleigh model for a porous absorber and of the MFM is described in section 2.12.

2.2 Sound propagation in acoustic media

This section addresses theoretical aspects of sound propagation in acoustic media and its generation and interaction with acoustic boundaries.

2.2.1 Euler equation of motion

If air is assumed to be an inviscid fluid, no viscous forces of any type act on any portion of the air medium. Under this assumption, the fluid cannot sustain any shear stress. In addition, the normal stress components (σ) at any point in the fluid are all identical and equal to the value of the pressure (p) at that point. Hence, the stress tensor reduces to [21]:

$$\sigma_{xy} = 0, \quad \sigma_{xz} = 0, \quad \sigma_{yz} = 0 \tag{2.1}$$

$$\sigma_{xx} = -p, \quad \sigma_{yy} = -p, \quad \sigma_{zz} = -p \tag{2.2}$$

The use of the stress tensor components is particularly important when defining vibroacoustic problems as discussed in chapters 3 and 6. The momentum equation relates the particle velocity of an element of fluid with the corresponding pressure applied to it. In the case of an inviscid fluid, the momentum equation is given by the Euler equation [2]:

$$\frac{\partial v_i}{\partial t} = -\frac{1}{\rho_o}\nabla p \tag{2.3}$$

where ρ_o is the density of air and ∇ is the gradient operator. This is a vector equation whose Cartesian components are as follows:

$$\rho_o \frac{\partial v_x}{\partial t} = -\frac{\partial p}{\partial x} \tag{2.4}$$

$$\rho_o \frac{\partial v_y}{\partial t} = -\frac{\partial p}{\partial y} \tag{2.5}$$

$$\rho_o \frac{\partial v_z}{\partial t} = -\frac{\partial p}{\partial z} \tag{2.6}$$

2.2.2 Continuity equation

The continuity equation expresses conservation of mass for the fluid motion. The following form of the continuity equation (Eq. 2.7) takes into account both the conservation of mass and the equation of state for a perfect gas. It must be satisfied at all points in the acoustic medium:

$$\frac{\partial p}{\partial t} = -\rho_o c^2 \nabla \cdot v_i \tag{2.7}$$

where p is the acoustic pressure, v_i is the velocity vector and c is the speed of sound in air, which is given by [22]:

$$c = 331 + 0.6T \tag{2.8}$$

where T is the temperature of air in °C.

Expanding the index notation of equation 2.7 using Cartesian coordinates, the following form is obtained:

$$\frac{\partial p}{\partial t} = -\rho_o c^2 \left(\frac{\partial v_x}{\partial x} + \frac{\partial v_y}{\partial y} + \frac{\partial v_z}{\partial z} \right) \tag{2.9}$$

2.3 Implementation of the FDTD method

2.3.1 Field variables in acoustics

The field variables that are used to model sound propagation through an acoustic medium are the acoustic pressure p and the acoustic particle velocity v_i of the medium. The acoustic pressure is a scalar variable, i.e. it is described only by a single component at each point in space. For the medium of air it indicates a deviation from the static equilibrium value of atmospheric pressure and can therefore assume negative values. The particle velocity v_i is a vector variable, comprising n components in n-dimensional space. It indicates the direction of the cyclic motion of air particles that is associated with the propagation of sound. In this thesis, acoustic pressure and particle velocity are denoted as field variables for the acoustics problems.

2.3.2 Implementation of field variables in FDTD

Use of FDTD in this thesis follows from the basic approach proposed by Bootledoren [18], where the variables of velocity and pressure are offset both in time and in space, in an arrangement known as a 'staggered grid' [23]. The diagram in Figure

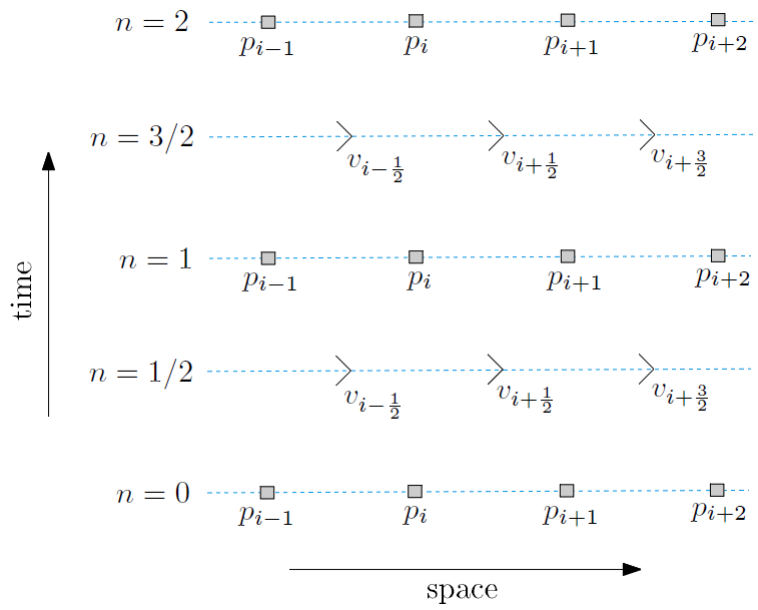

Figure 2.1: One-dimensional staggered FDTD grid.

2.1 illustrates a staggered grid for a one-dimensional space. A staggered grid representing two-dimensional space is shown in Figure 2.2. This type of grid arrangement is often called a Yee cell, after Kane Yee, who originally proposed it in 1966 [1]. By convention, the pressure variables are assigned integers for their corresponding time and spatial indexes, whereas the velocity variables are assigned fractions.

The implementation of the staggered grid requires a careful mapping between the fraction indexes shown in Figures 2.1 and 2.2 and the corresponding computational indexes implemented in a digital computer programming language, that must be integers. One practical example of the implementation of the field variable indexes can be found in the source code written in Python in Appendix III, with the corresponding output shown in Figure 2.4. Reference [24] also contains a code snippet for use in Matlab/Octave. In addition, the book by Sullivan [25] contains code written in the C programming language that covers one-, two- and three-dimensional electromagnetic and acoustic FDTD simulations, including the implementation of the PML boundaries.

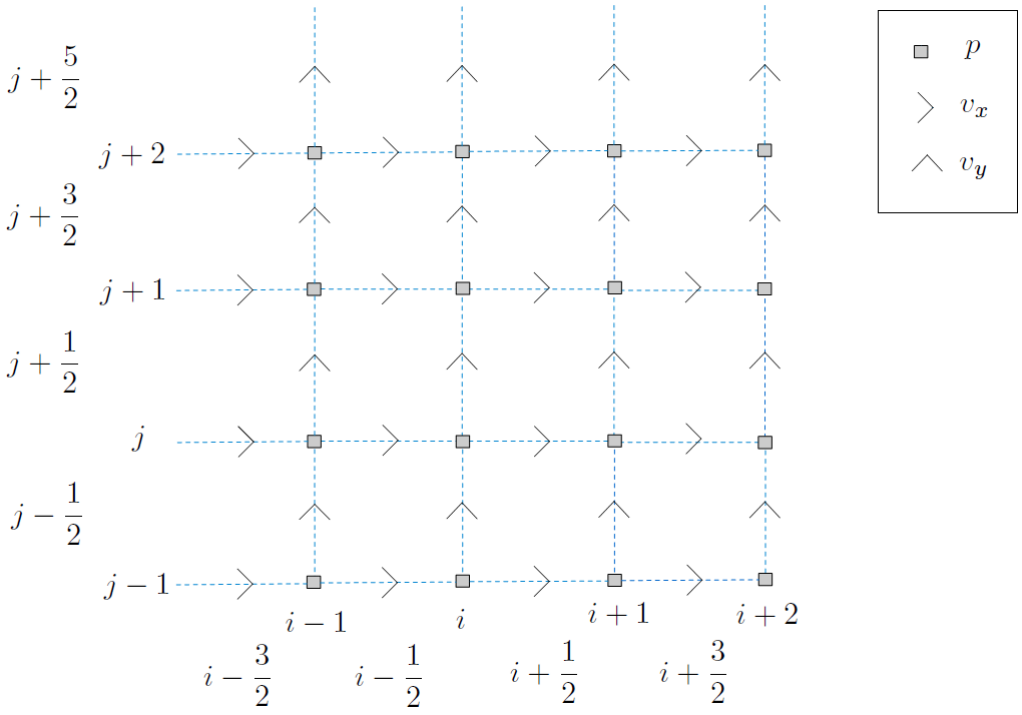

Figure 2.2: Two dimensional acoustic FDTD grid.

2.3.3 Discrete form of the Euler equations

In three dimensions, the discretization of the momentum equations 2.4-2.6 leads to the following set of algebraic equations:

$$v_x^{n+\frac{1}{2}}\Big|_{i+\frac{1}{2},j,k} = v_x^{n-\frac{1}{2}}\Big|_{i+\frac{1}{2},j,k} - \frac{\Delta t}{\rho_o \Delta x}\left(p^n|_{i+1,j,k} - p^n|_{i,j,k}\right) \tag{2.10}$$

$$v_y^{n+\frac{1}{2}}\Big|_{i,j+\frac{1}{2},k} = v_y^{n-\frac{1}{2}}\Big|_{i,j+\frac{1}{2},k} - \frac{\Delta t}{\rho_o \Delta y}\left(p^n|_{i,j+1,k} - p^n|_{i,j,k}\right) \tag{2.11}$$

$$v_z^{n+\frac{1}{2}}\Big|_{i,j,k+\frac{1}{2}} = v_z^{n-\frac{1}{2}}\Big|_{i,j,k+\frac{1}{2}} - \frac{\Delta t}{\rho_o \Delta z}\left(p^n|_{i,j,k+1} - p^n|_{i,j,k}\right) \tag{2.12}$$

The discretization of the continuity equation (2.9) results in the equation:

$$p^{n+1}\Big|_{i,j,k} = p^{n}|_{i,j,k} - \frac{\rho_o c^2 \Delta t}{\Delta x}\left(v_x^{n+\frac{1}{2}}\Big|_{i+\frac{1}{2},j,k} - v_x^{n+\frac{1}{2}}\Big|_{i-\frac{1}{2},j,k}\right) - \\ - \frac{\rho_o c^2 \Delta t}{\Delta y}\left(v_y^{n+\frac{1}{2}}\Big|_{i,j+\frac{1}{2},k} - v_y^{n+\frac{1}{2}}\Big|_{i,j-\frac{1}{2},k}\right) - \\ - \frac{\rho_o c^2 \Delta t}{\Delta z}\left(v_z^{n+\frac{1}{2}}\Big|_{i,j,k+\frac{1}{2}} - v_z^{n+\frac{1}{2}}\Big|_{i,j,k-\frac{1}{2}}\right) \quad (2.13)$$

However, as noted in section 2.3.2, care must be taken when implementing equations 2.10-2.13 using a programming language. The mapping between the integer and non-integer indices and the corresponding computational indices needs to be considered. A two-dimensional example of such a mapping is shown in Figure 2.3, where the computational indices are indicated in blue and red for the pressure and velocity nodes, respectively.

2.3.4 FDTD update equations in two dimensions

To gain insight into the implementation of the FDTD three-dimensional update equations, it is convenient to consider the two-dimensional version of the discrete field equations:

$$p^{n+1}\Big|_{i,j} = p^{n}|_{i,j} - \frac{\rho_o c^2 \Delta t}{\Delta x}\left(v_x^{n+\frac{1}{2}}\Big|_{i+\frac{1}{2},j} - v_x^{n+\frac{1}{2}}\Big|_{i-\frac{1}{2},j}\right) - \\ - \frac{\rho_o c^2 \Delta t}{\Delta y}\left(v_y^{n+\frac{1}{2}}\Big|_{i,j+\frac{1}{2}} - v_y^{n+\frac{1}{2}}\Big|_{i,j-\frac{1}{2}}\right) \quad (2.14)$$

$$v_x^{n+\frac{1}{2}}\Big|_{i+\frac{1}{2},j} = v_x^{n-\frac{1}{2}}\Big|_{i+\frac{1}{2},j} - \frac{\Delta t}{\rho_o \Delta x}\left(p^{n}|_{i+1,j} - p^{n}|_{i,j}\right) \quad (2.15)$$

$$v_y^{n+\frac{1}{2}}\Big|_{i,j+\frac{1}{2}} = v_y^{n-\frac{1}{2}}\Big|_{i,j+\frac{1}{2}} - \frac{\Delta t}{\rho_o \Delta y}\left(p^{n}|_{i,j+1} - p^{n}|_{i,j}\right) \quad (2.16)$$

First, the derivation will concern the computation of the spatial indices i, j and then it will consider the computation of the time index n. In order to visualise the spatial

implementation process of the two-dimensional field equations, it is useful to consider a finite-difference stencil [26]. The FD stencil considered for equation 2.14 is shown in Figure 2.3. In order to convert equation 2.14 into a form that can be directly implemented using a programming language it is necessary to map the indexes of pressure and velocity nodes of the stencil into computational indexes. For the sake of simplicity, the pressure at node (i, j) is considered for the derivation. Using Figure 2.3 the following mapping between analytical and computational indexes are obtained for the pressure and velocity nodes:

$$p^{n+1}\Big|_{i,j} \rightarrow p^{n+1}\Big|_{2,1} \tag{2.17}$$

$$p^{n}|_{i,j} \rightarrow p^{n}|_{2,1} \tag{2.18}$$

$$v_x^{n+\frac{1}{2}}\Big|_{i+\frac{1}{2},j} \rightarrow v_x^{n+\frac{1}{2}}\Big|_{3,1} \tag{2.19}$$

$$v_x^{n+\frac{1}{2}}\Big|_{i-\frac{1}{2},j} \rightarrow v_x^{n+\frac{1}{2}}\Big|_{2,1} \tag{2.20}$$

$$v_y^{n+\frac{1}{2}}\Big|_{i,j+\frac{1}{2}} \rightarrow v_y^{n+\frac{1}{2}}\Big|_{2,2} \tag{2.21}$$

$$v_y^{n+\frac{1}{2}}\Big|_{i,j-\frac{1}{2}} \rightarrow v_y^{n+\frac{1}{2}}\Big|_{2,1} \tag{2.22}$$

The variables in the update equation 2.14 have been transposed to a stencil at a particular location centered at position (2,1). Equation 2.14 can now be written for

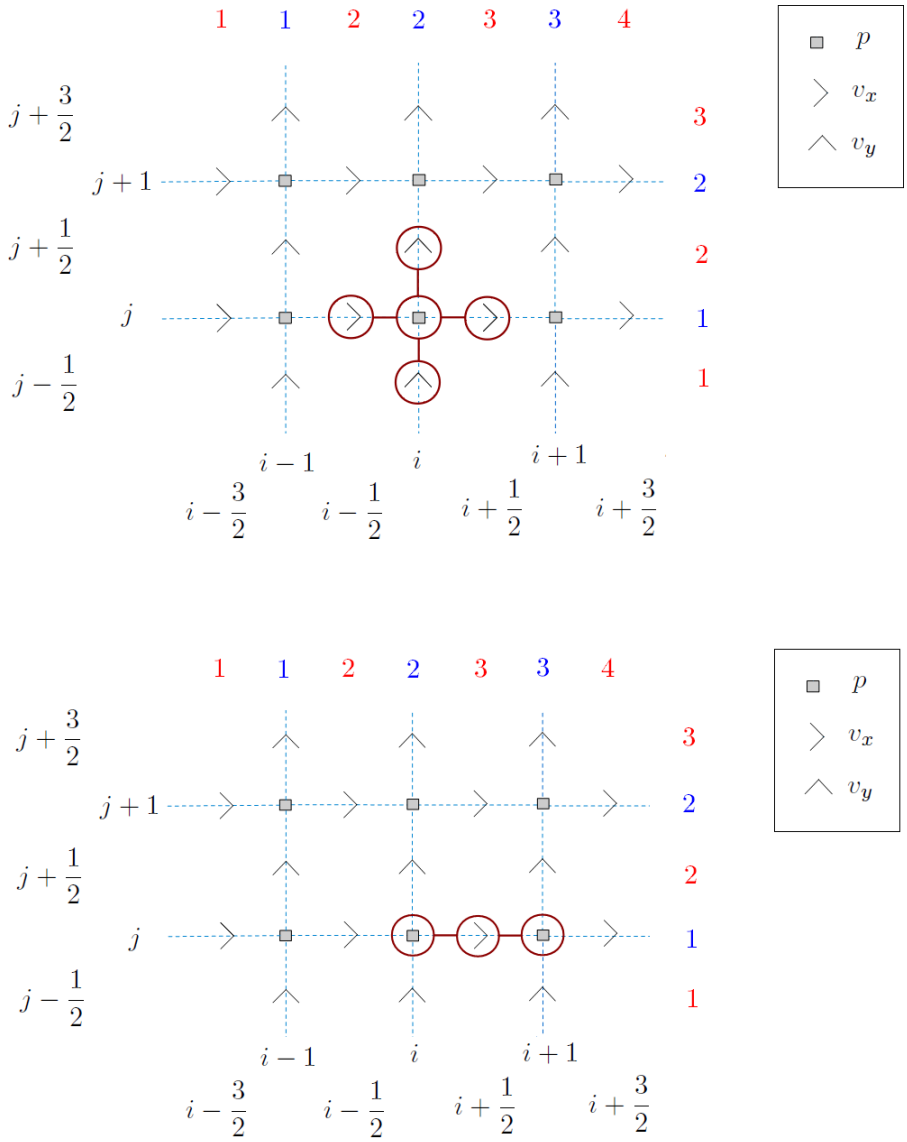

Figure 2.3: Stencil for equation (2.3.4). The computational indices corresponding to integers (blue) and fractions (red) are also indicated

this particular grid position:

$$p^{n+1}\Big|_{2,1} = p^{n}|_{2,1} - \rho_o c^2 \Delta t \left[\frac{1}{\Delta x} \left(v_x^{n+\frac{1}{2}}\Big|_{3,1} - v_x^{n+\frac{1}{2}}\Big|_{2,1} \right) - \frac{1}{\Delta y} \left(v_y^{n+\frac{1}{2}}\Big|_{2,2} - v_y^{n+\frac{1}{2}}\Big|_{2,1} \right) \right] \quad (2.23)$$

The terms $p^{n+1}|_{2,1}$ and $p^{n}|_{2,1}$ are effectively the same variable where the value of $p^{n}|_{2,1}$ is overwritten by the updated value of $p^{n+1}|_{2,1}$. Hence, as the time index n increases, the values of the variables p, v_x and v_y are consecutively overwritten by their updated instances. It is therefore possible to simplify the notation used in equation 2.3.4 and drop the superscript n:

$$p|_{2,1} = p|_{2,1} - \rho_o c^2 \Delta t \left[\frac{1}{\Delta x} \left[v_x|_{3,1} - v_x|_{2,1} \right] - \frac{1}{\Delta y} \left[v_y|_{2,2} - v_y|_{2,1} \right] \right] \quad (2.24)$$

Equation 2.24 is the continuity update equation for the pressure node centered at position (2,1). It is important to consider the variables p, v_x and v_y to be implemented as bidimensional arrays with computation indexes given by i and j. It is now necessary to generalise equation 2.24 to any node (i, j) in the grid:

$$p|_{i,j} = p|_{i,j} - \rho_o c^2 \Delta t \left[\frac{1}{\Delta x} \left[v_x|_{i+1,j} - v_x|_{i,j} \right] - \frac{1}{\Delta y} \left[v_y|_{i,j+1} - v_y|_{i,j} \right] \right] \quad (2.25)$$

Equation 2.25 is the two-dimensional continuity update equation that is actually implemented in a computer program and is valid for any spatial indices (i,j). The update momentum equations for the velocity in the x- and y-directions can be derived in the same manner. Considering the velocity update equation 2.15 and Figure 2.3-b the following mapping between analytical and computational indexes

are obtained for the pressure and velocity nodes along the x-direction:

$$v_x^{n+\frac{1}{2}}\Big|_{i+\frac{1}{2},j} \rightarrow v_x^{n+\frac{1}{2}}\Big|_{3,1} \tag{2.26}$$

$$v_x^{n-\frac{1}{2}}\Big|_{i+\frac{1}{2},j} \rightarrow v_x^{n-\frac{1}{2}}\Big|_{3,1} \tag{2.27}$$

$$p^n|_{i+1,j} \rightarrow p^n|_{3,1} \tag{2.28}$$

$$p^n|_{i,j} \rightarrow p^n|_{2,1} \tag{2.29}$$

Substituting the mapping defined by relations 2.26 - 2.29 into equation 2.15, the following equation is obtained:

$$v_x^{n+\frac{1}{2}}\Big|_{3,1} = v_x^{n-\frac{1}{2}}\Big|_{3,1} - \frac{\Delta t}{\rho_o \Delta x}\left[p^n|_{3,1} - p^n|_{2,1}\right] \tag{2.30}$$

Generalizing equation 2.30 to indices (i, j) and taking into account that $v_x^{n+\frac{1}{2}}$ is assigned the value of $v_x^{n-\frac{1}{2}}$, the following equation is obtained:

$$v_x|_{i,j} = v_x|_{i,j} - \frac{\Delta t}{\rho_o \Delta x}\left[p|_{i,j} - p|_{i-1,j}\right] \tag{2.31}$$

Following the same procedure for the velocity in the y-direction, the following equation is obtained:

$$v_y|_{i,j} = v_y|_{i,j} - \frac{\Delta t}{\rho_o \Delta y}\left[p|_{i,j} - p|_{i,j-1}\right] \tag{2.32}$$

For each time iteration n, equations 2.25 and 2.32 are computed and the field variables are consequently updated until the desired time duration for the simulation is reached. This update cycle can be visualised in the flow diagrams shown in Figure 2.13.

2.3.5 FDTD update equations in three dimensions

The extension of the update equations 2.25 and 2.32 to three-dimensional space follows directly from the two-dimensional case. The three-dimensional continuity update equation is given by:

$$p|_{i,j,k} = p|_{i,j,k} - \rho_o c^2 \Delta t \left[\frac{1}{\Delta x}\left(v_x|_{i+1,j,k} - v_x|_{i,j,k}\right) - \frac{1}{\Delta y}\left(v_y|_{i,j+1,k} - v_x|_{i,j,k}\right) - \frac{1}{\Delta z}\left(v_z|_{i,j,k+1} - v_z|_{i,j,k}\right)\right. \tag{2.33}$$

The 3D momentum update equations implemented in FDTD are given by:

$$v_x|_{i,j,k} = v_x|_{i,j,k} - \frac{\Delta t}{\rho_o \Delta x}\left[p|_{i,j,k} - p|_{i-1,j,k}\right] \tag{2.34}$$

$$v_y|_{i,j,k} = v_y|_{i,j,k} - \frac{\Delta t}{\rho_o \Delta y}\left[p|_{i,j,k} - p|_{i,j-1,k}\right] \tag{2.35}$$

$$v_z|_{i,j,k} = v_z|_{i,j,k} - \frac{\Delta t}{\rho_o \Delta z}\left[p|_{i,j,k} - p|_{i,j,k-1}\right] \tag{2.36}$$

2.4 Literature review of the FDTD method

The FDTD method was originally developed to solve practical problems in electromagnetism [1]. One of the earliest references to the analogy between the FDTD implementation of electromagnetic radiation and acoustic wave propagation routines was noted by Kunz [2], who described the possibility to use the Euler and the continuity equations as an acoustic FDTD analog to the Maxwell curl equations that are used to describe electromagnetic phenomena. Hence, most of the literature on FDTD for electromagnetic problems can be very useful for acoustics and references to these works will be made.

The FDTD method has been implemented in a number of different numerical approaches. In this section, some of the most important approaches and corresponding aspects that differentiate these such as field variables, type of numerical grids, use of implicit or explicit time solvers, approximation of space derivatives, and coordinate systems are discussed. The following sections provide a survey of different FDTD implementations.

2.4.1 Field variables

While the most common approach to acoustic FDTD requires both velocity and pressure fields to be calculated, there are alternative methods that only require the pressure field to be calculated [27]. One of the main advantages of requiring only the pressure field for the calculations is a significant saving in memory resources. However, representation of the acoustic boundary conditions is more complex requiring the implementation of digital filters. The formulation for both pressure and particle velocity from the work of Yokota et al. [16] has been used in this thesis.

2.4.2 Grid geometry

The use of Cartesian numerical grids in FDTD has a natural disadvantage: it must represent any curved boundaries by using staircase geometry, which can be inefficient when the spatial resolution required is high. A variety of coordinate systems other than the standard Cartesian coordinate system have been implemented in FDTD. Examples include a hexagonal coordinate system that was used to model the propagation of electromagnetic radiation on the surface of the earth caused by lightning [28]. Moreover, the use of conformal grids overcomes this disadvantage by allowing the use of non-regular grids, which will allow modelling geometries that cannot be specified correctly using a specific type of coordinate system, such as Cartesian coordinates. Several conformal FDTD methods are available in the literature [29, 30, 31]. In addition to the use of non-Cartesian coordinate systems and non-regular grids, another closely related method to FDTD, the finite volume method [32, 33] can also be used to accurately represent curved surfaces. In this thesis, the FDTD models do not contain curved surfaces; hence, the use of Cartesian grids provides a good approximation to their geometry.

2.4.3 Explicit and implicit methods

In the original FDTD formulation [1], time marching is explicit, and therefore the Courant condition imposes a limit on the maximum time step required to obtain stable simulations. Alternative formulations exist that are not subject to the requirements dictated by the Courant condition. One of these formulations is known as the Alternating-Direction Implicit FDTD (ADI-FDTD) and is known to be unconditionally stable [34], meaning that simulations are stable even if the time step is above that dictated by the Courant condition. In this thesis the explicit method is chosen for its simplicity and the need for additional resources is compensated by using a new scaling approach.

2.4.4 Approximation of space derivatives

In order to approximate the spatial derivative of pressure, p, that is required to solve the FDTD equations (section 2.3.3), standard FDTD uses two neighbouring points from the domain (taking the x-direction as an example):

$$\left.\frac{dp}{dx}\right|_{x=i\Delta x}^{n} \approx \frac{p|_{i+1}^{n} - p|_{i}^{n}}{\Delta x} \tag{2.37}$$

where n denotes the time index upon which the spatial derivative is evaluated. Alternative FDTD formulations have been proposed which use four points from the domain, in what is known as a fourth-order finite-difference approximation [35, 36]:

$$\left.\frac{dp}{dx}\right|_{x=i\Delta x}^{n} \approx \frac{-p|_{i+2}^{n} + 27\,p|_{i+1}^{n} - 27\,p|_{i-1}^{n} - p|_{i-2}^{n}}{24\Delta x} \tag{2.38}$$

Both second-order and fourth-order approaches use local functions to approximate spatial derivatives of a given analytical equation. A class of methods called 'spectral methods' use global functions to approximate spatial derivatives, resulting in more accurate approximations of the spatial derivatives [37, 38]. These global functions can be found using the differentiation property of the Fourier transform [39]:

$$\frac{dp(x)}{dx} \overset{FT}{\longleftrightarrow} \mathbf{i}k_x\tilde{P}(k_x) \tag{2.39}$$

where $\tilde{P}(k_x)$ is the complex Fourier transform pair of $p(x)$. Equation 2.39 establishes a connection between the derivatives of a function and its Fourier transform. The derivative of $p(x)$ can therefore be approximated by:

$$\frac{d}{dx}p(i\Delta x) \approx \mathcal{F}^{-1}\left\{\mathbf{i}k_x\mathcal{F}\left\{p(i\Delta x)\right\}\right\} \tag{2.40}$$

where the symbol $\mathcal{F}$ and $\mathcal{F}^{-1}$ denote the Fourier transform and the respective inverse. Numerically the Fourier transform of a function is often evaluated using the

Fast Fourier Transform (FFT) algorithm. This class of methods can be implemented with widely available, validated FFT and IFFT routines readily available in most numerical software libraries.

In this thesis the two-point approximation of the spatial derivatives is used.

2.4.5 Types of sound sources

Different approaches can be used to implement sound sources in FDTD. If the source calculation cells follow the values dictated by the driving function, irrespective of the state of their neighbour cells the type of source is called a 'hard' source, since it scatters sound waves that are incident upon it. On the other hand, if a sound source follows the driving function but does not scatter the sound field in which it is embedded, the source is termed a 'transparent' source [40]. A visualization of two hard FDTD pressure sources can be seen in Figure 2.4, where two Gaussian pulses are positioned close to one another and the scattering of sound by each source is visible around the source position. All the sources considered in this thesis, whether acoustic and vibrational, follow the behaviour of a 'hard' source.

2.4.6 Spatial offset of field variables

In most FDTD approaches, the field variables are offset in space and time, in an arrangement known as a 'staggered' grid. The main reason for the offset of field variables is to reduce discretization errors and prevent instabilities [41]. However, the spatial offset introduced by staggered grids increases the difficulty of implementing boundary conditions and handling source and receiver locations [41]. Hence, there are a number of alternative implementations in which the field variables are only partially offset [42] or share the same positions in space and time [43]. In this thesis the staggered grid approach is chosen in order to prevent instabilities and reduce discretization error.

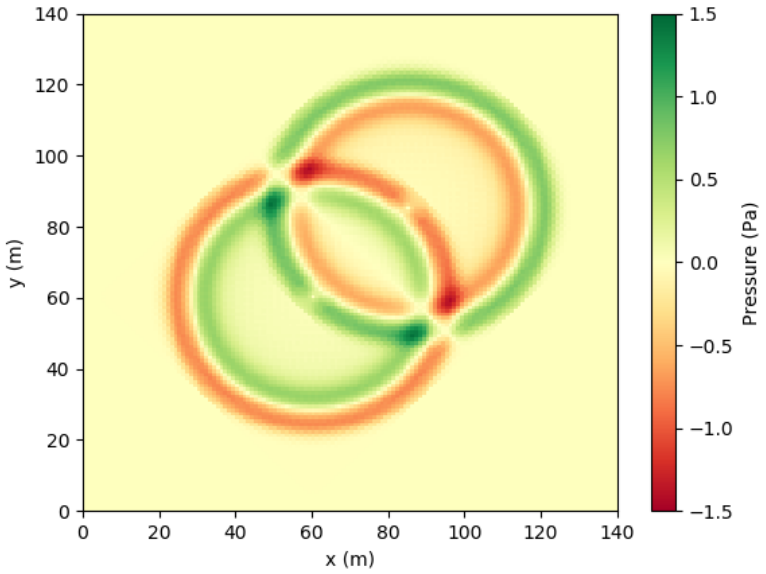

Figure 2.4: Two hard Gaussian sources with opposite phases. The source positions are (60m,60m) and (85m,85m).

2.4.7 Outer radiation boundary conditions

In order to simulate an acoustic free field it is necessary to create a domain which avoids reflections from the numerical boundaries that is caused by the finite size of the modelling space. This can be achieved by implementing Outer Radiation Boundary Conditions (ORBCs). There are a number of ORBCs detailed in the literature [2]. One of the most commonly used is the Perfectly Matched Layer (PML) approach. PML boundaries are numerical boundaries that are not physically meaningful but provide almost complete absorption of waves that are incident at the edges of the numerical domain. PML boundaries were introduced by Berenger in 1994 [44] in the context of electromagnetics, but were adapted to other fields such as acoustics [45].

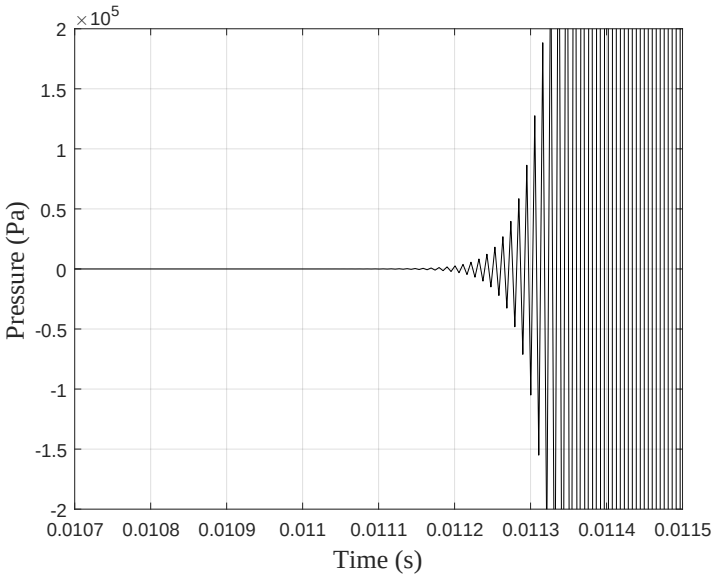

Figure 2.5: Output example of a simulation showing instability, occuring before 0.0114 s.

2.5 Stability

A numerical simulation is said to be stable if it produces bounded output when operating over bounded input [35]. An example of the output of an unstable numerical simulation is shown in Figure 2.5.

A necessary, but not sufficient condition [46] for stability in the FDTD method is the Courant stability condition:

$$\Delta t \leq \left[C \sqrt{\left(\frac{1}{\Delta x}\right)^2 + \left(\frac{1}{\Delta y}\right)^2 + \left(\frac{1}{\Delta z}\right)^2} \right]^{-1} \tag{2.41}$$

where C is the highest phase velocity of any wave motion within the frequency range of source excitation [47] and Δx, Δy and Δz are the spatial resolutions in the x-, y- and z-directions respectively. In the case of acoustic wave propagation, C will take the value of c, the phase velocity of sound waves propagating in air, which is given by equation (2.8). The Courant condition is based on the fact that a wave traveling at a speed C takes a time $\Delta t = \Delta h/C$ to travel between two adjacent source and target cells separated by a distance Δh. If the time step is set

larger than $\Delta h/C$, it will create a non-zero value at the target cell, even though the wave has not physically reached it. This situation would violate causality and result in numerical instability [48]. Other factors such as damping and boundary conditions can also give rise to unstable solutions [2, 46] and therefore equation 2.41 is a necessary but not sufficient condition to guarantee numerical stability. Hence, given a particular simulation, Δt must always be checked for the time period that is chosen for the FDTD simulation. Stability can be obtained using a time step is used which is smaller than that given by the Courant condition [2]. However, the ideal time step to minimise numerical dispersion errors is as close as possible to that dictated by the Courant condition [2].

2.6 Numerical dispersion

The FDTD algorithm can also introduce non-physical dispersion in the propagation of waves in a phenomenon that is known as 'numerical dispersion'. When the numerical medium is dispersive, the phase velocity of the numerical waves depends on their wavelength and grid density [35]. In a one-dimensional FDTD simulation, the dispersion relation is given by [35]:

$$\left[\frac{1}{c\Delta t}\sin\left(\frac{\omega\Delta t}{2}\right)\right]^2 = \left[\frac{1}{\Delta x}\sin\left(\frac{k_x\Delta x}{2}\right)\right]^2 \tag{2.42}$$

where ω denotes angular frequency and k_x denotes wavenumber. As shown in section 2.6.1, Equation 2.42 reduces to the ideal dispersion relation of an acoustic medium, $k_x = \omega/c$ when Δt is set to the Courant limit, which in one dimension is $\Delta t = \Delta x/c$. This indicates that numerical dispersion is completely avoidable in one-dimensional simulations, provided the time step is set to the Courant limit. Figure 2.6 illustrates the effect of numerical dispersion on the one-dimensional propagation of a triangular pulse. The waveform of the triangular pulse is unaffected when the time step is set to match the Courant limit, indicating there is no numerical dispersion. However, when the time step is set to 90% of the value dictated by the Courant limit, the waveform of

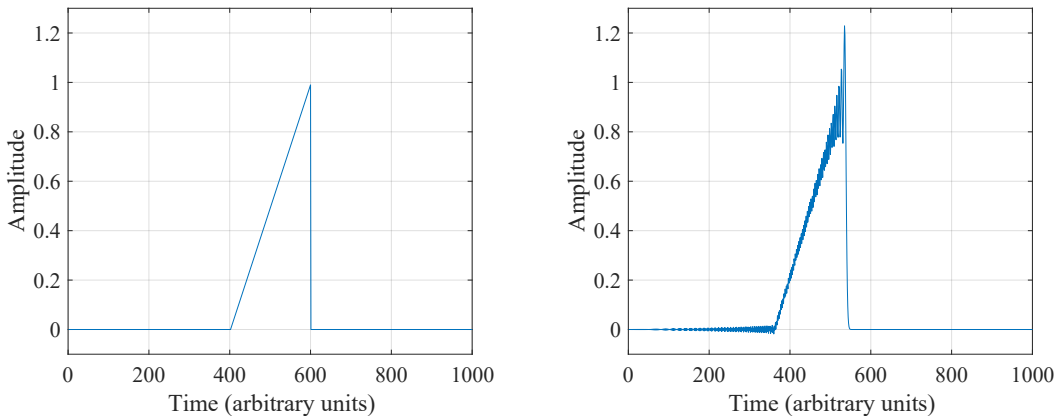

Figure 2.6: Triangular pulse propagation in one-dimensional FDTD where the time step is set to 100% (left) and 90% (right) of the Courant limit.

the triangular pulse undergoes noticeable distortion as the pulse propagates through the dispersive medium.

In a two or three dimensional FDTD grid, numerical dispersion causes waves to travel at different speeds along different directions. In these cases, numerical dispersion is generally unavoidable, except in the case of a plane wave travelling along the diagonal directions at the Courant time step. The severity of the numerical dispersion will depend on several factors such as the direction of propagation in respect to the grid and the size of the grid elements compared to the wavelength of the numerical waves [48].

The numerical dispersion relation corresponding to the three-dimensional finite difference scheme, presented in section 2.3.3, is given by extending equation 2.42 [48, 35]:

$$\left[\frac{1}{c\Delta t}\sin\left(\frac{\omega\Delta t}{2}\right)\right]^2 = \left[\frac{1}{\Delta x}\sin\left(\frac{k_x\Delta x}{2}\right)\right]^2 + \left[\frac{1}{\Delta y}\sin\left(\frac{k_y\Delta y}{2}\right)\right]^2 + \left[\frac{1}{\Delta z}\sin\left(\frac{k_z\Delta z}{2}\right)\right]^2 \quad (2.43)$$

If the spatial resolution of the FDTD model is increased, it is possible to reduce the numerical dispersion. In fact, by letting $\Delta t \to 0$, $\Delta x \to 0$, $\Delta y \to 0$ and $\Delta z \to 0$, it can be shown that equation 2.43 converges to the ideal dispersion relation of a

non-dispersive medium (provided $\Delta t, \Delta x, \Delta y$ and Δz follow the Courant condition 2.41) [35]:

$$\left(\frac{\omega}{c}\right)^2 = (k_x)^2 + (k_y)^2 + (k_z)^2 \tag{2.44}$$

A variety of alternative approaches to the standard FDTD finite difference scheme have been developed that seek to minimise errors due to numerical dispersion, which include [35]:

- Use of higher order differencing schemes [49, 36];
- Use of hexagonal grids [32];
- Use of the Fourier transform to calculate spatial derivatives [37].

2.6.1 Reduction of the one-dimensional FDTD dispersion relation to the ideal dispersion relation

The relation that describes numerical dispersion in a 1D FDTD standard explicit algorithm is given by:

$$\left[\frac{1}{c\Delta t}\sin\left(\frac{\omega\Delta t}{2}\right)\right]^2 = \left[\frac{1}{\Delta x}\sin\left(\frac{k_x\Delta x}{2}\right)\right]^2$$

If the time step is set to $\Delta t = \Delta x/c$, the Courant limit, the previous relation simplifies to:

$$\left[\frac{1}{\Delta x}\sin\left(\frac{\omega\Delta x}{2c}\right)\right]^2 = \left[\frac{1}{\Delta x}\sin\left(\frac{k_x\Delta x}{2}\right)\right]^2$$

Taking the square root on both sides and cancelling out the repeating terms yields:

$$\sin\left(\frac{\omega\Delta x}{2c}\right) = \sin\left(\frac{k_x\Delta x}{2}\right)$$

Taking the arcsine of both sides of the equation the ideal dispersion relation is obtained:

$$k_x = \omega/c$$

2.7 Sound sources

One of the simplest types of sound source is that of a pulsating sphere with radius r_o, where its surface vibrates with a velocity s_o. As the surface of the sphere moves, it will displace a volume of fluid around it, since the velocity at the surface of the sphere must be equal to the velocity of the air particles adjacent to it. The volume velocity Q of a vanishingly small pulsating sphere is then defined as [50]:

$$Q = \lim_{r_\mathrm{o} \to 0} s_\mathrm{o} 4\pi r_\mathrm{o}^2 \tag{2.45}$$

The volume velocity provides a measure of the quantity of air moved per unit time and is expressed in units of m^3/s. Given a time history of $Q(t)$, the corresponding sound pressure $p(r,t)$ radiated by a point source at a distance r from the source is given by [51]:

$$p(r,t) = \frac{\rho_\mathrm{o}}{4\pi r} \frac{dQ(t - r/c)}{dt} \tag{2.46}$$

The ideal pulsating sphere source is therefore a point source exhibiting radial symmetry in the radiated sound field. This type of source is called a monopole point source. Equation 2.46 also indicates that the time history of the radiated pressure from a point monopole source follows the time derivative of the corresponding volume velocity function.

2.7.1 Complex sound sources

More complex sound sources, such as vibrating surfaces can usually be decomposed into a number of simple monopole sources, where the total radiation is calculated via the Rayleigh integral [52]:

$$p(r,t) = \frac{i\omega\rho_o}{2\pi} e^{i\omega t} \iint_S \frac{\tilde{v}_n(r_s) e^{-ik|r-r_s|}}{|r-r_s|} dS, \tag{2.47}$$

where $\tilde{v}_n$ is the component of the complex velocity ($\tilde{v}_n = |v_n|\, e^{i\phi}$) that is perpendicular to the vibrating surface, r_s is the position of the monopole source on the vibrating surface, dS is the infinitesimal area of the monopole source and S is the defining surface area of the vibrating surface.

A moving-coil loudspeaker operated at low frequencies can be approximated as a piston source, where the the loudspeaker diaphragm is assumed to vibrate with equal phase and magnitude [53]. A piston with radius r_o behaves like a monopole source in the low-frequency region where $kr_\mathrm{o} << 1$ [54]. Therefore the low frequency radiation of an electrodynamic loudspeaker can be approximated as that of a monopole, provided the wavelength of the radiated sound is much larger than any of the dimensions of the loudspeaker cabinet [55]. This fact is of importance in this thesis as a loudspeaker operating at low frequencies was used in the FDTD acoustic models and corresponding experimental validations. The radiation pattern of the loudspeaker used for this research work was experimentally validated to be that of a monopole source.

2.8 FDTD acoustic sources

The sound source is a loudspeaker which is implemented in FDTD as a 'hard' velocity source, as described in section 2.4.5. The loudspeaker cone points upwards into the

room (z-direction - see Figure 2.9) and was experimentally characterized to be acting as a piston in the frequency range of interest, as discussed in section 2.7.1 . For this reason a uniform driving function can be applied over the surface area of the cone on the FDTD grid. In this thesis, the driving function used for the numerical simulations is a Gaussian pulse specified in terms of a z-direction velocity v_z, which has the form [46]:

$$v_z(t) = \frac{1}{\sqrt{2\pi}\sigma_\mathrm{o}} e^{-(t-t_\mathrm{o})^2/2\sigma_\mathrm{o}^2} \tag{2.48}$$

where t_o indicates the mean value of the Gaussian pulse or, equivalently, the time offset from the origin and σ_o represents the spread of the pulse over the time axis. The constant σ_o is primarily responsible for the frequency content of the pulse. Increasing values of σ_o will result in wider pulses with lower frequency components. Equation 2.48 also indicates that the analytical form of the Gaussian pulse does not have a defined starting time nor does it have an end time. Hence, in numerical computations, the Gaussian pulse must be truncated in such a way as not to significantly change its frequency characteristics.

One of the main advantages of the Gaussian pulse resides in its simplicity and in the fact that the analytical form of its frequency spectrum is known [46]:

$$V_z(\omega) = e^{-i\omega\sigma_\mathrm{o}} e^{-\omega^2\sigma_\mathrm{o}^2/2} \tag{2.49}$$

Inspection of equation 2.49 shows that the magnitude of the frequency spectrum of a Gaussian pulse is itself another Gaussian pulse. This implies that a Gaussian pulse must contain a non-zero static component of the frequency spectrum (0 Hz). This can be problematic, especially if displacements are being calculated, where the 0 Hz component would correspond to static deformation. However, when a Gaussian pulse waveform (equation 2.48) is used to excite the velocity component of the diaphragm of a loudspeaker, the actual sound pressure radiated from its diaphragm follows the derivative of this driving function, which contains no static (0 Hz) component. The derivative of the Gaussian pulse is a function of the form [46]:

$$v_z(t) = -\frac{1}{\sqrt{2\pi}} \frac{(t - t_o)}{\sigma_o^3} e^{-(t-t_o)^2/2\sigma_o^2} \tag{2.50}$$

This fact is discussed in detail in section 2.7, where it is mentioned that the radiated sound pressure $p(t)$ from a volume velocity source with a time dependence $v(t)$ takes its derivative form, $p(t) \propto v'(t)$. The analytical frequency spectrum of the time derivative of the Gaussian pulse is given by the following equation [46]:

$$V_z(\omega) = i\omega e^{-i\omega\sigma_o} e^{-\omega^2\sigma_o^2/2} \tag{2.51}$$

As can be deduced from equation 2.51, the static component of the time derivative of the Gaussian pulse is zero. Hence, the radiated derivative of the Gaussian pulse avoids the problems that can arise with static excitation.

In order to implement a Gaussian pulse in FDTD, equation 2.48 was discretized to a finite number of values:

$$v_z(n) = \frac{1}{\sqrt{2\pi}\sigma_o} e^{-(t(n)-t_o)^2/2\sigma_o^2} \tag{2.52}$$

where v_z indicates the vertical z-component of the velocity that was used to implement the source (Figure 2.9). As mentioned previously, the choice of σ_o will mostly depend on the desired frequency range of excitation. Figures 2.7 and 2.8 depict the waveforms and corresponding frequency spectra for a Gaussian pulse and its derivative. It can be seen that the static component is the highest of the frequency components in the case of the Gaussian pulse and is vanishingly small for the derivative of the Gaussian pulse. Since the numerical Gaussian pulse must be a truncated version of the analytical pulse, the choice of t_o should ensure that the discrete pulse approximates the analytical pulse in a reasonable way, and that can be checked by applying a DFT to the truncated pulse.

Figure 2.9 shows the FDTD implementation of the loudspeaker sound source used in this thesis, for the x-direction (horizontal) and the z-direction (vertical). The

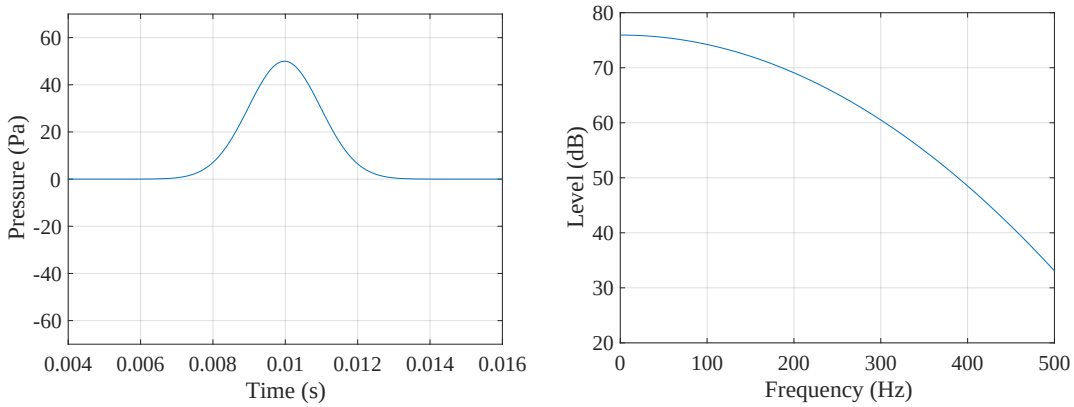

Figure 2.7: Example of a Gaussian pulse ($t_o = 0.01$s, $\sigma_o = 0.001$s) waveform (left) and corresponding magnitude frequency spectrum (right).

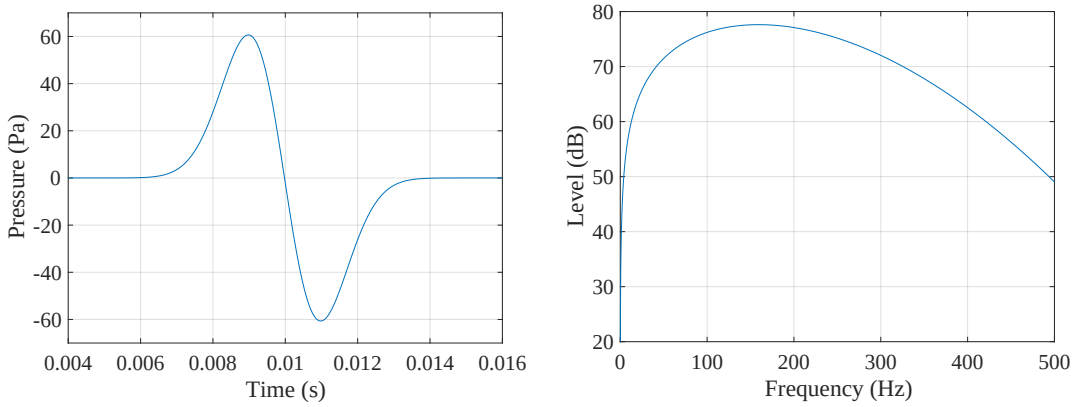

Figure 2.8: Example of the derivative of the Gaussian pulse ($t_o = 0.01$s, $\sigma_o = 0.001$s) waveform (left) and corresponding magnitude frequency spectrum (right).

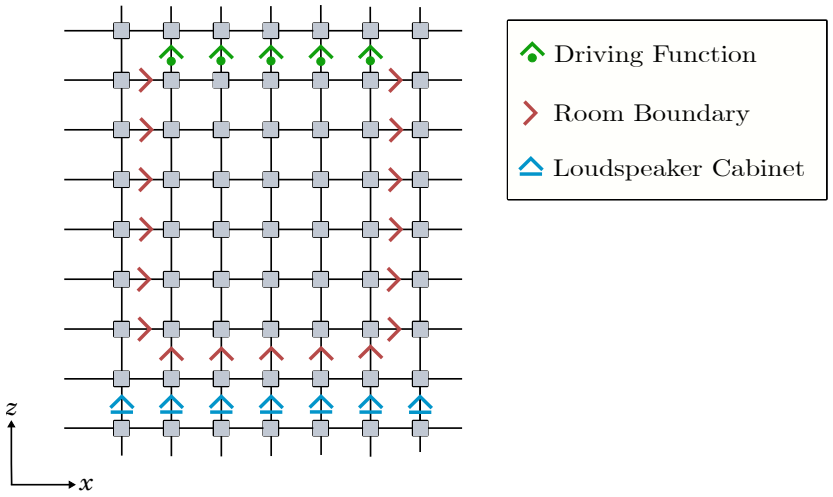

Figure 2.9: FDTD implementation of the loudspeaker as a hard velocity source.

velocity elements representing the loudspeaker cone were assigned the same velocity values that correspond to the measured cone velocity with transient excitation from a Gaussian pulse, which will be referred to as the driving function. The other velocity elements that form the boundary are set to zero to represent the rigid boundaries of the loudspeaker cabinet. Implementing the loudspeaker in this way emulates a piston on the surface of a sealed cabinet, since all elements of the diaphragm move with the same velocity.

2.9 Boundary conditions

The boundary conditions for acoustic problems are usually expressed in terms of acoustic impedance, i.e. the ratio of sound pressure measured at a point on the surface to the velocity component that is normal to the boundary, v_n, at the same measurement position. The normal acoustic surface impedance $Z_\mathrm{a,n}$ is defined as

$$Z_\mathrm{a,n} = \frac{p}{v_\mathrm{n}} \tag{2.53}$$

The normal acoustic surface impedance is expressed in units of Pa.s/m.

The specific acoustic impedance is also often used and is defined as the ratio of the

normal acoustic surface impedance to the characteristic impedance of the medium:

$$Z_{\mathrm{a,s}} = \frac{Z_{\mathrm{a,n}}}{\rho_o c} \tag{2.54}$$

The specific acoustic impedance is a dimensionless quantity.

2.9.1 Estimation of the specific acoustic impedance

Several methods can be used to estimate the specific acoustic impedance of a surface.

One method to estimate an average specific acoustic impedance of all the surfaces present in a room is to perform acoustic measurements in the room and measure the damping constants, δ_n, associated with each mode in a given frequency interval. The damping constant associated with a particular room mode n with indices (p, q, r) is calculated using the following expression [56]:

$$\delta_n = \pi \Delta f / f_{\mathrm{o}} \tag{2.55}$$

where Δf corresponds to the 3dB down points associated with each modal peak, as described in the literature [57, 58]. The damping constant, δ_n, is related to the specific acoustic impedance using the following equation [57]:

$$Z_{\mathrm{a,s}} = \frac{c_{\mathrm{o}}}{\delta_n} \left(\frac{\varepsilon_{p,n}}{L_x} + \frac{\varepsilon_{q,n}}{L_y} + \frac{\varepsilon_{r,n}}{L_z} \right) \tag{2.56}$$

where $\varepsilon_{p,n} = 1$ if $p = 0$ and $\varepsilon_{p,n} = 2$ otherwise. The same applies to the other two modal indices, q and r. The average specific acoustic impedance can be calculated once the values of specific acoustic impedance are known for a number of room modes.

2.10 FDTD implementation of acoustic boundary conditions

In this thesis, all the acoustic boundary conditions used were frequency-independent and locally reactive.

Considering the three Cartesian directions, the FDTD equations for frequency-independent acoustic boundary conditions assume the following form [16]:

$$v_x^{n+\frac{1}{2}}\Big|_{i+\frac{1}{2},j,k} = p^n|_{i,j,k}\,/Z_{a,x} \tag{2.57}$$

$$v_y^{n+\frac{1}{2}}\Big|_{i,j+\frac{1}{2},k} = p^n|_{i,j,k}\,/Z_{a,y} \tag{2.58}$$

$$v_z^{n+\frac{1}{2}}\Big|_{i,j,k+\frac{1}{2}} = p^n|_{i,j,k}\,/Z_{a,z} \tag{2.59}$$

where $Z_{a,x}$, $Z_{a,y}$ and $Z_{a,z}$ are the acoustic surface impedance along the x, y and z directions. In order to model more general frequency-dependent boundary boundary conditions, other methods do exist, such as the approach developed by Sakamoto et al [4] based on a mass-spring-damper model or using infinite impulse response filters [59].

2.11 Sound propagation in porous media

Models that describe sound propagation inside porous materials range from detailed theoretical models such as Biot theory for sound propagation within an elastic frame (i.e. the solid constituent of a porous material) [60] to empirical models that use the concept of an equivalent fluid such as the model from Delany and Bazley [61]. For a comprehensive review of different prediction models, see the works by Allard [62] and Cox [63].

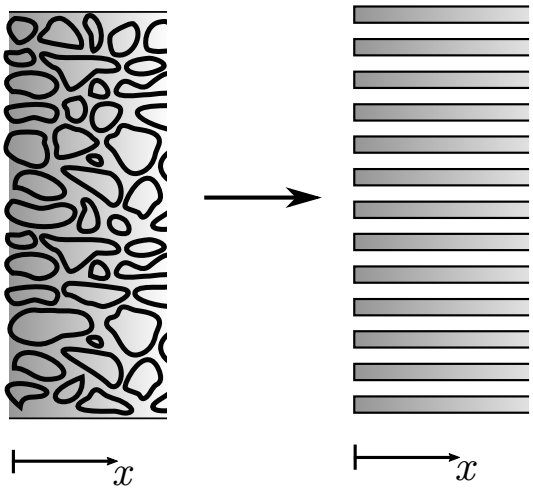

Figure 2.10: Rayleigh model: approximation of an open cell porous material as a set of parallel narrow channels.

This section describes one of these models, the Rayleigh model [56], which has previously been incorporated into FDTD to model the acoustic behaviour of a porous sound absorber [24]. A new model was developed during this research, a Moving Frame Model (MFM) to overcome the assumption of the Rayleigh model that the frame of the porous material is rigid and stationary.

2.11.1 Rayleigh model

Sound propagation inside a porous material is incorporated in the FDTD model using the Rayleigh model [56]. This model treats the porous material as a set of parallel narrow channels that are connected to the air outside the material, as shown in Figure 2.10. These channels are assumed to be embedded in a rigid frame. As the air particles propagate through the narrow channels, there are viscous losses which lead to the conversion of mechanical energy into heat. These losses are characterised by the airflow resistance of the channel which describes the ease with which air can flow through a material. Assuming, the air flows at a constant velocity $\overline{v}$ throughout the cross sectional area of the tube, the specific airflow resistance per unit length of channel, R_s, is given by:

$$R_s = -\frac{1}{\overline{v}}\frac{\partial p}{\partial x} \tag{2.60}$$

where the SI units of the specific airflow resistance are Pa.s./m. Specific airflow resistance can be directly measured with a sample of thickness d, cross-sectional area S by establishing a pressure differential Δp across the sample and therefore forcing a volume V of air through the sample during a time T. For homogeneous materials, the airflow resistivity (Pa.s./m^2) , r, is then calculated from [64]:

$$r = -\frac{TS}{V}\frac{\Delta p}{d} \tag{2.61}$$

The acoustic field inside each air channel for an arbitrary spatial orientation is described by [65]:

$$\rho_o \frac{\partial \overline{v}_i}{\partial t} + \nabla p + r\overline{v}_i = 0 \tag{2.62}$$

where $\overline{v}_i$ is the average air particle velocity developed across each air channel of the porous material along the i^{th} direction. This is a simplification, since the actual velocity profile that develops across the air channel is not constant but is zero at the boundaries and reaches its maximum at the middle section of the air channel [56]. In three-dimensional space, the momentum vector equation (2.62) can be decomposed into Cartesian components as follows:

$$\rho_o \frac{\partial \overline{v}_x}{\partial t} + \frac{\partial p}{\partial x} + r_x\overline{v}_x = 0 \tag{2.63}$$

$$\rho_o \frac{\partial \overline{v}_y}{\partial t} + \frac{\partial p}{\partial y} + r_y\overline{v}_y = 0 \tag{2.64}$$

$$\rho_o \frac{\partial \overline{v}_z}{\partial t} + \frac{\partial p}{\partial z} + r_z\overline{v}_z = 0 \tag{2.65}$$

where r_x, r_y and r_z denote the airflow resistivities along the x-, y- and z-directions as it is possible for a non-homogeneous porous material to have different airflow resistivities along different directions, typically along the thickness (longitudinal) and lateral directions of a sheet of porous material [57]. Various empirical formulae and measured data for longitudinal and lateral air flow resistivities are available in the literature [63, 57]. The continuity equation that is used to model a porous

material is the same as equation (2.9), but it is necessary to consider the average particle velocity of air across the channels:

$$\frac{\partial p}{\partial t} = -\rho_o c^2 \left(\frac{\partial \overline{v}_x}{\partial x} + \frac{\partial \overline{v}_y}{\partial y} + \frac{\partial \overline{v}_z}{\partial z} \right) \tag{2.66}$$

For example, in one dimension (along the x-direction), the continuity equation reduces to:

$$\frac{\partial p}{\partial t} + \rho_o c^2 \frac{\partial \overline{v}_x}{\partial x} = 0 \tag{2.67}$$

The Rayleigh model provides an approximate description of the losses that occur due to the friction between the air particles and the rigid frame of the porous material. However, it assumes that the rigid frame remains stationary.

The Rayleigh model is valid for a range of frequencies ω that satisfy the relation [56]:

$$\omega \lesssim \frac{4r}{\rho_o} \tag{2.68}$$

2.11.2 Moving Frame Model

The Rayleigh model provides an approximate description of the losses that occur due to the friction between the air particles and the rigid frame of the porous material. However, it assumes that the rigid frame of the porous panel remains stationary. At 'low' frequencies the movement of the air particles inside the porous material cause the frame to move due to its low mass impedance [66]. If the frame of the porous panel is allowed to move along the direction of the narrow air channels (Figure 2.10) and the velocity of the air particles is considered in relation to the frame for the resistive term in equation 2.62, it is possible to account for the motion of the frame in FDTD with a Moving Frame Model (MFM) by rewriting equation (2.62) as

$$\rho_o \frac{\partial \overline{v}_i}{\partial t} + \overrightarrow{\nabla} p + r v_{\text{air|frame}} = 0 \tag{2.69}$$

where $v_{\text{air|frame}}$ is the velocity of the air particles $\overline{v}_i$ relative to the frame velocity, v_{F}, given by:

$$v_{\text{air|frame}} = \overline{v}_i - v_{\text{F}} \tag{2.70}$$

The pressure inside the porous material is updated using the equation of continuity for the Rayleigh model (equation (2.66)) with the density of air. The following assumptions are now made in order to calculate the frame motion for the porous panel:

1. The porous panel is a limp mass with no bending stiffness.
2. Each element of the panel can be treated as being independent from its surrounding elements.
3. The frame is perfectly rigid and therefore does not undergo wave motion.

Therefore each volume element of the porous panel can be approximated as a lumped mass and the corresponding equation of motion can be written as:

$$\Delta p = m_{\text{S}} \frac{\partial v_{\text{F}}}{\partial t} \tag{2.71}$$

where Δp represents the pressure difference across the porous panel element, m_{S} is the mass per unit area of the panel. The pressure gradient Δp is calculated from the two pressure nodes that are adjacent to opposite sides of the panel. Once the pressure gradient is known, Equation (2.71) is used to calculate the frame velocity v_{F}. Once the frame velocity is known, the velocity of the air particles inside the air channel is calculated using equation (2.69). The MFM calculation procedure is illustrated using a flow diagram in Figure 2.13.

The MFM can be used for porous panels that partially or completely divide a room. For the latter this leads to a spring-mass-spring resonance as shown in Figure 2.11, which is not considered in existing literature.

For the system in Figure 2.11, the frequency at which the spring-mass-spring reso-

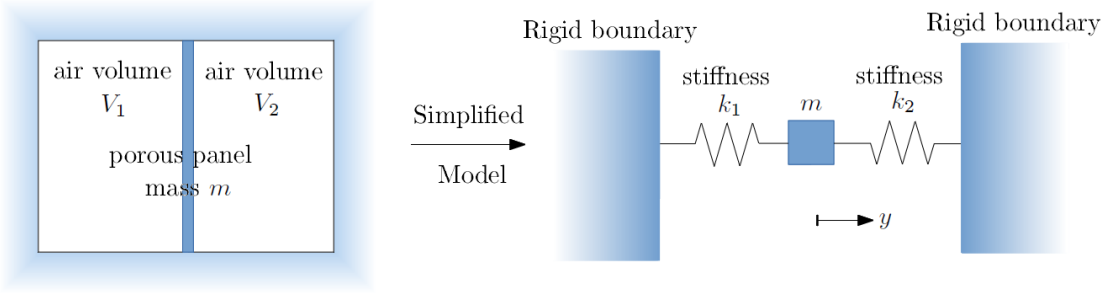

Figure 2.11: Room volume separated by a porous panel (left) and its equivalent spring-mass-spring model (right).

nance, f_o, occurs is given by:

$$f_o = \frac{1}{2\pi}\sqrt{\frac{k_1 + k_2}{m}} \tag{2.72}$$

where m is the total mass of the panel and k_1 and k_2 are the stiffness corresponding to each enclosed volume of air on either side of the porous panel. The stiffness values k_1 and k_2 are calculated using [54]:

$$k = \rho_o c^2 S^2 / V \tag{2.73}$$

where V is the volume of air and S is the area of the porous panel.

2.12 FDTD implementation of the porous material

This section describes the implementation of an FDTD model of a porous material. The implementation is based on the Rayleigh model for a porous material, which was previously used by Suzuki et al [24]. However, there are a few limitations inherent to the Rayleigh model, particularly the assumption of a stationary frame which limits the accuracy of the FDTD predictions. Hence, a new Moving Frame Model (MFM), described in section 2.11.2, was developed in this thesis to overcome this limitation and its implementation is described in this section.

2.12.1 Rayleigh model of a porous material

As mentioned in section 2.11.1, the continuity equation for a porous material is identical to that previously considered for the air medium.

Discretization of the momentum equations that describe the sound field inside a porous material (equations 2.63 - 2.65) leads to

$$v_x^{n+\frac{1}{2}}\Big|_{i+\frac{1}{2},j,k} = \frac{1}{\rho_o + r_x \Delta t}\left[-\frac{\Delta t}{\Delta x}\left(p^n|_{i+1,j,k} - p^n|_{i,j,k}\right) + \rho_o\, v_x^{n-\frac{1}{2}}\Big|_{i+\frac{1}{2},j,k}\right] \tag{2.74}$$

$$v_y^{n+\frac{1}{2}}\Big|_{i,j+\frac{1}{2},k} = \frac{1}{\rho_o + r_y \Delta t}\left[-\frac{\Delta t}{\Delta y}\left(p^n|_{i,j+1,k} - p^n|_{i,j,k}\right) + \rho_o\, v_y^{n-\frac{1}{2}}\Big|_{i,j+\frac{1}{2},k}\right] \tag{2.75}$$

$$v_z^{n+\frac{1}{2}}\Big|_{i,j,k+\frac{1}{2}} = \frac{1}{\rho_o + r_z \Delta t}\left[-\frac{\Delta t}{\Delta z}\left(p^n|_{i,j,k+1} - p^n|_{i,j,k}\right) + \rho_o\, v_z^{n-\frac{1}{2}}\Big|_{i,j,k+\frac{1}{2}}\right] \tag{2.76}$$

These update equations model the sound field inside the porous material. If the airflow resistivity is set to zero, equations 2.74-2.76 reduce to equations 2.10-2.12, respectively.

2.12.2 Moving frame model

The variable $v_{\text{air|frame}}$ in equation 2.69, denoting the velocity of the air particles relative to the frame velocity is given in discretized form by:

$$v_{\text{air|frame}}{}^{n+\frac{1}{2}}\Big|_{i+\frac{1}{2}} = v^{n+\frac{1}{2}}\Big|_{i+\frac{1}{2}} - v_{\text{F}}^{n+\frac{1}{2}} \tag{2.77}$$

Figure 2.12 shows an example of the lumped mass in the thickness direction of the panel which is represented by two velocity elements. The volume element with mass m (shaded blue) is subject to a pressure gradient (which in this example is $p_{i+1} - p_{i-1}$)

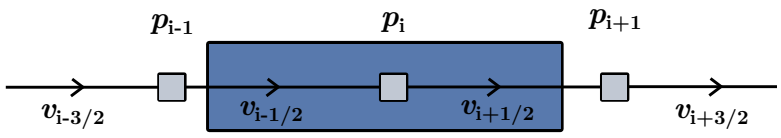

Figure 2.12: Example volume element with a mass m and velocity v_F representing the porous panel

such that all points within it move with the same velocity, v_F. After some algebraic manipulation, discretisation of equations 2.69 and 2.71 results in:

$$v_\mathrm{F}^{n+\frac{1}{2}} = -\frac{\Delta t}{m_\mathrm{S}}\left(p^n|_{i+1} - p^n|_{i-1}\right) + v_\mathrm{F}^{n-\frac{1}{2}} \tag{2.78}$$

$$v^{n+\frac{1}{2}}\Big|_{i+\frac{1}{2}} = \frac{1}{\rho_\mathrm{o} + r\Delta t}\left[-\frac{\Delta t}{\Delta x}\left(p^n|_{i+1} - p^n|_i\right) + \rho_\mathrm{o}\, v^{n-\frac{1}{2}}\Big|_{i+\frac{1}{2}} + r\Delta t v_\mathrm{F}^{n+\frac{1}{2}}\right] \tag{2.79}$$

If the mass per unit area of the panel m_S approaches infinity, the frame velocity v_F will approach zero and equation 2.79 reduces to equations 2.74, 2.75 or 2.76 depending on the direction being evaluated. The motion of the panel is assumed to be unrestricted in the y-direction; hence only equations 2.78 and 2.79 are used to calculate the panel motion in this direction.

The MFM is implemented in such a way that knowledge of k_1 and k_2 in equation 2.72 is not required for calculation of f_o. This is because movement of the frame is inherently included in FDTD update equations 2.78 and 2.79 regardless of the volume of the room or whether the porous panel partially or completely divides the room. This inherent connection between the frame velocity v_F and the acoustic field variables p and v is illustrated in Figure 2.13. The flow diagrams show the calculation sequence followed by the FDTD main loop and compares a basic acoustic FDTD routine with another that considers the MFM. In the case of the MFM diagram, it can be seen that any changes in the frame velocity will effect subsequent calculations of the pressure and velocity fields.

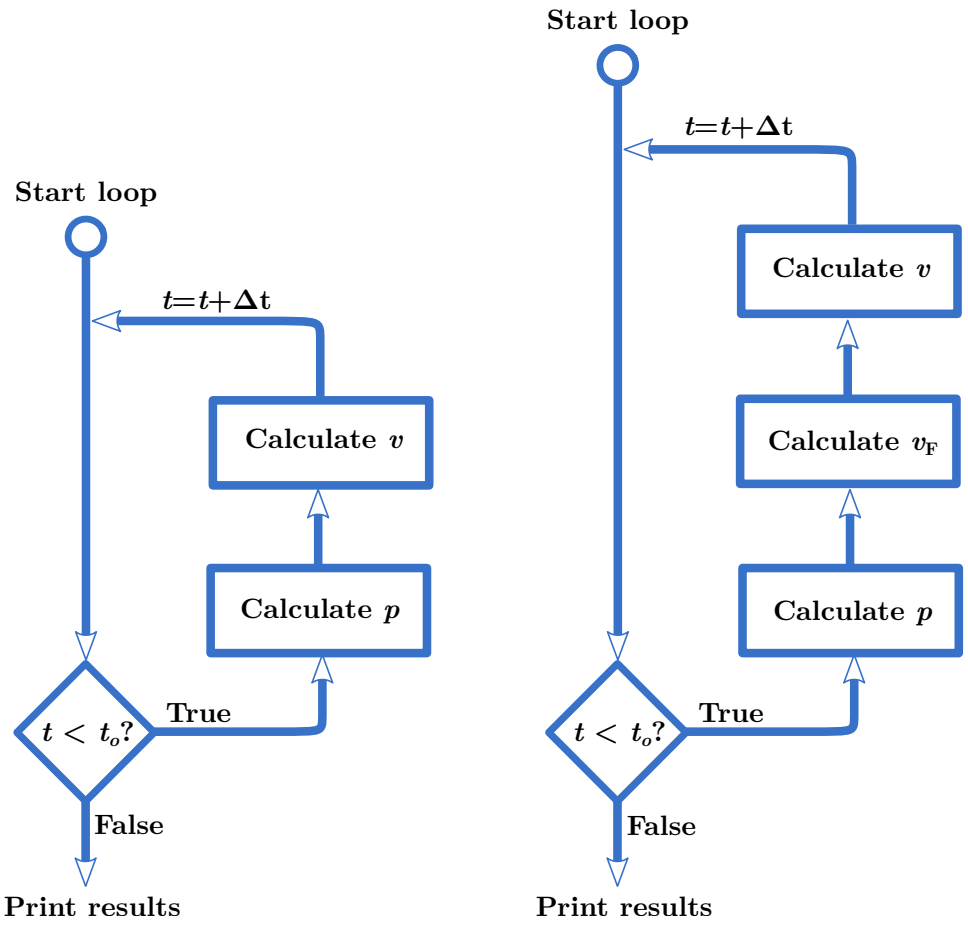

Figure 2.13: Flow diagrams indicating the acoustic FDTD routine (left) and the routine including the Moving Frame Model (right)

2.13 Conclusions

This chapter addressed theoretical aspects of sound propagation in air by introducing the field variables and equations used to describe acoustics problems. The implementation of the corresponding FDTD update acoustic equations was derived and described alongside the theoretical aspects. For porous materials that divide a space, a new model with a moving frame was introduced along with its derivation. This gives the potential for the existence of a spring-mass-spring resonance for acoustic cavities separated by a porous material.

3 Implementation of FDTD for vibroacoustics

3.1 Introduction

This chapter addresses both theoretical and numerical aspects that are required to implement FDTD for vibration and vibroacoustics problems.

Section 3.2 outlines a brief literature review on vibroacoustics FDTD.

Section 3.3 considers some theoretical aspects of sound propagation in purely elastic solid media, e.g. media where no losses in mechanical energy occur. A brief summary of the elastic wave types that can occur in thin plate structures and corresponding phase velocities is also included in this section.

Section 3.4 introduces the modelling of damping and the focus will turn to sound propagation in viscoealstic media. The tensor form of the constitutive and momentum equations are introduced in this section. The vector form of the two- and three-dimensional field equations for viscoelastic propagation is introduced in section 3.5, for the two- and three-dimensional cases.

Section 3.6 describes the field variables necessary to model vibration problems in FDTD and section 3.7 describes the implementation of the viscoelastic update equations in FDTD.

Section 3.8, includes a description on the frequency characteristics of the viscoelastic damping model described in the preceding sections which is used for the FDTD simulations in this thesis.

Section 3.9 describes the factors that need to be considered to ensure stability of a viscoelastic FDTD simulation.

Section 3.10 describes the implementation of vibration sources in FDTD.

Section 3.11 describes the implementation of simply supported boundaries in FDTD.

Section 3.12 introduces a new approach to modelling the air/solid boundary conditions, which results in significant computational efficiency and simplified implementation when compared to the standard approach.

In section 3.13 a new 'scaling approach' to formulating vibroacoustics problems is introduced. The scaling approach consists of scaling the geometrical and dynamical characteristics of a systems in a way which greatly increases computational efficiency.

3.2 Literature review on FDTD for vibroacoustics

This section presents a brief literature review of the FDTD method as applied to vibration and vibroacoustics, covering fundamental aspects such as the field variables used and the type and geometry of numerical grid used in the calculations.

3.2.1 Field variables

In terms of field variables, several formulations have been used in FDTD to describe elastic wave propagation. These include formulations based on displacement and stress, formulations based on velocity and stress, and formulations based only on displacement [67]. In terms of vibroacoustics, the velocity and stress field variable formulation has been combined with the air pressure and particle velocity as described by Toyoda *et al* [68]. In this thesis, the field variables that were implemented in the vibroacoustics FDTD model are based on the work of Toyoda *et al* [68].

3.2.2 Grid geometry

The simplest type of grid geometry encoutered in vibration FDTD is the rectangular grid. There are several examples illustrating the use of a rectangular grid geometry, such as the work by Schroeder *et al.* [10]. More complex grid geometries have been implemented. Cylindrical [8] and spherical coordinates [69] are examples of complex grid geometries used in vibration FDTD.

3.2.3 Explicit and implicit methods

The field variables are related by algebraic equations, formulated in the time domain. In this thesis, these equations are arranged so that they can be solved explicitly, following the work by Toyoda *et al* [68]. Other arrangements of the discretized equations to allow the use of implicit time solvers have also been described in the literature [67], but these are not considered here given the increased complexity of their implementation.

3.2.4 Spatial offset of field variables

In FDTD the two continuous field variables of stress and velocity are discretized at several positions and can be offset in space, forming an arrangement known as a staggered grid. Other approaches do exist where the field variables are partially spatially offset or can be located at the same positions [67]. In this thesis, the staggered grid approach was used.

3.2.5 Outer radiation boundary conditions

As mentioned in chapter 2, it is necessary, in order to solve problems that require open boundaries, to implement the Perfectly Matched Layers (PML). The PML boundaries have been adapted to vibration FDTD, as can be found in the work of Hastings *et al* [70].

3.3 Sound propagation in purely elastic media

The propagation of mechanical waves in three-dimensional solid elastic media is modelled using a system of two tensor equations [71, 72], the momentum equation:

$$\rho \frac{\partial v_i}{\partial t} = \frac{\partial \sigma_{ji}}{\partial x_j} \tag{3.1}$$

where ρ is the density of the elastic solid medium, and the constitutive equation:

$$\sigma_{ij} = C_{ijkl} \epsilon_{kl} \tag{3.2}$$

where C_{ijkl} is the stiffness tensor of rank 4 [71, 72]. The strain tensor is related to the material element displacement field by [72]:

$$\epsilon_{ij} = \frac{1}{2} \left(\frac{\partial u_j}{\partial x_i} + \frac{\partial u_i}{\partial x_j} \right) \tag{3.3}$$

3.3.1 Momentum equation

The momentum equation describes the relationship between the stress tensor acting on an element of solid material and the resulting state of motion of that element.

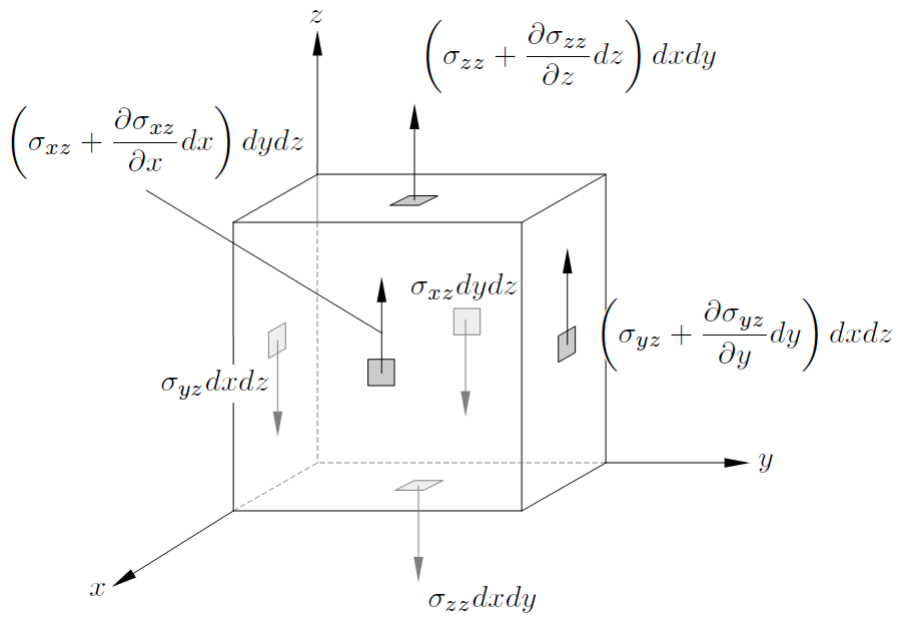

Figure 3.1: Normal and shear stresses acting along the z-direction of a Cartesian element of a solid medium.

Figure 3.1 illustrates the infinitesimal forces acting on the z direction of motion of a solid medium element. Equation 3.1, the momentum equation, is a tensor equation. If expanded in Cartesian coordinates, it is equivalent to the following system of first-order partial differential equations:

$$\rho \frac{\partial v_x}{\partial t} = \frac{\partial \sigma_{xx}}{\partial x} + \frac{\partial \sigma_{xy}}{\partial y} + \frac{\partial \sigma_{xz}}{\partial z} \tag{3.4}$$

$$\rho \frac{\partial v_y}{\partial t} = \frac{\partial \sigma_{xy}}{\partial x} + \frac{\partial \sigma_{yy}}{\partial y} + \frac{\partial \sigma_{yz}}{\partial z} \tag{3.5}$$

$$\rho \frac{\partial v_z}{\partial t} = \frac{\partial \sigma_{zx}}{\partial x} + \frac{\partial \sigma_{yz}}{\partial y} + \frac{\partial \sigma_{zz}}{\partial z} \tag{3.6}$$

The momentum equations (3.4)-(3.6) can be derived using the diagram shown in figure (3.1). This diagram illustrates the infinitesimal forces acting on the z direction of motion of a solid medium element. If a force balance is taken, the following relation is obtained:

$$\left(\sigma_{zz} + \frac{\partial \sigma_{zz}}{\partial z} dz\right) dxdy + \left(\sigma_{yz} + \frac{\partial \sigma_{yz}}{\partial y} dy\right) dxdz + \\ + \left(\sigma_{xz} + \frac{\partial \sigma_{xz}}{\partial x} dx\right) dydz - \sigma_{zz} dxdy - \\ - \sigma_{yz} dydz - \sigma_{xz} dxdz = \rho \frac{\partial v_z}{\partial t} dxdydz$$

which is equivalent to

$$\frac{\partial \sigma_{zz}}{\partial z} dxdydz + \frac{\partial \sigma_{yz}}{\partial y} dxdydz + \frac{\partial \sigma_{xz}}{\partial x} dxdydz = \rho \frac{\partial v_z}{\partial t} dxdydz$$

which reduces to

$$\frac{\partial \sigma_{zz}}{\partial z} + \frac{\partial \sigma_{yz}}{\partial y} + \frac{\partial \sigma_{xz}}{\partial x} = \rho \frac{\partial v_z}{\partial t}$$

which is identical to equation (3.6).

3.3.2 Constitutive equation

The constitutive equation describes the relation between the stress applied on an element of the solid medium and the corresponding deformation of that element. The 4^{th} rank stiffness tensor C_{ijkl} introduced in equation 3.2 contains 36 independent elastic constants. However, if the propagation medium is assumed to be isotopic, the number of elastic constants is reduced to two independent constants. Under the assumption of isotropy, equation 3.2 can be simplified to [72]:

$$\sigma_{ij} = \lambda \epsilon_{kk} \delta_{ij} + 2\mu \epsilon_{ij} \tag{3.7}$$

where λ and μ correspond to the first and second Lamé constants, respectively. The constant μ is the shear modulus which is commonly denoted as G in the literature.

3.3.3 Elastic waves occurring in thin plates

This thesis primarily concerns the modelling of thin plates [73] using a general three-dimensional FDTD method that, for flexibility, can support all wave types. There are four types of structure-borne sound waves that occur over the audio frequency range in thin plates: bending, transverse shear, quasi-longitudinal and dilatational waves [73].

For the low-frequency vibroacoustic applications that are considered for engineering structures in this thesis it is often bending waves that are of primary interest. For this reason the validity of the general three-dimensional FDTD method in reproducing thin plate bending wave motion is assessed numerically. A comparison of FDTD and analytical bending wave theory for thin plates [73] is shown in Appendix II through consideration of both mode shapes and eigenfrequencies. These results confirm the validity of the general three-dimensional FDTD method for simulating thin plate bending wave theory.

3.3.3.1 Phase velocity

Since the stability of the explicit FDTD method is limited by the Courant condition (equation 2.41), it is important to discuss the phase velocities of each type of wave.

For dilatational waves, the phase velocity c_{D} is given by [73]:

$$c_{\mathrm{D}} = \sqrt{\frac{2\mu\,(1-\nu)}{\rho\,(1-2\nu)}} \tag{3.8}$$

where ν is Poisson's ratio.

For quasi-longitudinal waves, the phase velocity c_{L} is given by [73]:

$$c_{\mathrm{L}} = \sqrt{\frac{E}{\rho\,(1-\nu^2)}} \tag{3.9}$$

where E is Young's modulus.

For bending waves, the phase velocity c_{B} is given by [73]:

$$c_{\mathrm{B}} = \sqrt{\frac{2\pi f h c_{\mathrm{L}}}{\sqrt{12}}} \tag{3.10}$$

For transverse shear waves, the phase velocity c_{T} is given by [73]:

$$c_{\mathrm{T}} = c_{\mathrm{L}}\sqrt{\frac{1-\nu}{2}} \tag{3.11}$$

3.4 Sound propagation in viscoelastic media

In order to model the propagation of sound in media that is subject to dissipation of mechanical energy, two different types of damping mechanisms are considered in the implementation of the FDTD method. The combination of these two damping mechanisms results in a frequency-dependent damping whose characteristics are similar to that obtained when using Rayleigh damping. The method described in this thesis largely follows from that presented by Toyoda *et al* [71].

3.4.1 Momentum equation

The first type of damping mechanism considered in this work is implemented in the momentum equation (3.1)[71]:

$$\rho \frac{\partial v_i}{\partial t} = \frac{\partial \sigma_{ji}}{\partial x_j} - \beta v_i \tag{3.12}$$

The term βv_i describes damping that is proportional to the velocity of each element of the solid medium. It is worth noting that this form of damping is proportional only to the velocity of the element, regardless of the velocities of its neighbour elements, i.e. how the material deforms. It can equally be thought as a body force per unit volume that is responsible for the dissipation of mechanical energy.

3.4.2 Constitutive equation

In order to model the elastic deformation of a material and consequent dissipation of mechanical energy, it is necessary to consider the theory of viscoelasticity, which encompasses the theories of elasticity and viscosity. The constitutive equation for a solid in which the propagation of sound occurs with dissipation of energy is determined using the theory of viscoelasticity.

Basic viscoelasticity theory considers a solid material to be composed of a network of ideal springs and dashpots, where elastic strain energy is stored at the springs and dissipation of energy as heat occurs at the dashpots [74]. This viscoelastic formulation of the solid medium allows for dissipation of energy as the material deforms, and it will be shown that the rate of energy dissipation depends on how the viscoelastic medium deforms.

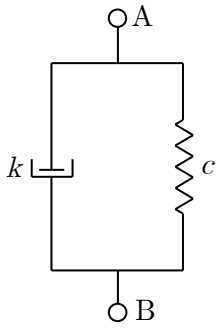

Figure 3.2: Basic Voigt element.

3.4.2.1 One-dimensional constitutive equation

A linear viscoelastic material is idealized to consist of a linear network of elastic elements (e.g. springs) and viscous elements (e.g. dashpots). In the basic Voigt model, depicted in Figure 3.2, a spring (with associated stiffness k) and a dashpot (with associated damping c) are connected in parallel. This results in the deformation of the spring being the same as the deformation of the dashpot, when a force F is applied to endpoints A and B. The corresponding constitutive equation is given by [74]:

$$F(t) = k\epsilon(t) + c\frac{d\epsilon(t)}{dt} \tag{3.13}$$

where ϵ denotes the strain tensor. The Voigt model was chosen to simulate the viscoelastic behaviour of the plate.

3.4.2.2 Three-dimensional constitutive equation

A three-dimensional viscoelastic constitutive relation based on the linear Voigt element is used to complement the damping form discussed in the previous section. Equation 3.2 was modified to take into account mechanical energy losses:

$$\sigma_{ij}(t) = C_{ijkl}\epsilon_{kl} + \xi_{ijkl}\varepsilon_{kl} \tag{3.14}$$

where ξ_{ijkl} is the viscosity tensor. The rate-of-strain tensor, ε_{kl} is related to the material velocity field by:

$$\varepsilon_{ij} = \frac{d\epsilon_{ij}}{dt} = \frac{1}{2}\left(\frac{\partial^2 u_j}{\partial x_i \partial t} + \frac{\partial^2 v_i}{\partial x_j \partial t}\right) = \frac{1}{2}\left(\frac{\partial v_j}{\partial x_i} + \frac{\partial v_i}{\partial x_j}\right) \tag{3.15}$$

Considering equations 3.14 and 3.15, it can be seen that this type of damping is proportional to the gradient of the components of the velocity field.

The first term of the right-hand side of equation 3.14 corresponds to the stresses originated by purely elastic deformations and the second term represents the stress that are caused by viscous behaviour of the solid medium. However, if the propagation medium is assumed to be isotropic, equation 3.14 can be simplified into

$$\sigma_{ij} = \lambda \epsilon_{kk}\delta_{ij} + 2\mu\epsilon_{ij} + \chi\frac{d\epsilon_{kk}}{dt}\delta_{ij} + 2\gamma\frac{d\epsilon_{ij}}{dt} \tag{3.16}$$

where χ and γ are viscous constants responsible for energy dissipation. The term ϵ_{kk} is defined by:

$$\epsilon_{kk} = \frac{\partial u_i}{\partial x_i} = \sum_i \frac{\partial u_i}{\partial x_i} \tag{3.17}$$

Since FDTD is a time marching method, the time derivative must be taken on both sides of equation 3.16 in order to implement it:

$$\frac{d\sigma_{ij}}{dt} = \lambda \varepsilon_{kk}\delta_{ij} + 2\mu\varepsilon_{ij} + \chi\frac{d\varepsilon_{kk}}{dt}\delta_{ij} + 2\gamma\frac{d\varepsilon_{ij}}{dt} \tag{3.18}$$

where the term ε_{kk} is defined by:

$$\varepsilon_{kk} = \frac{\partial v_i}{\partial x_i} = \sum_i \frac{\partial v_i}{\partial x_i} \tag{3.19}$$

Substituting equations 3.15 and 3.19 into equation 3.18, one obtains the constitutive relation between stress and velocity fields for a given solid material element:

$$\frac{\partial \sigma_{ij}}{\partial t} = \lambda\frac{\partial v_i}{\partial x_i}\delta_{ij} + \mu\left(\frac{\partial v_j}{\partial x_i} + \frac{\partial v_i}{\partial x_j}\right) + \chi\frac{\partial}{\partial t}\frac{\partial v_i}{\partial x_i}\delta_{ij} + \gamma\frac{\partial}{\partial t}\frac{\partial v_j}{\partial x_i} + \gamma\frac{\partial}{\partial t}\frac{\partial v_i}{\partial x_j} \tag{3.20}$$

A useful substitution is found by applying Clairaut's theorem of the equivalence of reversed mixed derivatives to equation (3.20)[75]. Reversing the order of the mixed derivatives of the viscous terms, the following equation is obtained:

$$\frac{\partial \sigma_{ij}}{\partial t} = \lambda \frac{\partial v_i}{\partial x_i}\delta_{ij} + \mu\left(\frac{\partial v_j}{\partial x_i} + \frac{\partial v_i}{\partial x_j}\right) + \chi \frac{\partial}{\partial x_i}\frac{\partial v_i}{\partial t}\delta_{ij} + \gamma \frac{\partial}{\partial x_i}\frac{\partial v_j}{\partial t} + \gamma \frac{\partial}{\partial x_j}\frac{\partial v_i}{\partial t} \tag{3.21}$$

It is noted that

$$\frac{\partial v_i}{\partial t} = a_i \tag{3.22}$$

Hence, the advantage of reversing the partial derivatives is that the more familiar quantity acceleration a_i is now being considered for the computation of the viscous terms, instead of using the spatial derivative of the velocity. In this thesis, Clairaut's theorem is used to derive the field equations that describe structure-borne sound propagation in solid materials.

3.5 Full form of the viscoelastic field equations

In the previous section, the tensor form of the viscoelastic momentum and constitutive equations was presented. In this section, the tensor form of these two equations is expanded to obtain the corresponding system of linear partial differential equations.

3.5.1 Two dimensionions

When two-dimensional Cartesian space is taken into account, there are only five variables to be considered and equations (3.12) and (3.18) reduce to a system of five partial differential equations. Considering the xz-plane, the system of equations

is:

$$\rho\frac{\partial\sigma_{xx}}{\partial t} = (\lambda+2\mu)\frac{\partial v_x}{\partial x} + \lambda\frac{\partial v_z}{\partial z} + (\chi+2\gamma)\frac{\partial^2 v_x}{\partial x\partial t} + \chi\frac{\partial^2 v_z}{\partial z\partial t} \tag{3.23}$$

$$\rho\frac{\partial\sigma_{zz}}{\partial t} = \lambda\frac{\partial v_x}{\partial x} + (\lambda+2\mu)\frac{\partial v_z}{\partial z} + \chi\frac{\partial^2 v_x}{\partial x\partial t} + (\chi+2\gamma)\frac{\partial^2 v_z}{\partial z\partial t} \tag{3.24}$$

$$\rho\frac{\partial\sigma_{xz}}{\partial t} = \mu\left(\frac{\partial v_x}{\partial z} + \frac{\partial v_z}{\partial x}\right) + \gamma\left(\frac{\partial^2 v_x}{\partial z\partial t} + \frac{\partial^2 v_z}{\partial x\partial t}\right) \tag{3.25}$$

$$\rho\frac{\partial v_x}{\partial t} = \frac{\partial\sigma_{xx}}{\partial x} + \frac{\partial\sigma_{xz}}{\partial z} - \beta v_x \tag{3.26}$$

$$\rho\frac{\partial v_z}{\partial t} = \frac{\partial\sigma_{zx}}{\partial x} + \frac{\partial\sigma_{zz}}{\partial z} - \beta v_z \tag{3.27}$$

where v_x and v_z are the velocity variables and σ_{xx}, σ_{zz} and σ_{xz} are the stress variables.

3.5.2 Three dimensions

In three dimensions, the system comprising the two tensor equations 3.12 and 3.18 encompasses the nine first-order linear differential equations that are necessary to solve for the nine field variables of stress and velocity. These equations can be written in full form as follows:

$$\frac{\partial\sigma_{xx}}{\partial t} = (\lambda+2\mu)\frac{\partial v_x}{\partial x} + \lambda\frac{\partial v_y}{\partial y} + \lambda\frac{\partial v_z}{\partial z} + (\chi+2\gamma)\frac{\partial^2 v_x}{\partial x\partial t} + \chi\frac{\partial^2 v_y}{\partial y\partial t} + \chi\frac{\partial^2 v_z}{\partial z\partial t} \tag{3.28}$$

$$\frac{\partial\sigma_{yy}}{\partial t} = \lambda\frac{\partial v_x}{\partial x} + (\lambda+2\mu)\frac{\partial v_y}{\partial y} + \lambda\frac{\partial v_z}{\partial z} + \chi\frac{\partial^2 v_x}{\partial x\partial t} + (\chi+2\gamma)\frac{\partial^2 v_y}{\partial y\partial t} + \chi\frac{\partial^2 v_z}{\partial z\partial t} \tag{3.29}$$

$$\frac{\partial\sigma_{zz}}{\partial t} = \lambda\frac{\partial v_x}{\partial x} + \lambda\frac{\partial v_y}{\partial y} + (\lambda+2\mu)\frac{\partial v_z}{\partial z} + \chi\frac{\partial^2 v_x}{\partial x\partial t} + \chi\frac{\partial^2 v_y}{\partial y\partial t} + (\chi+2\gamma)\frac{\partial^2 v_z}{\partial z\partial t} \tag{3.30}$$

$$\frac{\partial \sigma_{xz}}{\partial t} = \mu \left(\frac{\partial v_x}{\partial z} + \frac{\partial v_z}{\partial x} \right) + \gamma \left(\frac{\partial^2 v_x}{\partial z \partial t} + \frac{\partial^2 v_z}{\partial x \partial t} \right) \tag{3.31}$$

$$\frac{\partial \sigma_{yz}}{\partial t} = \mu \left(\frac{\partial v_y}{\partial z} + \frac{\partial v_z}{\partial y} \right) + \gamma \left(\frac{\partial^2 v_y}{\partial z \partial t} + \frac{\partial^2 v_z}{\partial y \partial t} \right) \tag{3.32}$$

$$\frac{\partial \sigma_{xy}}{\partial t} = \mu \left(\frac{\partial v_x}{\partial y} + \frac{\partial v_y}{\partial x} \right) + \gamma \left(\frac{\partial^2 v_x}{\partial y \partial t} + \frac{\partial^2 v_y}{\partial x \partial t} \right) \tag{3.33}$$

$$\rho \frac{\partial v_x}{\partial t} = \frac{\partial \sigma_{xx}}{\partial x} + \frac{\partial \sigma_{xy}}{\partial y} + \frac{\partial \sigma_{xz}}{\partial z} - \beta v_x \tag{3.34}$$

$$\rho \frac{\partial v_y}{\partial t} = \frac{\partial \sigma_{xy}}{\partial x} + \frac{\partial \sigma_{yy}}{\partial y} + \frac{\partial \sigma_{yz}}{\partial z} - \beta v_y \tag{3.35}$$

$$\rho \frac{\partial v_z}{\partial t} = \frac{\partial \sigma_{zx}}{\partial x} + \frac{\partial \sigma_{yz}}{\partial y} + \frac{\partial \sigma_{zz}}{\partial z} - \beta v_z \tag{3.36}$$

The constants β, χ and γ account for the losses of mechanical energy losses in the system, as was discussed in the analysis carried out in section 3.4.

3.6 FDTD vibration field variables

This section describes the field variables necessary to formulate vibracoustics problems and the corresponding implementation in FDTD.

3.6.1 Vibration

As mentioned in section 3.2.1, the field variables used in this thesis to model propagation of elastic waves are the velocity v_i and stress σ. In three dimensional space, the velocity variable comprises the components v_x, v_y and v_z, and indicates the di-

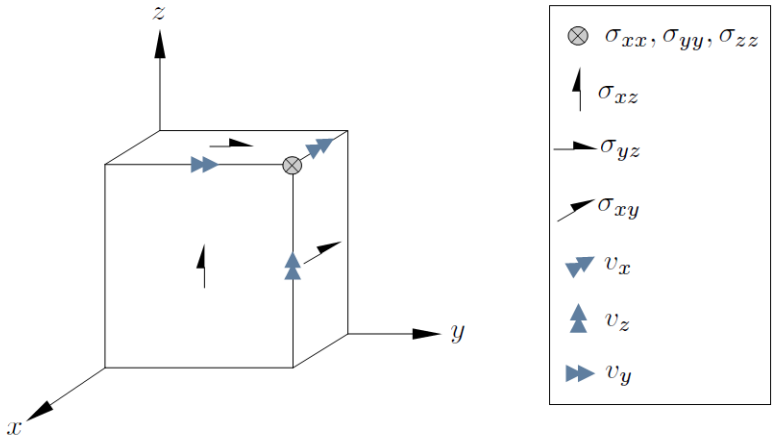

Figure 3.3: Three-dimensional staggered grid arrangement of a FDTD calculation cell.

rection of the cyclic motion of the solid material particles that are associated with the corresponding vibrations. The stress σ is a tensor variable which comprises six independent components, σ_{xx}, σ_{yy}, σ_{zz}, σ_{xy}, σ_{xz} and σ_{yz}. The stress tensor establishes the relation between the cyclic stress applied to a material element and the corresponding cyclic deformation of that element. In this thesis, the velocity and stress components are denoted as field variables for the vibration problems.

3.6.2 Arrangement of vibration field variables in FDTD

Figure 3.3 illustrates the spatial arrangement of the field variables within a single three dimensional calculation staggered grid cell [10, 68] used for this thesis. These single calculation cells are combined together to form a larger structure, such as a thin plate or a solid parallelepiped. Figure 3.3 indicates that the field variables are generally offset in space except for the normal components of the stress tensor, which are located at the same spatial position in the calculation cell. In this work, the positions along the x, y and z axis are denoted by the indexes i, j and k respectively. It is useful to consider a two-dimensional version of the staggered grid arrangement, so the spatial indexes of the variables can be visualised. Figure 3.4 illustrates a two-dimensional staggered grid for a FDTD vibration problem, where the indexes i and j correspond to the positions along the x- and y-directions.

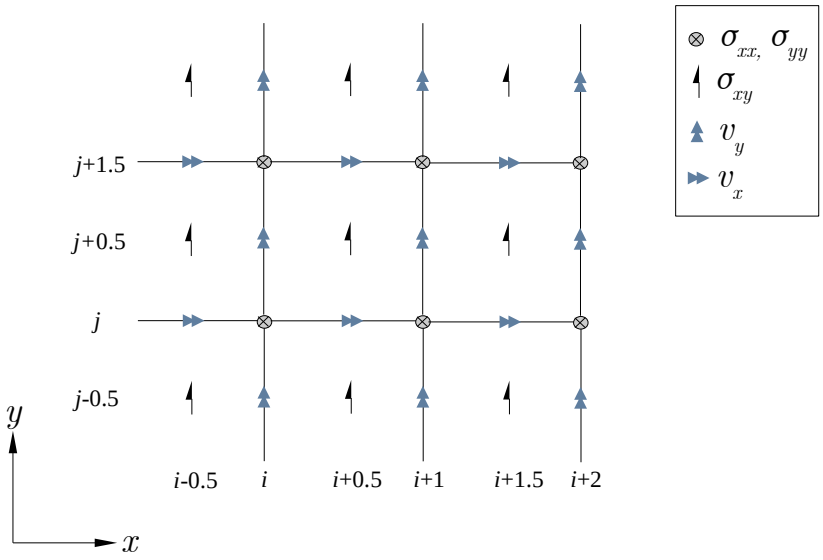

Figure 3.4: Two-dimensional staggered grid arrangement of a FDTD calculation cell.

3.7 FDTD viscoelastic update equations

In this section the discrete versions of the momentum and constitutive equations presented in section 3.5 are indicated. The spatial indices i, j, k correspond to the Cartesian x-, y- and z-directions.

3.7.1 Two-dimensional FDTD equations

The lattice shown in Figure 3.4 shows how the two-dimensional components of stress and velocity are placed at different positions forming a staggered grid. However, the normal stress components, σ_{xx} and σ_{yy}, are placed at the same position. In addition to the spatial offset, there is also an offset in time, where the stress components are calculated at different times to the velocity components.

Based on the space lattice shown in Figure 3.4, equation 3.27 is discretized as fol-

lows:

$$v_y^{n+\frac{1}{2}}\Big|_{i,j+\frac{1}{2}} = v_y^{n-\frac{1}{2}}\Big|_{i,j+\frac{1}{2}} + \frac{\Delta t}{\rho}\left[D_x\sigma_{xy}^n\Big|_{i-\frac{1}{2},j+\frac{1}{2}} + D_y\sigma_{yy}^n\Big|_{i,j} - \beta v_y^{n-\frac{1}{2}}\Big|_{i,j+\frac{1}{2}}\right] \quad (3.37)$$

where D denotes the forward difference, as defined in Appendix I.

In order to discretize equation 3.24, the mixed derivatives can be reversed using Clairaut's theorem:

$$\frac{\partial}{\partial t}\left(\frac{\partial v_y}{\partial y}\right) = \frac{\partial}{\partial y}\left(\frac{\partial v_y}{\partial t}\right) = \frac{\partial a_y}{\partial y} \quad (3.38)$$

where a_z represents the acceleration in the z-direction. In discrete form it is calculated from v_z using:

$$a_y^{n+1}\Big|_{i,j} = \frac{v_y^{n+1}\Big|_{i,j} - v_y^n\Big|_{i,j}}{\Delta t} \quad (3.39)$$

Using this variable substitution, equation 3.24 is discretized as:

$$\sigma_{yy}^{n+1}\Big|_{i,j} = \sigma_{yy}^n\Big|_{i,j} + \Delta t\left[\lambda\, D_x v_x^{n+\frac{1}{2}}\Big|_{i-\frac{1}{2},j} + (\lambda+2\mu)\, D_y v_y^{n+\frac{1}{2}}\Big|_{i,j-\frac{1}{2}} + \chi\, D_x a_x^{n+\frac{1}{2}}\Big|_{i-\frac{1}{2},j} + (\chi+2\gamma)\, D_y a_y^{n+\frac{1}{2}}\Big|_{i,j-\frac{1}{2}}\right] \quad (3.40)$$

Equations 3.37 and 3.40 essentially form the update equations for v_z and σ_{zz}, respectively. The nature of the method is that the value of a variable at a given instant of time is calculated directly from the values obtained at previous instants of time. Note that in order to transform equations 3.37 and 3.40 into a form that can be implemented using a programming language, the indexes of the field array variables must be integers and cannot be fractions.

3.7.2 Three-dimensional FDTD equations

For the vibroacoustic problem considered in this thesis, the variables are arranged in three-dimensional space according to a lattice described by Schroeder *et al* [10]. The discretization of the constitutive equations 3.28 - 3.33 and momentum equations 3.34 - 3.36 is analogous to the discretization process described in section 3.7.1. The three-dimensional equations will necessarily have more terms than their corresponding two-dimensional equations, since it is necessary to consider the non-zero velocity field in the y-direction, v_y. The discrete three dimensional form of the constitutive equations 3.28 - 3.33 is then:

$$\begin{aligned}\sigma_{xx}^{n+1}\Big|_{i,j,k} = \sigma_{xx}^{n}|_{i,j,k} + \\ + \Delta t \Bigg[(\lambda+2\mu)\, D_x v_x^{n+\frac{1}{2}}\Big|_{i-\frac{1}{2},j,k} + \lambda\, D_y v_y^{n+\frac{1}{2}}\Big|_{i,j-\frac{1}{2},k} + \\ + \lambda\, D_z v_z^{n+\frac{1}{2}}\Big|_{i,j,k-\frac{1}{2}} + (\chi+2\gamma)\, D_x a_x^{n+\frac{1}{2}}\Big|_{i-\frac{1}{2},j,k} + \\ + \chi\, D_y a_y^{n+\frac{1}{2}}\Big|_{i,j-\frac{1}{2},k} + \chi\, D_z a_z^{n+\frac{1}{2}}\Big|_{i,j,k-\frac{1}{2}}\Bigg] \end{aligned} \tag{3.41}$$

$$\begin{aligned}\sigma_{yy}^{n+1}\Big|_{i,j,k} = \sigma_{yy}^{n}\Big|_{i,j,k} + \\ + \Delta t \Bigg[\lambda\, D_x v_x^{n+\frac{1}{2}}\Big|_{i-\frac{1}{2},j,k} + (\lambda+2\mu)\, D_y v_y^{n+\frac{1}{2}}\Big|_{i,j-\frac{1}{2},k} + \\ + \lambda\, D_z v_z^{n+\frac{1}{2}}\Big|_{i,j,k-\frac{1}{2}} + \chi\, D_x a_x^{n+\frac{1}{2}}\Big|_{i-\frac{1}{2},j,k} + \\ + (\chi+2\gamma)\, D_y a_y^{n+\frac{1}{2}}\Big|_{i,j-\frac{1}{2},k} + \chi\, D_z a_z^{n+\frac{1}{2}}\Big|_{i,j,k-\frac{1}{2}}\Bigg] \end{aligned} \tag{3.42}$$

$$\sigma_{zz}^{n+1}\Big|_{i,j,k} = \sigma_{zz}^{n}|_{i,j,k} + \\ + \Delta t \left[\lambda \, D_x v_x^{n+\frac{1}{2}}\Big|_{i-\frac{1}{2},j,k} + \lambda \, D_y v_y^{n+\frac{1}{2}}\Big|_{i,j-\frac{1}{2},k} + \right. \\ + (\lambda + 2\mu) \, D_z v_z^{n+\frac{1}{2}}\Big|_{i,j,k-\frac{1}{2}} + \chi \, D_x a_x^{n+\frac{1}{2}}\Big|_{i-\frac{1}{2},j,k} + \\ \left. + \chi \, D_y a_y^{n+\frac{1}{2}}\Big|_{i,j-\frac{1}{2},k} + (\chi + 2\gamma) \, D_z a_z^{n+\frac{1}{2}}\Big|_{i,j,k-\frac{1}{2}} \right] \quad (3.43)$$

$$\sigma_{xz}^{n+1}\Big|_{i,j,k} = \sigma_{xz}^{n}|_{i,j,k} + \\ + \Delta t \left[\mu \left(D_z v_y^{n+\frac{1}{2}}\Big|_{i-\frac{1}{2},j,k} + D_y v_z^{n+\frac{1}{2}}\Big|_{i,j,k+\frac{1}{2}} \right) + \right. \\ \left. + \gamma \left(D_z a_x^{n+\frac{1}{2}}\Big|_{i-\frac{1}{2},j,k} + D_x a_z^{n+\frac{1}{2}}\Big|_{i,j,k+\frac{1}{2}} \right) \right] \quad (3.44)$$

$$\sigma_{yz}^{n+1}\Big|_{i,j,k} = \sigma_{yz}^{n}\Big|_{i,j,k} + \\ + \Delta t \left[\mu \left(D_z v_y^{n+\frac{1}{2}}\Big|_{i,j-\frac{1}{2},k} + D_y v_z^{n+\frac{1}{2}}\Big|_{i,j,k+\frac{1}{2}} \right) + \right. \\ \left. + \gamma \left(D_z a_y^{n+\frac{1}{2}}\Big|_{i,j-\frac{1}{2},k} + D_z a_z^{n+\frac{1}{2}}\Big|_{i,j,k+\frac{1}{2}} \right) \right] \quad (3.45)$$

$$\sigma_{xy}^{n+1}\Big|_{i,j,k} = \sigma_{xy}^{n}\Big|_{i,j,k} + \\ + \Delta t \left[\mu \left(D_y v_x^{n+\frac{1}{2}}\Big|_{i-\frac{1}{2},j,k} + D_x v_y^{n+\frac{1}{2}}\Big|_{i,j+\frac{1}{2},k} \right) + \right. \\ \left. + \gamma \left(D_y a_x^{n+\frac{1}{2}}\Big|_{i-\frac{1}{2},j,k} + D_x a_y^{n+\frac{1}{2}}\Big|_{i,j+\frac{1}{2},k} \right) \right] \quad (3.46)$$

The discrete three dimensional form of the momentum equations 3.34 - 3.36 is the following:

$$v_x^{n+\frac{1}{2}}\Big|_{i+\frac{1}{2},j,k} = v_x^{n-\frac{1}{2}}\Big|_{i+\frac{1}{2},j,k} + \\ + \frac{\Delta t}{\rho}\left[D_x\sigma_{xx}^n|_{i,j,k} + D_y\sigma_{xy}^n\Big|_{i,j,k} + D_z\sigma_{xz}^n|_{i,j,k} - \beta v_x^{n-\frac{1}{2}}\Big|_{i+\frac{1}{2},j,k}\right] \quad (3.47)$$

$$v_y^{n+\frac{1}{2}}\Big|_{i,j+\frac{1}{2},k} = v_y^{n-\frac{1}{2}}\Big|_{i,j+\frac{1}{2},k} + \\ + \frac{\Delta t}{\rho}\left[D_x\sigma_{xy}^n\Big|_{i,j,k} + D_y\sigma_{yy}^n\Big|_{i,j,k} + D_z\sigma_{yz}^n\Big|_{i,j,k} - \beta v_y^{n-\frac{1}{2}}\Big|_{i,j+\frac{1}{2},k}\right] \quad (3.48)$$

$$v_z^{n+\frac{1}{2}}\Big|_{i,j,k+\frac{1}{2}} = v_z^{n-\frac{1}{2}}\Big|_{i,j,k+\frac{1}{2}} + \\ + \frac{\Delta t}{\rho}\left[D_x\sigma_{xz}^n|_{i,j,k} + D_y\sigma_{yz}^n\Big|_{i,j,k} + D_z\sigma_{zz}^n|_{i,j,k} - \beta v_z^{n-\frac{1}{2}}\Big|_{i,j,k+\frac{1}{2}}\right] \quad (3.49)$$

3.8 Damping frequency characteristics

Ideally, it would be possible to derive a model of damping that would provide loss factors with an arbitrary frequency dependence. A very general description of damping can be obtained by using a 'relaxation function' approach [76]. According to this approach, the stress depends on the time history of the strains, rather than just its instantaneous value. The relation between stress and strain assumes the following form [73]:

$$\sigma(t) = E_1\epsilon(t) - \int_0^\infty \epsilon(t-\Delta t)\varphi(\Delta t)d(\Delta t) \quad (3.50)$$

where $\varphi(\Delta t)$ are the relaxation functions, given by:

$$\varphi(\Delta t) = \frac{E_2}{\tau}e^{-\Delta t/\tau} \quad (3.51)$$

where E_2 is a constant and τ is the relaxation time. If a given frequency-dependent profile is desired, more complex relaxation functions can be obtained by adding more terms containing different relation times. The disadvantage of the 'relaxation function' approach is that it leads to complex constitutive relations. Nonetheless, this method has been successfully implemented in FDTD [77].

The approach used in this thesis, developed by Toyoda et al [71], is to model viscoelastic damping by employing two constants in the constitutive equation 3.16 and another constant in the momentum equation 3.12. This approach results in a internal loss factor that depends on frequency in a similar way to mechanical systems that follow Rayleigh damping [71]. The constant β results in damping that is proportional to velocity. The frequency dependence of the β loss factor curve is inversely proportional to frequency. The constants γ and χ result in equivalent frequency characteristics, as can be found through numerical experiments; hence it is possible to consider just γ and set χ to zero whilst still obtaining a general Rayleigh damping profile. Therefore using only the constants β and γ, the frequency-dependent loss factor is well approximated by the following relation [78]:

$$\eta = \frac{\beta}{\rho\omega} + \frac{\omega\gamma}{E} \tag{3.52}$$

In this thesis the frequency-dependent loss factor of the plate is determined from measurements and the damping coefficients are calculated so that the resulting internal loss factor used in FDTD follows the loss factor measured for the actual plate as closely as possible. Appendix IV indicates how β, γ and χ can be varied to achieve different frequency-dependent profiles for the loss factors.

3.9 Stability of vibroacoustic simulations

As mentioned in section 2.5, the Courant condition (equation 2.41) determines the maximum possible value for the time step in the explicit FDTD model. In the

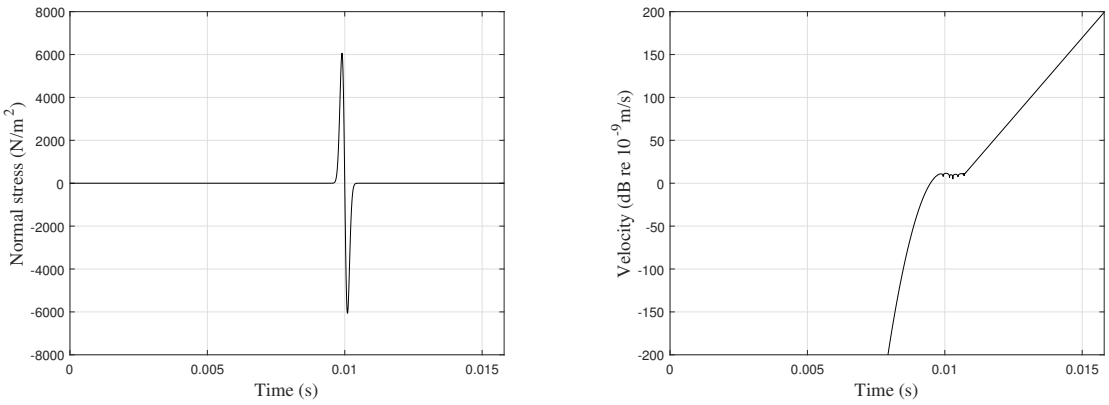

Figure 3.5: Example of numerical instability obtained using a inadequate time step for an aluminium plate. Stress excitation (left) and corresponding velocity level response (right).

Courant condition, C is the highest phase velocity of any wave motion within the frequency range of excitation. In this thesis, the mechanical behaviour of thin plates is approximated and therefore the phase velocities mentioned in section 3.3.3.1 need to be considered, within the frequency range of the simulation, for stability analysis.If the chosen time step does not satisfy the inequality in equation 2.41, the solution becomes unstable, i.e., the response will be unbounded. In practice, other factors such as damping and boundary conditions can also give rise to unstable solutions, even at time steps shorter than those determined by the Courant condition, as this condition is a necessary but not sufficient condition for stability [35]. Hence the aim is to find the largest possible value of time step that provides a stable solution over the time period of the FDTD simulation.

3.10 Vibration source

A widely used type of source in vibration and vibroacoustics simulations is the 'hard' source, where a prescribed time function, a designated 'driving' function, is assigned to a stress or velocity component. This type of source is described by

Schneider [40]. The time history of the source node is dictated only by the 'driving' function, irrespective of the state of its neighbour nodes. For example, considering a normal stress source along the z-direction defined at grid positions (i, j), its time history is defined by:

$$\sigma_{zz}^{n}|_{i,j} = f\,(n) \tag{3.53}$$

where f denotes the 'driving' function. When the stress values σ_{zz}^{n} are converted to forces F_z^n, so that mobilities can be calculated, the 'driving' function must be multiplied by the area perpendicular to the direction of the source. In the case of a source defined along the z-direction, it is necessary to multiply the 'driving' function by the spatial resolutions along the x-and y-directions:

$$F_z^n|_{i,j} = \sigma_{zz}^{n}|_{i,j}\,\Delta x \Delta y \tag{3.54}$$

The simulations in this thesis use a 'hard' vibration source. For this source the normal stress component in the z-direction is assigned a time dependence $F(t)$, which is converted into $\sigma_{zz}(t)$ through division by the area of a single horizontal grid cell, $\Delta x \Delta y$. The time dependence used was the derivative of the Gaussian pulse (section 2.8) in order to avoid static loading and corresponding deformation of the plate. The vibration source node follows the driving function irrespective of the state of its neighbour nodes.

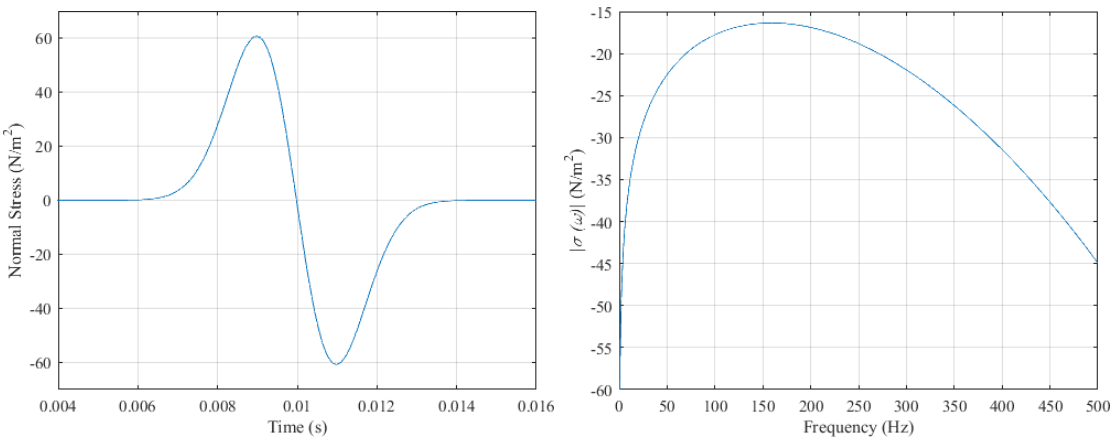

Figure 3.6: Vibration hard source: Time-dependent normal stress (left) and corresponding magnitude of the Fourier spectrum (right).

3.11 Simply supported boundary conditions

For the edges of the three-dimensional plate, the implementation of its boundaries aims to approximate the following conditions corresponding to a simply-supported two-dimensional thin plate [79]:

$$\begin{cases} w = 0, M_x = 0 & \text{for } x = 0, L_y \\ w = 0, M_y = 0 & \text{for } y = 0, L_x \end{cases} \tag{3.55}$$

where w denotes displacement in the z-direction and M_x and M_y indicate the bending moments along the x- and y-directions respectively.

To implement simply-supported boundaries using the general viscoelastic FDTD formulation, only the kinematic condition $w = 0$ needs to be specified. This is approximately carried out by assigning a value of zero to the vertical velocities that are located on the mid-plane around the plate edges as shown in Figure 3.7. As shown in the same figure, the lateral velocity components of the plate edges are calculated like the other velocity components of interior of the plate. The validity of this approximation is confirmed in the analytical/FDTD eigenfrequency comparison results obtained for a simply supported plate that are shown in table 6.2. In this diagram the velocity nodes of the air particles are represented by a single arrow whereas the velocity of the solid medium is represented by a double arrow. Note that the approach described here differs from the implementation used for dimension-reduced models [80] which require both displacement and bending moment conditions.

The boundary conditions defined in this section refer to the plate edges. The solid-air boundary conditions that cover the remainder of the domain are described in the following section 3.12.

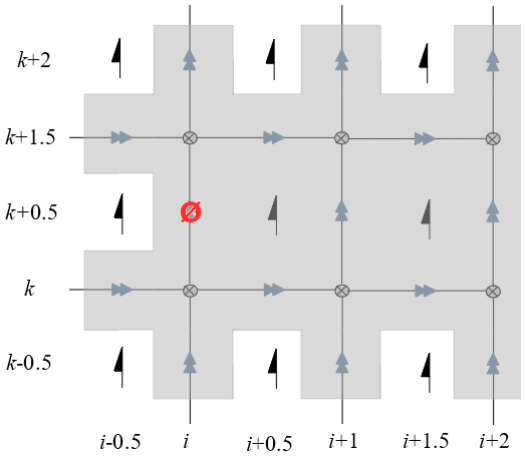

Figure 3.7: Lattice diagram for a cross-section through the solid medium (shaded grey) indicating the implementation of the simply-supported boundary condition using a velocity node set to zero which is shown in red.

3.12 Simplified air/solid boundary conditions

The aim of the new solid/air boundary conditions which is developed in this section is to provide an alternative to the approach of Toyoda *et al* [81] that is less complex and brings significant computational advantages.

3.12.1 Theoretical background

For the velocity nodes at the boundary between air and solid media, Toyoda *et al* [81] split the velocity update equation into two equations involving a forward difference and a backward difference. These equations are then combined to form a new equation, where the space step across the boundary is divided by a factor of two and the density at the boundary between the two media is averaged. The halving of the space step across the boundary will lead to a smaller time step being required for the simulation to be stable, according to the Courant Condition (equation 2.41). This type of boundary condition is referred to in this thesis as the 'standard approach'. In order to avoid the time step implications required by the standard approach, the implementation developed in this thesis considers the update equations for the

velocity nodes that lie on the boundaries to have the same form as the other solid medium velocity update equation (Equation 3.37) for which the density equals that of the actual solid and the space steps across the boundaries remain unchanged. However, in this thesis both the pressure and stress fields are modelled; hence the velocity update equation for a boundary node must include both pressure and stress terms, as indicated in equation 3.56:

$$v_z^{n+\frac{1}{2}}\Big|_{i,k+\frac{1}{2}} = v_z^{n-\frac{1}{2}}\Big|_{i,k+\frac{1}{2}} + \frac{\Delta t}{\rho}\left[\frac{\sigma_{xz}^n|_{i+\frac{1}{2},k+\frac{1}{2}} - \sigma_{xz}^n|_{i-\frac{1}{2},k+\frac{1}{2}}}{\Delta x} + \frac{\sigma_{zz}^n|_{i,k+1} + p^n|_{i,k}}{\Delta z} - \beta v_z^{n-\frac{1}{2}}\Big|_{i,k+\frac{1}{2}}\right] \quad (3.56)$$

It is assumed that compression corresponds to a positive pressure increment, whereas in terms of stress tensors the same compression is assumed to be a negative stress increment (σ_{xx}=σ_{yy}=σ_{zz}=$-p$) [62]. This sign convention is used in equation 3.56. The shear stress nodes adjacent to the boundary are set to zero because air is assumed to be an inviscid medium. This approach to implementing solid-air boundaries is used in this thesis and will be referred to as a 'simplified approach' because the implementation requires fewer calculations than the standard approach. For convenience the derivation considers a plate lying in a Cartesian coordinate plane, although it is feasible (but more complex) to consider other plate orientations.

The standard and simplified approaches result in the pattern shown in Figure 3.8. Note that the principle applies to all nodes of the solid medium that are adjacent to the surrounding medium, not just the upper and lower surfaces of the solid medium. In this lattice diagram, the simplified approach results in boundary conditions for the plate which appear to be 'ragged', although in terms of its eigenfrequencies the plate behaves as if it has smooth edges. Note that the eigenfrequencies correspond to a different set of physical dimensions as might be expected from the number of nodes in the solid medium. The physical dimensions along a given direction using the simplified boundary conditions are referred to as 'effective' dimensions, which are $L_{x,\text{eff}}$, $L_{y,\text{eff}}$ and $L_{z,\text{eff}}$. Considering the number of normal stress nodes assigned

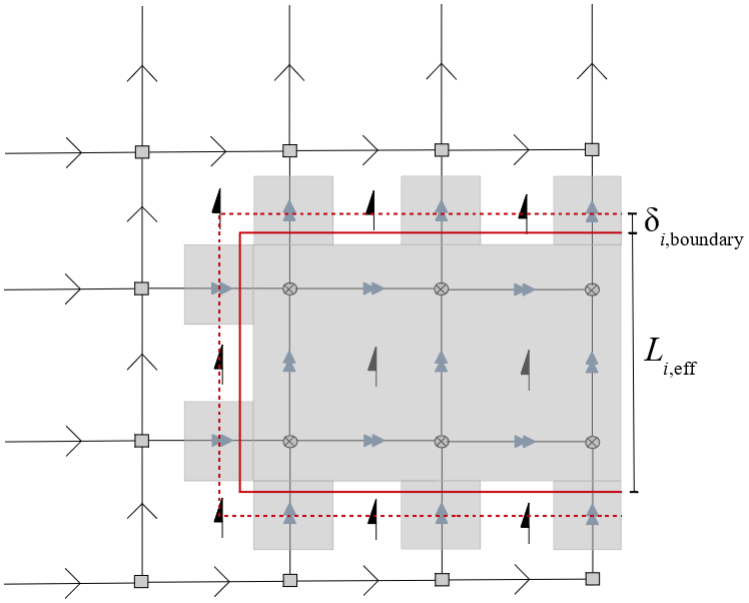

Figure 3.8: Lattice diagram indicating the solid medium (shaded grey), the expected boundary between the air and the solid medium (red dashed line) and the effective boundary (red solid line).

to the plate, or by considering the standard approach, the physical dimensions that are to be expected, are referred to as 'expected' dimensions, $L_{x,\text{exp}}$, $L_{y,\text{exp}}$ and $L_{z,\text{exp}}$. In Figure 3.8, the spatial offset along the i^{th} Cartesian direction between $L_{i,\text{eff}}$ and $L_{i,\text{exp}}$ is denoted by $\delta_{i,\text{boundary}}$. $L_{i,\text{eff}}$ can be obtained from $L_{i,\text{exp}}$ via the relation $L_{i,\text{eff}} = L_{i,\text{exp}} - 2\delta_{i,\text{boundary}}$. Hence, it is necessary to quantify $\delta_{i,\text{boundary}}$ in order to predict $L_{i,\text{eff}}$ from $L_{i,\text{exp}}$ and to be able to design plates with a prescribed set of dimensions.

To quantify the value of $\delta_{i,\text{boundary}}$ along a given direction i of the plate, a number of numerical tests are now carried out. These tests are based on the assumption that the mismatch between the expected and effective dimensions along a given direction must vanish as the number of calculation cells in that direction is increased. Therefore, tests are carried out with the minimum possible number of nodes along the thickness direction of the plate (two normal stress nodes) and the largest possible number of nodes along the other two lateral directions. The difference between the eigenfrequencies obtained from the FDTD model using the simplified approach and the eigenfrequencies corresponding to a plate with the expected dimensions given by equation 3.58 is primarily due to the difference between the expected and

the effective thickness of the plate. Although it is only possible to identify an approximate value for $\delta_{i,\text{boundary}}$ using this numerical approach, this approximation becomes more accurate as the number of lateral calculation cells increases.

To carry out these tests, consider the analytical equation for the prediction of the eigenfrequencies $f_{p,q}$ for the bending modes (p,q) of a simply-supported plate in the xy plane [57]:

$$f_{p,q} = \frac{\pi L_z c_\text{L}}{2\sqrt{12}} \left[\left(\frac{p}{L_x} \right)^2 + \left(\frac{q}{L_y} \right)^2 \right] \tag{3.57}$$

where L_z is the plate thickness, c_L is the quasi-longitudinal wavespeed and L_x and L_y are the lengths of the plate along the x- and y-directions, respectively.

The eigenfrequencies of a plate with expected dimensions are calculated as follows:

$$f_{p,q}^\text{exp} = \frac{\pi L_{z,\text{exp}} c_\text{L}}{2\sqrt{12}} \left[\left(\frac{p}{L_{x,\text{exp}}} \right)^2 + \left(\frac{q}{L_{y,\text{exp}}} \right)^2 \right] \tag{3.58}$$

and the eigenfrequencies of a plate with effective dimensions are given by:

$$f_{p,q}^\text{eff} = \frac{\pi L_{z,\text{eff}} c_\text{L}}{2\sqrt{12}} \left[\left(\frac{p}{L_{x,\text{eff}}} \right)^2 + \left(\frac{q}{L_{y,\text{eff}}} \right)^2 \right] \tag{3.59}$$

As the number of lateral nodes along the x- and y-directions is increased, the accuracy is increased for the two approximations: $L_{x,\text{eff}} \approx L_{x,\text{exp}}$ and $L_{y,\text{eff}} \approx L_{y,\text{exp}}$. The number of normal stress nodes across the thickness (z-direction) of the plate is set to two. This is the minimum number to allow bending wave motion where the lower stress node is strained and the upper node is under compression, and vice-versa. Hence, $L_{z,\text{exp}} = 2\Delta z$.

With the approximations for the expected and effective lengths across the lateral directions of the plate, the expected and effective eigenfrequencies are then related to the expected and effective thicknesses of the thin plate by:

$$f_{p,q}^\text{eff} / f_{p,q}^\text{exp} = L_{z,\text{eff}} / L_{z,\text{exp}} \tag{3.60}$$

Number of nodes	20	40	60	80	100	120
$f_{1,1}^{\text{eff}}/f_{1,1}^{\text{exp}}(-)$	0.68	0.69	0.69	0.69	0.70	0.70

Table 3.1: Ratios of eigenfrequencies obtained using effective and expected boundaries using different numbers of normal stress nodes

Since $L_{z,\text{eff}} = L_{z,\text{exp}} - 2\delta_{z,\text{boundary}}$ it can be shown that

$$\delta_{z,\text{boundary}} = \frac{L_{z,\text{exp}}}{2}\left(1 - \frac{f_{p,q}^{\text{eff}}}{f_{p,q}^{\text{exp}}}\right) \tag{3.61}$$

Since $L_{z,\text{exp}} = 2\Delta z$, the following equation relates $\delta_{z,\text{boundary}}$ to the spatial resolution along the z-direction:

$$\delta_{z,\text{boundary}} = \Delta z\left(1 - \frac{f_{p,q}^{\text{eff}}}{f_{p,q}^{\text{exp}}}\right) \tag{3.62}$$

Equation 3.62 can also be used to relate $\delta_{i,\text{boundary}}$ to the spatial resolution along the i^{th} direction.

In principle, equation 3.62 applies to any plate mode (p,q); however, the numerical tests use the lowest fundamental mode (p=q=1) to determine the effective thickness because higher modes are increasingly affected by numerical errors such as spatial discretization and numerical dispersion.

The numerical tests are carried out using undamped plates (arbitrary material properties) with two normal stress nodes along the thickness direction (for example, see Figure 3.8 where i corresponds to the z-direction) and a varying number of normal stress nodes along each of the horizontal x- and y-directions. The spatial resolution is set to 0.025 m in all directions so the expected plate thickness h_{exp} is 0.05 m. The results are given in Table 3.1 in terms of the ratio $f_{1,1}^{\text{eff}}/f_{1,1}^{\text{exp}}$. Assuming that the mismatch between the expected and effective lengths along a given direction vanishes as the number of nodes is increased in that direction, the ratio of 0.70 obtained using 120 stress nodes can be considered to be the most accurate; hence the value of $\delta_{z,\text{boundary}}$ is calculated to be $\delta_{z,\text{boundary}} = (1 - 0.7)\,\Delta z = 0.3\Delta z$. Therefore, the relation between $\delta_{i,\text{boundary}}$ and the spatial resolution along the i^{th} direction, denoted by x_i, is also given by $\delta_{i,\text{boundary}} = (1 - 0.7)\,\Delta x_i = 0.3\Delta x_i$

3.12.2 Example application

In this section, an example is used to define a methodology using the simplified boundaries approach to model a generic plate with a prescribed set of dimensions. In order to model a plate with n normal stress nodes and a side length of $L_{x,\text{eff}}$ along the x-direction, it is necessary to set the spatial resolution, Δx, to: $L_{x,\text{eff}} = n\Delta x - 2\times 0.3\Delta x \iff \Delta x = L_{x,\text{eff}}/(n-0.6)$. It can be seen that the spatial resolution which is required along that direction is defined by $\Delta x = L_x/(n-0.6)$ rather than $\Delta x = L_x/n$, where n is the number of normal stress nodes along a given direction. If n is set to two, which represents the number of stress nodes along the thickness direction, the space step along the thickness direction needed to implement the simplified boundary conditions approach is around 40% larger than that required using the approach described by Toyoda *et al* [81]. This larger space step provides significant computational benefits because the FDTD time step will be larger and the number of iteration required to reach a given time interval will be reduced.

3.13 Scaling of vibroacoustic fields

The Courant condition (equation 2.41) dictates the maximum possible value for the time step in the FDTD model given a grid size $(\Delta x, \Delta y, \Delta z)$ [2, 35]. The smaller the time step, the longer it will take the simulation to run a given time interval. If Δt does not satisfy the inequality in Equation 2.41, the solution becomes unstable, i.e. for transient excitation the response will tend to infinity.

It can be computationally expensive to run a large vibroacoustic model with a fine spatial resolution, especially because wavespeeds (e.g. for quasi-longitudinal waves on structures) are significantly higher in solids than in air. Such a fine spatial resolution is often required when dealing with geometrically thin objects, such as a thin plate radiating onto a room. Several approaches to model fine geometric

details embedded in large FDTD models have been primarily concerned with the use of non-uniform grids, parallelization of the FDTD computations and the use of dimension-reduced models. The parallelization of FDTD consists of splitting the routine calculations and memory over a number of CPU and GPU units, enabling shorter computation times. In FDTD, parallelization has been implemented by a variety of authors in a number of research fields such as electrodynamics [35], vibration [82], acoustics [83] and vibroacoustics [68]. The use of subgrids allocates a finer spatial resolution to regions that require more detail whilst using a coarser resolution elsewhere [35, 49]. Sub-gridding techniques have also been applied to acoustics problems [3, 84], but is seemingly not yet used in vibroacoustics. The use of dimension-reduced models is another alternative to model the vibration of geometrically thin structures embedded in large acoustic domains. In these models, a one- or two-dimensional grid is used to solve the bending wave equations for a beam or a thin plate, respectively, and are coupled with a three-dimensional acoustic grid. The procedure of converting a three-dimensional solid structure into a two-dimensional structure results in significant memory savings and reduced computation times. The two-dimensional implementation of thin plates has been carried out using Kirchhoff-Love theory [85] and for two-dimensional thick plates using Mindlin-Reissner theory [86]. Dimension-reduced models have also been used to study structure-borne sound transmission in beam-plate composite structures [87]. In this thesis, an alternative formulation is proposed for the vibroacoustic problem to yield much faster results, in the sense of requiring less calculations to obtain a vibroacoustic prediction, than using only a non-parallelized standard FDTD approach, based on the work of Toyoda *et al* [68]. The main issue with vibroacoustic models is that if the spatial resolution is kept constant, a large number of cells are required to represent the whole domain. With a fine spatial resolution, the required time step will be very small as a consequence of the Courant condition. To overcome this problem, the proposal is to model a larger structure that has the same vibration characteristics as the actual structure and couple it to the acoustic medium because a coarse spatial resolution will result in a larger time step.

3.13.1 Methodology

Once the equivalent structure is identified and processed, the results can be scaled back to represent the actual structure. Assuming the thickness direction of the plate is coincident with the z-direction (vertical direction), the following steps are used to scale the vibroacoustic model:

(1) A scaling factor $s > 1$ is chosen and a plate with the same eigenfrequencies as the actual plate is identified where the side dimensions of the scaled plate are $L_{x'} = sL_x$ and $L_{y'} = sL_y$ respectively. In order to obtain the same bending eigenfrequencies (given by equation. 3.57), the thickness of the scaled plate is $h' = s^2h$.

(2) The spatial resolution of the scaled problem is then dictated by the dimensions of the scaled plate to give $\Delta x' = s\Delta x$, $\Delta y' = s\Delta y$ and $\Delta z' = s^2\Delta z$, which in turn results in a synchronous time step $\Delta t'$ step for both the plate solid medium and the acoustic medium. In addition to scaling the plate, the x-,y- and z-dimensions of the cavity also need to be scaled up by a factor of s to match the scaled x- and y-dimensions of the plate and to maintain the eigenfrequencies of the cavity. The scaled acoustic cavity with dimensions $L_{x'} = sL_x$, $L_{y'} = sL_y$ and $L_{z'} = sL_z$ is modelled using the aforementioned spatial resolutions: $\Delta x'$, $\Delta y'$ and $\Delta z'$. Uniform scaling of the x-,y- and z-dimensions of the cavity by a factor of s results in the use of fewer calculation cells along the z-direction because the space step is larger along this direction ($\Delta z' = s^2\Delta z > s\Delta z$), requiring a factor of s fewer cells than if the spatial resolution along the z-direction was given by $z' = s\Delta z$. The advantage of requiring fewer cavity cells along the z-direction is not exclusive to explicit FDTD routines that depend on the Courant condition as it could be used to increase the computational efficiency of other prediction methods. To calculate the eigenfrequencies of a scaled rectangular room so that they equal those of the actual room, the speed of sound in air must be scaled using $c' = sc$, such that:

$$f'_{n_x,n_y,n_z} = \frac{sc}{2}\sqrt{\left(\frac{n_x}{sL_x}\right)^2 + \left(\frac{n_y}{sL_y}\right)^2 + \left(\frac{n_z}{sL_z}\right)^2} \tag{3.63}$$

where $f_n^{'}$ denotes the eigenfrequencies of the scaled room.

(3) It is important that the absorption that occurs at the acoustic boundaries of the scaled model remain invariant. Since the sound absorption of a boundary is directly dependent on the specific acoustic impedance, the characteristic acoustic impedance of the air medium must remain constant. Since the speed of sound in air was scaled using $c' = sc$, the density of the air medium has to be scaled using $\rho_o' = \rho_o/s$ so that $c'\rho' = c\rho$.

(4) The magnitude of the driving-point mobility for the scaled plate needs to be offset from that of the actual plate. The driving-point mobility Y_{dp} of a simply-supported isotropic plate is given by:

$$Y_{\mathrm{dp}} = \frac{v}{F} = \frac{i4\omega}{\rho L_z S} \sum_{p=1}^{\infty} \sum_{q=1}^{\infty} \frac{\psi_{p,q}^2(x,y)}{\omega_{p,q}^2 (1 + i\eta) - \omega^2} \tag{3.64}$$

where $i^2 = -1$, S is the surface area of the plate, $\psi_{p,q}^2(x,y)$ is the local bending mode shape, and $\omega_{p,q}$ denotes the angular mode frequency.

Since the mode shapes, eigenfrequencies and loss factors are the same for the actual and scaled plates, the only difference between their transfer mobilities is in the absolute value. Taking the absolute value of the transfer mobility yields:

$$|Y_{\mathrm{dp}}| = \left|\frac{v}{F}\right| = \left|\frac{i4\omega}{\rho L_z S}\right| \left|\sum_{p=1}^{\infty} \sum_{q=1}^{\infty} \frac{\psi_{p,q}^2(x,y)}{\omega_{p,q}^2 (1 + i\eta) - \omega^2}\right| \tag{3.65}$$

Hence the following ratio is expected between the driving-point mobility of the scaled and actual plates:

$$\frac{|Y_{\mathrm{dp}}|_{\mathrm{scaled}}}{|Y_{\mathrm{dp}}|_{\mathrm{actual}}} = \frac{L_z S}{L_z' S'} = \frac{L_z L_x L_y}{L_z' L_x' L_y'} = \frac{L_z L_x L_y}{s^2 L_z s L_x' s L_y'} = s^{-4} \tag{3.66}$$

This result indicates that the magnitude of the scaled driving-point mobility is smaller than that of the actual plate, by a factor of s^{-4} or when considering mobility in decibels using $20\log_{10}(|Y_{\mathrm{dp}}|)$, by $80\log_{10}(s)$ dB. Therefore the results obtained should be scaled accordingly, in order to account for this offset in the magnitude of

the driving-point mobilities. For the model used for the experimental validation in this thesis, $s = 6$ and therefore the shift in level is ≈ 62 dB.

3.13.2 Scaling of sound fields in rooms

The sound field occurring in a rectangular room with dimensions L_x, L_y and L_z is characterised by the following eigenfrequencies $f_{p,q,r}$ [57]:

$$f_{p,q,r} = \frac{c}{2}\sqrt{\left(\frac{p}{L_x}\right)^2 + \left(\frac{q}{L_y}\right)^2 + \left(\frac{r}{L_z}\right)^2} \tag{3.67}$$

where p, q and r are positive integers and correspond to room mode numbers. The eigenfrequencies of a room whose dimensions have been scaled by a factor of s are given by:

$$f'_{p,q,r} = \frac{c}{2}\sqrt{\left(\frac{p}{sL_x}\right)^2 + \left(\frac{q}{sL_y}\right)^2 + \left(\frac{r}{sL_z}\right)^2} = \frac{c}{2s}\sqrt{\left(\frac{p}{L_x}\right)^2 + \left(\frac{q}{L_y}\right)^2 + \left(\frac{r}{L_z}\right)^2} \tag{3.68}$$

Hence, in order to keep the same eigenfrequencies, the speed of sound c needs to be multiplied by a factor of s, hence the scaled speed of sound $c' = sc$.

3.13.3 Extension to other topologies

The scaling approach is readily applied to more complex problems involving a number of geometrically parallel thin plates and/or acoustic cavities as illustrated by the examples in Figure 3.9. This includes the situation which simulates a sound transmission suite that can be used to determine impact or airborne sound insulation (Figure 3.9-d). When scaling a thin plate, the spatial resolution across its lateral dimensions is scaled by a factor of s, whereas the spatial resolution along the thickness direction must be scaled by a factor of s^2, so that the eigenfrequencies predicted by equation 3.57 remain invariant. This scaling of the spatial resolution can be considered as a coordinate transformation that applies to the whole FDTD

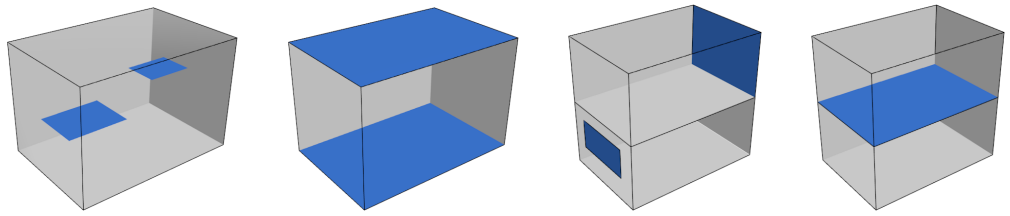

(a) (b) (c) (d)

Figure 3.9: Examples of valid configurations for the scaling method: (a) and (b) two isolated, parallel plates, (c) two isolated plates that each face into an acoustic cavity and (d) two acoustic spaces separated by a plate. Scaled thin vibrating plates are shown in blue with the grey surfaces representing the boundaries of the acoustic cavity.

model, given by:

$$\begin{cases} x' = sx \\ y' = sy \\ z' = s^2 z \end{cases} \tag{3.69}$$

For models involving one or more parallel plates, the scaling of their dimensions will be congruent because their lateral dimensions will be scaled by a common factor of s and their thickness direction will be scaled by a common factor of s^2. Therefore all the scaled plates will preserve the dynamic characteristics of the actual plates. For example, the plates shown in Figure 3.9-b can be simultaneously scaled if the thickness value for each of the two plates is set to $h_1' = s^2 h_1$ and $h_2' = s^2 h_2$. Additionally, since both plates use the same scaling factor, their lateral dimensions are given by $L_{x1}' = sL_{x1}$, $L_{y1}' = sL_{y1}$ and $L_{x2}' = sL_{x2}$, $L_{y2}' = sL_{y2}$.

3.13.4 Extension to other plate boundary conditions

In this section, the effects on scaling of having a set different boundary conditions other than the simply supported will be investigated.

The out-of-plane eigenfrequencies corresponding to the mode indices (m, n) of a

Boundary conditions	G_x	H_x	J_x
Pinned-pinned	m	m^2	m^2
Clamped-pinned	$m+\frac{1}{2}$	$\left(m+\frac{1}{2}\right)^2\left[1-\frac{4}{(2m+1)\pi}\right]$	$\left(m+\frac{1}{2}\right)^2\left[1-\frac{4}{(2m+1)\pi}\right]$
Free-free	$m+\frac{1}{2}$	$\left(m+\frac{1}{2}\right)^2\left[1-\frac{4}{(2m+1)\pi}\right]$	$\left(m+\frac{1}{2}\right)^2\left[1+\frac{12}{(2m+1)\pi}\right]$
Clamped-free	$m+\frac{1}{2}$	$\left(m+\frac{1}{2}\right)^2\left[1-\frac{4}{(2m+1)\pi}\right]$	$\left(m+\frac{1}{2}\right)^2\left[1+\frac{4}{(2m+1)\pi}\right]$
Clamped-pinned	$m+\frac{1}{4}$	$\left(m+\frac{1}{4}\right)^2\left[1-\frac{4}{(4m+1)\pi}\right]$	$\left(m+\frac{1}{4}\right)^2\left[1-\frac{4}{(4m+1)\pi}\right]$
Free-pinned	$m+\frac{1}{4}$	$\left(m+\frac{1}{4}\right)^2\left[1-\frac{4}{(4m+1)\pi}\right]$	$\left(m+\frac{1}{2}\right)^2\left[1+\frac{12}{(4m+1)\pi}\right]$

Table 3.2: Constants G_x, H_x and J_x for $m > 1$

rectangular thin plate subject to any arbitrary combination of free, simply supported and clamped conditions applied to its boundaries were originally approximated by Warburton [88] and summarised by Fahy *et al.*[89]:

$$\omega_{mn} = \frac{hc_L}{2\sqrt{3}}\left(\frac{\pi}{L_x}\right)^2 q_{mn} \tag{3.70}$$

where the term q_{mn} is given by

$$q_{mn} = \sqrt{G_x^4(m) + G_y^4(n)\left(\frac{L_x}{L_y}\right)^4 + 2\left(\frac{L_x}{L_y}\right)^2\left[\nu H_x(m)H_y(n) + (1-\nu)J_x(m)J_y(n)\right]} \tag{3.71}$$

The constants G_x, H_x, J_x, G_y, H_y and J_y are characteristic of each type of boundary condition and can be found for a great number of possible combinations in the work published by Warburton [88]. Table 3.2 shows the expressions for G_x, H_x and J_x as a function of the mode index m. The expressions for H_y, J_y and J_y are identical with the index m replaced for n.

These constants depend exclusevely on the mode indices m and n.

When the lateral dimensions of the plate are scaled by a factor of s, the corresponding

eigenfrequencies of the scaled system are given by:

$$\omega'_{mn} = \frac{hc_L}{2\sqrt{3}} \left(\frac{\pi}{sL_x} \right)^2 q_{mn} \tag{3.72}$$

The term q_{mn} remains unaffected by geometric scaling, since the constants G_x, G_y, H_x, H_y, J_x and J_y depend exclusively on the on the mode indices m and n and the scaling factors on the terms sL_x/sL_y do cancel out. Hence, to obtain the same eigenfrequencies as those of the unscaled system, it is necessary to scale the thickness of the plate by a factor of s^2.

It is therefore concluded that the scaling methodology for plates with any combination of free/clamped/simply supported boundaries is exactly the same as that used for simply supported plates.

3.13.5 Numerical efficiency of the scaling approach

As noted in section 3.13.1, the scaling approach requires a factor of s fewer elements than without scaling. In addition to the computational gain from the reduction in the number of elements, there is the additional benefit of being able to use a larger time step. The ratio between the time steps corresponding to the scaling and non-scaling approaches can be derived:

$$\frac{\Delta t'}{\Delta t} = \frac{\left[C\sqrt{\left(\frac{1}{\Delta x}\right)^2 + \left(\frac{1}{\Delta y}\right)^2 + \left(\frac{1}{\Delta z}\right)^2} \right]}{\left[C\sqrt{\left(\frac{1}{s\Delta x}\right)^2 + \left(\frac{1}{s\Delta y}\right)^2 + \left(\frac{1}{s^2\Delta z}\right)^2} \right]} \tag{3.73}$$

Equation 3.73 is not trivial to factorise or simplify, since the scaling factor s is not common to all the terms in the denominator. However, the gain in numerical efficiency can be estimated by assuming that $\Delta x \gg \Delta z$ and $\Delta y \gg \Delta z$ such that the corresponding terms for Δx and Δy in the Courant condition (equation 2.41) can be omitted. For thin plates this approximation is reasonable because the plate

thickness (z-direction) is typically at least one order of magnitude smaller than the lateral dimensions of the plate. Hence the relation between the original time step and the scaled time step can be estimated:

$$\frac{\Delta t'}{\Delta t} \approx \left[C\sqrt{\left(\frac{1}{\Delta z}\right)^2}\right] / \left[C\sqrt{\left(\frac{1}{s^2\Delta z}\right)^2}\right] = s^2 \tag{3.74}$$

Therefore the time step using the scaling approach is larger than that obtained without scaling by a factor of up to s^2. In addition, the scaling approach requires s fewer cells and the relationship between the scaled and original time steps is a maximum of s^2. Hence the total computational time of the scaled model is estimated to be reduced by a factor up to $s \times s^2 = s^3$ compared to the computation time needed for the original model. Note that this is the maximum possible reduction in computation time; the actual reduction in computation time will be less than s^3.

The scaling approach has the advantage of using larger time steps and fewer calculation cells than would be required without it. In addition, for plates with boundary conditions other than a combination of ideal free/clamped/ simply-supported boundaries, it is only necessary to be able to calculate or estimate the corresponding eigenfrequencies in order to identify the scaling factor for the z-direction.

3.13.6 Limitations

One limitation concerns the high-frequency limit for pure bending wave theory. If the thin plate frequency limit for the actual plate is [73]:

$$f_{\mathrm{B}} \approx 0.05\frac{c_{\mathrm{L}}}{h} \tag{3.75}$$

the limit for the scaled plate f'_{B} is given by $f'_{\mathrm{B}} = f_{\mathrm{B}}/s^2$ and the error in the simulation results will increase above this limit.

Another important factor that introduces errors when using the scaling approach is

numerical dispersion. When using the same space and time grid resolution for the air medium and solid medium additional numerical dispersion is introduced since wave propagation in the air medium occurs further away from the Courant limit than the wave propagation in the solid medium (which comparatively has a higher phase velocity). In addition, the larger the value used for the scaling factor, s, the less uniform the rectangular grid will be and the more problematic the numerical dispersion becomes. For the scaling factor value used in this thesis, $s = 6$, the experimental validation of the numerical results suggests that the effects of the numerical dispersion are negligible in the low frequency range considered in this thesis (< 200Hz).

3.14 Conclusions

This chapter covered both theoretical and numerical aspects of the application of FDTD to vibration and vibroacoustics problems. A new approach to model air/-solid boundaries was introduced. Two new approaches were introduced in order to gain computational efficiency and simplify the implementation of the FDTD models. The new 'simplified boundary approach' applies to modelling air/solid boundaries and results in significant computational advantage and simplified implementation when compared to the approach introduced by Toyoda *et al* [81]. The new 'scaling approach' scales the whole geometry and physical characteristics of the vibroacoustic model in order to reduce the computational cost of FDTD simulations when compared to the approach presented by Toyoda *et al* [68].

Both the 'scaling' approach and 'simplified boundary' approach lead to a significant increase in the time step that is required to run the simulations. This leads to a reduction in the maximum possible frequency for the analysis relating to the Nyquist frequency. However, this is not problematic for low-frequency applications below 250Hz that are primarily considered in this thesis for engineering structures such as small rooms in buildings, car cabins, or train carriages.

4 Experimental work

4.1 Introduction

This chapter describes the measurement procedures, and corresponding environments for all the experimental work carried out which can be divided into acoustic and vibroacoustic measurements.

Section 4.2 describes the measurement environment used for the acoustics and vibroacoustics experimental validations. The first set of measurements comprises a series of vibration and acoustic tests of the subwoofer used for the subsequent acoustics experimental work. These tests were carried out in the anechoic chamber and aim to characterise the dynamic behaviour of the subwoofer diaphragm when operating at low frequencies as well as its radiation pattern and were carried out inside an anechoic chamber. The remainder of the acoustic and vibroacoustic experiments described in this chapter were carried out in a small reverberation chamber.

Section 4.3 describes the measurements carried out to characterise the acoustic behaviour of the loudspeaker used for the acoustics measurements.

Section 4.4 describes the measurement procedure that was followed in order to estimate the damping constants of the room boundaries.

Section 4.5 details the measurement environment and setup used for the acoustic measurements that took place in the small reverberation chamber, where acoustic pressure grid measurements were carried out in the empty chamber and with the chamber divided and partially divided by a porous material.

Section 4.6 describes the procedure followed to measure the driving-point mobility of a thin aluminium plate.

Section 4.7 describes the vibroacoustic measurements that took place inside the small reverberation chamber, where the sound pressure field radiated by a mechanically point-excited aluminium plate was measured.

4.2 Acoustic chambers

The loudspeaker measurements (section 4.3) were carried out in the anechoic chamber of the Acoustics Research Unit, as shown in Figure 4.2. This chamber has dimensions 5 m × 4 m × 2.6 m. The sources were placed on resilient mountings to prevent the transmission of vibration to the metal supporting grid.

The experimental validations of the acoustics and vibroacoustics FDTD models (sections 4.4 - 4.7) were carried out in the small reverberation chamber. This chamber has dimensions 1.83 m × 2.87 m × 2.48 m and a volume of 13 m^3. The walls are brick with a painted plaster finish and the floor and ceiling are cast in situ concrete slabs. On one of the walls of the room, there is a heavy access door, that is primarily made of steel, with dimensions 78 cm × 216 cm. On the same wall, there is also a small 4 cm thick glass observation window, with dimensions 29 cm × 27.5 cm. There are a number of small objects inside the room that cannot be removed, such as two ceiling lamps, one fire alarm lamp and a cluster of electrical cables that connect the room to its exterior; these would have a negligible effect in the low-frequency range under investigation. The temperature of the reverberation room during the several measurement sessions varied between 20°C and 24°C.

4.3 Loudspeaker measurements

4.3.1 Equipment

The following equipment was used to carry out the loudspeaker measurements:

- USB Sound Card Trust 5.1 Surround;
- Sound Level Meter B&K type 2231;
- Microphone calibrator B&K type 4230;
- Omni-directional reference sound source B&K type 4204;
- Power amplifier B&K type 2706;
- Quad 50E power amplifier;
- TEAC CD Player CD-P1160D;
- Decade Attenuator, Tech Instruments co. LTD, model TE-111;
- FFT analyser - Multi Channel Data Station DS-9110;
- Accelerometer Conditioning Amplifier - BK Nexus;
- Laser vibrometer VH300+ OMETRON type No1/3030;
- Piston calibrator - BK type 4294;
- Celestion Csixs subwoofer loudspeaker (electronics removed);

4.3.2 Directivity measurements

The main purpose of this set of measurements is to test whether the Celestion subwoofer unit exhibits an omni-directional radiation pattern at frequencies below 150

Hz. To test this, the sound field was measured at seven different positions covering a hemisphere around the speaker. It was also necessary to verify whether the room would still be anechoic in this low frequency range, so that the results obtained would yield useful conclusions related to the actual behaviour of the speaker. To test this, the horizontal directional response of a known omnidirectional sound source was measured. This reference sound source consists of a fan type device manufactured by B&K, whose specifications indicate that the deviation in horizontal response should be less than 0.2 dB for frequencies above 100 Hz. Therefore any deviations above this range are not due to the speaker but rather to a possible non-anechoic measurement environment and/or experimental errors.

4.3.2.1 Measurement positions and results

In order to check whether the anechoic room could be considered anechoic below 150 Hz, a reference omni-directional sound source was placed in the centre of the chamber and placed on top of resilient material to prevent vibration of the floor of the chamber as indicated in Figure 4.2. In the first set of measurements, all the measurement positions were placed 1 m away from the source, forming angles of 120° between them. The average difference of sound pressure level obtained between the three positions above 100 Hz was 0.70 dB. The maximum difference between the measured levels was 2.7 dB and occured at 161 Hz. Since the maximum difference between the measured positions is less than 3 dB, the sound field in the anechoic chamber can be considered approximately anechoic above 100 Hz and below 150 Hz.

A second set of measurements was carried out in the centre of the anechoic room using four measurement positions, forming angles of 90° between them. Figure 4.1-a and -b shows a diagram where the orientation of the measurement positions in relation to the omni-directional reference source is indicated. Analysis of the results obtained for the four measurement positions indicate that the maximum difference in sound pressure level obtained was 2.4 dB. This confirms that the sound field inside the anechoic chamber can be approximated as a free field above 100 Hz (the cut-off

frequency for omni-directionality behaviour of the reference source) and below 150 Hz.

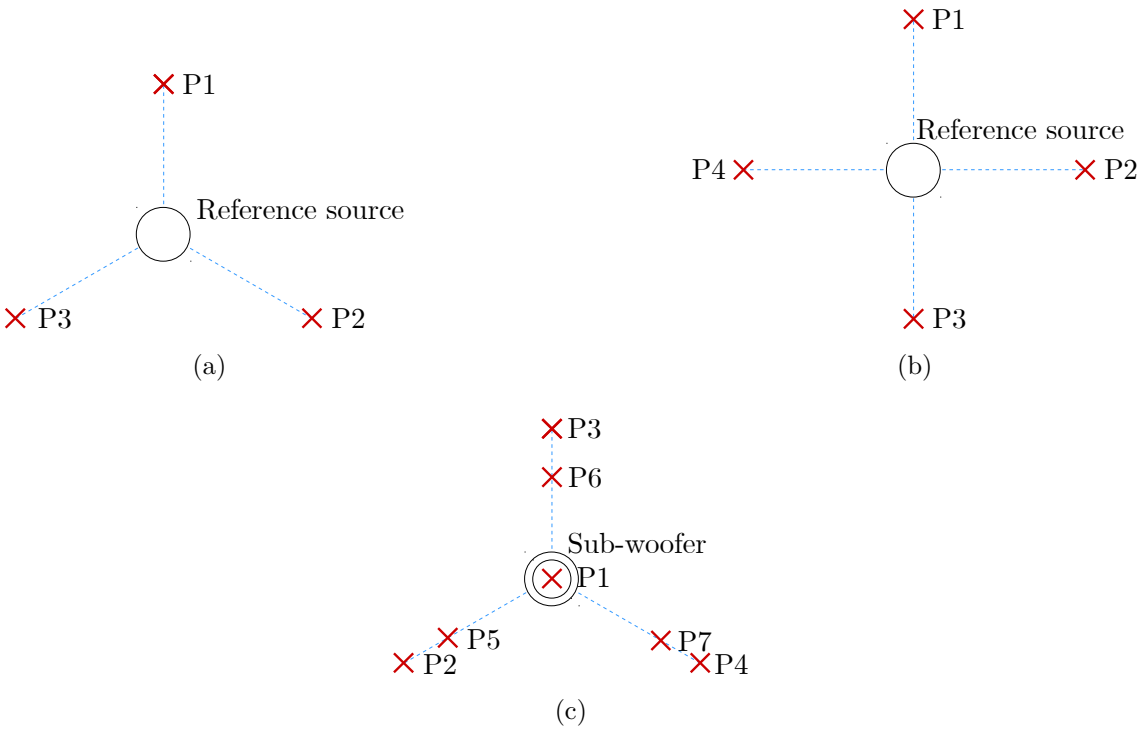

Figure 4.1: Measurement positions: a) and b) reference source c) subwoofer.

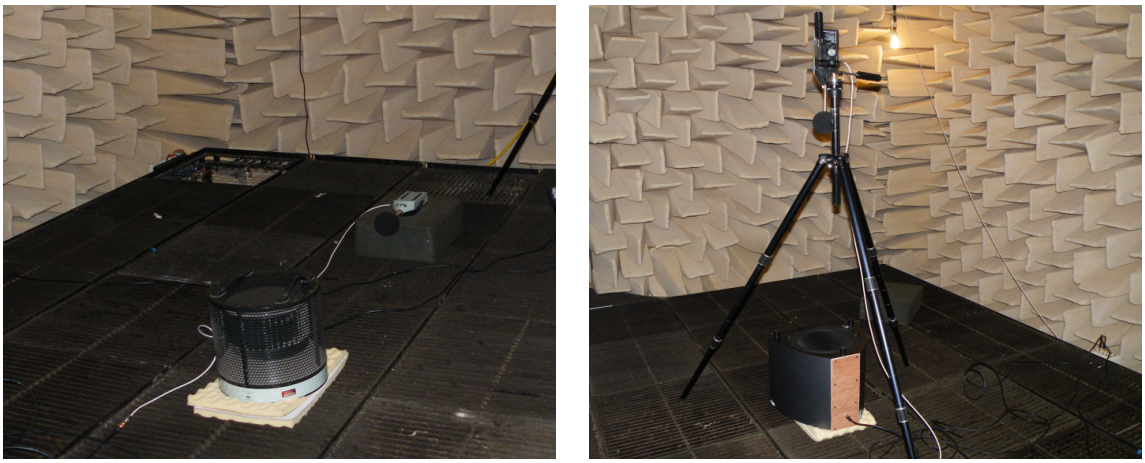

Figure 4.2: Directivity measurements in the anechoic chamber using the reference source (left) and subwoofer (right).

In order to measure the directivity of the subwoofer radiation pattern, a set of measurements was carried out in the anaechoic room. In this set of measurements, the Celestion subwoofer was placed at the centre of the chamber, with the diaphragm

facing up. Seven measurement positions were considered, covering a 1 m radius hemisphere around the speaker. The measurement positions used to measure directivity of the Celestion subwoofer are shown in Figure 4.1-c, where position 1 is located above the speaker, along its axis. Positions 2, 3 and 4 are located in the horizontal plane. Positions 5, 6 and 7 form an angle of 45° with the speaker and the horizontal plane. The results obtained for the directivity measurements of the Celestion subwoofer for the horizontal plane positions (positions 2, 3 and 4) are similar to those obtained using the omni-directional source in terms of differences in sound pressure levels. For the remaining positions, the maximum difference between responses in the frequency range between 100 Hz and 200 Hz is around 2.9 dB, confirming that it is reasonable to approximate the subwoofer as a omni-directional source in this range.

4.3.3 Measurement of loudspeaker cone velocity

The cone velocity of the subwoofer was measured at a number of different positions of its diaphragm, to assess whether its motion could be assumed to exhibit pistonic behaviour (Figure 4.3). This measurement was carried out using a laser vibrometer. The results, shown in Figure 4.4, indicate that for frequencies below 140 Hz the velocity levels obtained at the different cone positions show variations smaller than 3 dB. This is an indication that the assumption of pistonic behaviour of the speaker membrane is reasonable. Above this frequency limit, several positions of the diaphragm move with significantly different velocities indicating modal vibration of the subwoofer cone.

In order to check for non-linearities in the measurement chain, the polarity of the power amplifier was reversed and the cone accelerations corresponding to each polarity recorded. The acceleration response to reversed polarity was tested for two speaker configurations: diaphragm facing up and facing down. To reverse the polarity, the leads that connected the output of the power amplifier to the subwoofer were swapped. The results obtained (indicated in Figure 4.4) show that there were no

non-linearities observed for frequencies below 140 Hz when the subwoofer was facing up, as the accelerations measured for different polarities indicate a level difference of less than 3 dB. Above 140 Hz, reversal of the polarity of the loudspeaker results in significant cone acceleration possibly due to mechanical interference between the diaphragm of the speaker and the top plate of the magnet or some other component of the subwoofer.

The non-pistonic and non-linear behaviour observed in the subwoofer operation effectively limits the experimental validation to frequencies below 140 Hz.

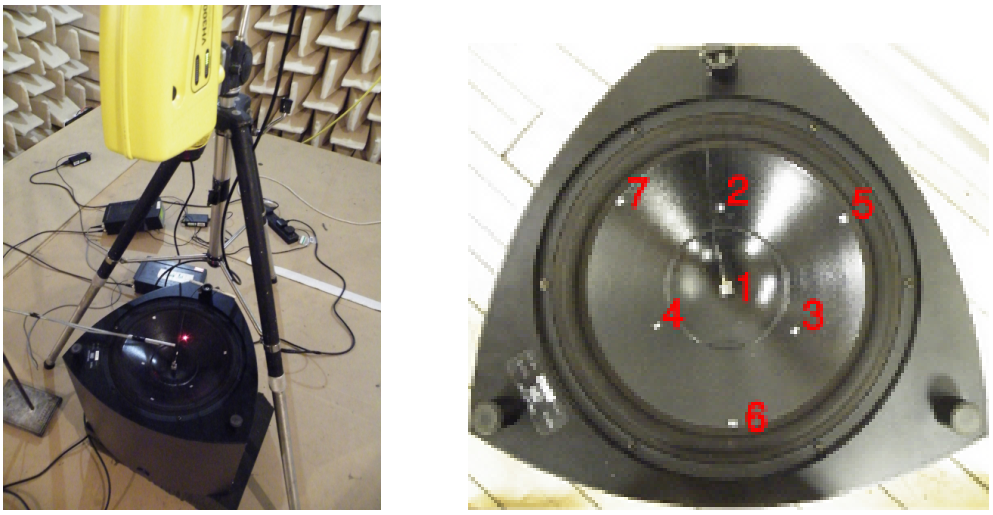

Figure 4.3: Measurement of subwoofer cone velocity using a laser vibrometer (left) and cone velocity measurement positions (right).

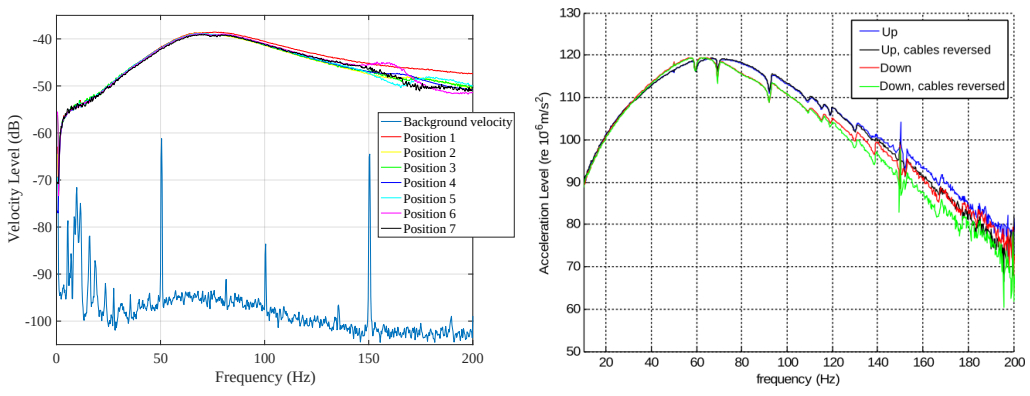

Figure 4.4: Velocity levels measured at different positions of the subwooder diaphragm (left) and the effect of reversing the polarity of the power amplifier on the subwoofer diaphragm (right).

4.4 Measurement of acoustic damping constants

This section contains the details of the experimental method used in the measurements of the damping constants that characterise the surface boundaries of the small reverberation chamber. In order to check for the influence of the measurement equipment in the chamber, a similar experiment was carried out in the room without any equipment.

4.4.1 Estimation of the reverberation times

For each resonance peak obtained in the room frequency response function, equation 2.55 was used to estimate the damping constant associated with that peak.

4.4.2 Equipment

The following equipment was used for this experiment:

- FFT analyser - Multi Channel Data Station DS-9110
- FFT analyser B&K type 2144
- B&K Nexus conditioning amplifier
- Microphone pre-amp type 2670;
- Microphone B&K type 4135;
- USB sound card Lexicon Lambda;
- Power amplifier B&K type 2706;
- Celestion Csixs subwoofer loudspeaker (electronics removed)

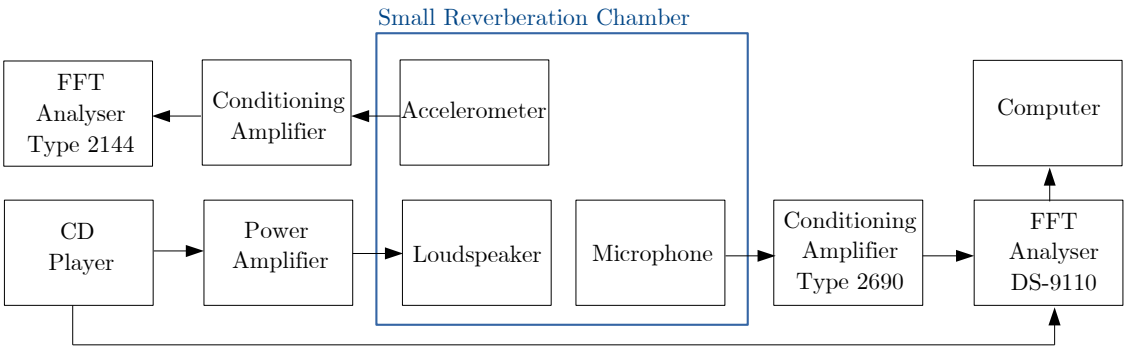

Figure 4.5: Setup used for the acoustic measurements

Figure 4.5 shows the measurement chain used for this experiment. The measurements were taken with a sampling rate of 44100 Hz and 16 bit depth. The recordings were clipped to 26,400,000 samples, corresponding to a recording duration of around 598.6 s. Each recording was then split into five sections of 5,280,000 samples. Each of these samples were divided into 64 sub-signals and the corresponding average spectrum was calculated. The final spectrum is then given by the average of the five spectra of each of the five sections that make up the original signal.

4.4.3 Source and microphone positions

Figure 4.6 shows a schematic indication of the source and the three receiver positions inside the small reverberation chamber. For all the measurement positions, the microphone was placed in the corner of the room (with the exception of the corner containing the subwoofer), at a distance of less than 1 cm from the walls and the floor. The subwoofer was placed with the diaphragm facing up, at a distance of less than 1 cm from the side walls (Figure 4.7-f). The reason for placing the microphones and subwoofer in the room corners is to be able to excite and detect all the room modes, with the highest possible amplitude. In order to prevent the transmission of vibration directly into the floor of the chamber, the subwoofer was mounted on top of resilient material.

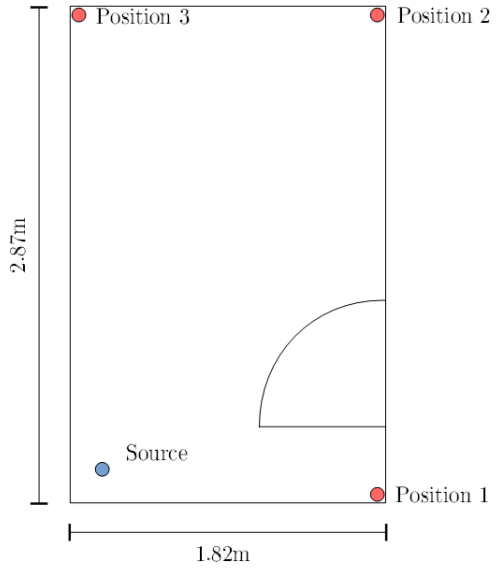

Figure 4.6: Positioning of the source and receivers inside the reverberation chamber.

4.5 Impulse response measurement of the room with porous material

The objective of the set of experiments described in this section is to measure the sound field in the small reverberation chamber when porous material is present. The porous material consisted of rock wool slabs 100 mm thick with dimensions 1.2 m x 0.6 m, and density of 100 kg/m^3. Measured values of airflow resistivity for the rock wool slabs were 48,820 Pa.s/m^2 in the thickness direction and 23,560 Pa.s/m^2 in the lateral direction [65]. The 13 m^3 reverberation chamber was used for the experimental validation. Measurements are carried out in three different room configurations: empty room, the room partially divided by a porous panel and the room completely divided by a porous panel. The source and receiver positions remain the same for all the different conditions. B&K Type 4135 free-field 1/4" microphones are used to measure the sound pressure level on a horizontal grid (6 x 8) and a vertical grid (6 x 7), as shown in Figure 4.8. The distance between receivers is 350 mm along the $x-$axis and 400 mm along the $y-$axis. The location index in the $y-$ and $z-$directions is referred to by row number and the location in the $x-$direction referred to by position number as shown in Figure 4.9. The loudspeaker is positioned facing upwards in one corner of the room, with the centre

of the cone at a height of 270 mm, a distance from the side walls of 210 mm in the $x-$direction and 180 mm in the $y-$direction. On Figures 4.8 and 4.9, the position of the centre of the cone is indicated by a red shaded circle.

4.5.1 List of equipment

The following equipment was used to carry out the acoustic impulse response measurements:

- Accelerometer B&K type 4393;
- Accelerometer conditioning amplifier B&K type 2692-OS4;
- Accelerometer conditioning Amplifier (custom made unit);
- Acoustic calibrator B&K type 4230;
- Dual channel real-time frequency analyser B&K type 2144;
- FFT analyser Onno Sokki Multi channel Data Station DS-9110;
- Loudspeaker Celestion Csixs (electronics removed);
- Microphone B&K type 4135;
- Microphone conditioning amplifier B&K type 2690
- Microphone power supply B&K type 2801;
- Microphone pre-amplifier B&K type 2670;
- Multimeter Precision Gold WG022;
- Power Amplifier B&K type 2706;
- TEAC CD Player CD-P1160D;
- Thermometer Meterman TRH22;

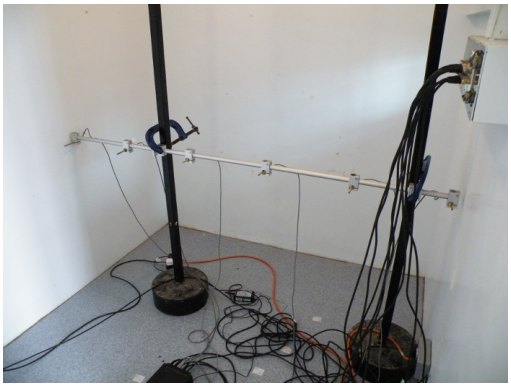

(a)

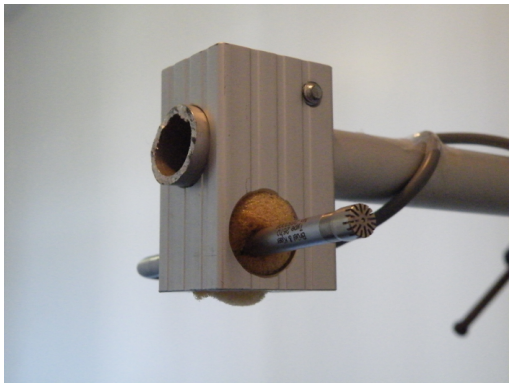

(b)

(c)

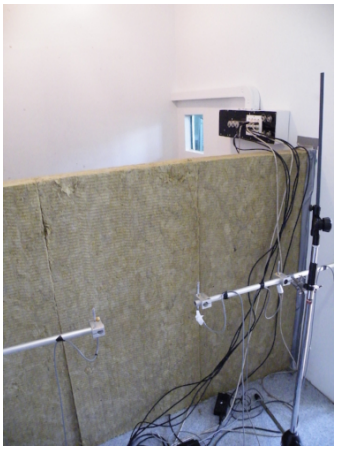

(d)

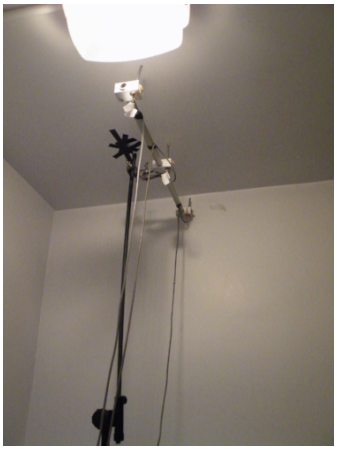

(e)

(f)

(g)

Figure 4.7: a) Microphone measurement array b) 1/4" microphones used for the experiments c) Porous panel deployed has full partition d) Porous panel deployed as partial partition e) Vertical microphone array. Celestion subwoofer used for the measurements: f) side view and g) view of the loudspeaker cone.

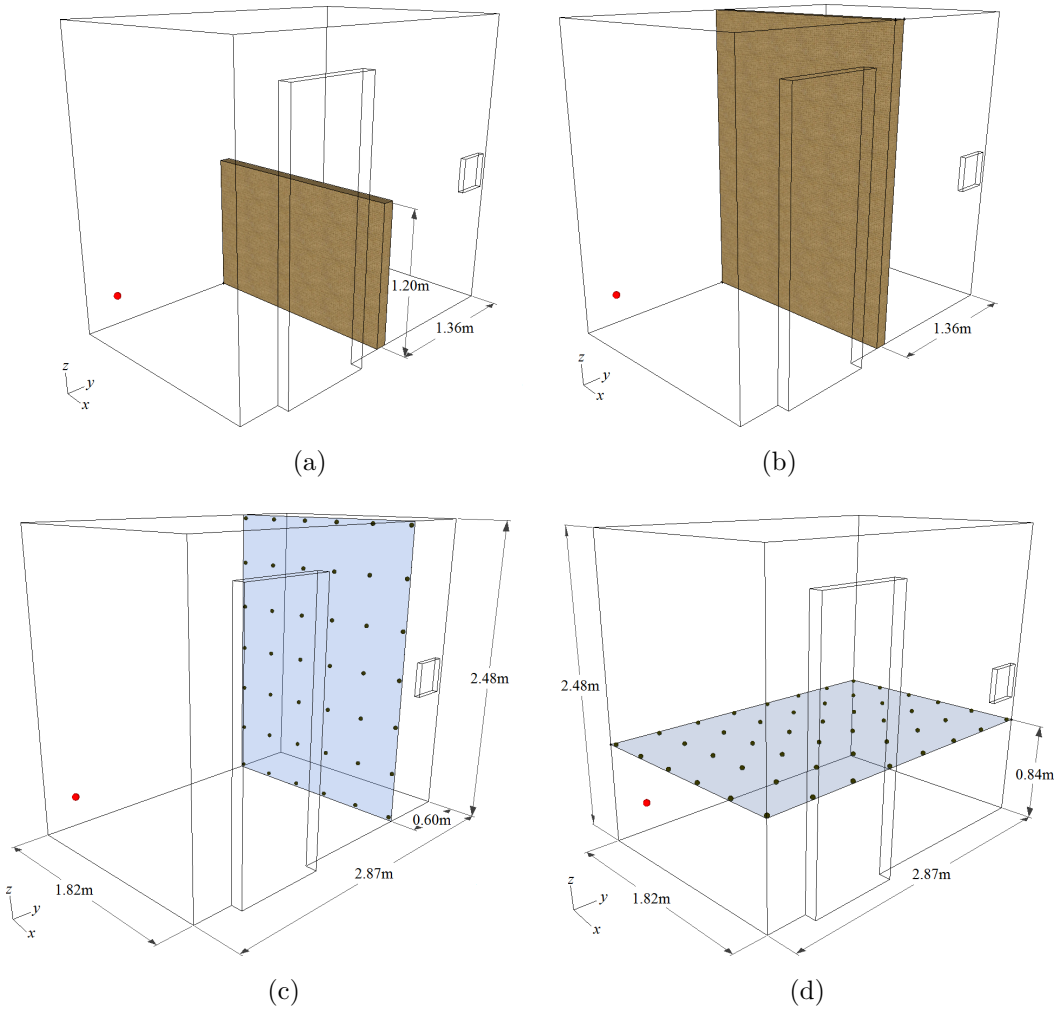

Figure 4.8: Reverberation room: (a) Horizontal measurement grid, (b) Vertical measurement grid, (c) Porous panel forming complete divider, (d) Porous panel forming partial divider. The centre of the loudspeaker cone is indicated by the red dot.

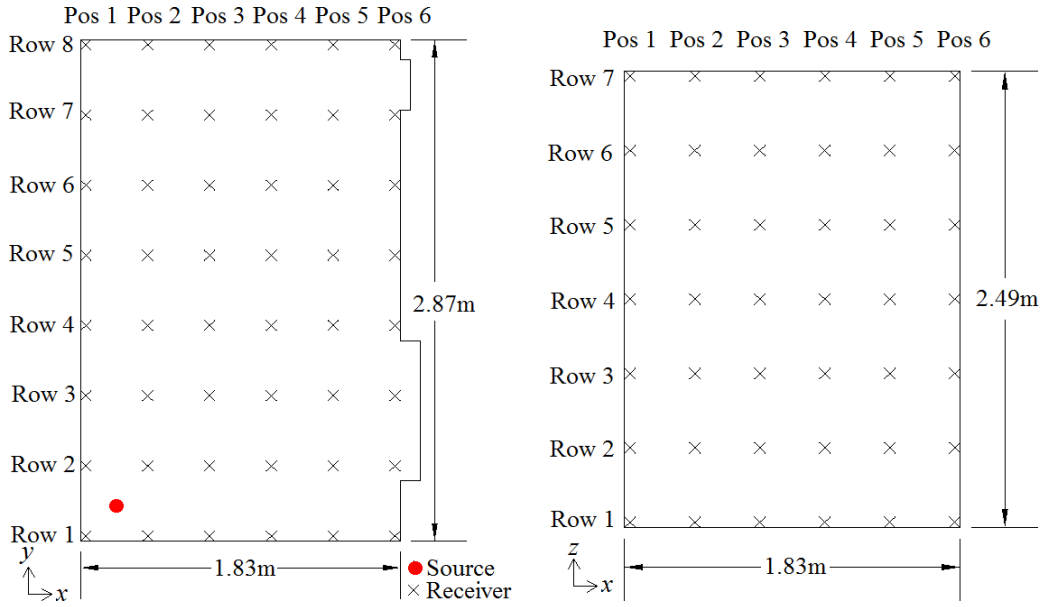

Figure 4.9: Source and receiver positions with row and position numbers for the horizontal grid (left) and vertical grid (right).

4.5.2 Positioning of the porous material

The rock wool slabs were positioned so that they would form a barrier dividing the room into two cavities whose air volumes are connected (Figure 4.7-d). The location of the barrier within the room is indicated in Figure 4.8. The height of the barrier corresponded to the height of an individual slab, which is 1.2 m. The cavity that contained the source is referred to in this thesis as the source cavity. The other cavity will be referred as the enclosed cavity. To allow access to the enclosed cavity volume one of the slabs had to be removed and replaced for both horizontal and vertical grid measurements.

4.5.3 Sound source

The source used for the measurements was a closed cabinet subwoofer (Celestion C6S 10" driver) with the electronics removed so that the unit is passive. Preliminary measurements confirmed that the loudspeaker could be modelled as a linear system with pistonic behaviour over the frequency range of interest which is below 140 Hz.

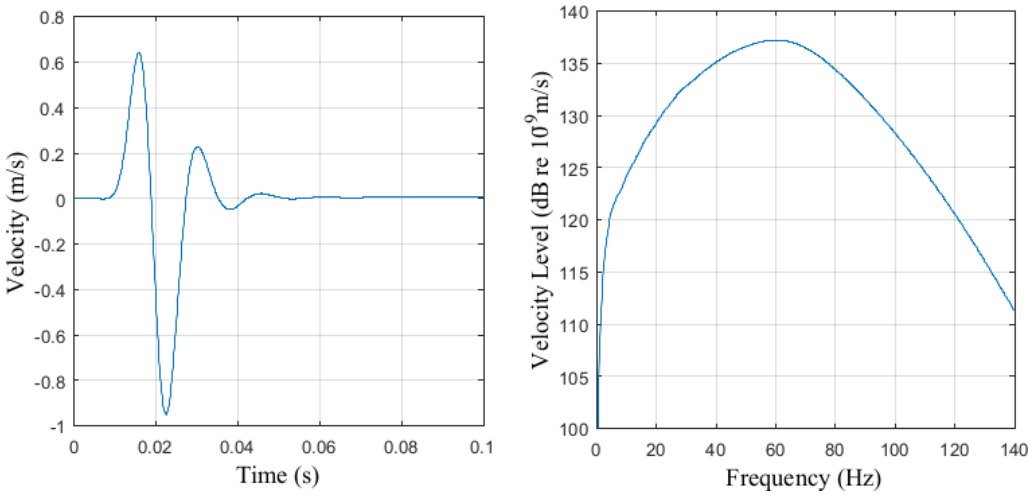

Figure 4.10: Measured velocity on the loudspeaker cone. Time history (left) and magnitude spectrum (right).

The input signal used for the measurements is a Gaussian pulse characterised by σ=2.7 ms and produced by the CD player at a sampling rate of 44.1 kHz and 16 bit encoding depth. A train of 10 pulses was used in order to obtain a smoother power spectrum, by averaging the measured responses. As the Gaussian pulse is modified by the loudspeaker, signal processing and amplification chain, the driving function used in the FDTD models is given by the measured velocity at the centre of the loudspeaker cone in the anechoic chamber and is shown in Figure 4.10. The subwoofer had a 1 cm aluminium cube attached to the centre of its cone. A B&K Type 4393 accelerometer with a weight of 2.4 g was glued (with Cyanoacrylate) to the top of the aluminium cube. This accelerometer was chosen for the measurement as its mass loading is negligible over the frequency range of interest. The approximate diameter of its cone is 11 cm and its height is approximately 35 cm. The speaker was supported on three small pieces of thick foam.

4.5.4 Microphone and source positions

The source and microphone receiver positions were kept constant for all the different configurations (empty room, room partially divided by a porous panel and fully divided by a porous panel) and are indicated in Figures 4.8 and 4.9. To carry out

Level	5%
Position	-200
Hysteresis	0
Slope	+

Table 4.1: Trigger settings used for the FFT analyser

the vertical grid measurements, two tripods were used to hold the microphones at the correct position (Figure 4.7-e). This arrangement was especially important in order to provide stability for the measurements positions that were close to the ceiling.

4.5.5 Monitoring of diaphragm acceleration

In order to ensure repeatibility the motion of the speaker cone throughout the measurements, its acceleration level was measured and recorded for each measurement row of both the horizontal and the vertical grid. The measured accelerations indicated no significantly different acceleration levels between the measurements, e.g. all the variations were within 1 dB for the 0 - 140 Hz frequency range.

4.5.6 FFT analyser

The frequency range was set to 200 Hz throughout all the measurements. The time window was set to 'rectangular'. The time averaging was set to 10 samples for the pulse. The trigger detection settings used are indicated in Table 4.1

4.5.7 Power amplifier

The open circuit output voltage level of the B&K power amplifier was measured using a 120 Hz sine signal played-back using the CD player. To measure the output voltage before each measurement session, the power amp was left on for at least 10 minutes to warm up. The power amplifier output voltage was measured before and after each measurement session in order to ensure the operation conditions remained constant.

4.5.8 Background noise level

Measurements of background noise level were necessary in order to confirm that the signal from the Gaussian driving function was at least 10 dB above the background noise. The background noise levels were measured using a Hanning time window with time averaging of 60 s. The bandwidth of the FFT analyser was 200 Hz. The background noise levels were measured at the beginning of every session with the power amplifier switched on and using the measurement settings previously described.

4.5.9 Valid frequency range

Since the signal output by the CD player rolls-off for frequencies below 20 Hz and the analysis carried out measuring velocity levels at several positions of the subwoofer cone (section 4.3.3) limited the valid higher frequency range to 140 Hz, the valid frequency range of the grid measurements is 20-140 Hz.

4.6 Measurement of the driving-point mobility on the plate

The set of driving-point mobility measurements was carried out in the small reverberation chamber as detailed in section 4.2. A 5 mm thick aluminium plate (1.2 m $\times$ 0.8 m) was supported on a steel metal frame which rested on a metal frame removed from a university desk. To avoid propagation of vibrations between the steel frame and the desk frame, a resilient rubber material was used to support the steel frame, as can be seen in Figure 4.14-b. The following physical properties for aluminium were taken from the literature [57]: ρ=2700 kg/m^3, $c_{\mathrm{L}} = 5100$ m/s and $\nu = 0.34$.

4.6.1 Equipment

The following equipment was used to carry out the measurement of the driving-point mobility:

- Accelerometer B&K type 4393;
- Accelerometer conditioning amplifier B&K type 2692-OS4;
- Acoustic calibrator B&K type 4230;
- Block calibration mass (3.85 Kg);
- Calibration force driver B&K type 4810;
- Dynamic shaker 400 Series Ling;
- FFT analyser Onno Sokki Multi channel Data Station DS-9110;
- Force transducer B&K type 8200;
- Microphone pre-amp type 2670;
- Microphone conditioning amplifier B&K type 2690

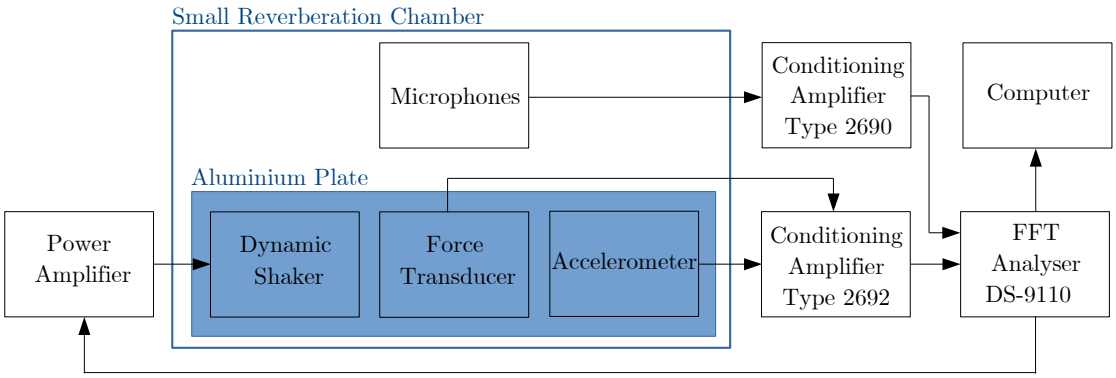

Figure 4.11: Setup used for the vibroacoustic measurements

- Microphone B&K type 4135;
- Multimeter Tenma 72-2050;
- Piston calibrator B&K type 4294;
- Power Amplifier B&K type 2706;
- Thermometer Meterman TRH22;

This equipment was connected as shown in Figure 4.11.

(a)

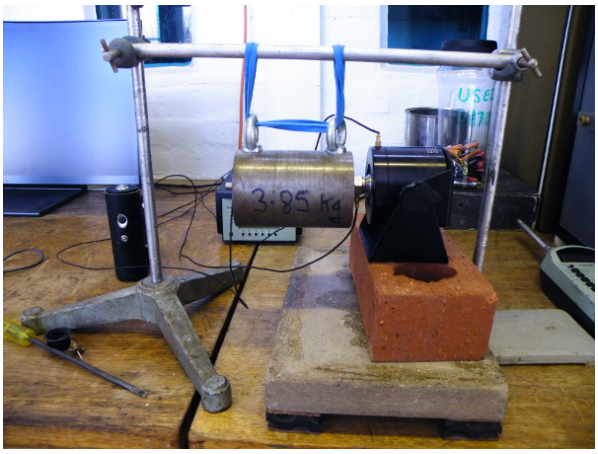

(b)

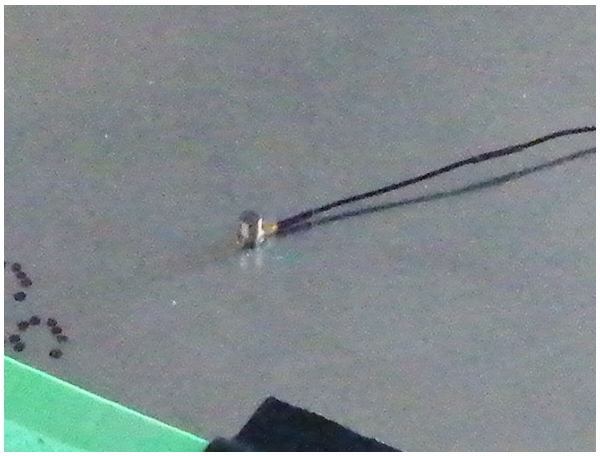

(c)

(d)

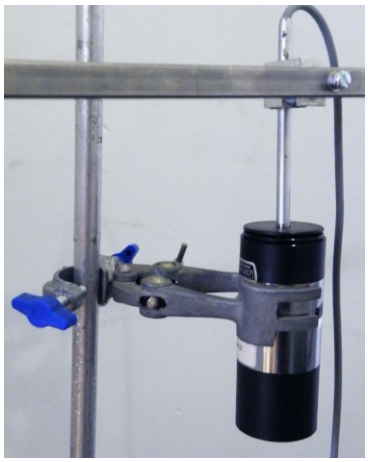

(e)

Figure 4.12: a) Small reverberation chamber b) Setup used to calibrate the force transducer c) Accelerometer mounted on aluminium plate d) Force transducer (top), dynamic shaker (bottom) e) Acoustic calibration microphone.

4.7 Impulse response measurement for the room excited by the plate

4.7.1 Measurement setup

A 5 mm thick aluminium plate (1.2 m × 0.8 m) was placed inside a 13 m^3 reverberation chamber (1.83 m × 2.87 m × 2.48 m) - see Figure 4.13-a. This configuration was chosen to validate the vibroacoustic FDTD model in the low-frequency range where the first two bending modes of the plate occurred below the fundamental acoustic mode of the cavity.

The plate is positioned at a height of 0.78 m above the floor using a metal frame as shown in Figure 4.14. The minimum distance between the short edge of the plate and the nearest wall is 0.53 m and between the long edge and the nearest wall is 0.33 m. A simply-supported boundary condition is applied around its edges by using a heavy steel frame with pins at 20 mm centres as described by Yin and Hopkins [90]. To provide damping similar to the Rayleigh curve, a viscoelastic damping material (Sylomer) is fixed onto the surface of the plate. Different configurations of damping material are applied over the surface with loss factors measured using the 3 dB down-points in the magnitude of the driving-point mobility. The diamond-shaped configuration shown in Figure 4.14 was chosen because the overall damping

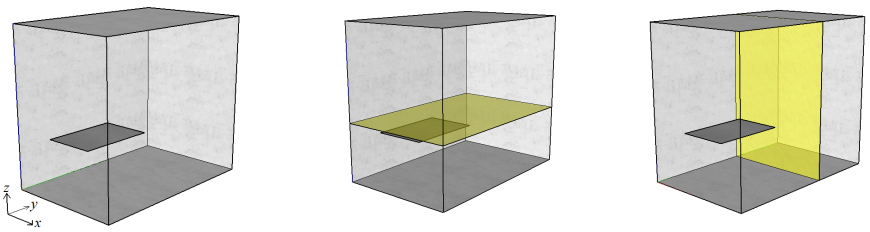

(a) (b) (c)

Figure 4.13: Reverberation room indicating (a) the plate (grey surface), (b) the horizontal measurement grid (yellow surface) and (c) the vertical measurement grid (yellow surface).

approximately follows a Rayleigh damping curve below 200 Hz.

Sound pressure measurements inside the chamber are taken using two grids, one horizontal grid (15 × 11 positions) and one vertical grid (13 × 11). Figure 4.13-a defines the x-, y- and z-directions for these grids. The horizontal grid is 0.84 m above the floor and 0.06 m above the plate (Figure 4.13-b). The vertical grid is 0.82 m from the back wall and 0.32 m from the edge of the plate (Figure 4.13-c). The distance between consecutive positions is 0.2 m in the x-direction for the horizontal grid, 0.18 m in the y-direction for both horizontal and vertical grids, and 0.2 m in the z-direction for the vertical grid. An array of six 1/4" microphones (B&K Type 4135 with B&K Type 2670 pre-amplifiers) is used to measure the sound pressure at the grid points. The worst case for the uncertainty in the microphone positioning at grid positions is estimated to be ±1.5 cm in the plane of the horizontal or vertical grid.

A force transducer (B&K Type 8200) and accelerometer (B&K Type 4393) are connected at the excitation point to allow continuous monitoring of the input force. This also allows measurement of the driving-point mobility in order to estimate the modal loss factors.

Since FDTD is a time domain method, several attempts were made in order to carry out the measurements using transient signals as source functions. However, there were experimental difficulties associated with these approaches, mostly manifesting as a rattle sound that would be radiated by the aluminium plate and also as a strong shifting of the fundamental resonance frequency of the plate, nearly every time the impulse source function was played. Hence, a steady state source signal had to be used and the comparison with the FDTD results will be carried out in the frequency domain.

The sound pressure and force signals are used to calculate a complex transfer function of pressure-to-force at all grid positions. These calculations were automatically handled within the Ono Sokki frequency analyser. The frequency resolution of the measurement analysis was set to 0.25 Hz and the maximum frequency of analysis was 200 Hz. Additionally, it also output the coherence function corresponding to

the measured transfer functions.

The measurement chain used for this experiment is shown in Figure 4.11, where it is indicated whether the equipment was placed inside the measurement chamber or fixed onto the aluminium plate. The position of the aluminium plate inside the room and the corresponding microphone measurement positions are indicated in Figure 4.15.

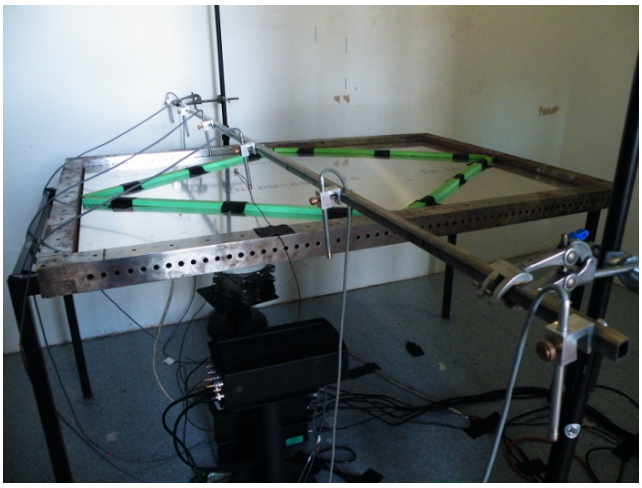

(a)

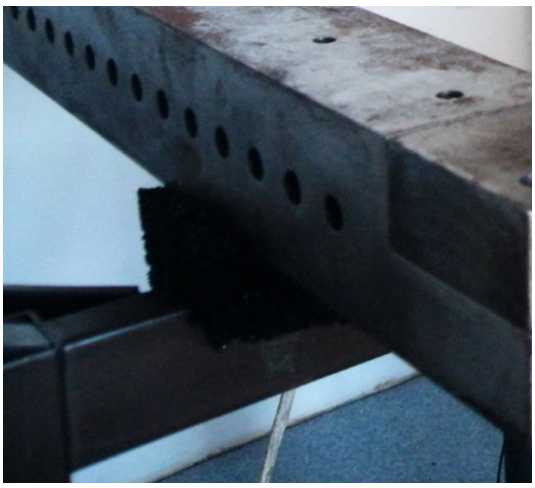

(b)

(c)

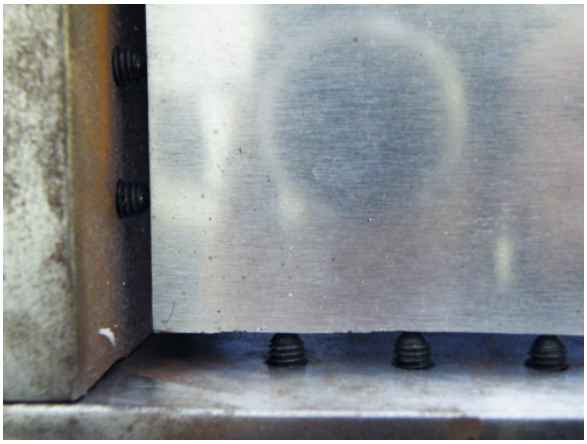

(d)

Figure 4.14: a) Aluminium plate with green viscoelastic material (NB Microphone array is also visible) b) Support conditions of the metal frame. c) Rubber isolator d) Detail of the support conditions at the edge of the aluminium plate.

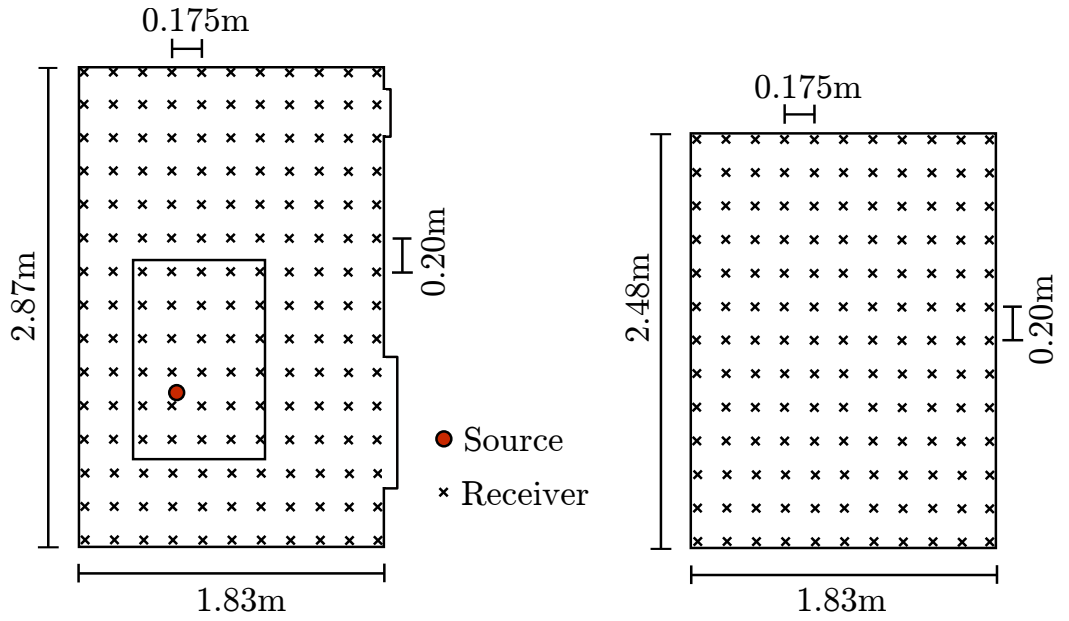

Figure 4.15: Source and receiver positions for the horizontal grid (left) and vertical grid (right).

4.7.2 Vibration source function

The type of excitation signal used for the experiments was a steady-state broadband signal. The Ono Sokki FFT analyser generates this signal using high-pass filtered pseudo-random sequences, with 1.2 V of amplitude and an offset of 0 V. During each measurement, the FFT analyser carried out a power sum average over a time period of 60 s using a Hanning time window. The maximum voltage of the FFT analyser channels was set to 3.16 V_{RMS} for the microphones and the accelerometer channel and 10 V_{RMS} for the force transducer channel.

4.7.3 Data processing

As described in section 4.7.1, the linear complex transfer function P/F was output by the frequency analyser. The magnitude of the transfer function was then calculated using:

$$|P(\omega)/F(\omega)| = \sqrt{\mathrm{Re}\left\{P(\omega)/F(\omega)\right\}^2 + \mathrm{Im}\left\{P(\omega)/F(\omega)\right\}^2} \tag{4.1}$$

The magnitude transfer functions were in 0.25 Hz lines linearly averaged into 1 Hz lines. Finally, the transfer function level was calculated from the 1 Hz resolution lines using:

$$20\log_{10}(|P(\omega)/F(\omega)|) \tag{4.2}$$

4.8 Summary

The details of the experimental work have been described in this chapter, including measurement equipment and measurement chain diagrams.

Descriptions were given of the measurements taken in the anechoic chamber in order to characterise the loudspeaker behaviour. In terms of its acoustic radiation, the results show that the subwoofer performed as a monopole radiation source. In terms of vibration of the subwoofer cone, the measurements confirmed its pistonic behaviour.

The experimental validation took place in a small reverberation chamber. The sound field in the room was measured with three different configurations: empty room, partially divided by porous absorber and completely divided by a porous panel. Details were also given on the vibroacoustic experiments with a point-excited plate in the reverberation chamber were carried out. Tests were carried out to confirm that the support conditions of the plate would provide repeatable conditions over time.

5 Validation of the acoustic FDTD model for an acoustic cavity containing porous panels

5.1 Introduction

This chapter concerns the experimental validation of the acoustic FDTD predictions and includes the implementation details of the FDTD model and a comparison between the results obtained in the simulations and those obtained in the corresponding measurements that were described in chapter 4.

Section 5.2 describes the implementation of the FDTD acoustic model for the small reverberation chamber described in chapter 4. The implementation of the subwoofer source and the porous panel is also disscussed in this section.

Section 5.3 presents the results obtained in the measurements of the room damping constants, which were described in section 4.4.

Section 5.4 presents a comparison between measured results and corresponding FDTD predictions obtained for a number of receiver positions in the small reverberation room under three different configurations: empty room, partially divided by a porous panel and completely divided by a porous panel. In addition, a comparison between FDTD simulations carried out with/without using the Moving Frame Model (MFM) is shown.

Section 5.5 presents the comparison between acoustic grid measurements carried out in the small reverberation chamber and the corresponding FDTD results for the same three different configurations that were described in section 5.4.

5.2 Implementation of the FDTD acoustics model

In order to validate the modelling techniques for porous materials described in chapter 2, an FDTD model of a small reverberation room has been created that incorporates a porous panel. The results obtained for this FDTD model are compared to those obtained in the corresponding measurements described in this chapter.

5.2.1 Numerical resolution

The spatial resolution of the FDTD model must be sufficiently fine to model the geometry of the room and the porous panel at the frequency range of interest. In the FDTD model considered in this thesis, the grid spacing was set to Δx=0.0589 m, Δy=0.0574 m, Δz=0.0578 m. Assuming a speed of sound of 343 m/s, this corresponds to $\Delta t = 9.77 \times 10^{-5} s$, i.e. a sampling frequency of 10240 Hz.

5.2.2 Frequency range

For the acoustic FDTD simulations, the frequency range of interest is limited by experimental constraints, particularly those related to the subwoofer behaviour used for the measurements. As detailed in section 4.3.3, the subwoofer no longer shows pistonic behaviour at frequencies above 140 Hz, which effectively sets an upper limit for the frequency range of interest of the FDTD simulations.

5.2.3 Boundary conditions

In the FDTD model, the reverberation room is embedded in an acoustic medium that emulates a free field through the implementation of PML boundaries such that any acoustic waves escaping the room walls towards its exterior are not reflected

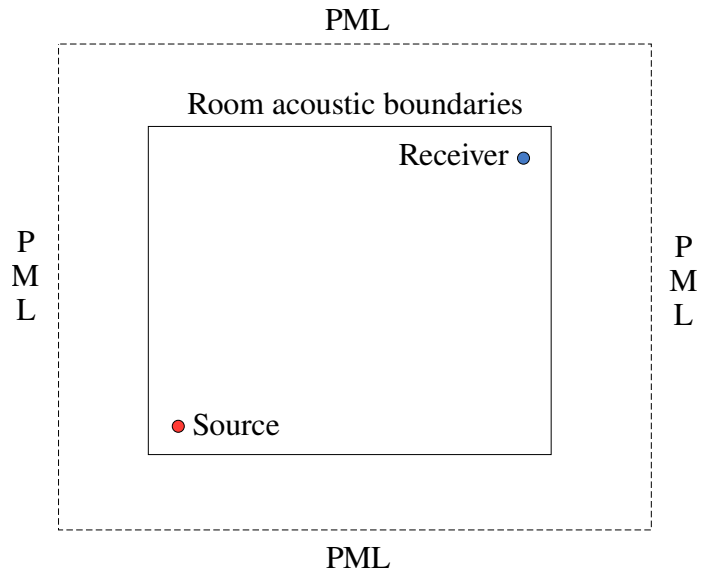

Figure 5.1: Example of PML boundaries implemented outside the room domain.

back at the edges of the numerical domain - see Figure 5.1.

All six boundaries of the room were assumed identical. The measurement of the damping constants of the room boundaries is described in section 4.4. The room boundary conditions were frequency-independent and were implemented using equations 2.57 - 2.59. The value considered for the specific acoustic impedance was 224.9, which corresponds to the average of the measured values of specific acoustic impedances obtained for the first 11 room modes (below 150 Hz), indicated in Tables 5.1 - 5.3.

5.2.4 Source

The sound source is a subwoofer loudspeaker which is implemented in FDTD as a hard velocity source. The loudspeaker cone points upwards into the room (z-direction) and was experimentally characterised to be acting as a piston in the frequency range of interest (below 140 Hz). For this reason a uniform driving function is applied over the surface area of the cone on the FDTD grid. Section 2.8 provides details on the implementation of FDTD velocity hard sources.

The driving function used in the FDTD models was obtained by measuring the veloc-

ity on the centre of the loudspeaker cone in an anechoic chamber. This measurement was carried out using a laser vibrometer (Figure 4.3), and the resulting time history is shown in Figure 4.10. The electrical signal used to drive the loudspeaker was a Gaussian pulse, as described in section 2.8.

5.2.5 Properties of the porous material

The porous material was rock wool, whose physical properties are described in section 4.5. According to equation 2.68, these values of airflow resistivity result in a maximum frequency limit of 25,913 Hz along the thickness direction and 12,505 Hz along the lateral directions of the porous panel. Both of these values are much higher than the 140 Hz frequency limit dictated by the experiments (section 5.2.2). These values of airflow resistivity were incorporated in equation 2.79 for each of the corresponding directions. As mentioned in section 2.11.2, the value of density used to model the porous material was that of air.

5.2.6 Numerical receiver positions

The sound field was sampled using two different grids, one horizontal ($xy-$plane) and the other vertical ($xz-$plane) as described in section 4.5.4 and shown in Figures 4.8 and 4.9. The horizontal grid consisted of 6×8 measurement positions, spaced by 350mm along the $x-$axis and 400mm along the $y-$axis. The vertical grid consisted of 6×7 positions, spaced by 350mm along the $x-$axis and 400mm along the $z-$axis.

p	q	r	**Frequency (Hz)**	$\boldsymbol{\delta}(\mathrm{s}^{-1})$	$\boldsymbol{Z}_{\mathrm{a,S}}(—)$
0	1	0	59.8	3.35	168.9
0	0	1	69.2	2.59	225.5
0	1	1	91.4	2.90	243.1
1	0	0	94.2	2.90	219.1
1	1	0	111.6	3.34	225.6
1	0	1	116.9	3.40	227.5
0	2	0	119.5	3.55	159.4
1	1	1	131.3	3.12	286.0
0	2	1	138.1	3.12	225.6
0	0	2	138.3	2.57	227.9
0	1	2	150.7	2.97	236.9

Table 5.1: Measured specific acoustic impedances for each normal mode - corner position 1

5.3 Results - Acoustic boundary damping constants

For the three corner microphone positions indicated in Figure 4.6, the specific acoustic impedances obtained from the measurements for each room mode are indicated in Tables 5.1 - 5.3. This indicates that although there is variation, it is reasonable to use an average value in the FDTD model. The value considered for the frequency-independent specific acoustic impedance was obtained from the average of the specific acoustic impedances obtained from the first 11 room modes for all three measurement positions, which is 224.9. This value was subsequently multiplied by the value of characteristic impedance of air to yield the average specific acoustic impedance of the room surfaces needed as input data in equations 2.57 - 2.59.

p	q	r	**Frequency (Hz)**	$\boldsymbol{\delta}(\mathrm{s}^{-1})$	$\boldsymbol{Z}_{\mathrm{a,S}}(—)$
0	1	0	59.2	3.34	169.3
0	0	1	68.5	2.59	225.8
0	1	1	90.6	2.90	242.8
1	0	0	93.4	2.90	218.8
1	1	0	110.6	3.38	223.2
1	0	1	115.9	3.41	226.9
0	2	0	118.5	3.55	159.4
1	1	1	130.1	3.13	285.2
0	2	1	136.9	2.58	273.2
0	0	2	137.1	2.58	226.9
0	1	2	149.3	2.98	236.4

Table 5.2: Measured specific acoustic impedances for each normal mode - corner position 2.

p	q	r	**Frequency (Hz)**	$\boldsymbol{\delta}(\mathrm{s}^{-1})$	$\boldsymbol{Z}_{\mathrm{a,S}}(—)$
0	1	0	59.2	3.37	167.7
0	0	1	68.5	2.58	226.2
0	1	1	90.6	2.89	243.5
1	0	0	93.4	2.89	219.5
1	1	0	110.6	3.35	225.0
1	0	1	115.9	3.41	226.5
0	2	0	118.5	3.51	161.1
1	1	1	130.1	3.16	282.4
0	2	1	136.9	2.56	274.6
0	0	2	137.1	2.56	228.0
0	1	2	149.3	3.01	233.8

Table 5.3: Measured specific acoustic impedances for each normal mode - corner position 3.

5.4 Results - Point responses

This section shows the comparison between acoustic measurements and corresponding FDTD predictions for a number of receiver positions in the small reverberation chamber under three different conditions: empty room, room partially divided by a porous panel and room completely divided by a porous panel.

The inclusion of the MFM (described in section 2.11.2) in FDTD with the porous panel has been assessed through comparison of FDTD results with measurements. Figures 5.2 - 5.5 show three different microphone positions taken from the measurement grids for the room when partially and completely divided by the porous panel respectively. The results show a resonance peak that occurs below the fundamental frequency of the room, the frequency at which this resonance occurs depends upon the configuration of the porous panel in the room.

For the configuration of the room that was completely divided by the porous panel, the frequency at which this resonance occurs can be estimated by considering the room as a spring-mass-spring system, as described in section 2.11.2. For the reverberation room with the panel as the system in Figure 2.11, the spring-mass-spring resonance frequency, f_o, is given by equation 2.72. The stiffness corresponding to each volume of air on either side of the porous panel is given by equation 2.11.2. The mass of the porous panel was calculated using its bulk density (100 kg/m^3) and its value is 0.1 m x 2.48 m x 1.82 m x 100 kg/m^3 = 45.13 kg. To this mass it is necessary to add the mass of the wooden plank support which is about 1.140 kg. The stiffnesses of air volumes 1 and 2 are given by:

$$k_1 = 1.2 \text{ kg/m}^3 \times (343 \text{ m/s})^2 \times (2.48 \text{ m} \times 1.82 \text{ m})^2 / (2.48 \text{ m} \times 1.82 \text{ m} \times 1.46 \text{ m})$$

$$k_1 = 4.365 \times 10^5 \text{N/m}$$

$$k_2 = 1.2 \text{ kg/m}^3 \times (343 \text{ m/s})^2 \times (2.48 \text{ m} \times 1.82 \text{ m})^2 / (2.48 \text{ m} \times 1.82 \text{ m} \times 1.46 \text{ m})$$

$$k_2 = 4.864 \times 10^5 \text{N/m}$$

From equation 2.72 the spring-mass-spring resonance frequency is 22.5 Hz.

For the room that is partially divided by the porous panel, inclusion of the MFM is necessary to correctly predict the lowest frequency peak in the spectrum, although it has negligible effect at higher frequencies. When the panel completely divides the room volume the results show that the MFM is essential to correctly predict sound pressure levels near the spring-mass-spring resonance otherwise errors up to 20 dB can be incurred. As previously mentioned, the spring-mass-spring resonance occurs below the first room mode and is calculated to be 22.5 Hz, although the shallow peak in the measurements is only evident at 27 Hz. There is an indication that the MFM can improve the FDTD predictions outside the damping controlled region (i.e., 3 dB bandwidth) of the room modes as can be seen between 70 Hz and 90 Hz on Figures 5.4 - 5.5.

Having demonstrated the validity of FDTD with MFM for the room with the porous panel, an additional comparison between FDTD and measurement results is shown in terms of magnitude, phase (wrapped) and impulse responses in Figures 5.6 - 5.10 at two different grid positions. The peak in the magnitude at 60 Hz shown in Figure 5.6 (empty room) corresponds to the lowest frequency room mode which is f_{010}, where the subscript indicates p, q, and r corresponding to the $x-$, $y-$ and $z-$ directions respectively. Close agreement between FDTD and measurements indicates that the impulse from the loudspeaker has been correctly incorporated as a hard velocity source in FDTD. It also indicates that it is reasonable to use a frequency-independent impedance for all the walls and floors. However, whilst FDTD predicts all the trends of the phase excursions there are occasional discrepancies which become most apparent when the phase wraps at 180°.

The cross-correlation coefficients obtained between the measured and the FDTD impulse responses are indicated by "Corr." in Figures 5.6 - 5.10. These are in the range 0.77 - 0.91. Although there are no similar cross-correlation coefficients quoted in the literature for a small room whose sound field is primarily dictated by its modal response, there are values from Sakamoto et al.[4] for a large concert hall with numerous diffusing elements. Those cross-correlation coefficients for measurements and FDTD were in the range 0.79 - 0.87; these values are similarly high to those obtained in this work. The close agreement of FDTD with measurements indicates

that there is potential to use the predicted impulse response for the purpose of auralisation.

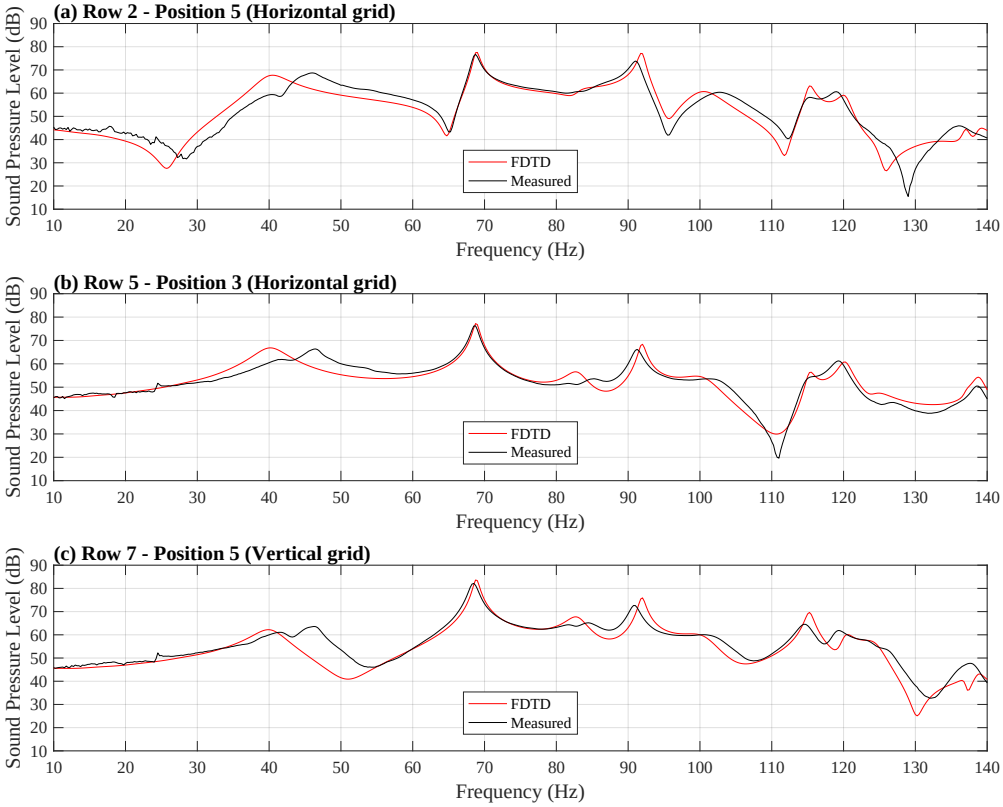

Figure 5.2: Room partially divided by porous panel: without MFM.

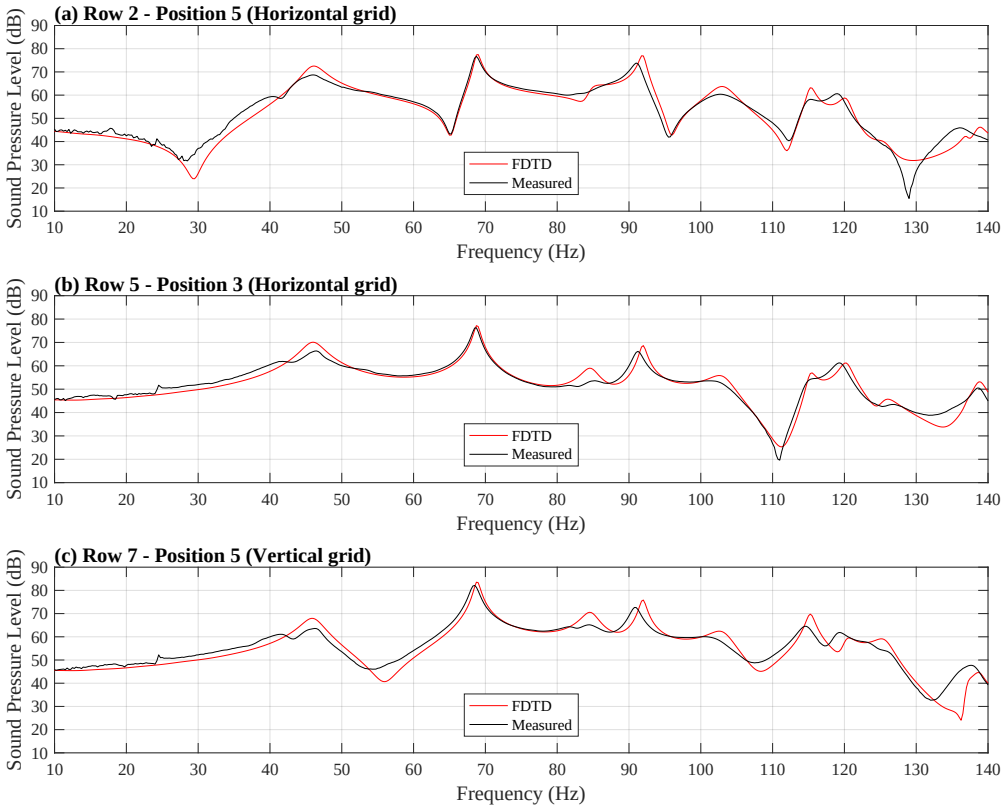

Figure 5.3: Room partially divided by porous absorber: with MFM.

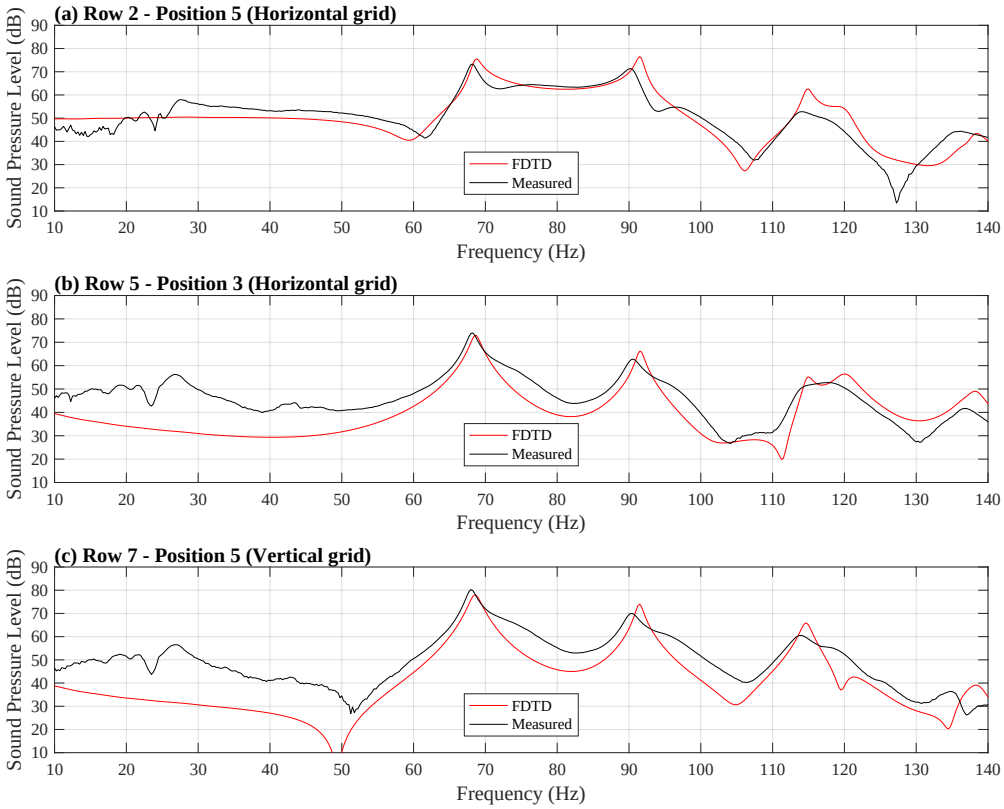

Figure 5.4: Room completely divided by porous panel: without MFM.

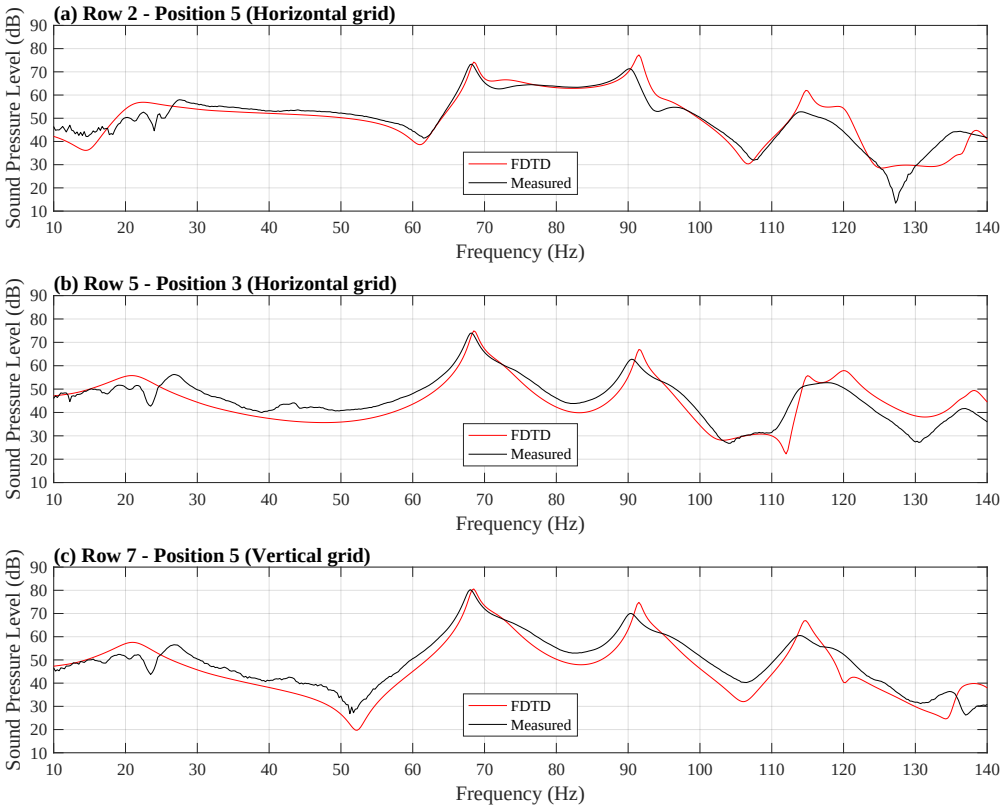

Figure 5.5: Room completely divided by porous absorber: with MFM.

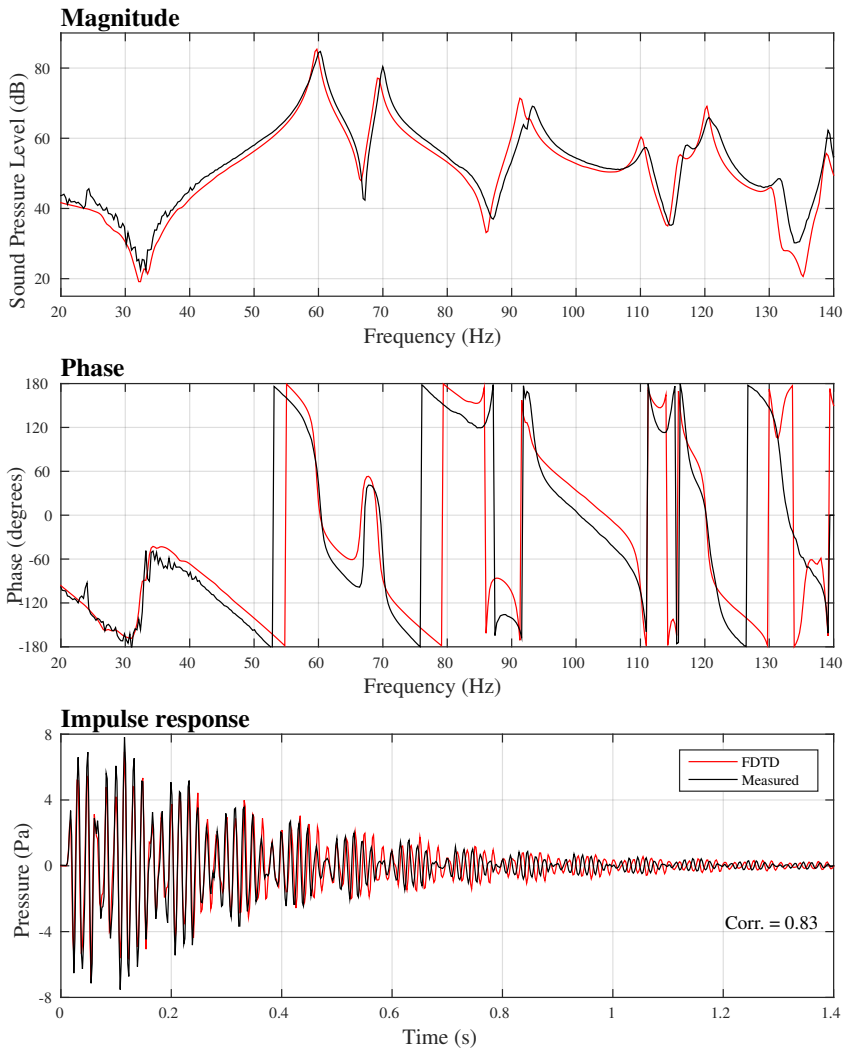

Figure 5.6: Empty room: FDTD and measured responses on the horizontal grid, Row 1 Position 4.

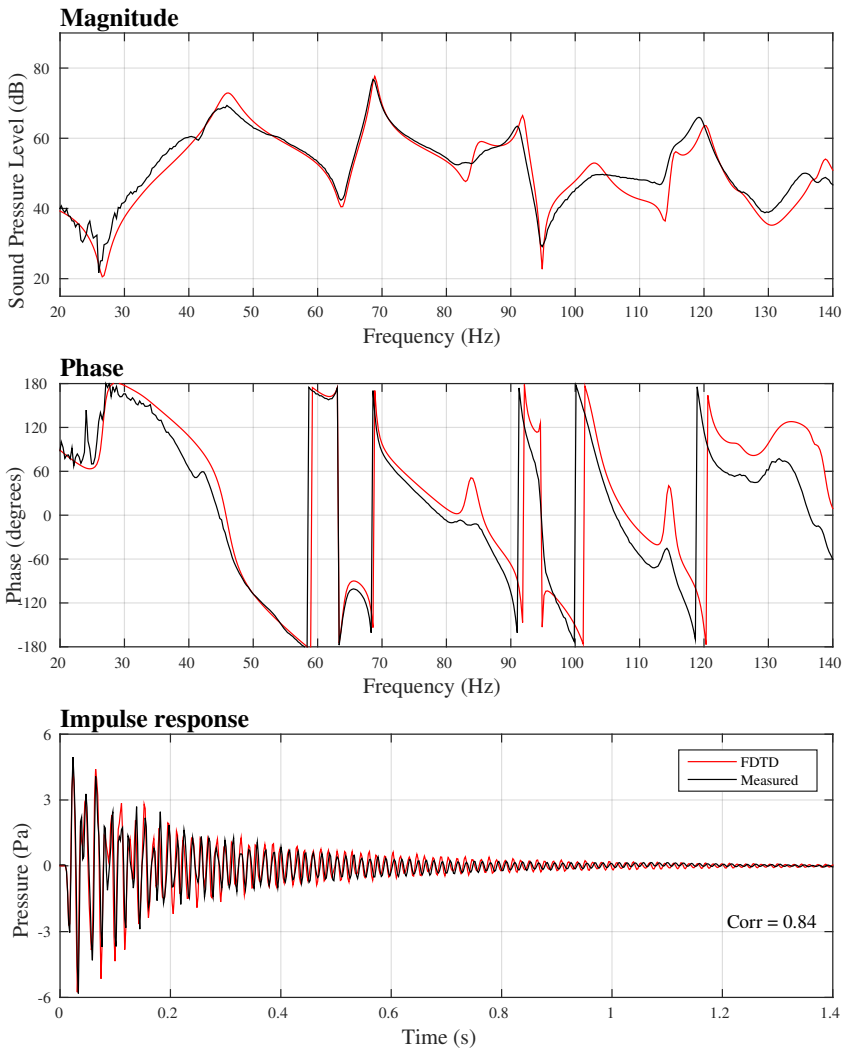

Figure 5.7: Room partially divided by a porous panel: FDTD and measured responses on the horizontal grid, Row 1 Position 4.

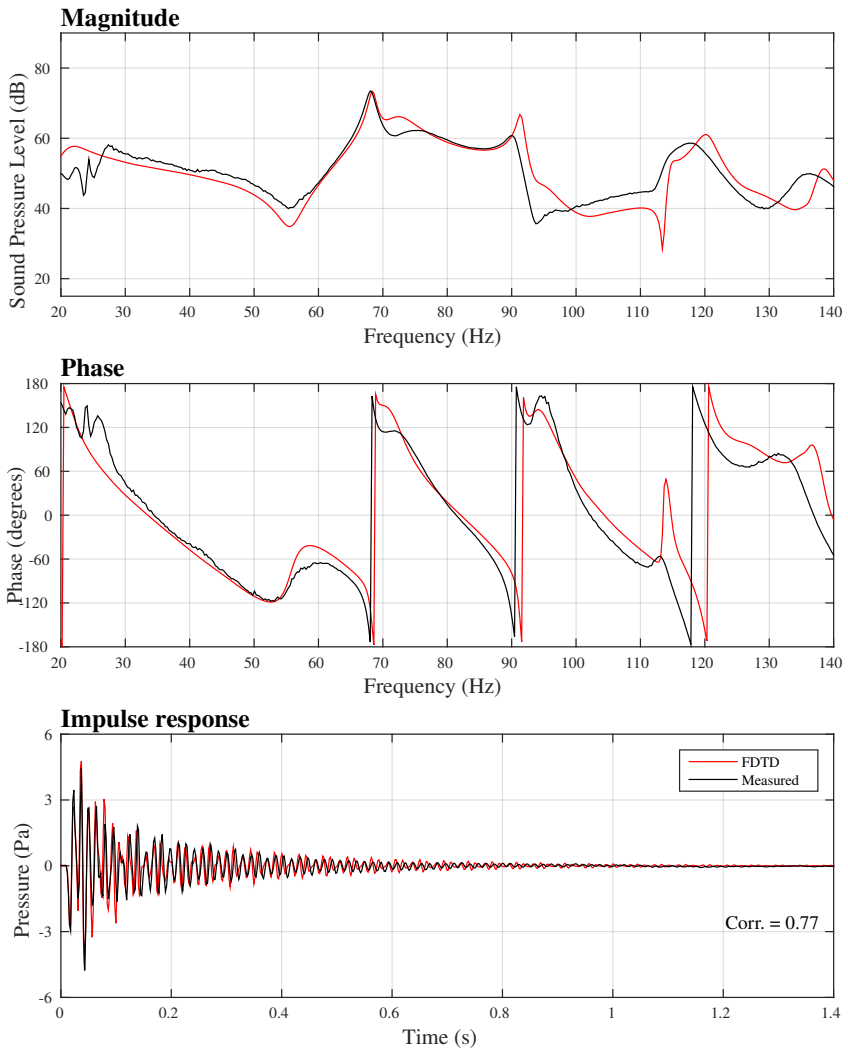

Figure 5.8: Room completely divided by a porous absorber: FDTD and measured responses on the horizontal grid, Row 1 Position 4.

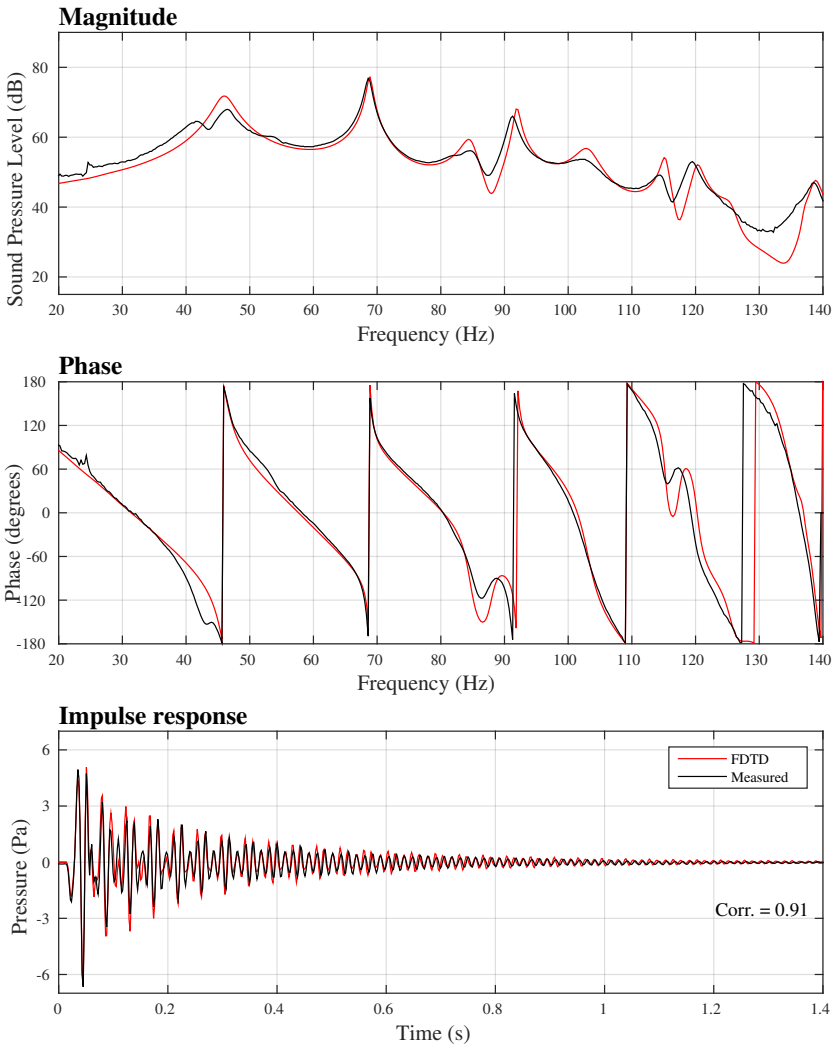

Figure 5.9: Room partially divided by a porous panel: FDTD and measured responses on the horizontal grid, Row 6 Position 4.

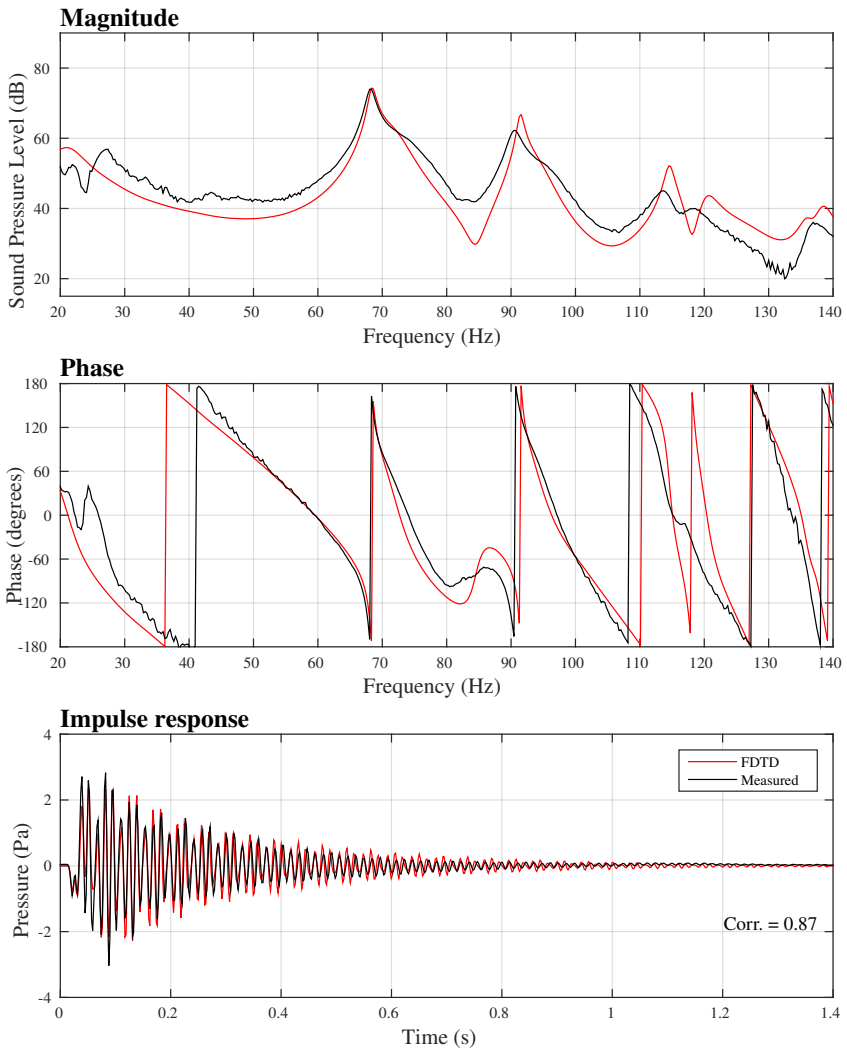

Figure 5.10: Room completely divided by a porous absorber: FDTD and measured responses on the horizontal grid, Row 6 Position 4.

5.5 Results - Contour plots

The final stage of the validation is to compare measurements with FDTD using the MFM in terms of the spatial variation of the sound pressure level over the measurement grids. The results obtained for the horizontal and vertical grids correspond to three different room configurations: empty room, room partially divided by a porous panel and room completely divided by a porous panel. The source and receiver positions are indicated in Figure 4.8 and the details of the experimental procedure are described in section 4.5.

5.5.1 Contour plots of spring-mass-spring resonances

This section shows the sound pressure level contour plots obtained at the two spring-mass-spring resonances observed when the room was completely and partially divided by the porous panel. Both spring-mass-spring resonances occur below the fundamental mode of the room, which occurs at 60 Hz.

The contour plots in Figures 5.11 and 5.12 show small variation in the spatial distribution of sound pressure level, in particular in those obtained for the vertical grid. However, FDTD successfully predicts the more significant spatial variation of sound pressure level, corresponding to the resonance horizontal grid for the partially divided room at 46 Hz (See Figure 5.11-c and -d).

FDTD predictions overestimate the measured sound pressure levels for the 46 Hz spring-mass-spring resonance by around 5 dB. However, there is close agreement between predicted and measured sound pressure levels for the first mass-spring-mass resonance.

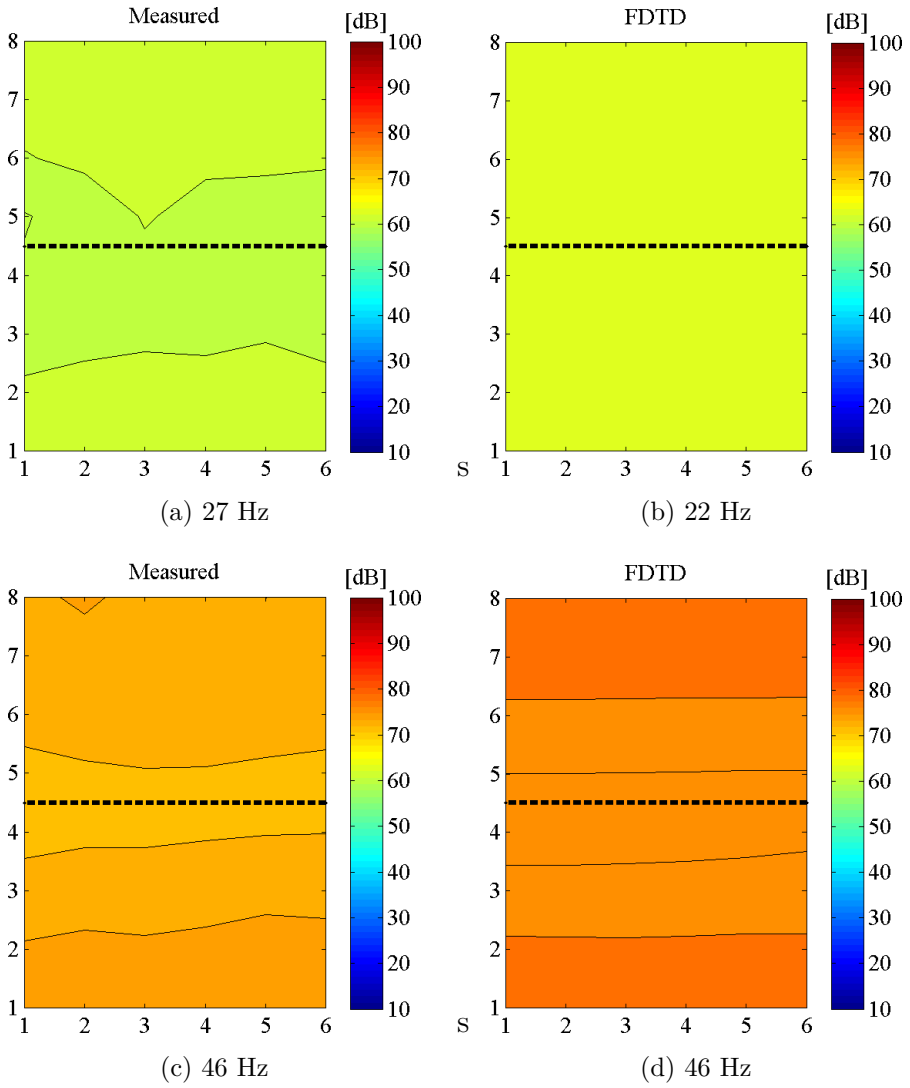

(a) 27 Hz (b) 22 Hz

(c) 46 Hz (d) 46 Hz

Figure 5.11: FDTD and measured sound pressure levels on the horizontal grid at the spring-mass-spring resonance for the room completely divided by the porous panel - a) and b) - and partially divided by the porous panel - c) and d). The black dashed line indicates the porous panel

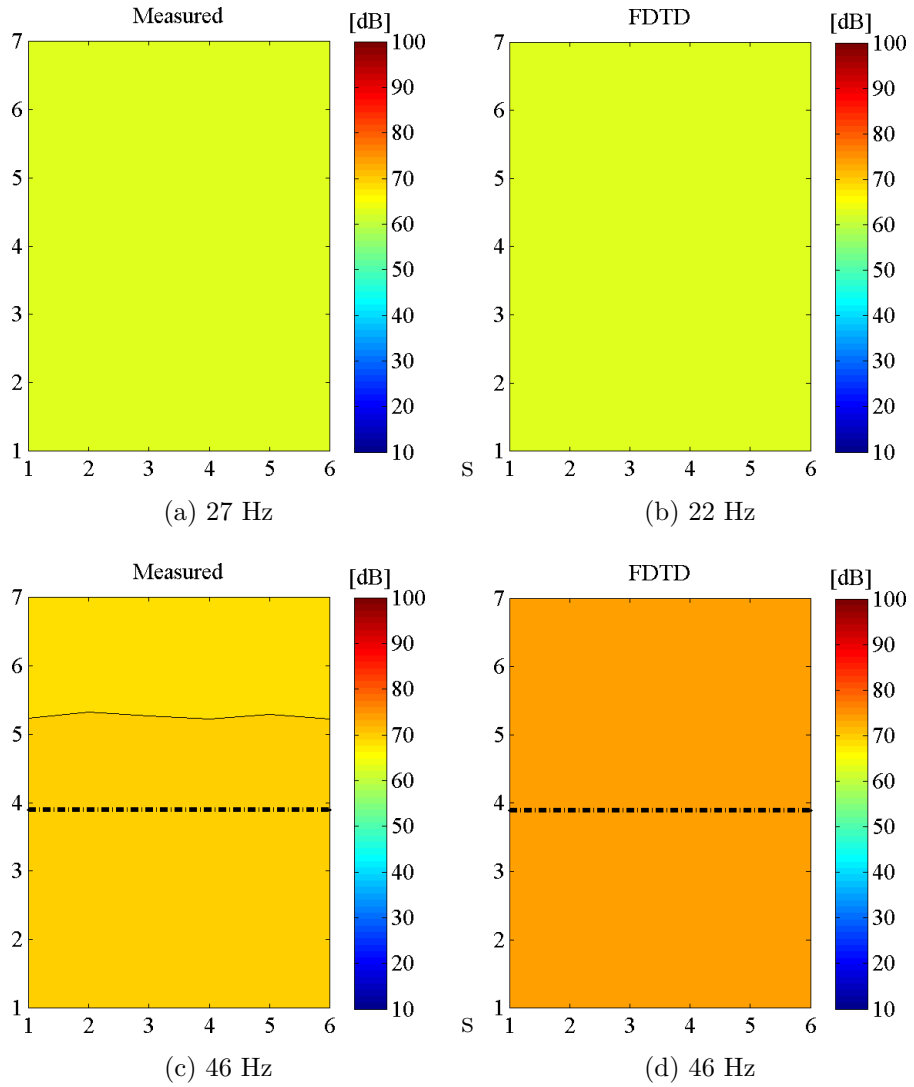

(a) 27 Hz (b) 22 Hz

(c) 46 Hz (d) 46 Hz

Figure 5.12: FDTD and measured sound pressure levels on the vertical grid at the spring-mass-spring resonance for the room completely divided by the porous panel - a) and b) - and partially divided by the porous panel - c) and d). The black dash-dot lines on (b) indicate the height of the porous panel that partially divides the room.

5.5.2 Contour plots at room resonances

This section shows a comparison between measured and predicted grid contour plots obtained at the modal resonances of the empty room. The source position and the number and positioning of the receivers used for each of the horizontal and vertical grid are described in section 4.5. Contour plots of the sound pressure level (dB re 2×10^{-5} Pa) with 1 Hz FFT lines are shown in Figures 5.13 - 5.28 for the eigenfrequencies indicated in Table 5.1. The results shown in Figures 5.13 - 5.20 correspond to the horizontal grid, while the results shown in Figures 5.21 - 5.28 correspond to the vertical grid.

It can be seen that the presence of the porous panel results in significant distortion of the empty room mode shapes, especially for mode shapes where the air particle velocity is high across the thickness of the porous panel. The results obtained show that the FDTD model of the porous absorber, which included the new MFM, successfully predicted the changes introduced in the mode shapes caused by the porous panel.

The close agreement between experimental data and numerical predictions was obtained for both horizontal and vertical grids, and for the three aforementioned room configurations. The horizonal grid contour plot shown in Figure 5.13 illustrates this, where the mode shape of the empty room corresponding to mode (0,1,0) undergoes great distortion introduced by the presence of the porous panel, since the air particle velocity is very high (SPL is low) across the thickness of the panel. One example where distortion occurs to a lesser extent can be seen in the results shown in Figure 5.18, where the porous panel is located close to a nodal line (anti-nodal line of sound pressure) of particle velocity across its thickness. Discrepancies between measurements and FDTD predictions can also be found, such as those observed in Figures 5.14-a and 5.22-a (70 Hz) and 5.15-a and 5.23-a (91 Hz), both of which refer to the empty room configuration, where discrepancies can be seen to occur mostly in the level of the modes. These discrepancies could be attributed to errors caused by the simplifying assumption of uniform damping of room walls as they are most

evident for the empty room configuration since the results obtained for the other two configurations are strongly affected by the presence of the porous panel. The level of agreement obtained in the comparison between FDTD results and experimental data for the empty room configuration is a significant improvement on that obtained in the work of Olesen [91] which (a) used a coarser measurement grid (60 cm $\times$ 60 cm) to validate the finite difference predictions, (b) was limited to a horizontal grid plane and (c) used 10dB steps in the contour plot which meant that it was not possible to identify the details between nodal and anti-nodal planes.

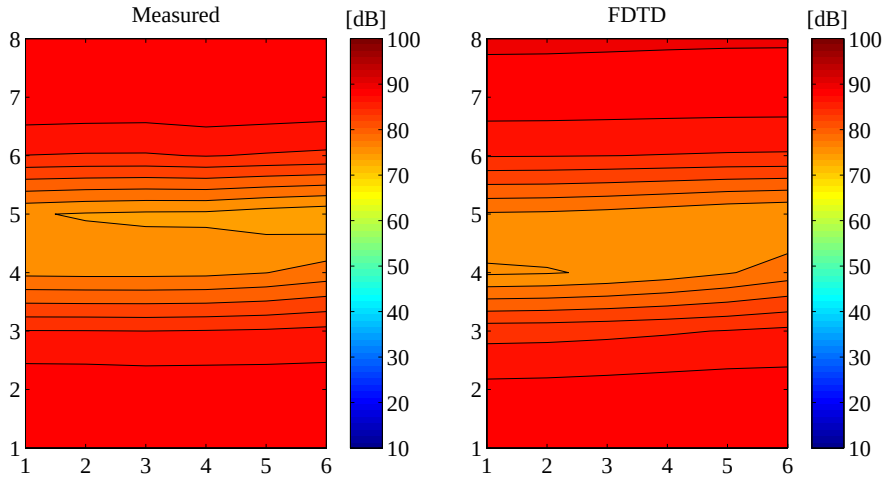

(a) Empty room

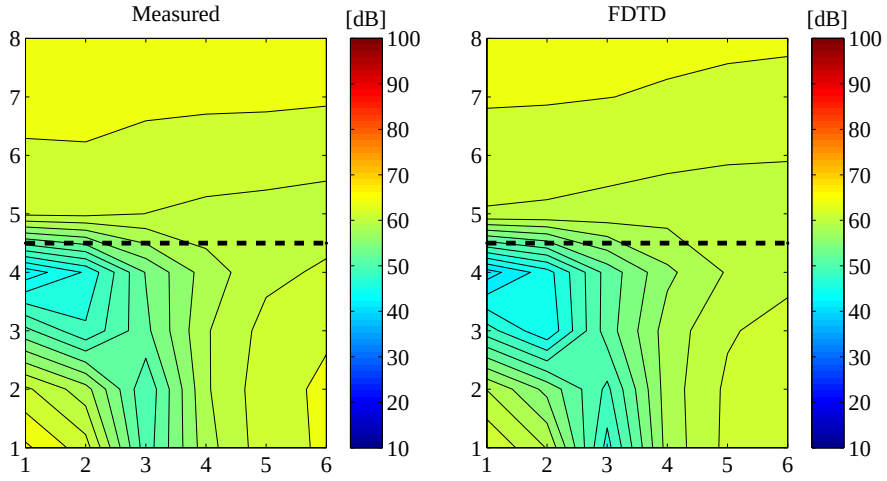

(b) Room partially divided by a porous panel

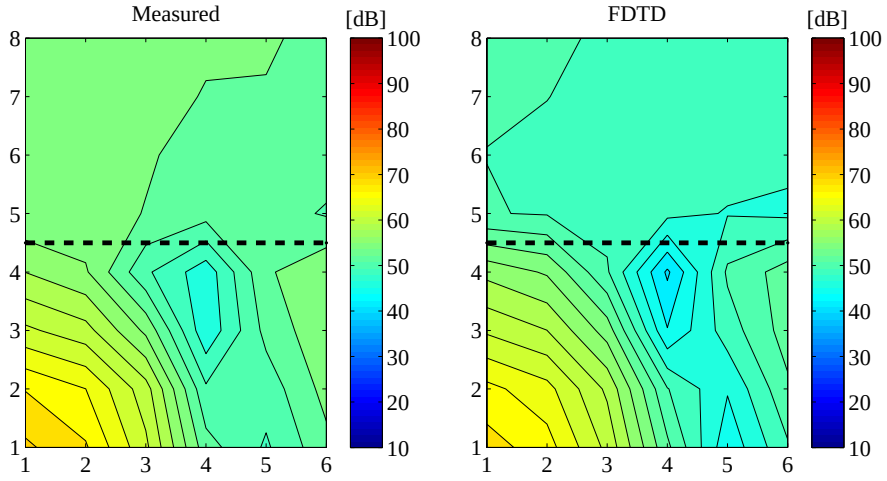

(c) Room completely divided by a porous panel

Figure 5.13: FDTD and measured responses on the horizontal grid at 60 Hz. The black dashed line indicates the porous panel

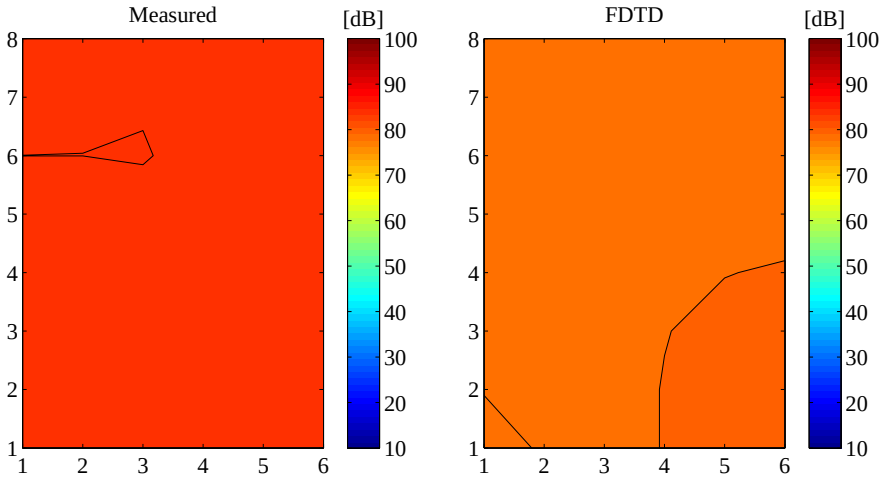

(a) Empty room

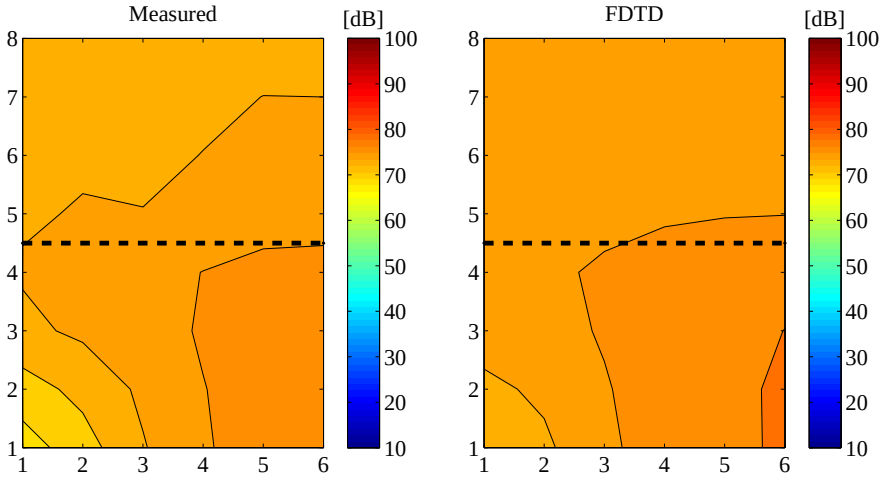

(b) Room partially divided by a porous panel

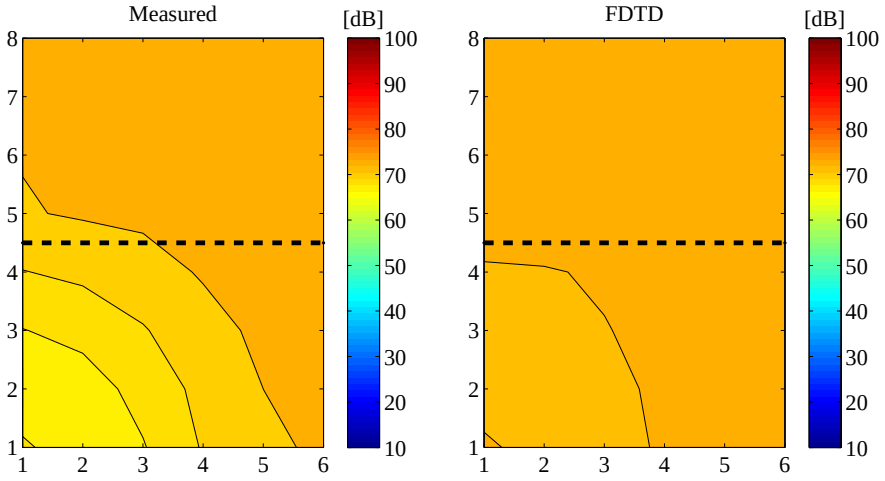

(c) Room completely divided by a porous panel

Figure 5.14: FDTD and measured responses on the horizontal grid at 70 Hz. The black dashed line indicates the porous panel.

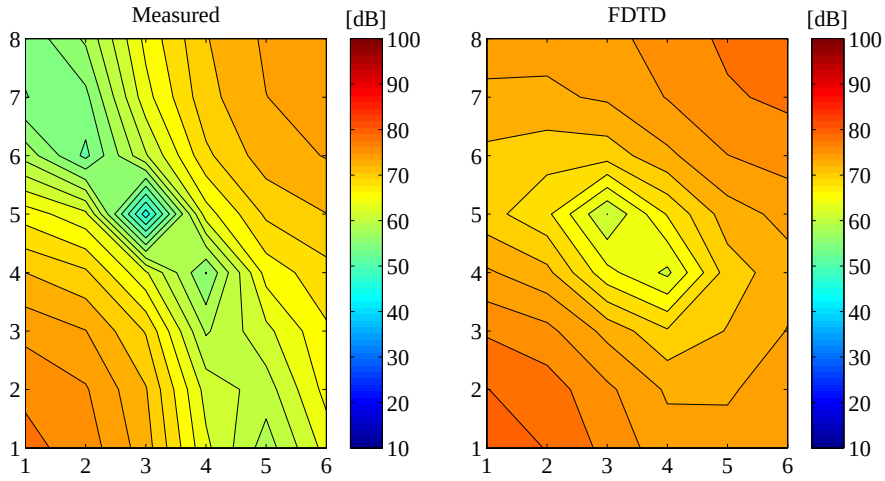

(a) Empty room

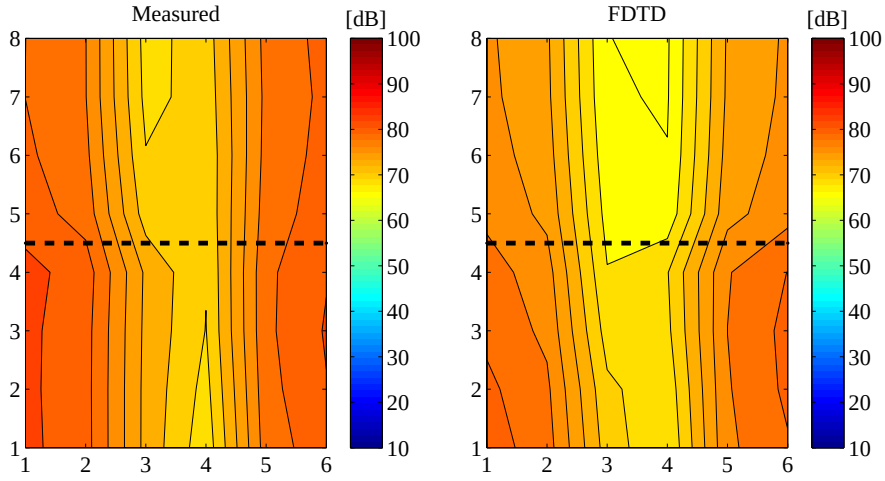

(b) Room partially divided by a porous panel

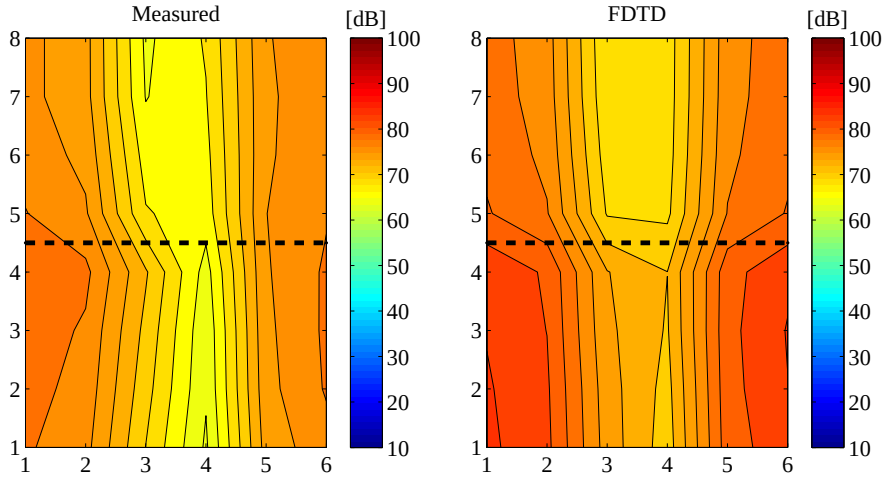

(c) Room completely divided by a porous panel

Figure 5.15: FDTD and measured responses on the horizontal grid at 91 Hz. The black dashed line indicates the porous panel.

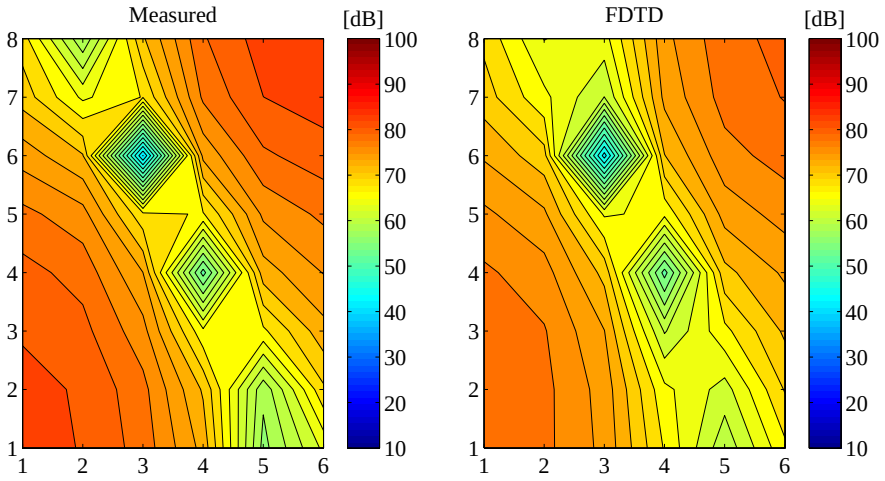

(a) Empty room

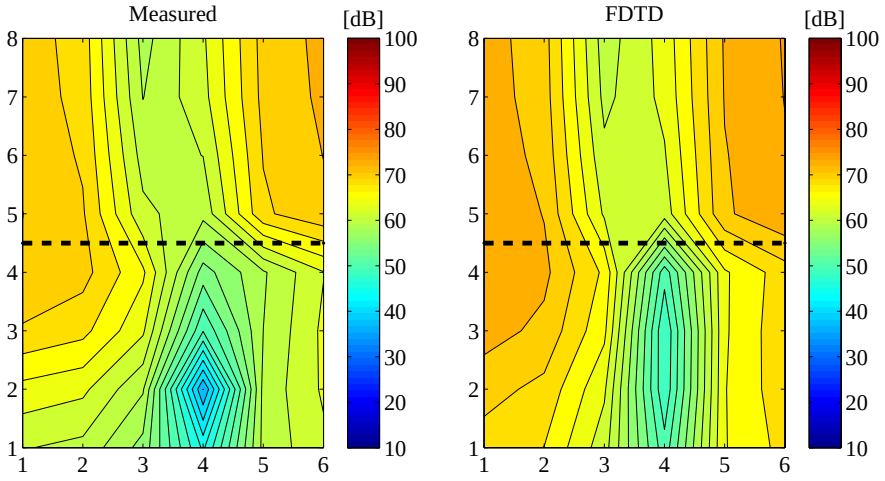

(b) Room partially divided by a porous panel

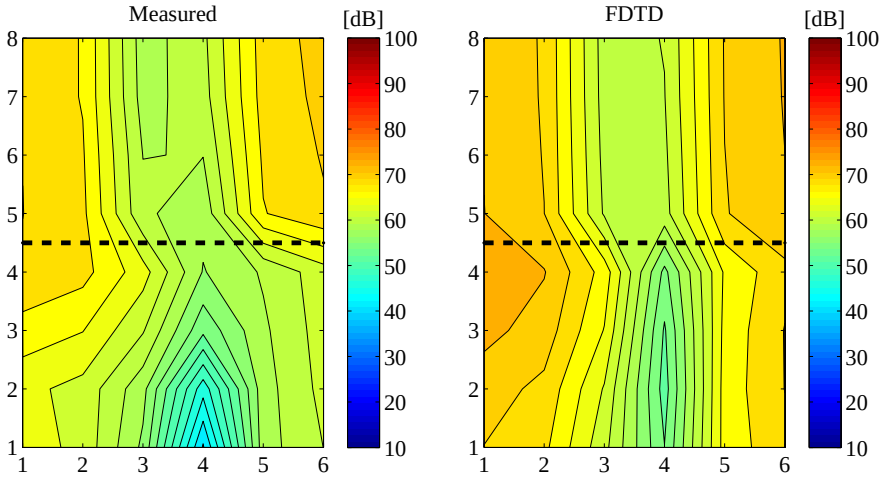

(c) Room completely divided by a porous panel

Figure 5.16: FDTD and measured responses on the horizontal grid at 94 Hz. The black dashed line indicates the porous panel.

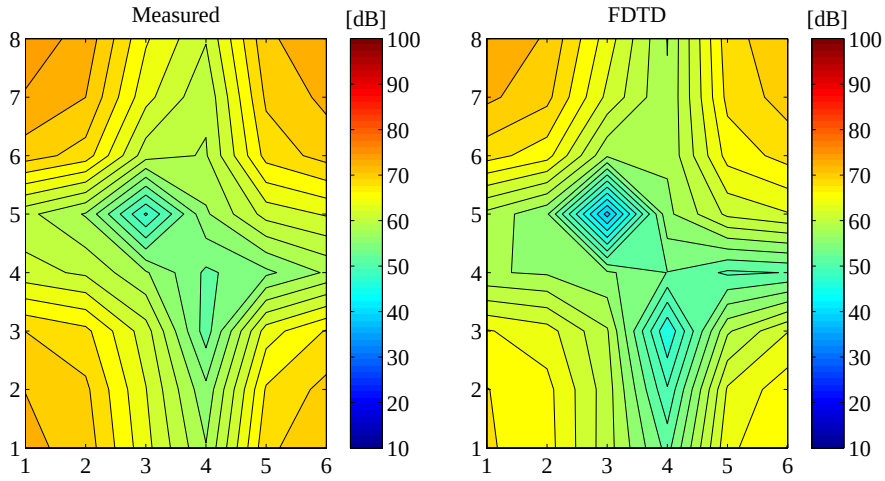

(a) Empty room

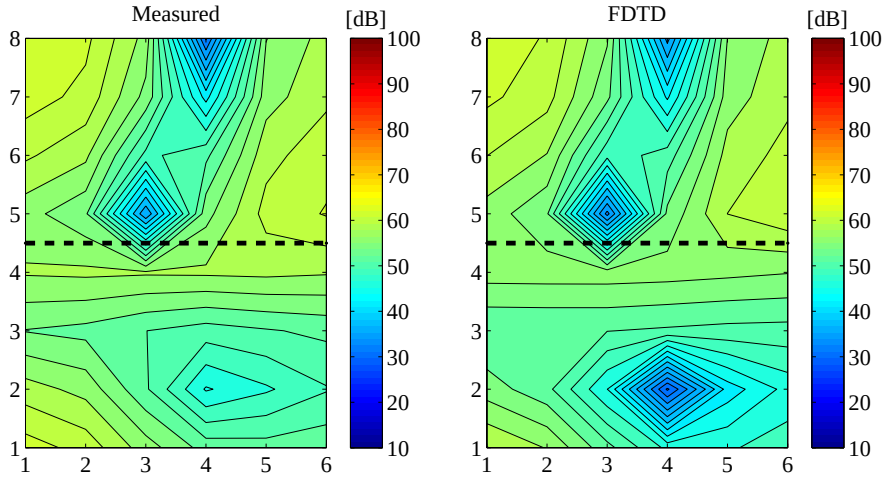

(b) Room partially divided by a porous panel

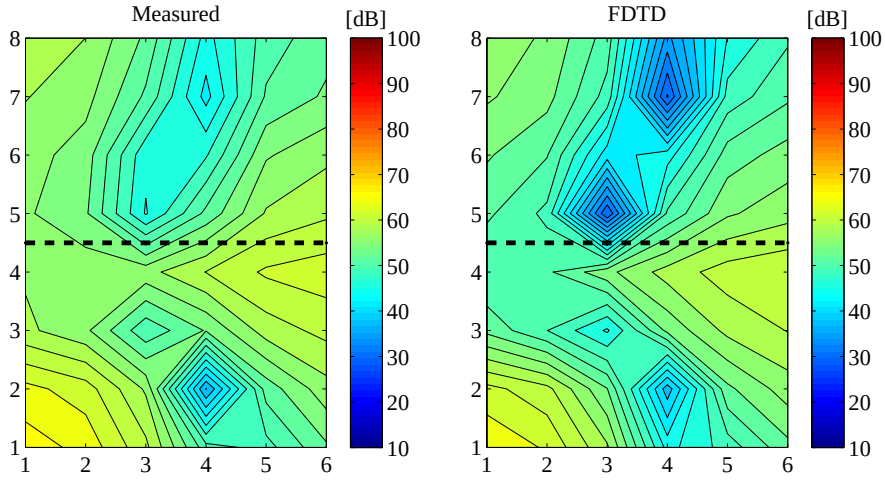

(c) Room completely divided by a porous panel

Figure 5.17: FDTD and measured responses on the horizontal grid at 112 Hz. The black dashed line indicates the porous panel.

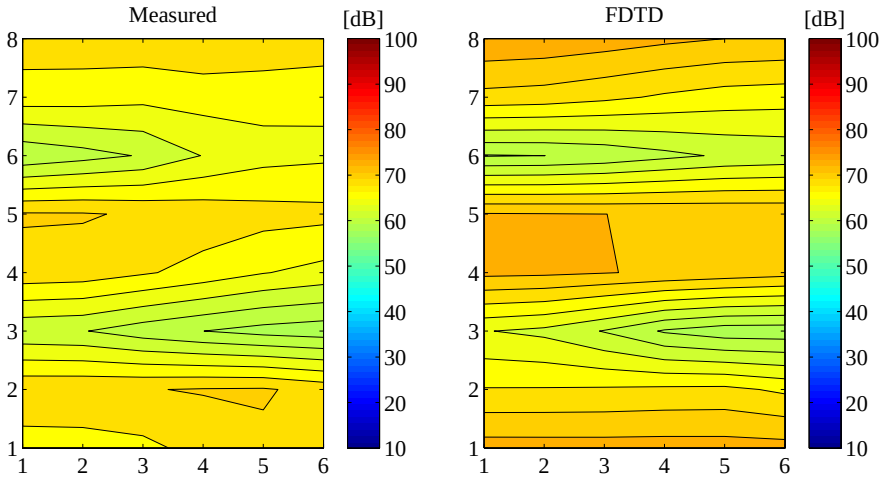

(a) Empty room

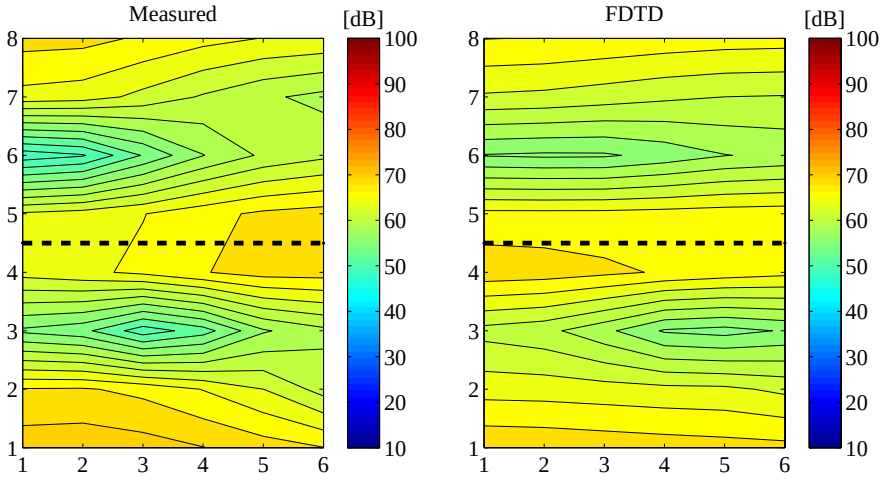

(b) Room partially divided by a porous panel

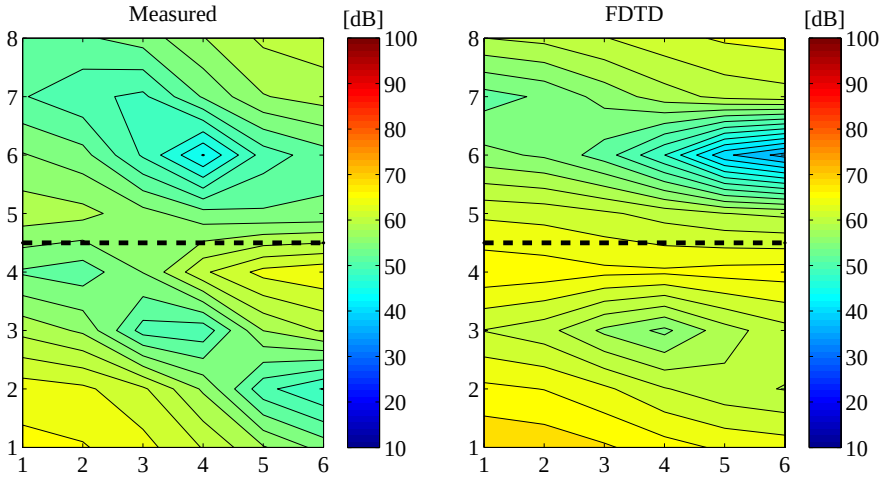

(c) Room completely divided by a porous panel

Figure 5.18: FDTD and measured responses on the horizontal grid at 120 Hz. The black dashed line indicates the porous panel.

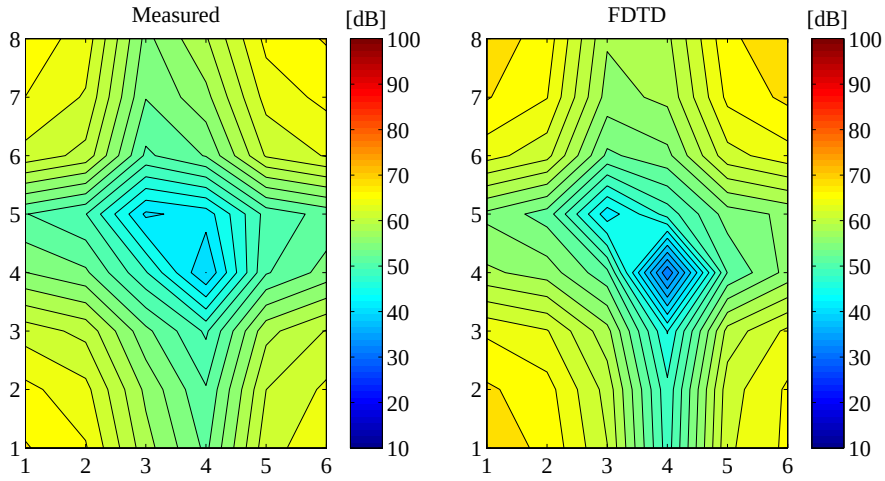

(a) Empty room

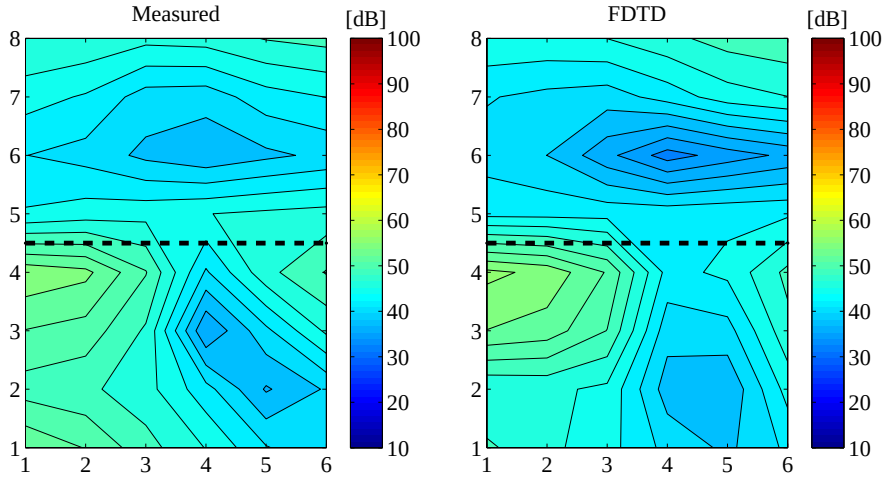

(b) Room partially divided by a porous panel

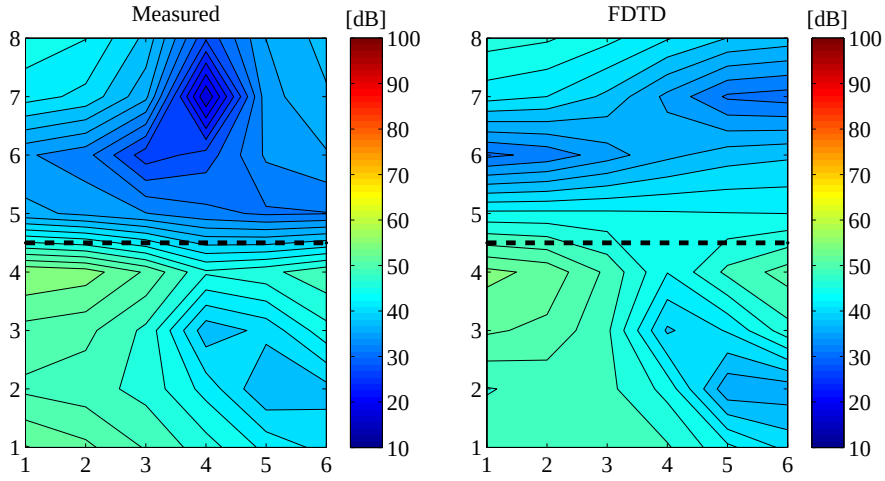

(c) Room completely divided by a porous panel

Figure 5.19: FDTD and measured responses on the horizontal grid at 131 Hz. The black dashed line indicates the porous panel.

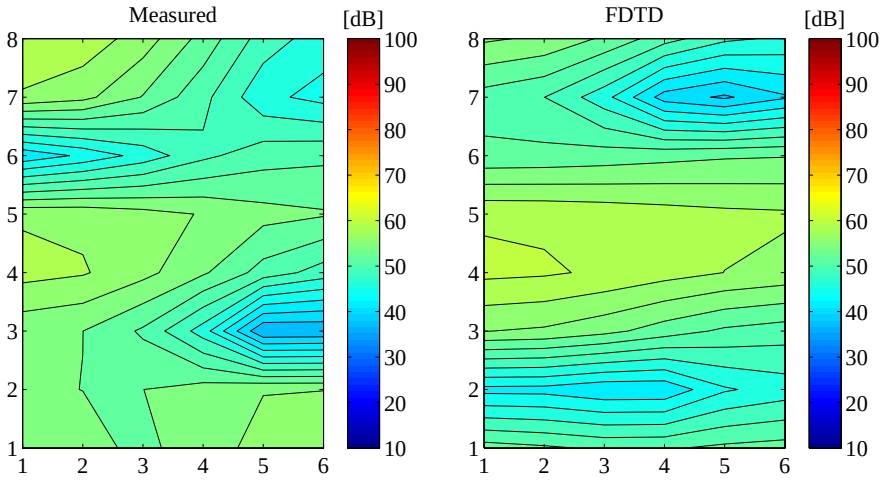

(a) Empty room

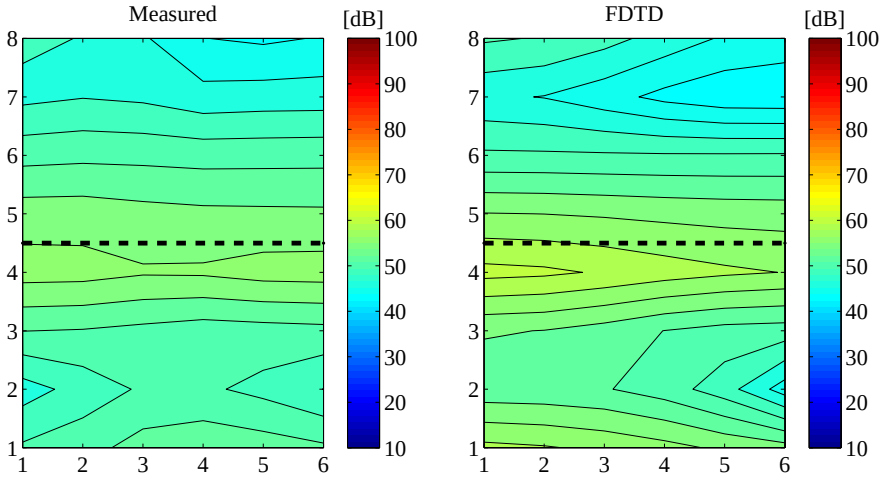

(b) Room partially divided by a porous panel

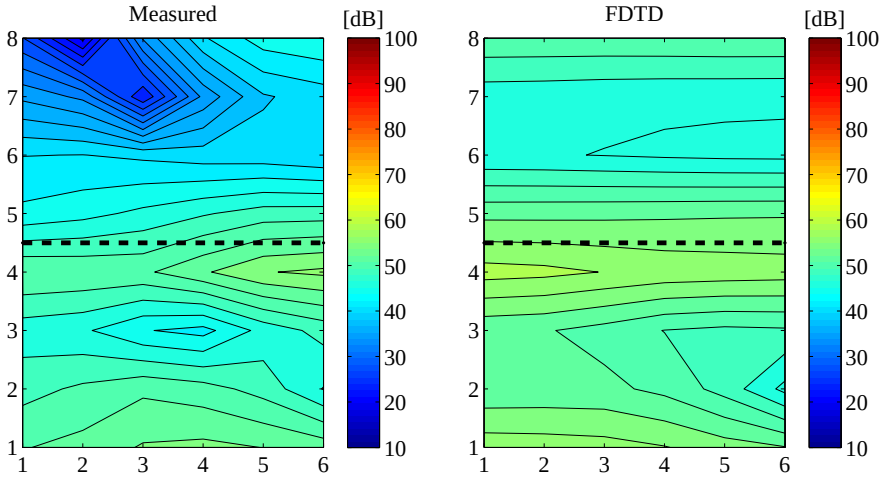

(c) Room completely divided by a porous panel.

Figure 5.20: FDTD and measured responses on the horizontal grid at 138 Hz. The black dashed line indicates the porous panel.

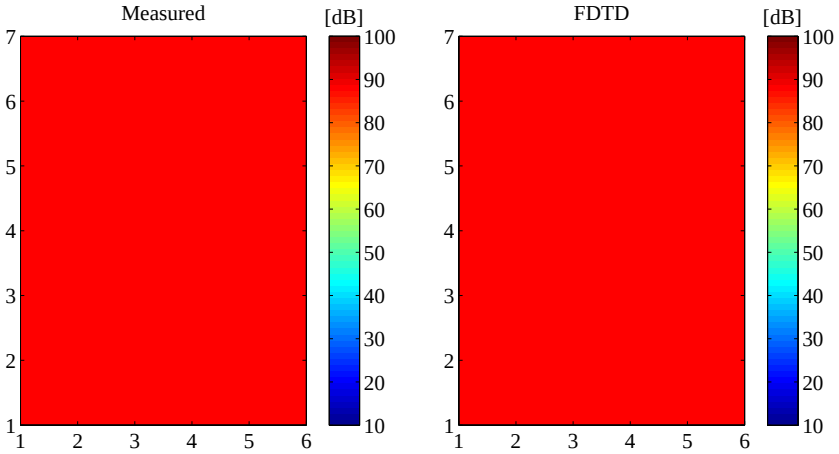

(a) Empty room

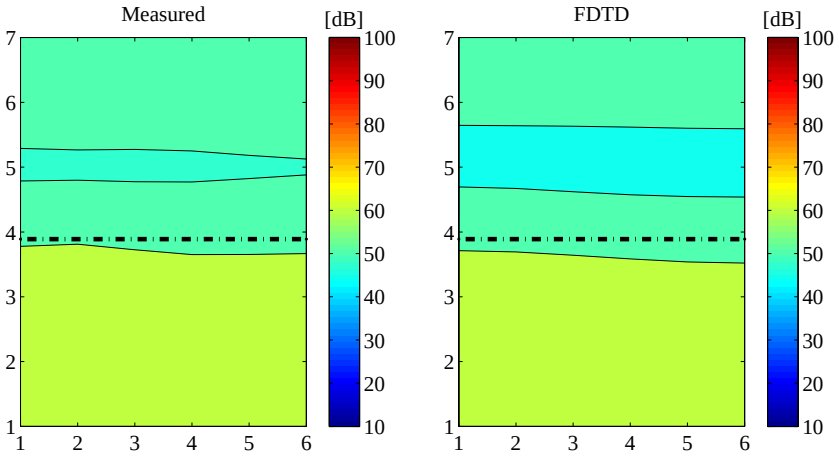

(b) Room partially divided by a porous panel

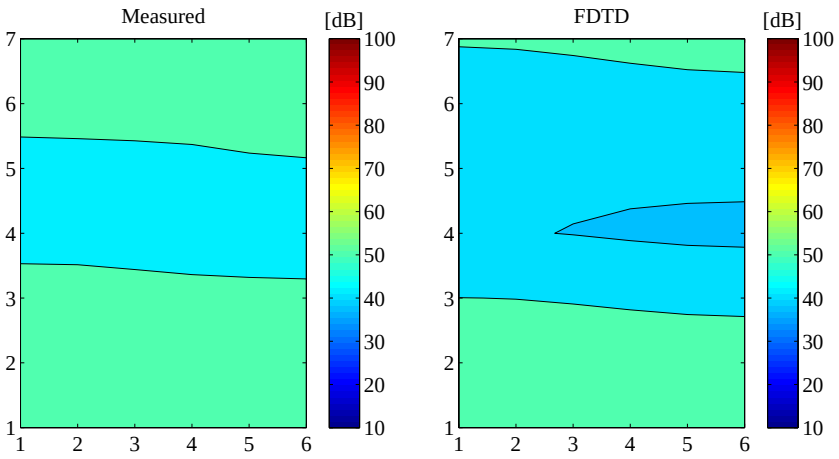

(c) Room completely divided by a porous panel

Figure 5.21: FDTD and measured responses on the vertical grid at 60 Hz. The black dash-dot lines on (b) indicate the height of the porous panel that partially divides the room.

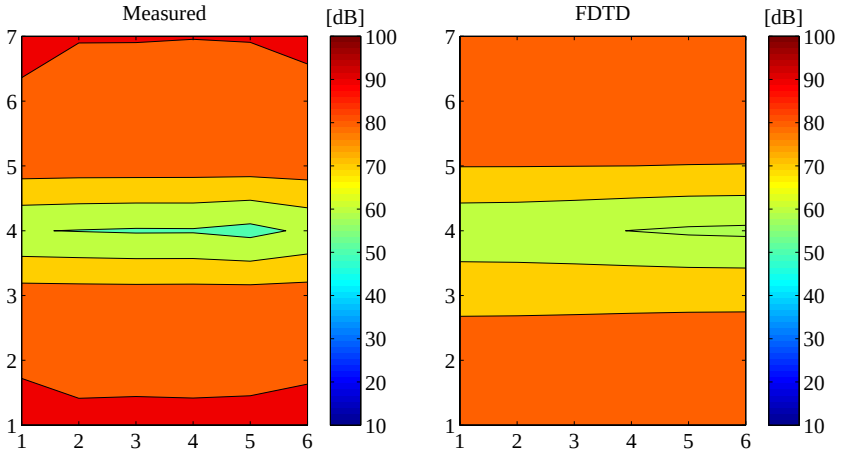

(a) Empty room

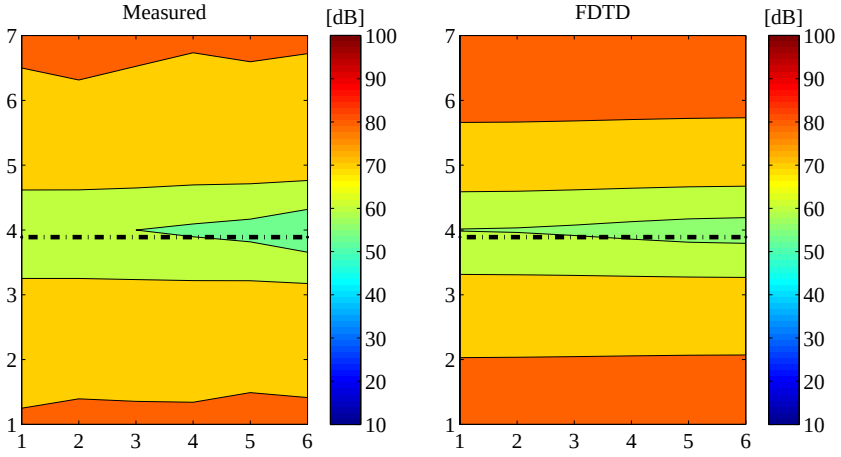

(b) Room partially divided by a porous panel

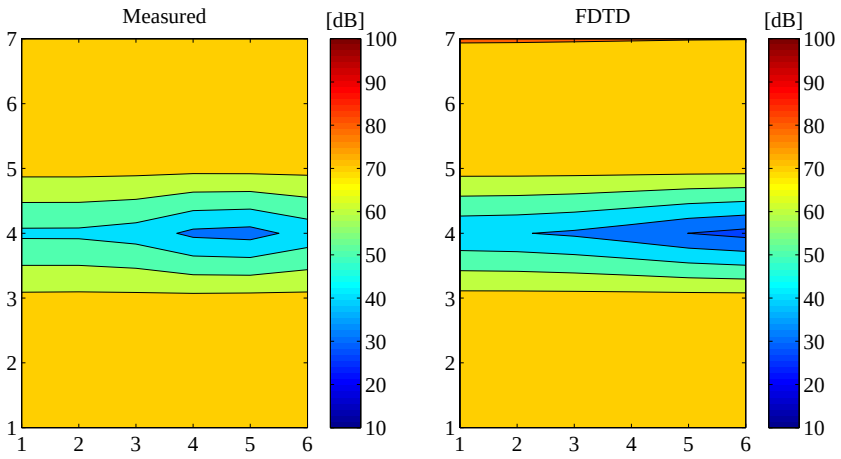

(c) Room completely divided by a porous panel

Figure 5.22: FDTD and measured responses on the vertical grid at 70 Hz. The black dash-dot lines on (b) indicate the height of the porous panel that partially divides the room.

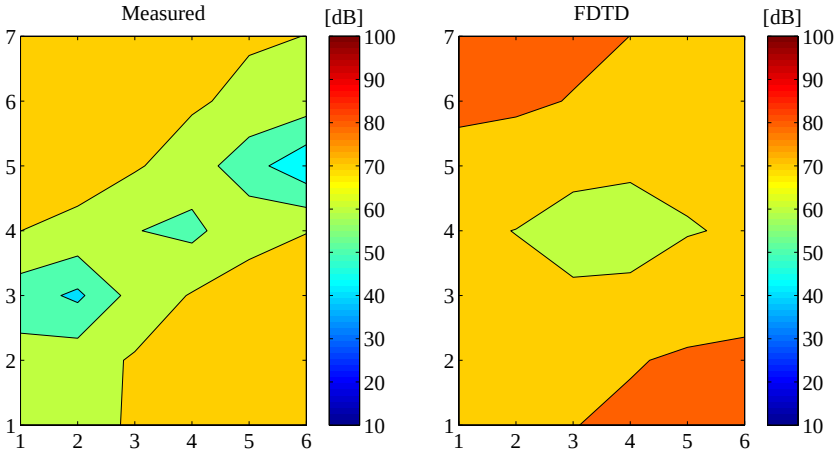

(a) Empty room

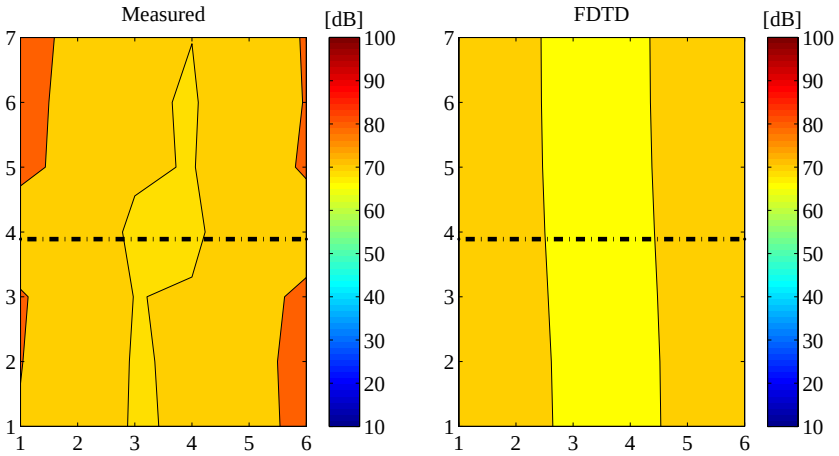

(b) Room partially divided by a porous panel

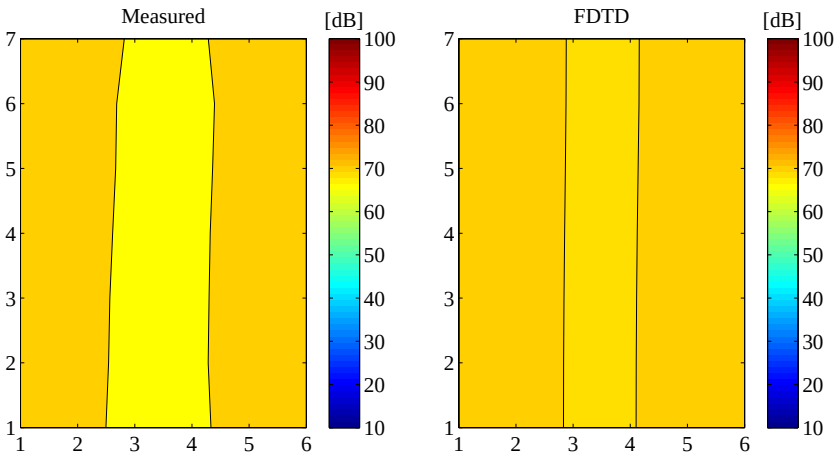

(c) Room completely divided by a porous panel

Figure 5.23: FDTD and measured responses on the vertical grid at 91 Hz. The black dash-dot lines on (b) indicate the height of the porous panel that partially divides the room.

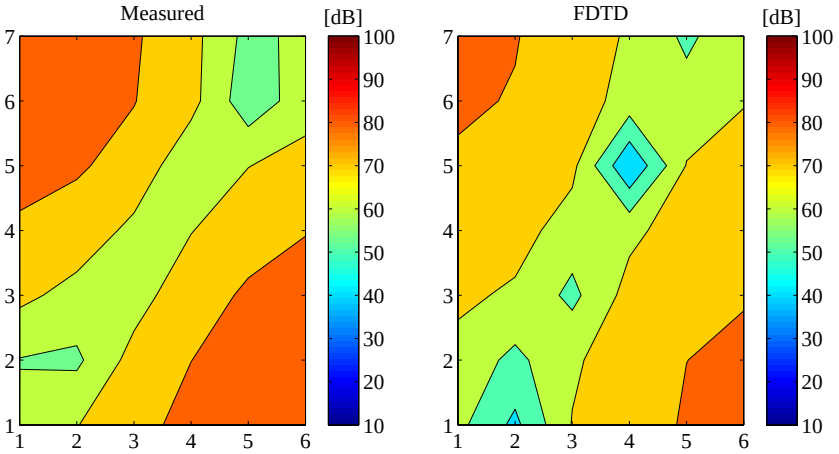

(a) Empty room

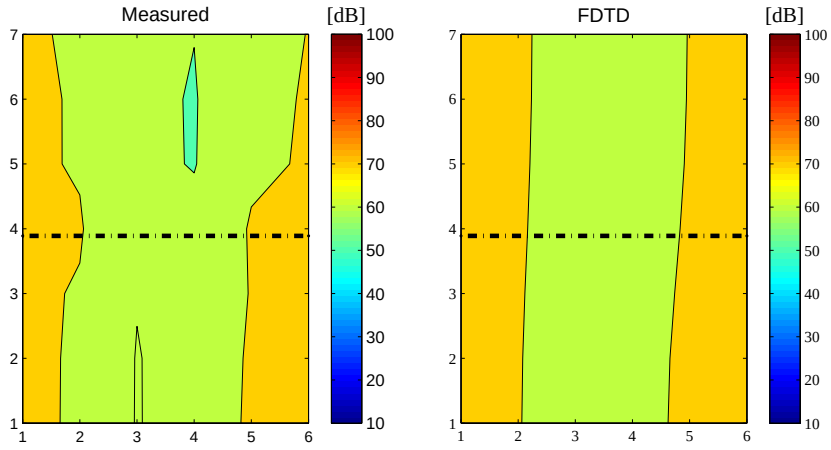

(b) Room partially divided by a porous panel

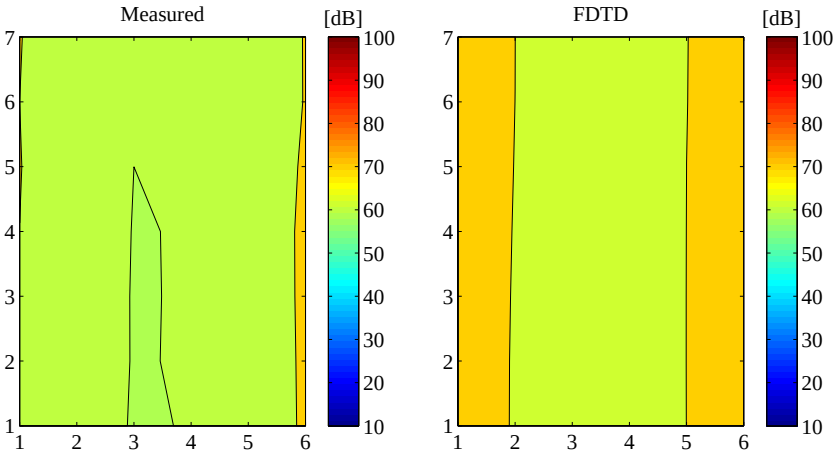

(c) Room completely divided by a porous panel

Figure 5.24: FDTD and measured responses on the vertical grid at 94 Hz. The black dash-dot lines on (b) indicate the height of the porous panel that partially divides the room.

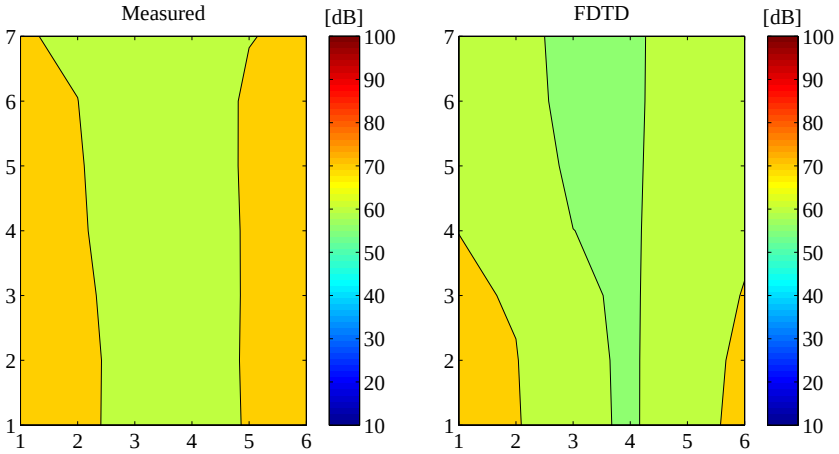

(a) Empty room

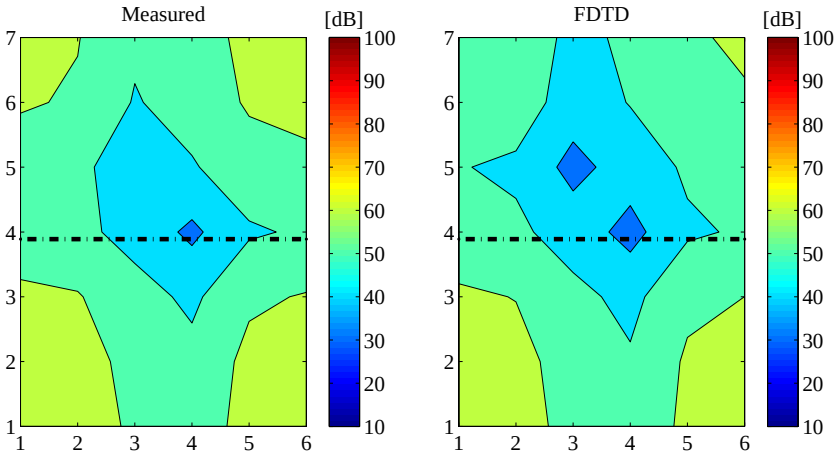

(b) Room partially divided by a porous panel

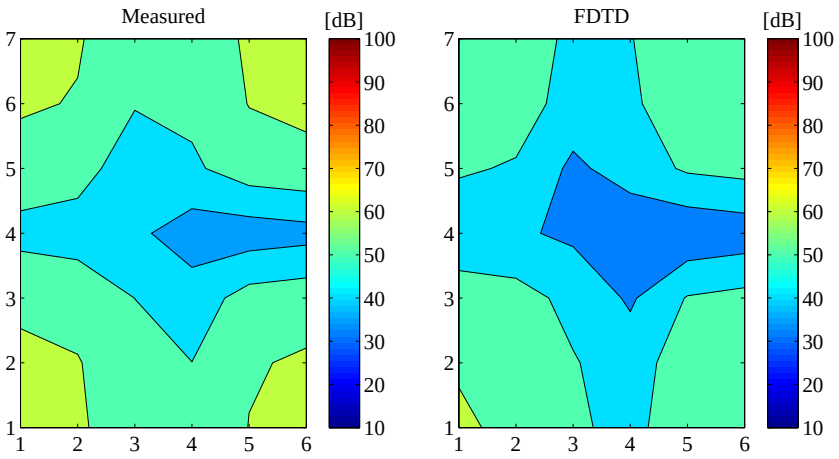

(c) Room completely divided by a porous panel

Figure 5.25: FDTD and measured responses on the vertical grid at 112 Hz. The black dash-dot lines on (b) indicate the height of the porous panel that partially divides the room.

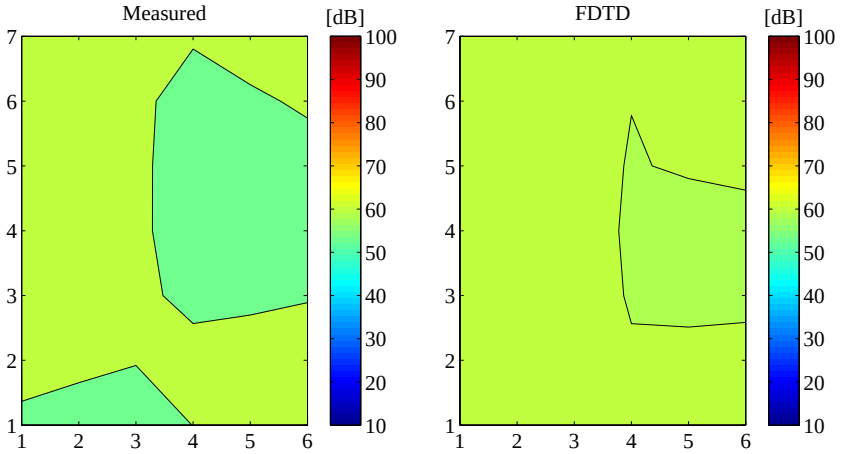

(a) Empty room

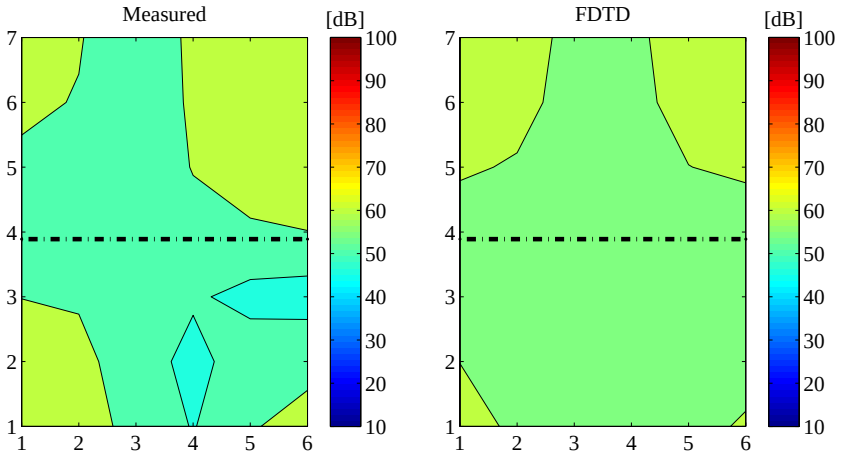

(b) Room partially divided by a porous panel

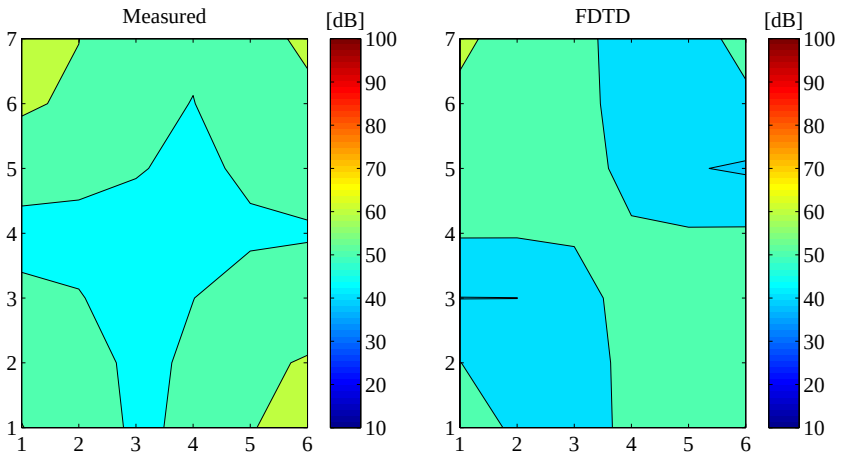

(c) Room completely divided by a porous panel

Figure 5.26: FDTD and measured responses on the vertical grid at 120 Hz. The black dash-dot lines on (b) indicate the height of the porous panel that partially divides the room.

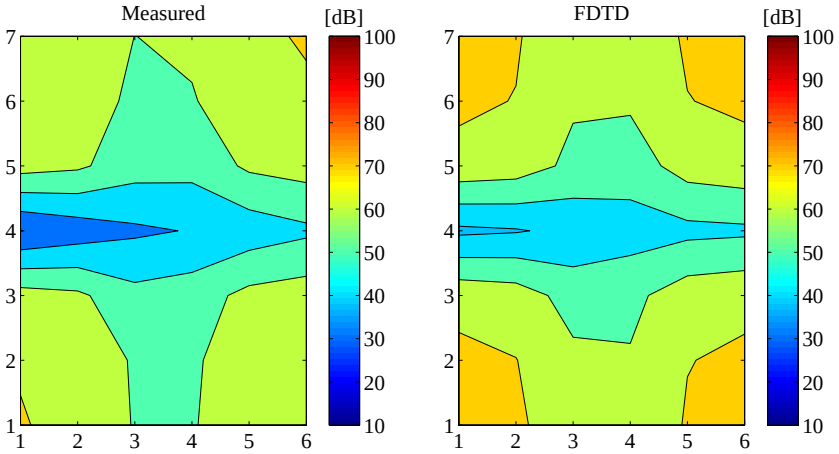

(a) Empty room

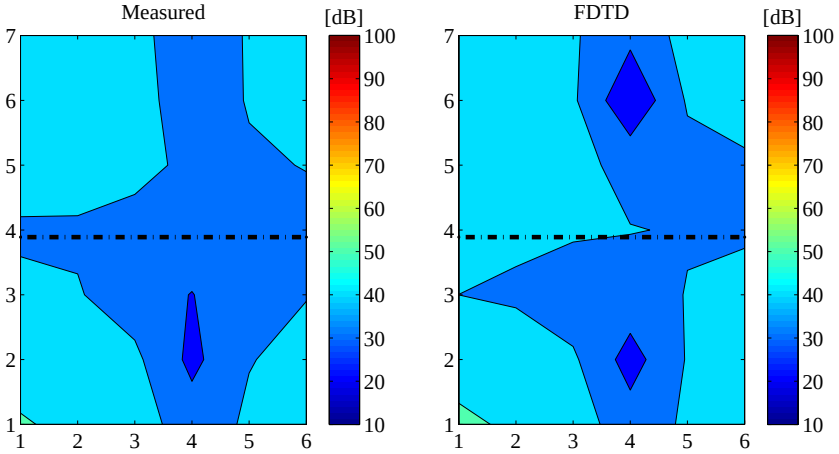

(b) Room partially divided by a porous panel

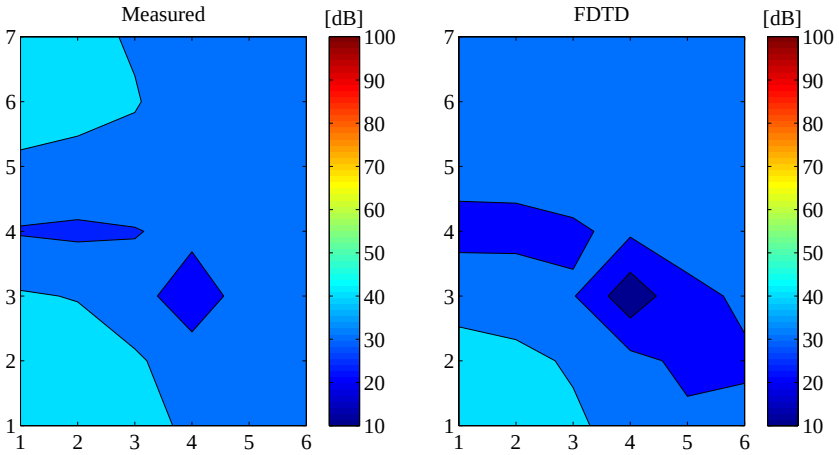

(c) Room completely divided by a porous panel

Figure 5.27: FDTD and measured responses on the vertical grid at 131 Hz. The black dash-dot lines on (b) indicate the height of the porous panel that partially divides the room.

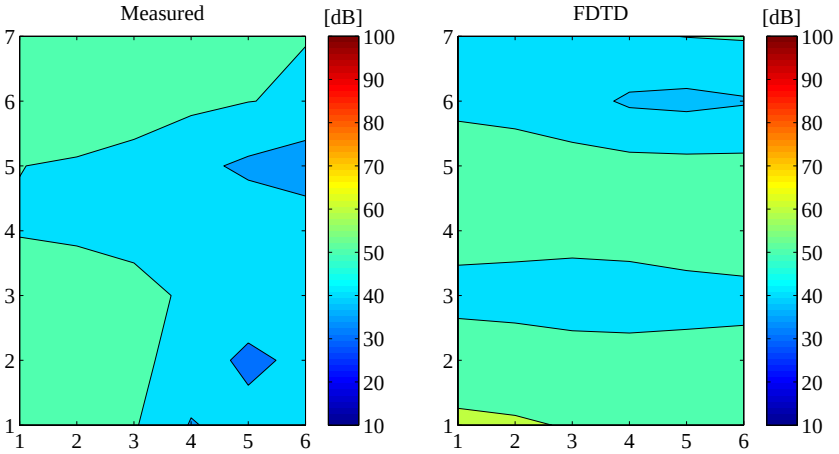

(a) Empty room

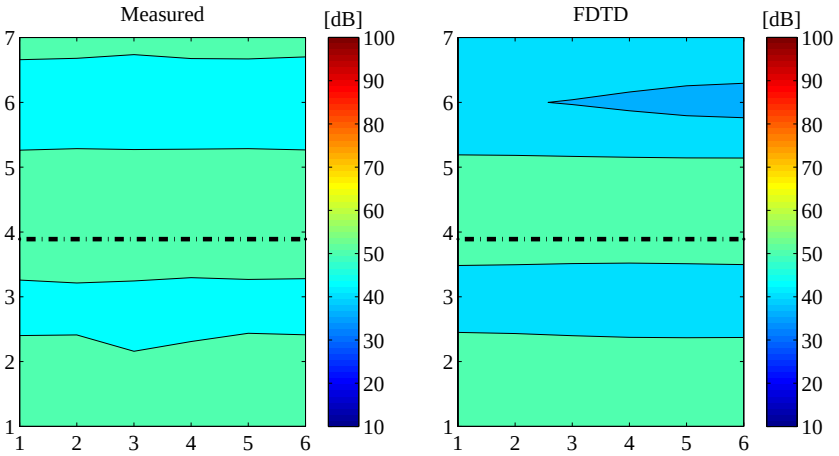

(b) Room partially divided by a porous panel

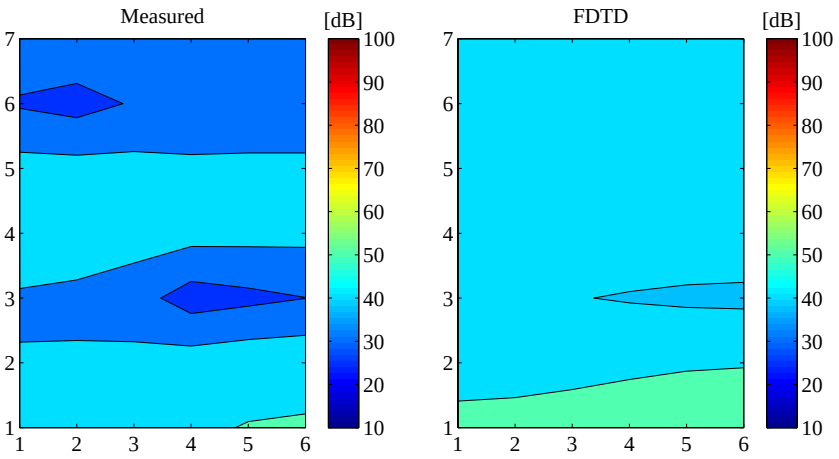

(c) Room completely divided by a porous panel

Figure 5.28: FDTD and measured responses on the vertical grid at 138 Hz. The black dash-dot lines on (b) indicate the height of the porous panel that partially divides the room.

5.6 Conclusions

The implementation of the FDTD acoustics model of the small reverberation chamber and the porous panel was described in this chapter. The prediction of low-frequency sound fields using FDTD in a small room incorporating a porous panel was investigated. Close agreement was obtained between FDTD and measurements in terms of time domain response and the corresponding magnitude and phase of the Fourier transforms. The experimental results indicate the existence of a spring-mass-spring resonance that occurs below the fundamental acoustic resonance of the room when the porous panel is present. The results show that the MFM enabled the FDTD model to estimate the higher response caused by this spring-mass-spring resonance. The contour plots obtained for the room eigenfrequencies show that the majority of measured features relating to the nodal and anti-nodal planes for the axial, tangential and oblique modes are predicted by the FDTD model. The close agreement between FDTD and measurements can be found over both horizontal and vertical measurement grids. This demonstrates the ability of FDTD to accurately predict the sound field with or without a porous panel that partially or completely divides the room.

The close agreement between FDTD and measurements shows that: (a) the Rayleigh model is valid for a room that is partially or completely divided by a porous panel of fibrous material, (b) an additional moving frame model is required in FDTD to introduce low-frequency panel motion and (c) a loudspeaker driven by a pulse can be accurately modelled in FDTD as a hard velocity source acting as a piston with all other velocity elements forming the cabinet set to zero to represent rigid boundaries.

6 Validation of the vibroacoustic FDTD model for a point-excited plate in an acoustic cavity

6.1 Introduction

This chapter concerns the experimental validation of the vibroacoustics FDTD model, corresponding to the prediction of the sound field produced by a mechanically excited aluminium plate.

Section 6.2 describes the numerical details of the FDTD model used for the small reverberation chamber that includes the aluminium plate.

Section 6.3 discusses the effects of numerical dispersion in the FDTD vibroacoustics model by comparing the resonances for the room and the aluminium plate with those calculated using analytical models.

Section 6.4 details the experimental validation of the FDTD predictions of the driving-point mobility of the aluminium plate.

Section 6.5 describes the experimental validation of the FDTD predictions in terms of frequency response contour plots of the small reverberation chamber excited by a vibrating aluminium plate. The results obtained for the experimental validation are discussed in terms of differences in level and mode shapes for the frequency response contour plots. The validity of the frequency response measurements is evaluated based on the coherence measurements.

6.2 FDTD implementation of a practical vibroacoustics model

To assess whether the scaling approach and simplified solid-air boundary conditions described in chapter 3 can be applied to practical vibroacoustic problems, a model of a simply-supported 5 mm thick aluminium plate inside a small reverberation chamber was created using FDTD. The accuracy of the FDTD predictions were experimentally validated using the experiment setup described in section 4.7. The comparison and discussion of the results obtained for this vibroacoustic FDTD model and the corresponding measurements is shown in sections 6.4 and 6.5.

6.2.1 Material properties

The physical properties assigned to the aluminium plate in the FDTD model were previously described in section 4.6. The values of these physical properties result in the following Lamé constants, $\mu = 2.32 \times 10^{10}$ N/m^2 and $\lambda = 4.92 \times 10^{10}$ N/m^2. In order to account for mechanical energy dissipation, the following Rayleigh damping constants were used to approximate the damping measured in the vibroacoustic experiments: $\beta = 11,000$ Ns/m^4, $\gamma = 0$ Ns/m^2 and $\chi = 0$ Ns/m^2.

The properties of air for the acoustic medium were set to ρ_o= 1.2 kg/m^3 and $c = 343$ m/s. A scaling factor of s=6 was chosen to carry out the simulations which gives ρ'_o=0.20 kg/m^3 and $c' = 2058$ m/s.

The Lamé and damping constants were used in the discretized version of the 3D constitutive equations 3.28 - 3.30. The density used in the FDTD equations corresponds to the discretized form of the 3D momentum equations 3.34 - 3.36.

6.2.2 Numerical resolution

The global Cartesian frame of reference used in the FDTD model is the same as previously shown in Figure 4.13. The spatial resolution used for the scaled FDTD model is $\Delta x'$=0.39 m, $\Delta y'$=0.35 m and $\Delta z'$=0.13 m. The largest wave speed that is accounted for in the vibroacoustic model is the quasi-longitudinal phase velocity of aluminium, 5100 m/s. As discussed in section 3.13, the largest time step which satisfied the Courant condition and provided stability was found to be 1.93×10^{-5} s. The simulations are carried out over a time interval of 4 s.

6.2.3 Boundary conditions

The acoustic boundary conditions of the reverberation chamber were modelled exactly as described in section 5.2.3, i.e. the boundaries were modelled as frequency independent with a value of specific acoustic impedance of 224.9.

6.2.4 Source function

The driving function assigned to the source is proportional to the first time derivative of the Gaussian pulse, which has the form:

$$\sigma_{zz}(t) = -A_{\mathrm{o}} \frac{(t - t_{\mathrm{o}})}{\sigma_{\mathrm{o}}^3} \exp\left[\frac{(t - t_{\mathrm{o}})^2}{2\sigma_{\mathrm{o}}^2}\right] \tag{6.1}$$

where t_{o} is the time offset and σ_{o} is the Gaussian width of the pulse and A_{o} is an amplitude constant which was assigned the value of 10^{-4} Ns^2/m^2. This particular waveform is chosen because its spectrum contains no energy at 0 Hz (which would represent static loading). The values chosen for t_{o} and σ_{o} determine the frequency content of the source function. In this thesis, $t_{\mathrm{o}} = 10$ ms and $\sigma_{\mathrm{o}} = 10^{-3}$ms. Refer back to Figure 3.6 for the waveform and frequency response of the pulse. It is

necessary that most of the power of the source function lies below the maximum frequency allowed by the domain discretization [18].

6.2.5 Frequency range of the FDTD analysis

It is necessary to estimate an upper frequency limit for the FDTD analysis; however, there is more than one factor that determines this limit. The sampling frequency used in the FDTD simulations is 51,724 Hz and according to the Nyquist sampling theorem this results in an upper limit of 25,862 Hz. In contrast, the upper limit due to the scaling approach for the aluminium plate with a scaling factor of six is 1418 Hz. In terms of spatial discretization for the air, the use of six computational cells per wavelength results in an upper limit of $\approx$ 870 Hz (based on $c' = sc$ =2040 m/s). For bending waves on the plate, six cells per wavelength gives an upper limit of $\approx$ 300 Hz; hence as this is the lowest value, it provides an estimate for the upper frequency limit of the FDTD simulation.

6.2.6 Stability of the simulation

The general FDTD implementation of the plate can potentially involve any type of vibratory wave motion. Hence, it is necessary to consider the different wave types that might occur in the problem. In this example, the FDTD simulation of a 5 mm thick aluminium plate followed a general approach that does not restrict any particular type of wave motion from propagating in the solid medium. Figure 6.1 shows the different wave types and corresponding phase velocities that occur below 500 Hz. Since the frequency range of interest is below 200 Hz, as this corresponds to the highest frequency of the measurements, the dilatational wave has the highest phase velocity, at a value of 6052 m/s. However, as discussed in section 3.9, it is not always possible to identify whether waves that have the highest phase velocity have actually been excited and therefore it was necessary to test several values of C (using equation 2.41) for stability. After assessing values for C in the range 5000 m/s

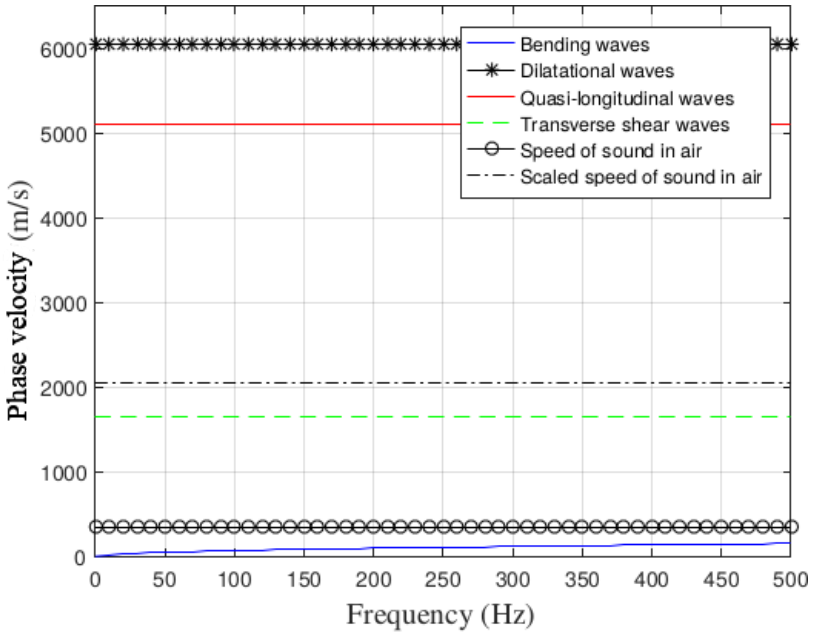

Figure 6.1: Phase velocities of different types of waves occurring in a aluminium plate 5 mm thick.

to 6100 m/s, it was concluded that the simulations stabilise at a value of C =6000 m/s, which is slightly lower than the phase velocity of dilatational waves. The value of C obtained for stability was found to be invariant with the type of excitation, whether out-of-plane or in-plane excitation. Therefore the value C =6000 m/s was used in the simulations to calculate the value of dt using equation 2.41.

6.2.7 Processing of numerical results

The output of the FDTD simulation consisted of a time history of transient pressure signals and a force driving function, each with a duration 4 s and a time step of 1.93×10^{-5} s. The force driving function $f(t)$ and the pressure time signals $p(t)$ were then Fourier transformed using FFT, which resulted in $P(\omega)$ and $F(\omega)$. In order to obtain the complex transfer function P/F the complex vectors $P(\omega)$ and $F(\omega)$ were pointwise divided. After obtaining the complex transfer function, its magnitude gives $|P(\omega)/F(\omega)|$. The level of the the magnitude of the transfer function was then calculated using $20\log_{10}(|P(\omega)/F(\omega)|)$. Finally, the logarithmic transfer function was linearly averaged over every 4 points (0.25 Hz each) giving a frequency resolution

of 1 Hz (this corresponds to that used for the measurements described in section 4.7.3).

6.2.8 Scaling of FDTD model

The vibroacoustic FDTD model uses a scaling factor of $s = 6$. After accounting for the total number of calculation cells and the time step used in the scaled model, the computation time was reduced by a factor of 170 compared to the original model. As expected (see section 3.13.5), this factor does not exceed the ratio of 216 that corresponds to s^3 which was estimated using equation 3.74.

6.3 Numerical dispersion

To assess numerical dispersion in the FDTD model for wave motion in the acoustic medium, a hard, point pressure source is implemented in one corner of the empty room (i.e., without the plate). The sound pressure response in a different corner is then used to identify modal peaks for comparison with the analytical eigenfrequencies that are calculated for an empty room with rigid boundaries (given by equation 3.63). Results for modes below 200 Hz are shown in Table 6.1. These indicate that the errors are less than 2.2%. To assess numerical dispersion for the elastic plate, analytical eigenfrequencies for a simply supported plate are compared with the modal peaks in the FDTD driving-point mobility below 200 Hz. The results are shown in Table 6.2 which indicates that the errors are no more than 5.1%. Hence, numerical dispersion can be considered to be negligible for both the air and plate below 200 Hz.

Mode	Analytical (Hz)	FDTD (Hz)	Difference (%)
1	60.3 f_{010}	60.0	0.5
2	69.8 f_{001}	68.9	1.3
3	92.3 f_{011}	91.0	1.4
4	94.6 f_{100}	95.0	-0.4
5	112.2 f_{110}	112.5	-0.3
6	117.6 f_{101}	117.3	0.3
7	120.6 f_{020}	119.2	1.2
8	132.1 f_{111}	131.7	0.3
9	139.4 f_{021}	136.4	2.2
10	139.6 f_{002}	137.8	1.3
11	152.1 f_{012}	148.9	2.1
12	153.3 f_{120}	152.5	0.5
13	168.4 f_{121}	166.1	1.4
14	168.6 f_{102}	167.8	0.5
15	179.1 f_{112}	176.7	1.4
16	181.0 f_{030}	178.4	1.4
17	184.5 f_{022}	182.0	1.4
18	189.2 f_{200}	189.4	-0.1
19	194.0 f_{031}	191.4	1.3
20	198.6 f_{210}	198.5	0.1

Table 6.1: Room - comparison of analytical eigenfrequencies and the frequencies of peaks in the room response from FDTD.

Mode	Analytical (Hz)	FDTD (Hz)	Difference (%)
1	26.1 f_{11}	27.5	-5.1
2	50.2 f_{21}	52.2	-3.9
3	80.3 f_{12}	83.0	-3.3
4	104.4 f_{22}	106.7	-2.2
5	146.0 f_{41}	145.0	0.7
6	200.0 f_{42}	195.7	2.2

Table 6.2: Plate - comparison between analytical eigenfrequencies and modal peaks in the FDTD driving-point mobility.

6.4 Driving-point mobility of the aluminium plate

Figure 6.2 shows the driving-point mobility after accounting for the level offset due to scaling and allows a comparison between FDTD and the measurements. A comparison of the frequencies at which the peaks occur in the measured and FDTD driving-point mobilities is shown in Table 6.3. The agreement confirms that the experimental setup provides a reasonable approximation of simply supported plate boundaries, with the largest difference (7.7%) occurring for mode 2, the f_{21} mode. This difference between measurement and prediction is similar to that obtained in the work by Toyoda et al [68]. Although their geometry and structural supports were different, differences of approximately 10% can be identified in their impedance level diagrams.

In addition to the agreement in the frequencies at which the peaks occur, reasonable agreement can be found in terms of level with differences ranging from 0.4 to 7 dB. This indicates that the approach used to model the damping of the plate is appropriate, which is also confirmed by comparing loss factors from measurements and FDTD obtained using the 3 dB down points in the driving-point mobility in Table 6.4. For the measured data, it was necessary to perform extra measurements employing zoom FFT technique [92] to increase the frequency resolution around the peaks. The agreement between measured and predicted loss factors is reasonable

for the first three modes but has errors of 50% for modes 4 and 5.

Chaigne and Lambourg [93] indicate how internal damping and radiation damping could be incorporated in time-domain models for three basic mechanisms of damping, which they list as thermoelasticity, viscoelasticity and radiation. This potentially has practical application to lightly damped musical instruments such as a cymbal, but it is of limited use to engineering structures such as buildings, aircraft or marine structures where the total loss factor of plates is determined by the sum of the internal losses, radiation losses, losses due to additional damping layers and structural coupling losses. As the latter two losses tend to dominate, the approach of Chaigne and Lambourg was not incorporated, and experimentally-determined values of the damping were incorporated in the model.

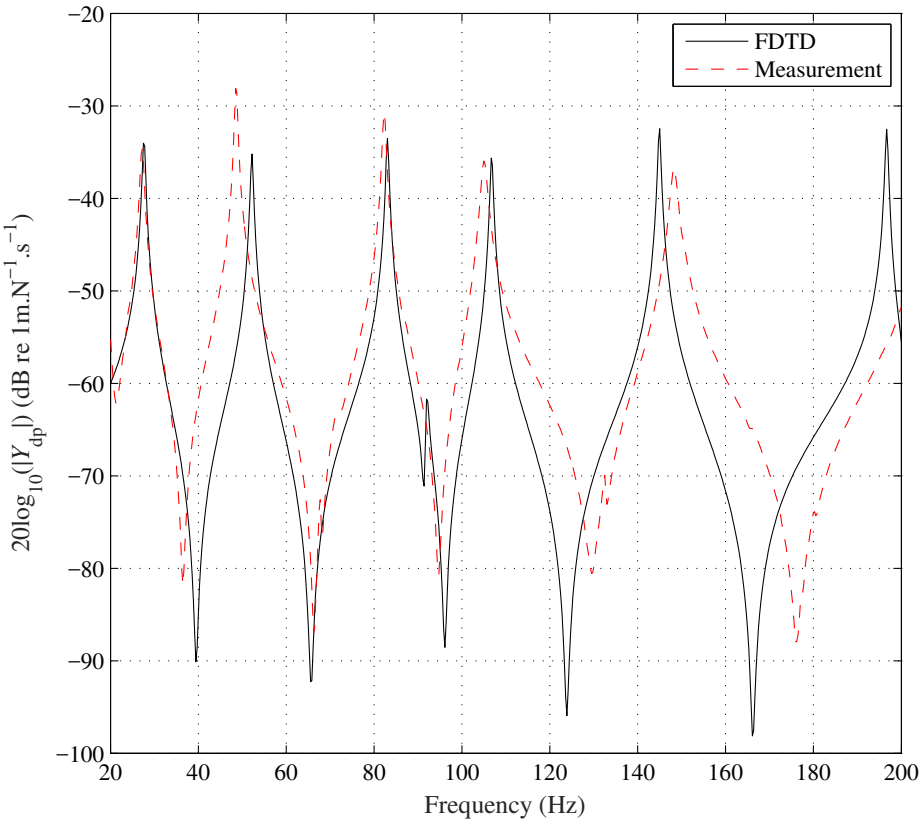

Figure 6.2: Plate - measured and FDTD driving-point mobilities.

Mode	Measured (Hz)	FDTD (Hz)	Difference (%)
1	27.3	27.5	0.9
2	48.5	52.2	7.7
3	82.3	83.0	1.0
4	105.0	106.7	1.6
5	148.3	145.0	-2.2

Table 6.3: Plate - comparison of measured and FDTD eigenfrequencies for the plate.

Mode	Measured (-)	FDTD (-)	Difference (%)
1	0.0269	0.0266	-1.4
2	0.0109	0.0125	15.1
3	0.0075	0.0078	3.8
4	0.0145	0.0066	-54.8
5	0.0112	0.0047	-57.8

Table 6.4: Plate - comparison of measured and FDTD loss factors.

6.4.1 Monitoring of driving-point mobilities

This section covers the details and the results of the measurement of the driving-point accelerance of an aluminium plate placed inside a reverberation chamber. The measured driving-point accelerance data was then converted into driving-point mobility by means of division by $i\omega$. The measurement of accelerance was used to investigate the modal loss factors of the plate and to monitor the power input to the electrodynamic shaker or the integrity of the plate supports throughout all the measurements. Such monitoring activities were needed to ensure that the experimental conditions remained constant. Figure 6.3 shows an overlay of all the driving-point mobilities that were captured throughout all the measurements. These show that the support conditions of the plate did not vary significantly over time because the level of the driving-point mobilities remained constant (within 0.5 dB) throughout the measurements and the corresponding resonance frequencies changed by less than 1 Hz.

Zoom FFT analysis was carried out in order to measure the loss factors associated with the modal peaks. Standard FFT was used to monitor the power input to the plate. Beeswax was used to fix the accelerometer on top of the aluminium plate.

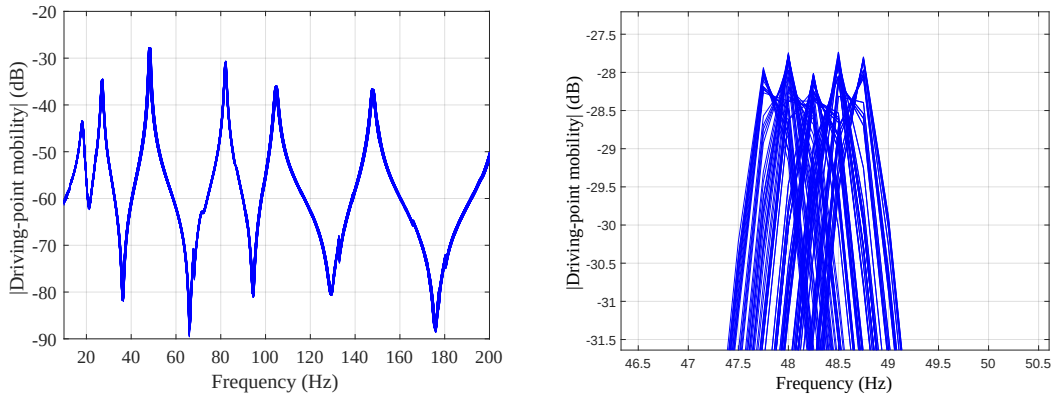

Figure 6.3: Overlay of the magnitude of measured driving-point mobilities: 0 Hz-200 Hz range (left) 44 Hz-53 Hz range (right).

6.5 Vibroacoustic response of the room due to point-excited aluminium plate

This section compares the results obtained in the FDTD vibroacoustic model to the corresponding measurements carried out in the small reverberation chamber. The comparison is carried out in terms of measured and predicted transfer functions and pressure-to-force transfer function contour plots.

6.5.1 Comparison of measured and predicted transfer functions

To assess the ability of FDTD to predict the spatial variation in sound pressure in the room, a comparison is now made between measured and FDTD magnitudes of the transfer functions. The transfer functions for all grid points in the vertical and horizontal grids are shown in Figures. 6.4 a) and b) and 6.4 c) and d) respectively. Peaks in these transfer functions correspond to global resonances of the plate-cavity system for which there are fifteen peaks below 200 Hz. For the first six of these global resonances, contour plots are shown in Figures 6.5 to 6.19 with the outline of the plate indicated using solid black lines and the source location indicated using a black cross. These plots allow comparisons of measurements and FDTD for the horizontal and vertical grids.

6.5.2 Comparison of measured and predicted contour plots

This section compares the predicted and measured transfer function contour plots. The discussion is limited to frequencies below 200 Hz since this corresponds to the highest frequency of the measurements.

At frequencies corresponding to plate modes f_{11} and f_{12} that occur below the lowest room mode f_{010}, the contour plots in Figures 6.5 and 6.6 show close agreement

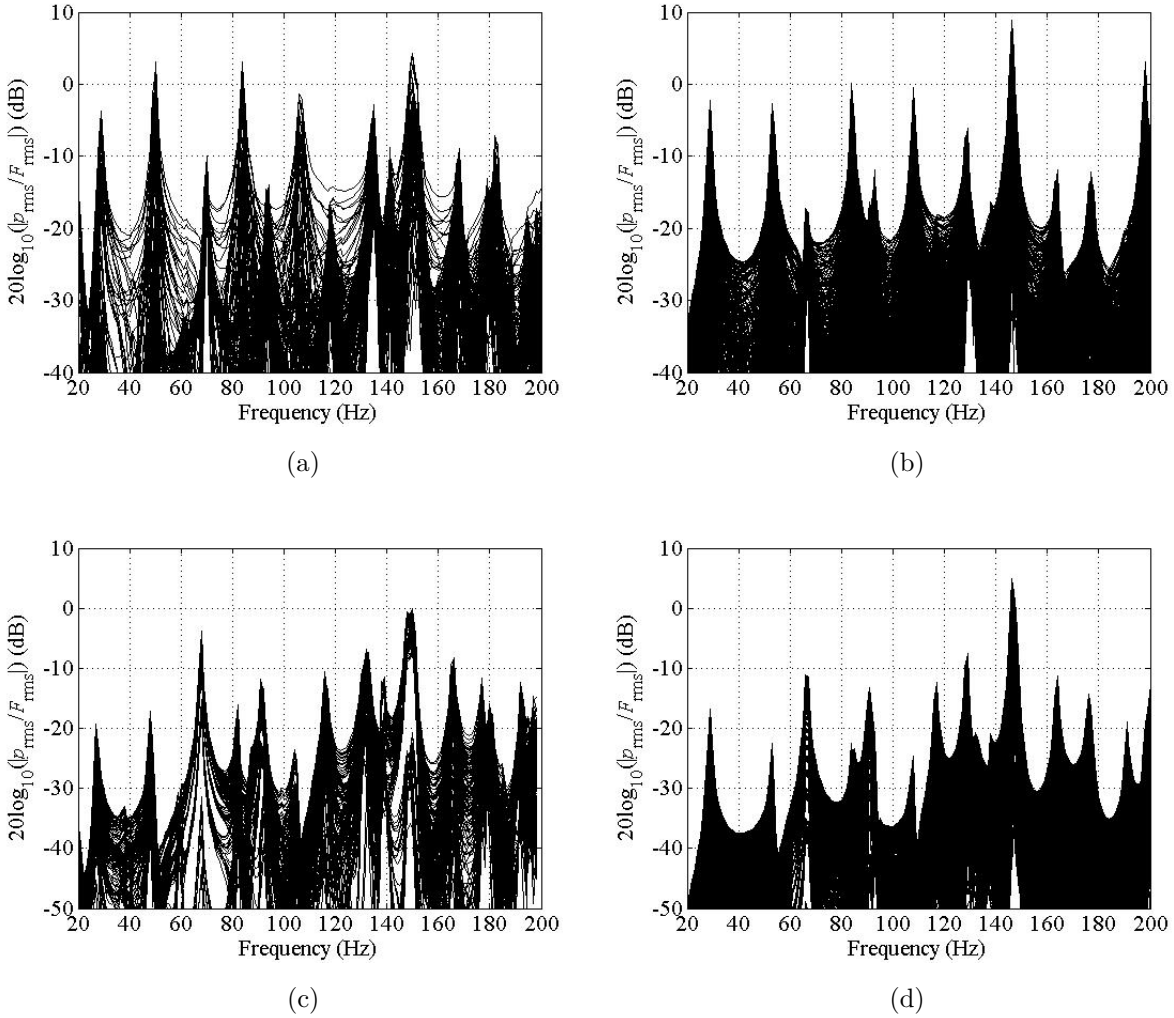

Figure 6.4: Transfer functions corresponding to all grid points in the vertical grid - (a) measured and (b) FDTD - and horizontal grid - (c) measured and (d) FDTD - overlaid.

between measurements and FDTD in terms of the spatial variation with particularly close agreement in Figure 6.5(a,b). For the horizontal grid, the sound pressure field corresponds to the vibration field of the plate mode. The results for the vertical grid show that the sound pressure level varies by up to 40 dB over the grid surface. This demonstrates that it is inappropriate to assume a uniform sound field (pressure zone) below the first room mode in a small acoustic cavity which is excited by a plate. Figure 6.7 shows the spatial variation above the lowest room mode at a frequency close to the lowest axial mode f_{001} (vertical direction) and in between plate modes f_{12} and f_{21}. In terms of the spatial variation in the horizontal and vertical grids, there is close agreement between measurements and FDTD, with the vertical grid showing the expected variation in sound pressure corresponding to the lowest axial mode in the vertical direction. However, FDTD underestimates the level by 8 dB for both grids. This issue in predicting the correct level has been observed to occur at other frequencies where there is a room mode that is in between plate modes where at least one of the plate modes f_{pq} has a p or q as an even number. This could be due to cancellation in the radiated field that occurs with the unbaffled plate in the FDTD model but does not occur exactly in the experimental setup due to the existence of the metal frame that supports the plate. The spatial variation in the horizontal grid is characterised by low sound pressure levels over the surface of the plate because in the vicinity of the plate it prevents the establishment of the mode shape for the lowest axial mode. Figure 6.8 shows the response at 82 Hz near the f_{12} plate mode which is inbetween room modes f_{001} and f_{011}. There is close agreement between measurements and FDTD for the horizontal grid in terms of the spatial variation and levels. However, there is less agreement for the vertical grid, particularly at grid positions that are at a higher elevation than the plate. Figure 6.9 shows close agreement between measurements and FDTD for the horizontal and vertical grids for the response at 92 Hz which is close to the lowest tangential room mode f_{011} and in between excited plate modes f_{21} and f_{22}. There is similarly close agreement in Figure 6.10 at 104 Hz which is close to the f_{22} plate mode and inbetween room modes f_{011} and f_{110}.

A possible reason for the differences in the results is due to the discrepancies in

the geometries of the measurements and the idealised numerical FDTD model. The small reverberation chamber is not a perfect cuboid and includes a number of features not included in the FDTD model such as a small observation window and a heavy steel door. Another potential source of error could be that of microphone positioning, especially when the measurement grid is located in a zone of high sound pressure gradient. However, positional errors seem unlikely because close agreement has been obtained for modes where very pronounced pressure gradients are visible, such as those corresponding to Figures 6.17 and 6.18. In addition, the boundary conditions of the real plate are only an approximation to a simply supported condition, and, at higher frequencies, this approximation could lead to significant deviations from the FDTD predictions. At frequencies above 190Hz the significant discrepancies obtained in terms of mode shapes and level along the horizontal plane are likely to be caused by the coarse measurement grid.

A comparison between the measured and predicted contour plots is summarised in Table 6.5, where the agreement in terms of level, shape and proximity to analytical room and plate modes is indicated. This comparison is primarily carried out in subjective terms as no exact numerical indicator or threshold is used to categorise the level of agreement. Where there is a lack of agreement in either the horizontal or the vertical plane for the same mode, a red coloured "H" (horizontal) or "V" (vertical) is used. Conversely, a green "H" or "V" indicates agreement in the horizontal or the vertical planes, respectively.

6.5.3 Level differences between predicted and measured modes

Tables 6.6 and 6.7 show the maximum level detected in each FDTD/measured contour plot for the horizontal and vertical grids, respectively. It also shows the corresponding average level, obtained using equation 6.2:

$$\overline{L} = 10\log_{10}\left(\frac{\sum_{i}^{N} 10^{L_i/10}}{N}\right) \tag{6.2}$$

n	Frequency (Hz)	Shape agreement	Level agreement	Frequency close to room mode	Frequency close to plate mode
1	27/28	Yes	Yes	No (below f_{010})	Yes (f_{11})
2	48/52	Yes	Yes	No (below f_{010})	Yes (f_{21})
3	68/65	Yes	H V	Yes (f_{001})	No (f_{21}–f_{12})
4	82/83	H V	Yes	No (f_{001}–f_{101})	Yes (f_{12})
5	92/90	Yes	Yes	Yes (f_{011})	Yes (f_{31}, FDTD only)
6	104/107	Yes	Yes	No (f_{011}–f_{110})	Yes (f_{22})
7	116/116	Yes	Yes	Yes (f_{101})	No (f_{22}–f_{41})
8	131/131	H V	H V	Yes (f_{111})	No (f_{22}–f_{41})
9	133/128	H V	Yes	Yes (f_{111})	No (f_{22}–f_{41})
10	139/137	H V	H V	Yes (f_{021}–f_{002})	No (f_{22}–f_{41})
11	148/145	Yes	H V	No (f_{002}–f_{012})	Yes (f_{41})
12	150/147	Yes	Yes	Yes (f_{012})	Yes (f_{41})
13	166/163	Yes	Yes	Yes (f_{121}–f_{102})	No (f_{41}–f_{42})
14	177/175	Yes	Yes	Yes (f_{112})	No (f_{41}–f_{42})
15	193/190	H V	H V	Yes (f_{031})	Yes (f_{42}, FDTD only)

Table 6.5: Evaluation of the agreement between measured and predicted mode shapes and transfer function levels.

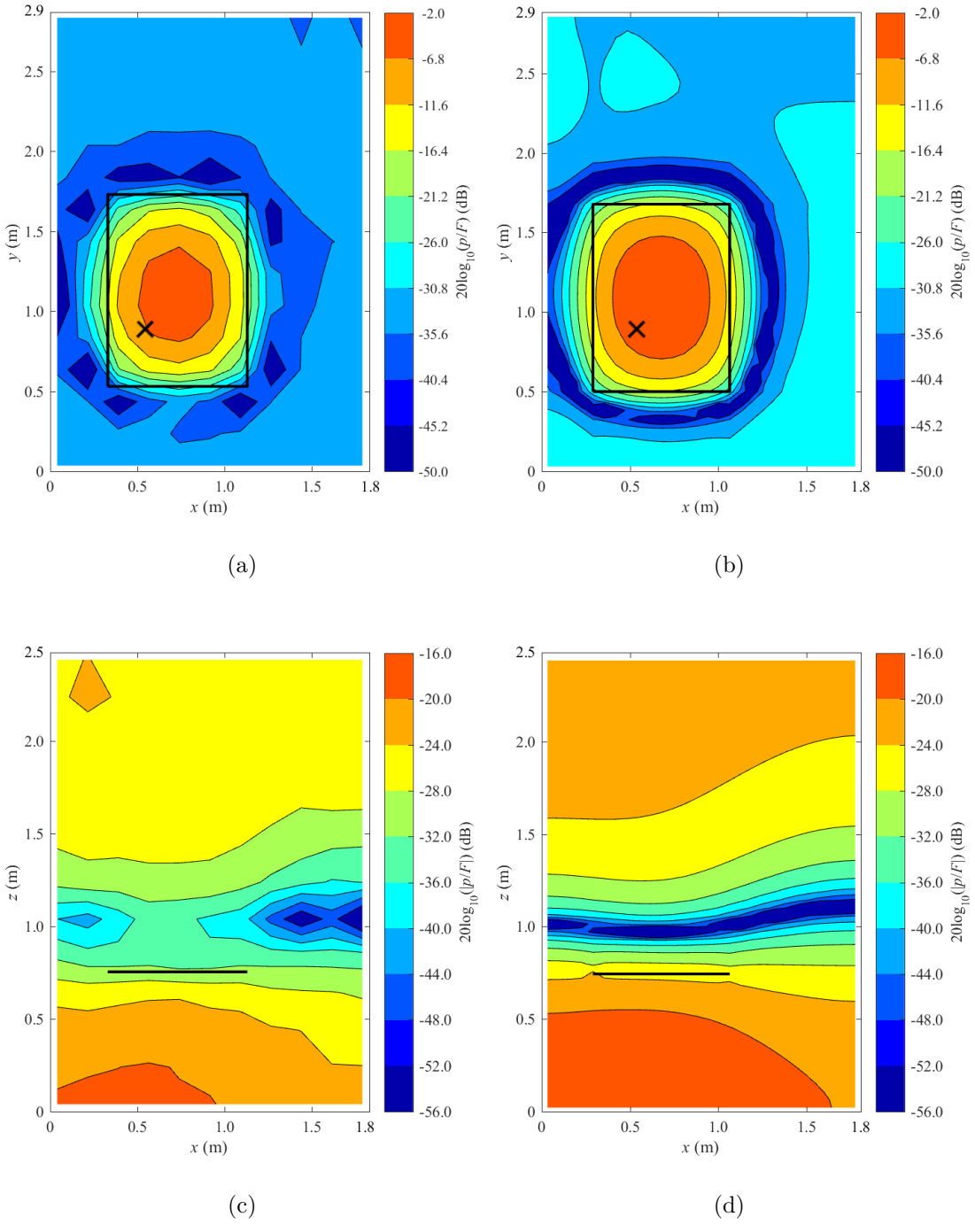

Figure 6.5: Transfer functions - Measured (27 Hz, left column) and FDTD (28 Hz, right column) for (a,b) horizontal grid and (c,d) vertical grid.

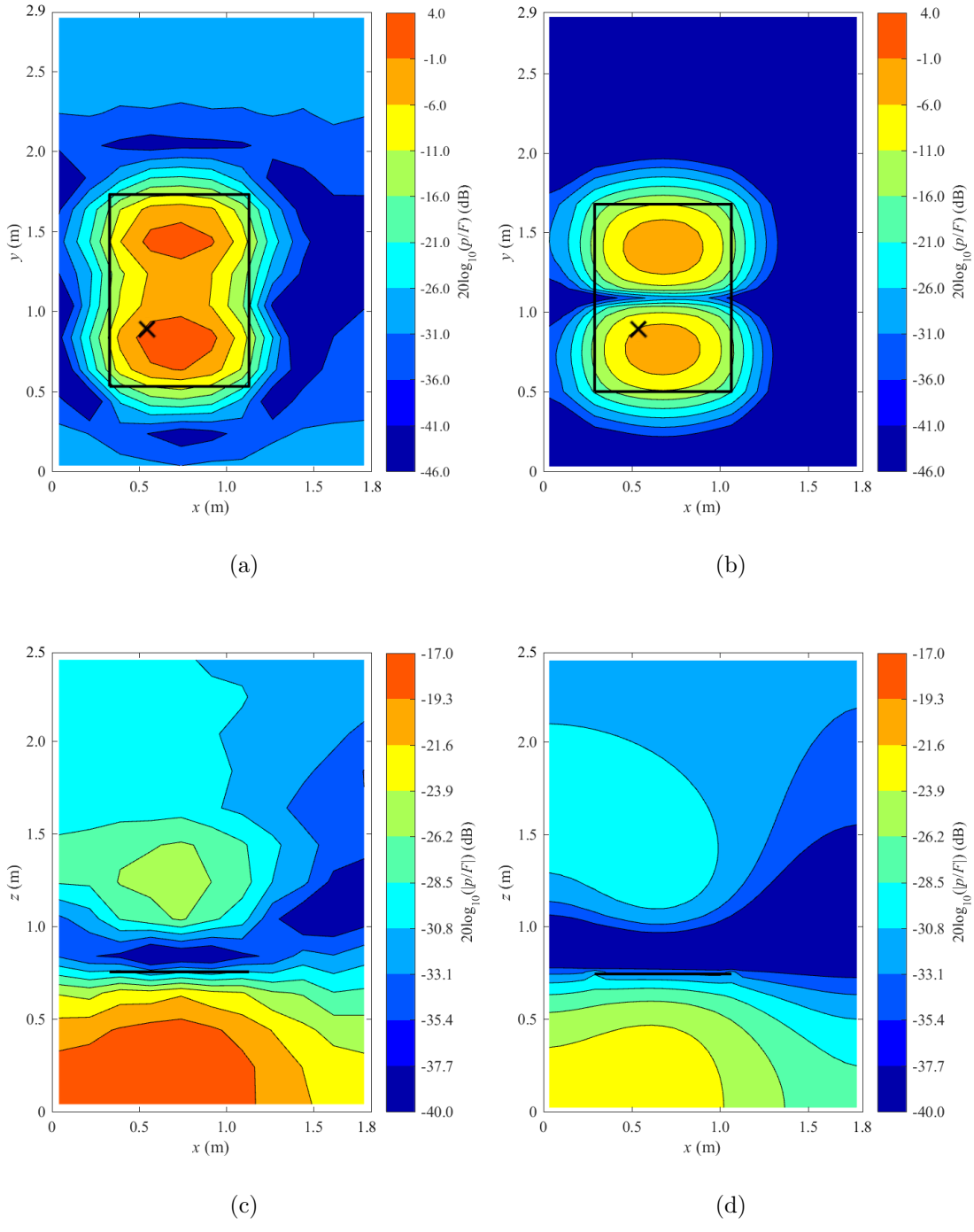

Figure 6.6: Transfer functions - Measured (48 Hz, left column) and FDTD (52 Hz, right column) for (a,b) horizontal grid and (c,d) vertical grid.

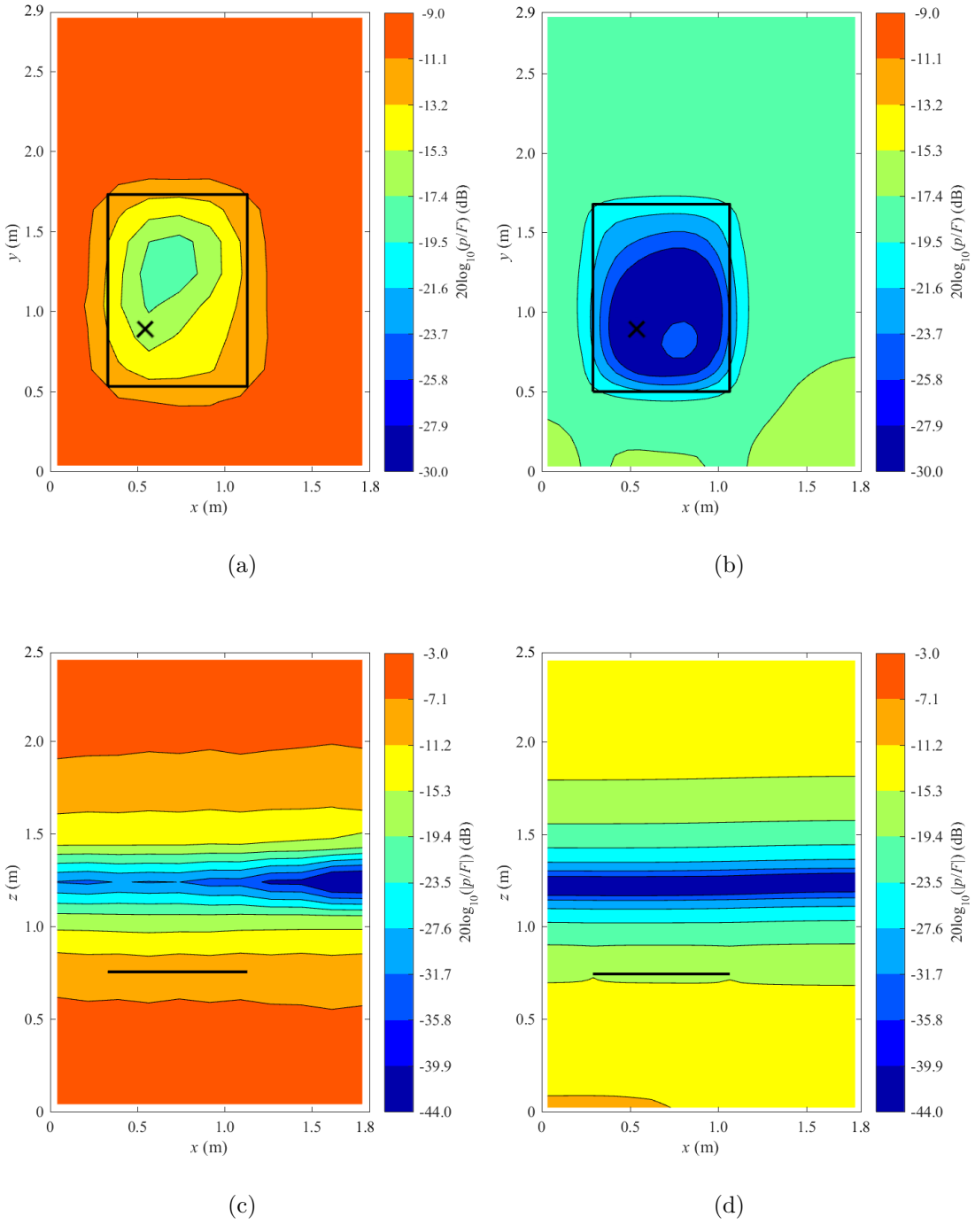

Figure 6.7: Transfer functions - Measured (68 Hz, left column) and FDTD (65 Hz, right column) for (a,b) horizontal grid and (c,d) vertical grid.

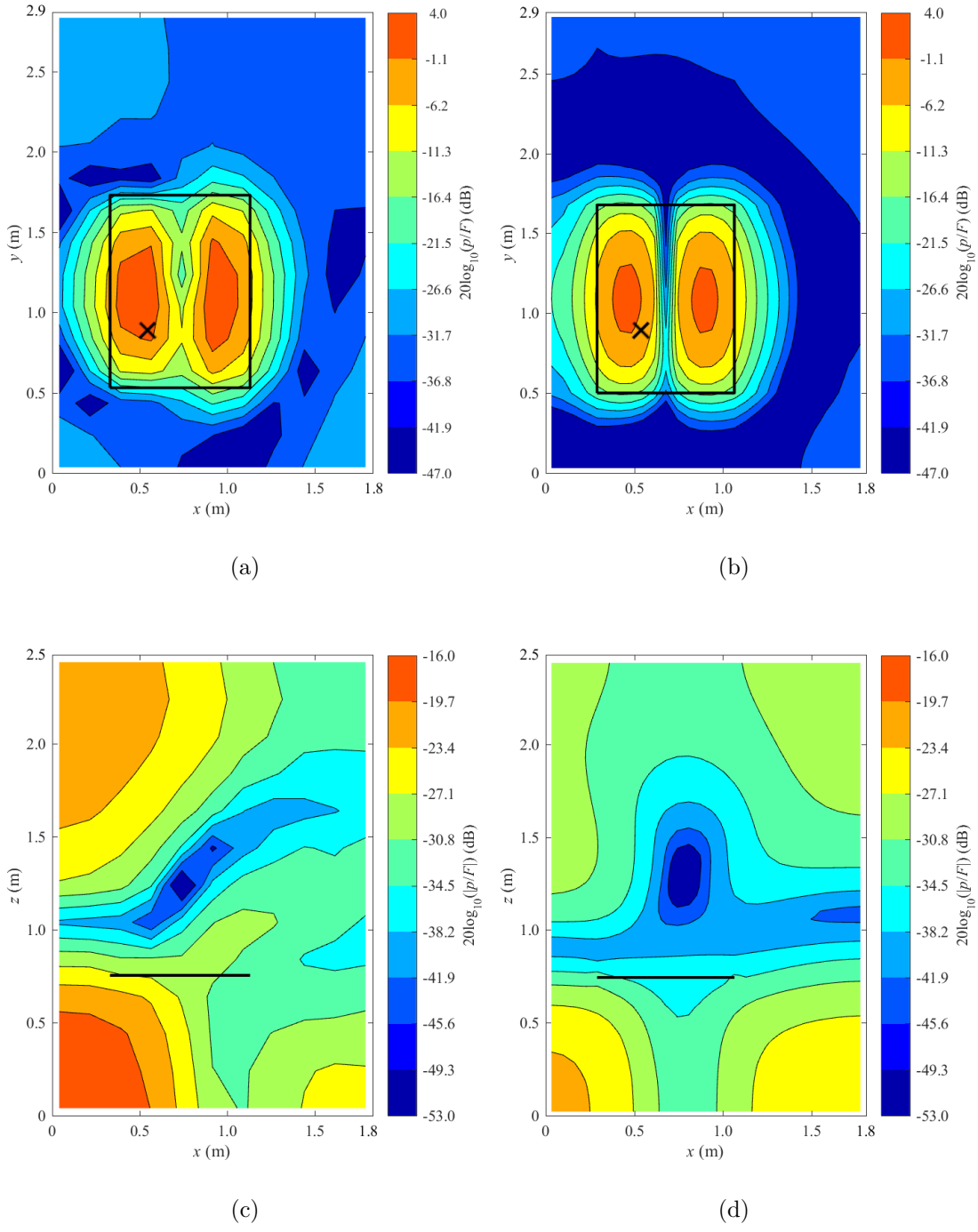

Figure 6.8: Transfer functions - Measured (82 Hz, left column) and FDTD (83 Hz, right column) for (a,b) horizontal grid and (c,d) vertical grid.

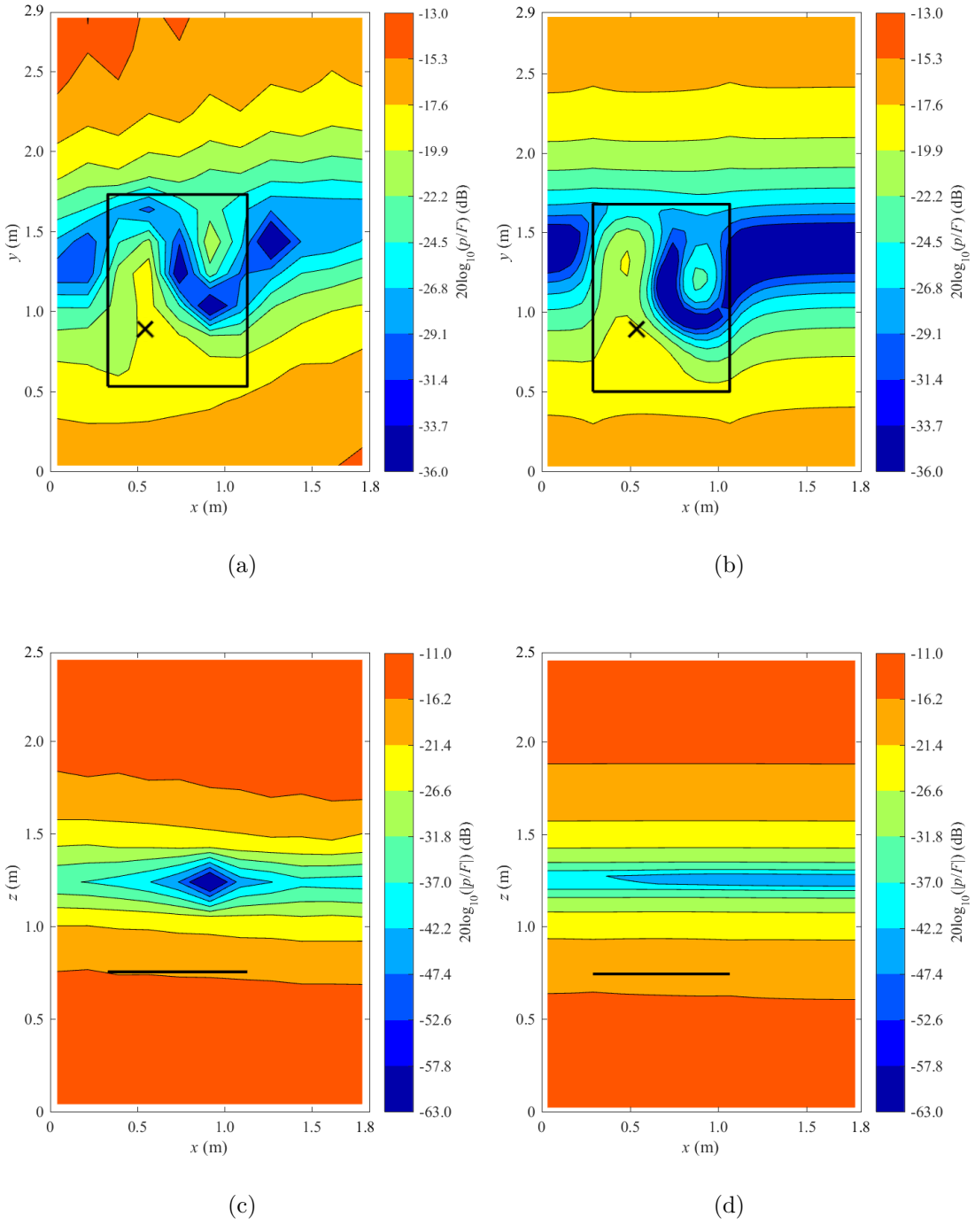

Figure 6.9: Transfer functions - Measured (92 Hz, left column) and FDTD (90 Hz, right column) for (a,b) horizontal grid and (c,d) vertical grid.

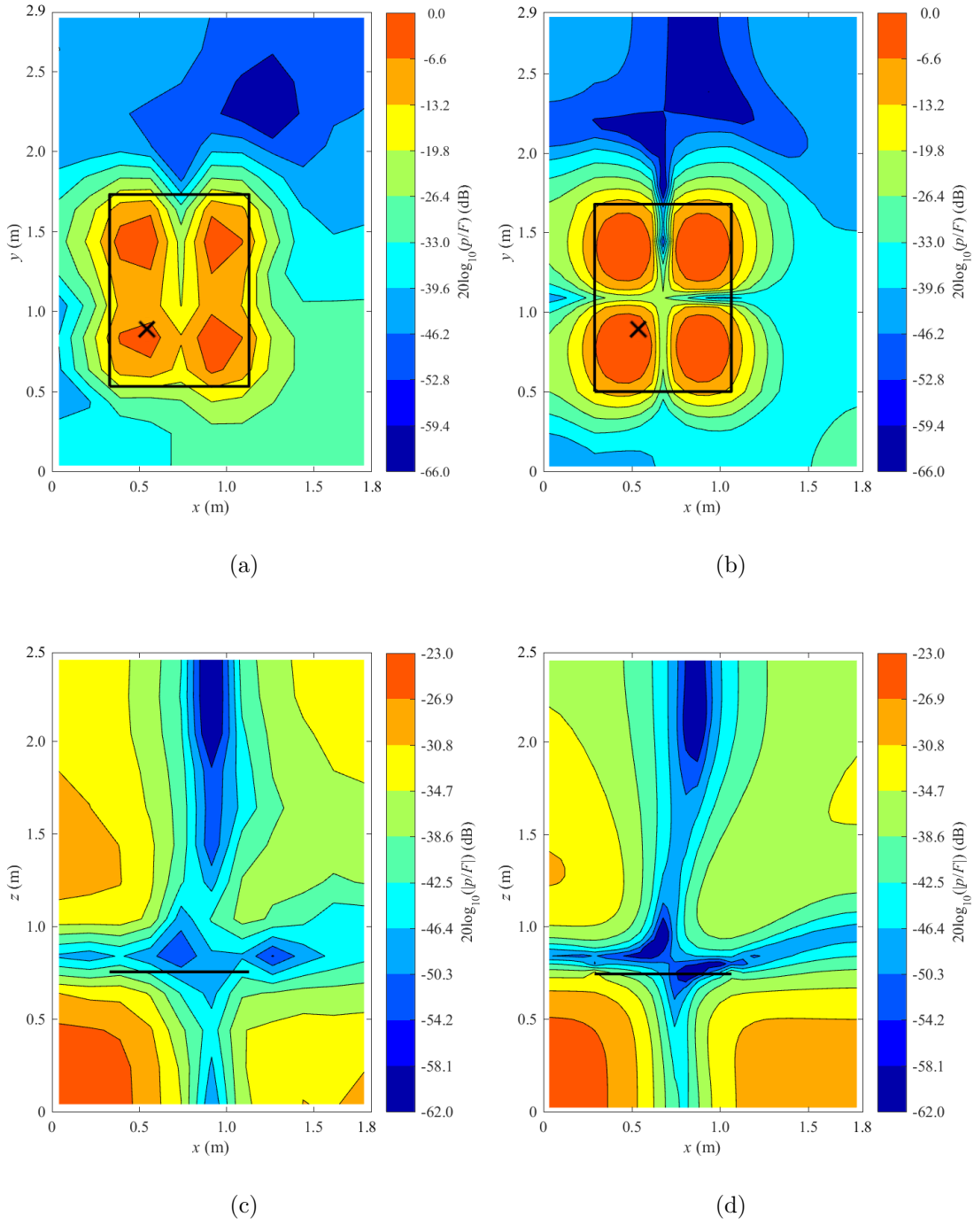

Figure 6.10: Transfer functions - Measured (104 Hz, left column) and FDTD (107 Hz, right column) for (a,b) horizontal grid and (c,d) vertical grid.

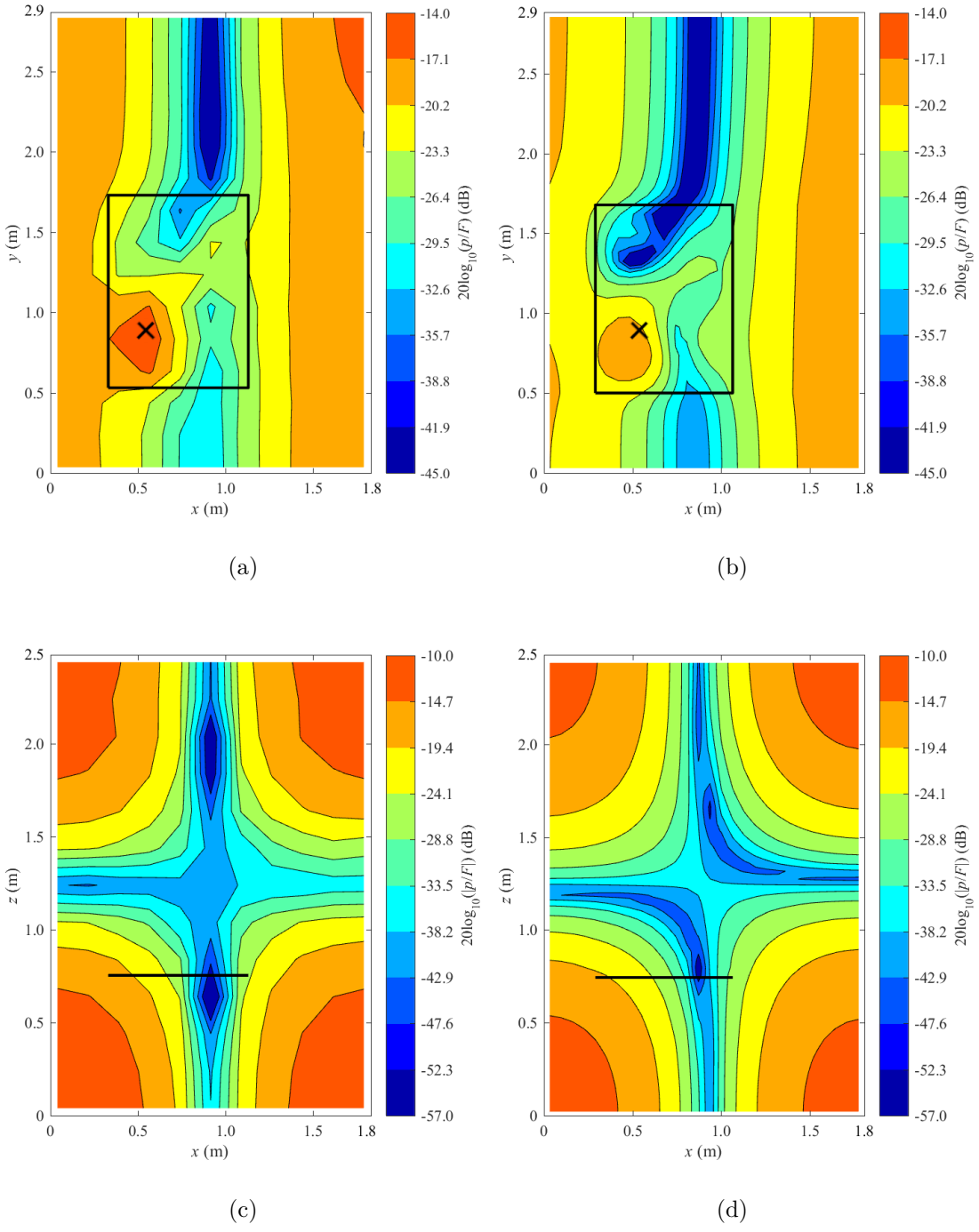

Figure 6.11: Transfer functions - Measured (116 Hz, left column) and FDTD (116 Hz, right column) for (a,b) horizontal grid and (c,d) vertical grid.

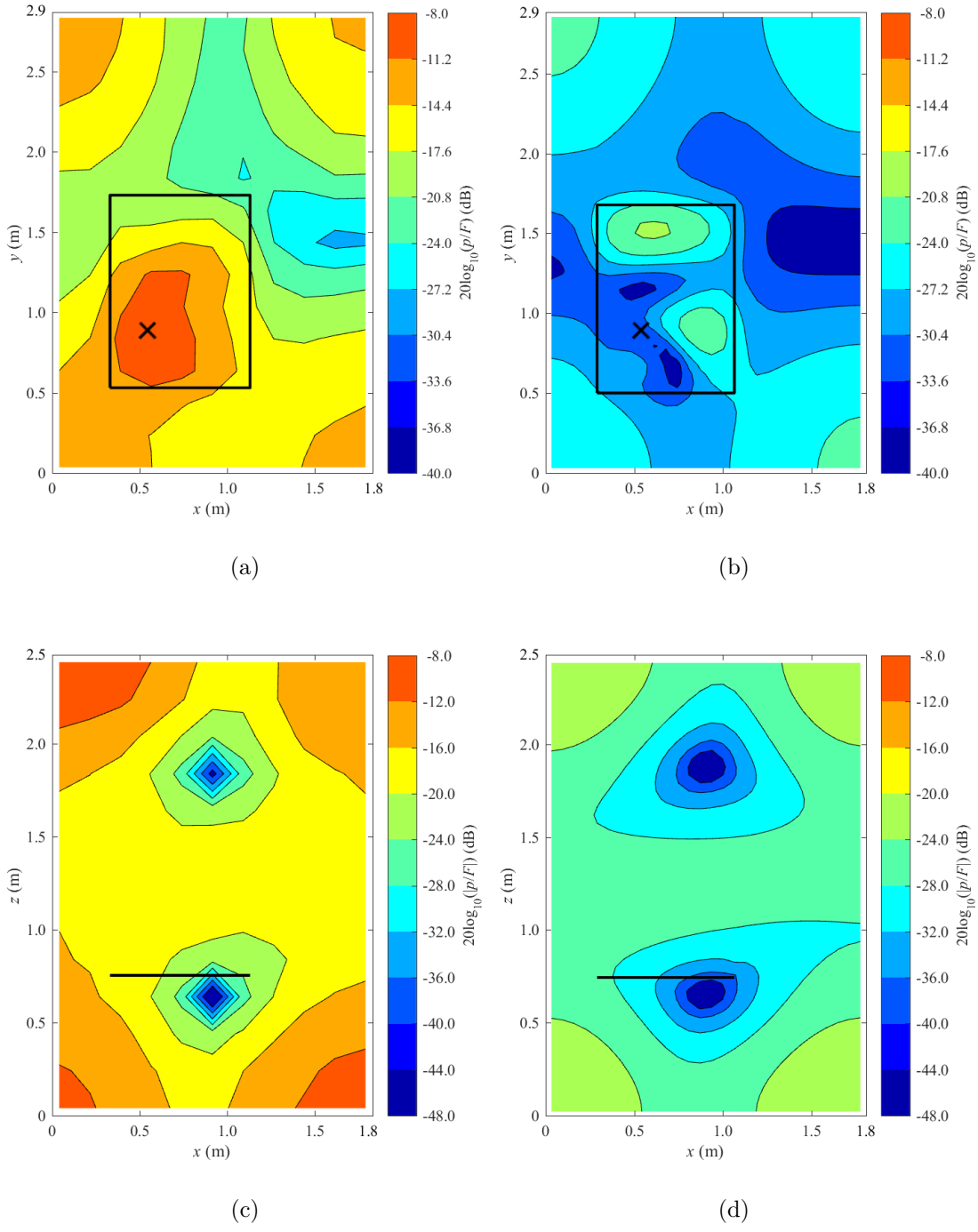

Figure 6.12: Transfer functions - Measured (131 Hz, left column) and FDTD (131 Hz, right column) for (a,b) horizontal grid and (c,d) vertical grid.

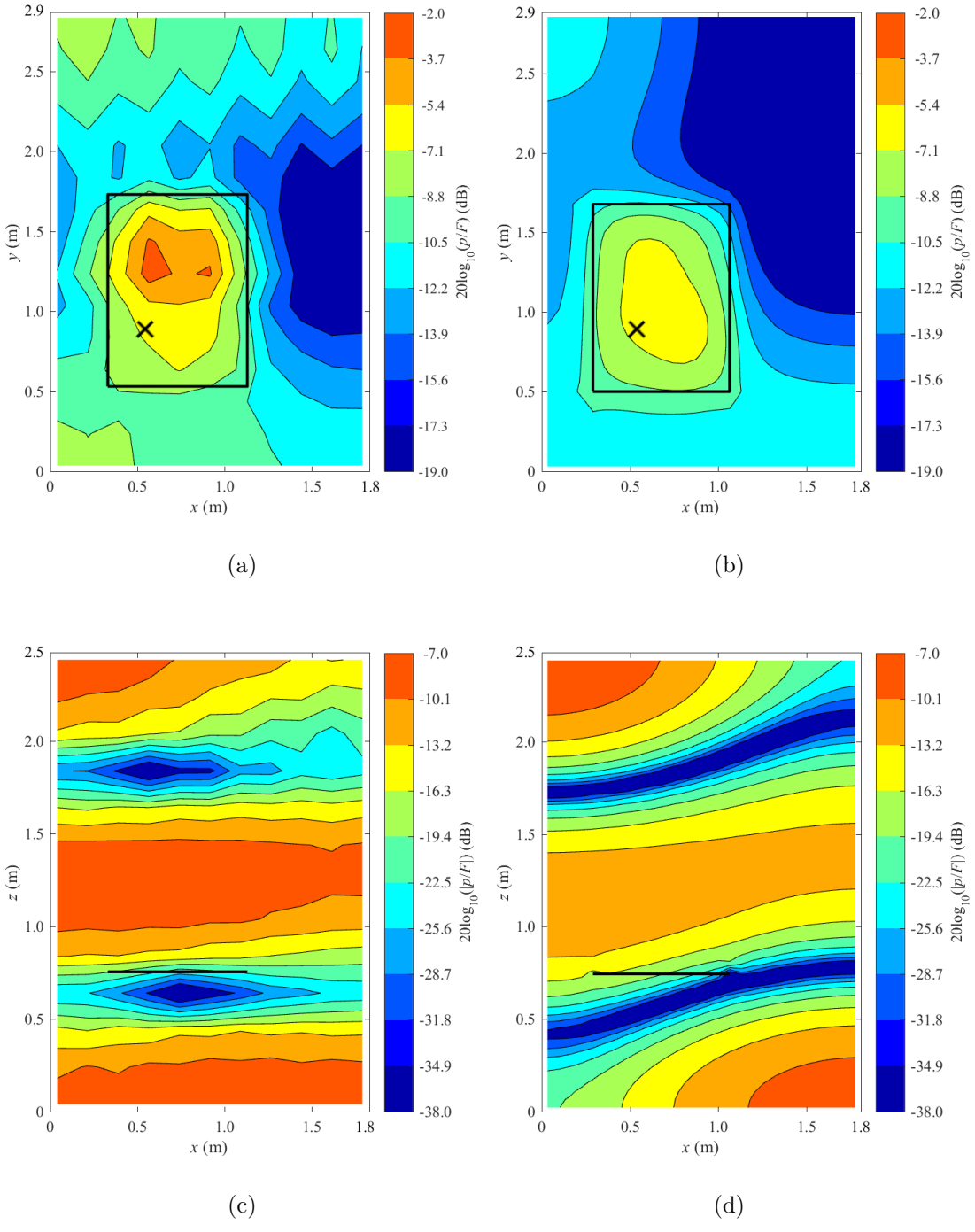

Figure 6.13: Transfer functions - Measured (133 Hz, left column) and FDTD (128 Hz, right column) for (a,b) horizontal grid and (c,d) vertical grid.

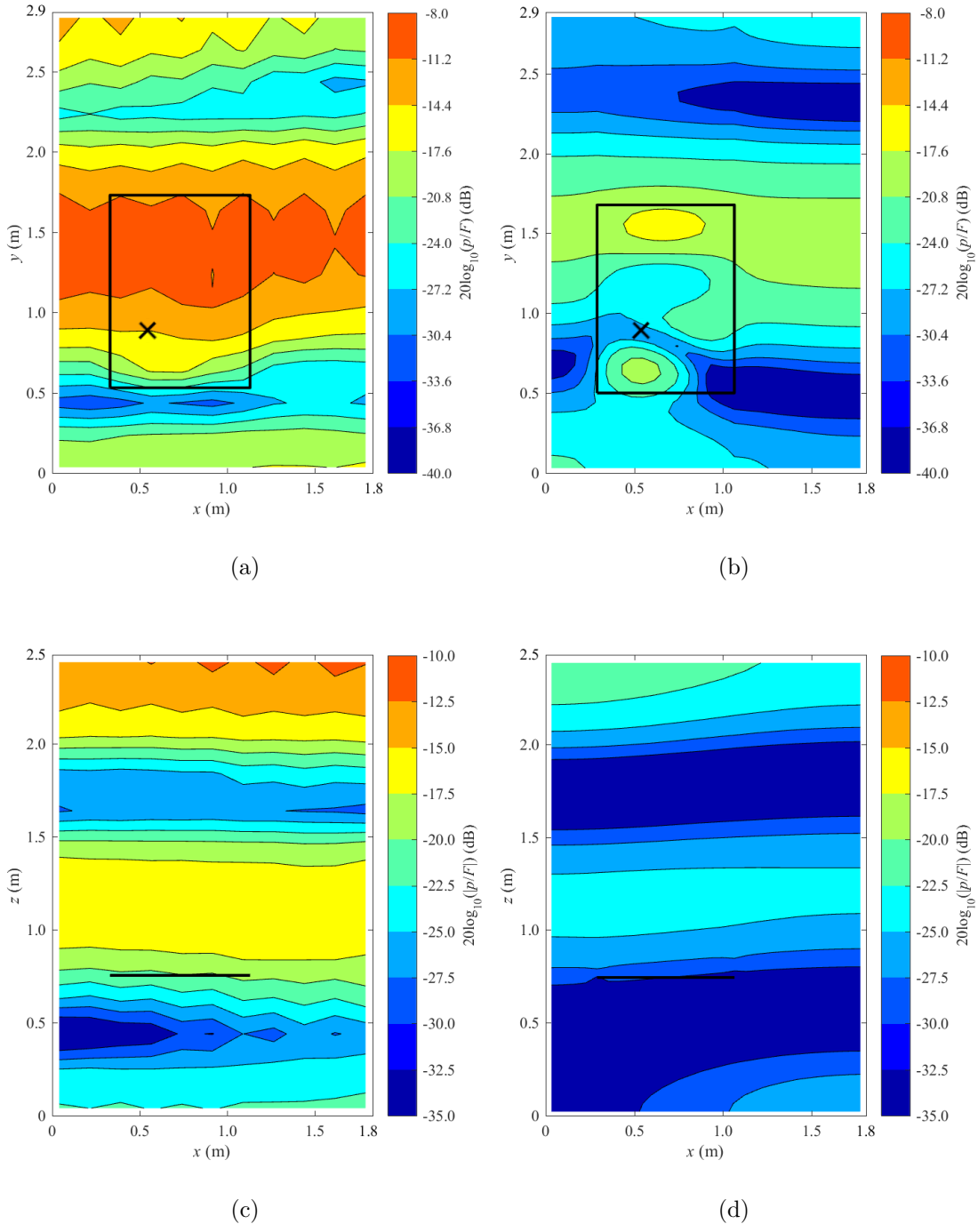

Figure 6.14: Transfer functions - Measured (139 Hz, left column) and FDTD (137 Hz, right column) for (a,b) horizontal grid and (c,d) vertical grid.

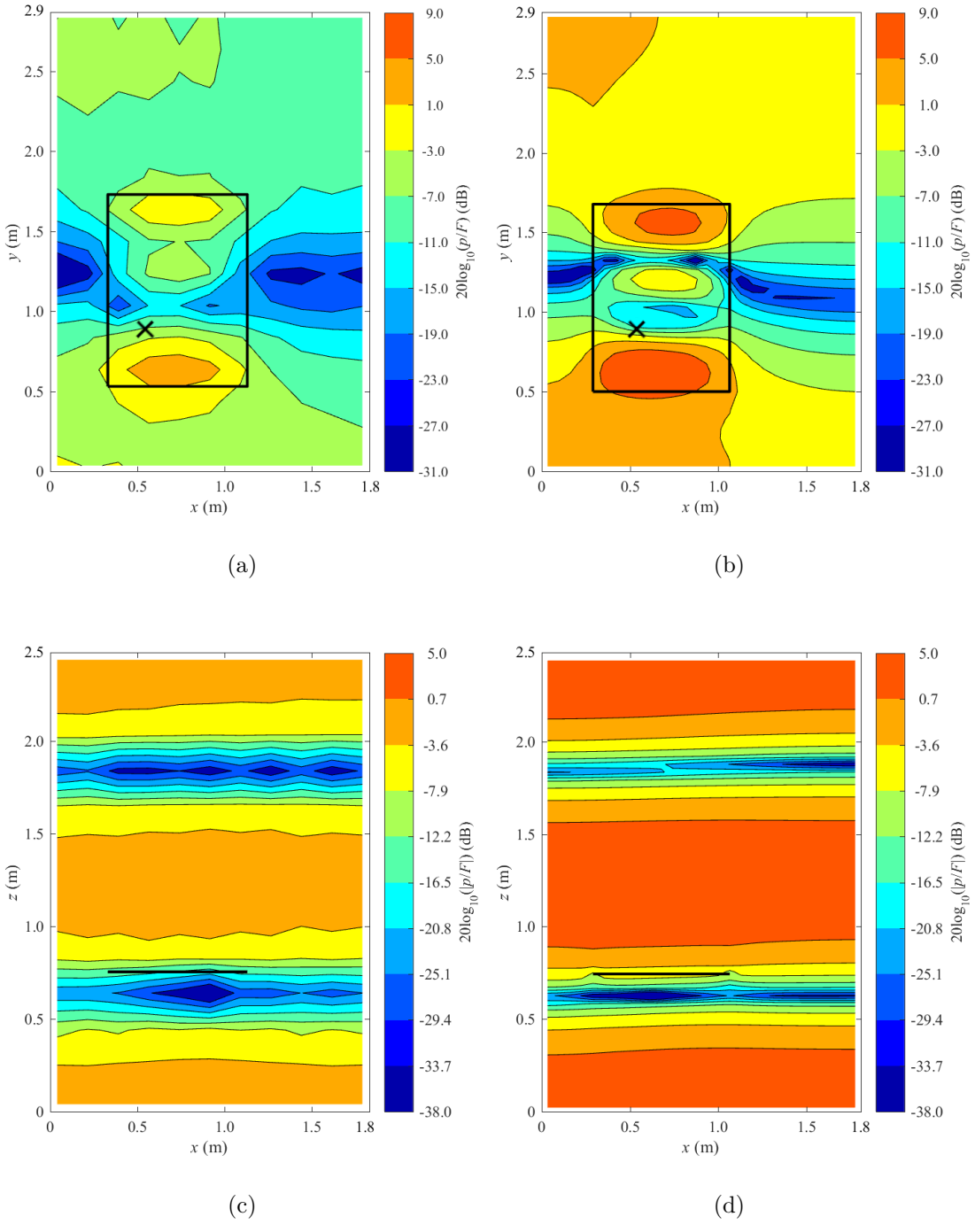

Figure 6.15: Transfer functions - Measured (148 Hz, left column) and FDTD (145 Hz, right column) for (a,b) horizontal grid and (c,d) vertical grid.

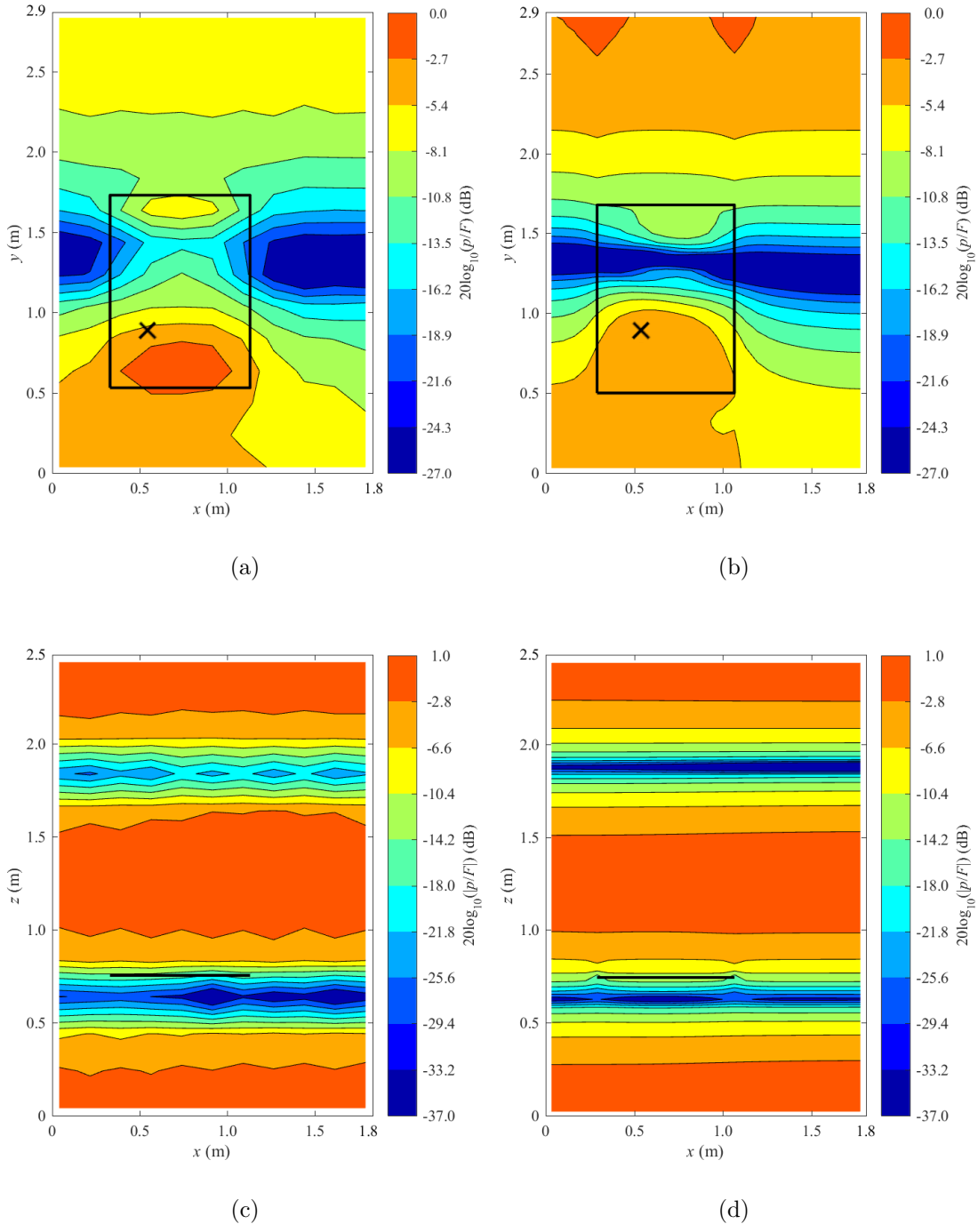

Figure 6.16: Transfer functions - Measured (150 Hz, left column) and FDTD (147 Hz, right column) for (a,b) horizontal grid and (c,d) vertical grid.

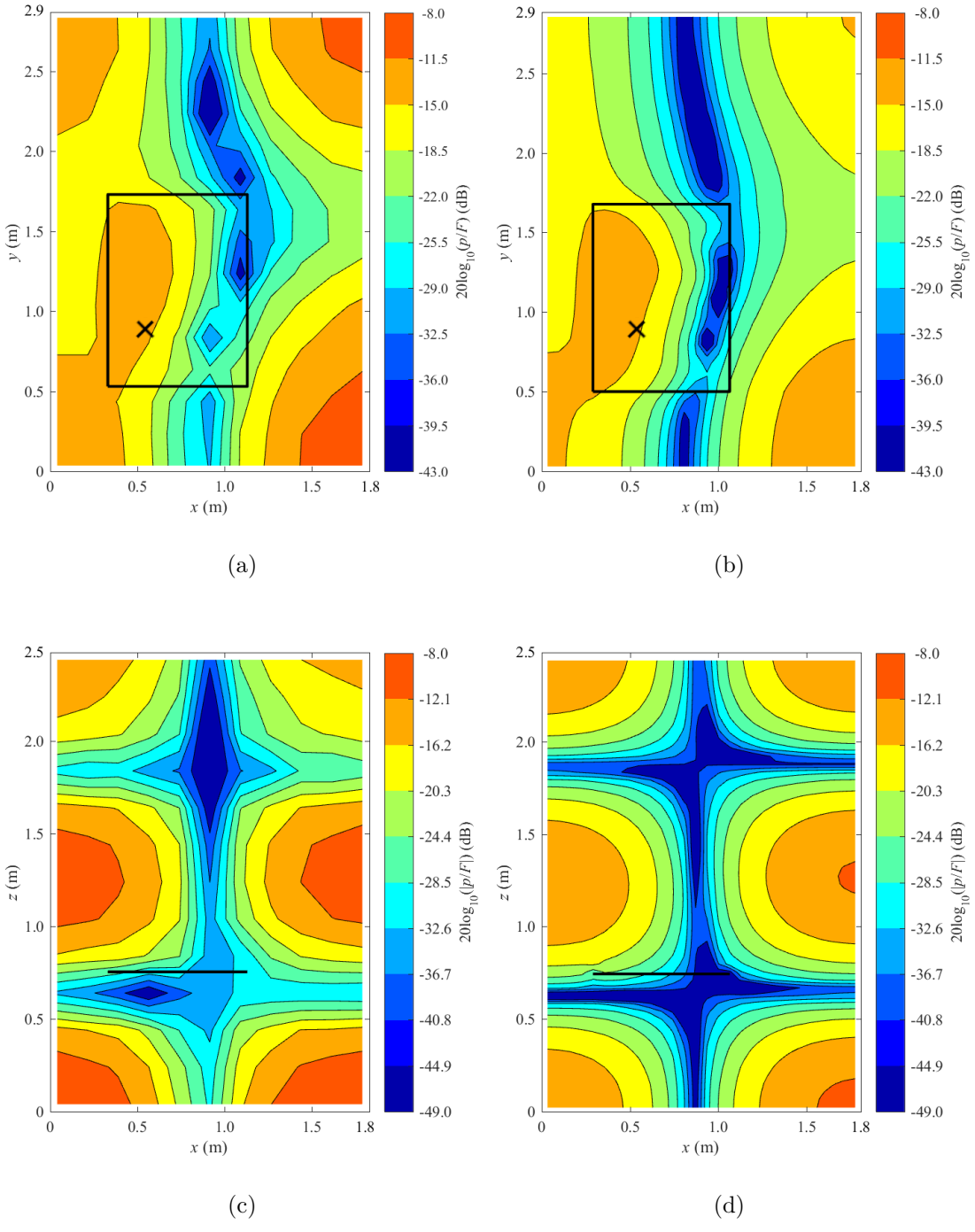

Figure 6.17: Transfer functions - Measured (166 Hz, left column) and FDTD (163 Hz, right column) for (a,b) horizontal grid and (c,d) vertical grid.

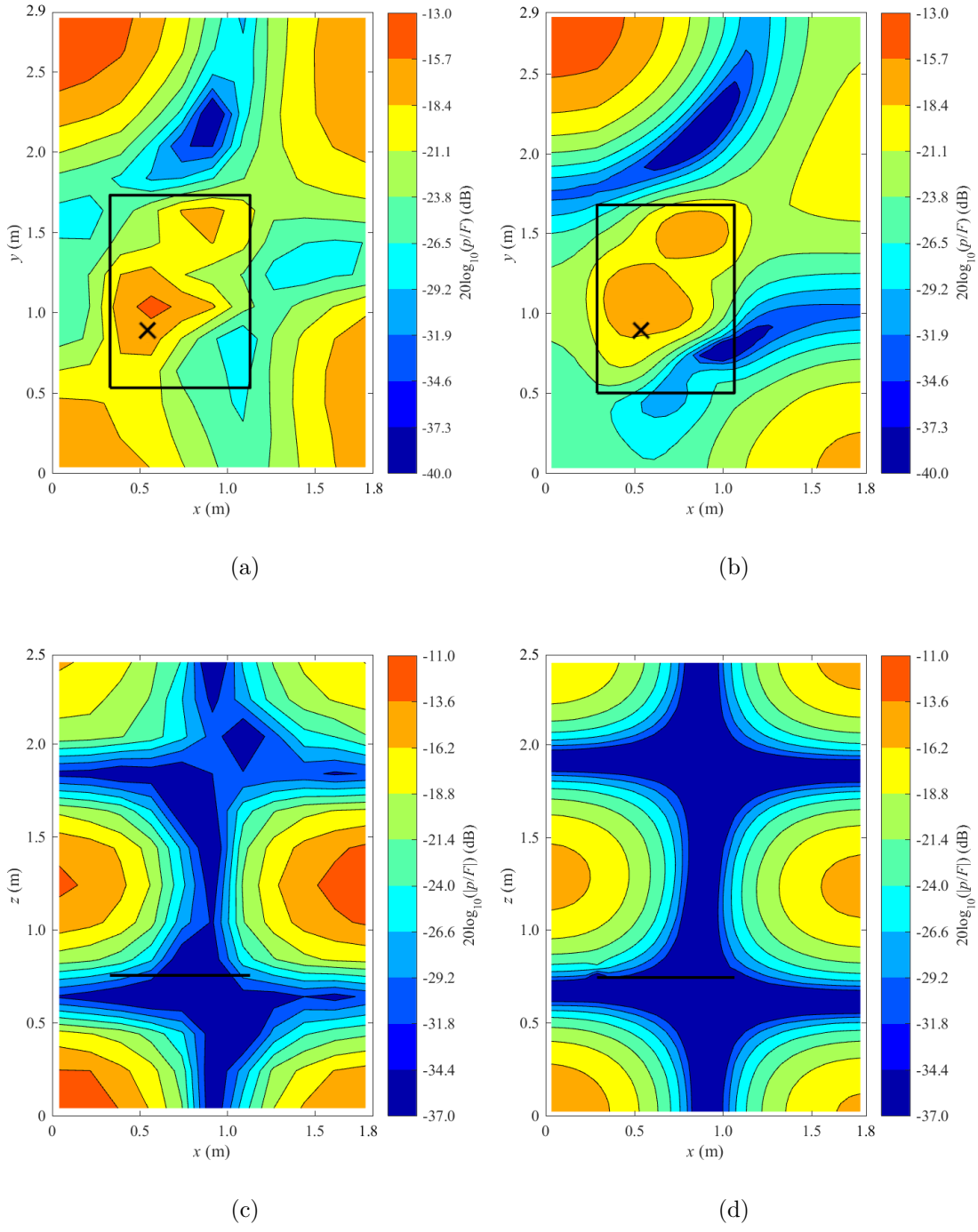

Figure 6.18: Transfer functions - Measured (177 Hz, left column) and FDTD (175 Hz, right column) for (a,b) horizontal grid and (c,d) vertical grid.

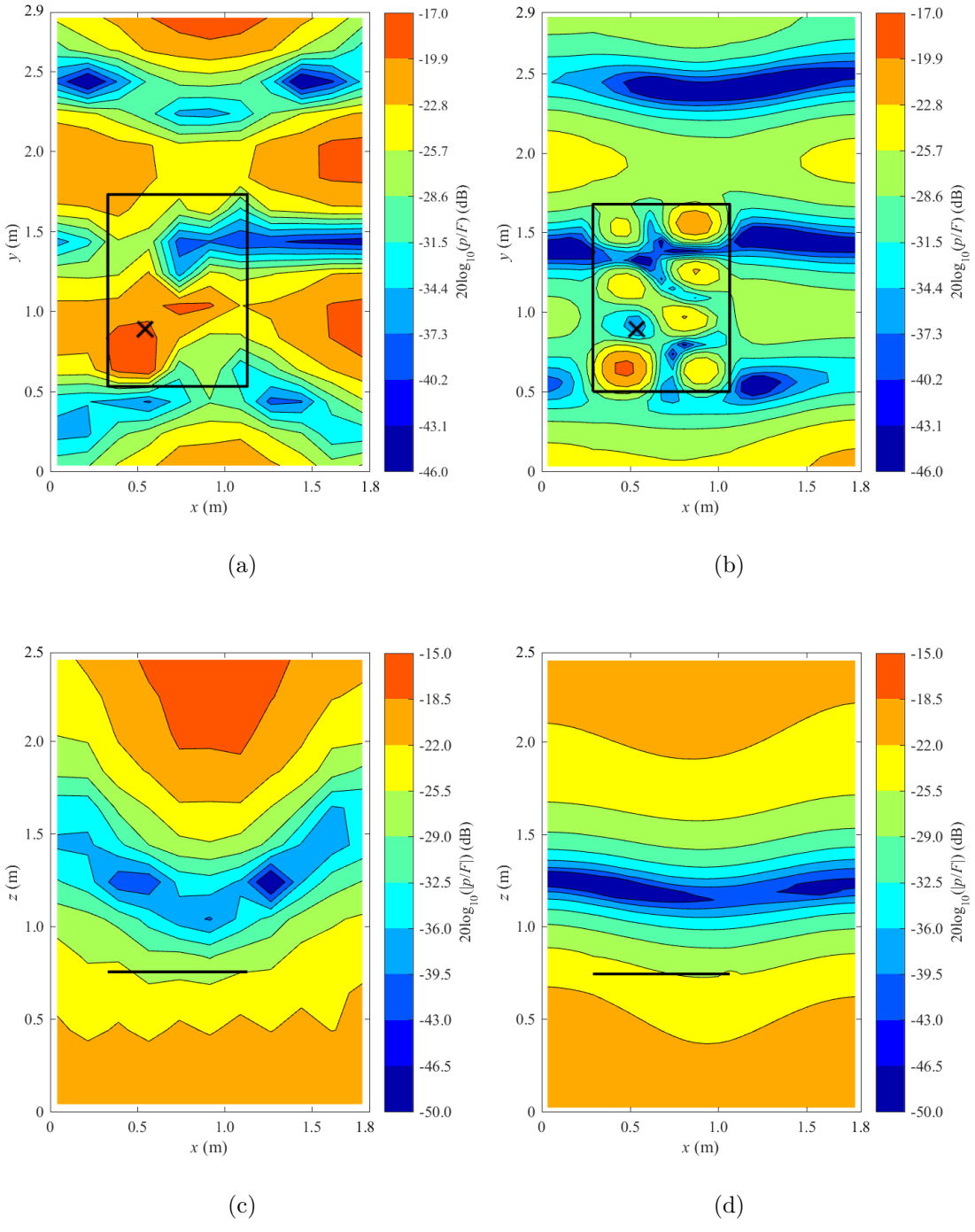

Figure 6.19: Transfer functions - Measured (193 Hz, left column) and FDTD (190 Hz, right column) for (a,b) horizontal grid and (c,d) vertical grid.

n	Measured			FDTD		
	Frequency (Hz)	Max. Level (dB)	Avg. Level (dB)	Frequency (Hz)	Max. Level (dB)	Avg. Level (dB)
1	27	-3.7	-23.5	28	-2.2	-20.3
2	48	3.2	-17.1	52	-2.7	-21.8
3	68	-9.9	-11	65	-17.2	-19.2
4	82	3.1	-16.8	83	0.4	-18.6
5	92	-13.9	-19.1	90	-16.3	-20.3
6	104	-1.3	-21.1	107	-0.2	-19.3
7	116	-14.4	-20.7	116	-17.8	-22.9
8	133	-2.9	-16.2	131	-20.3	-27.5
9	131	-8.6	-10.3	128	-6	-12.6
10	139	-8.8	-15.7	137	-16.3	-25.1
11	148	5	-7.1	145	9	-0.8
12	150	-0.2	-8	147	-2.4	-6.9
13	166	-8.9	-16.7	163	-11.8	-18.7
14	177	-13.1	-20.5	175	-13.9	-22.5
15	193	-17	-24.6	190	-19.3	-28.9

Table 6.6: Maximum transfer function values for the horizontal grid.

In order to indicate the accuracy after spatial-averaging, Figure 6.20 shows differences between the measured and FDTD spatial-average magnitude of the transfer functions for all fifteen peaks that occur below 200 Hz. This scatter plot indicates that 60% of the data points are within ±3dB, and that 76% are within ±6 dB.

6.5.4 Validity of the frequency response measurements

The validity of the frequency response function was checked using the coherence function. Considering $x(t)$ as the input signal and $y(t)$ as the output signal in the

n	Measured			FDTD		
	Frequency (Hz)	Max. Level (dB)	Avg. Level (dB)	Frequency (Hz)	Max. Level (dB)	Avg. Level (dB)
1	27	-19.3	-25.8	28	-16.8	-23.5
2	48	-17.1	-26.2	52	-22.4	-30.1
3	68	-3.7	-8	65	-11.2	-15.4
4	82	-16	-26.8	83	-22.4	-31.2
5	91	-11.8	-15.8	90	-13.2	-17.2
6	104	-23.6	-34.6	107	-24.5	-35.1
7	116	-10.6	-18.5	116	-12.3	-20.5
8	133	-7.3	-16.1	131	-20.5	-26.3
9	131	-9	-12.6	128	-7.5	-15.4
10	139	-10	-18.8	137	-20.8	-27.9
11	148	0	-4.9	145	4.9	0.4
12	150	0	-3.8	147	-0.3	-4.5
13	166	-8.3	-17.3	163	-11.3	-19.9
14	177	-11.6	-20.5	175	-14.3	-23
15	193	-15.5	-23.1	190	-18.8	-23.9

Table 6.7: Maximum transfer function values for the vertical grid.

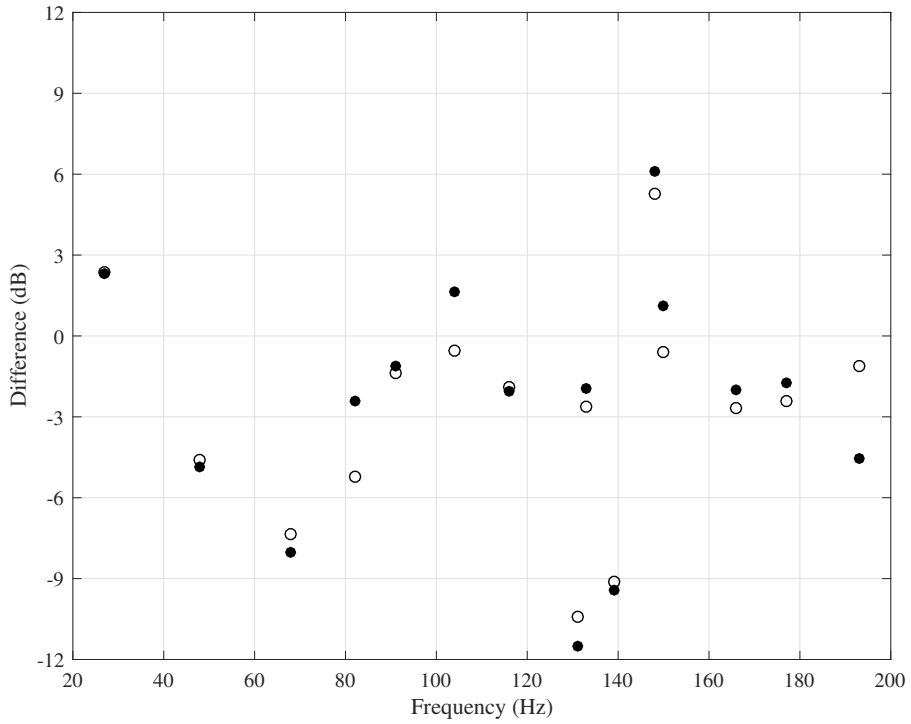

Figure 6.20: Differences between measured and predicted transfer function magnitudes for the horizontal (black circles) and vertical grids (white circles).

measurement, the coherence function is defined by [92]:

$$\gamma^2(\omega) = \frac{|G_{xy}(\omega)|^2}{G_{xx}(\omega).G_{yy}(\omega)} \tag{6.3}$$

The coherence function γ^2 indicates the extent to which two signals are linearly related. Its values are always between 0 and 1. If $\gamma^2 = 0$ there is no relationship between $x(t)$ and $y(t)$. If $\gamma^2 = 1$ the two signals are perfectly linearly related. The coherence function will assume values between 0 and 1 if any of the four conditions are met:

- There is a given amount of random noise contaminating the input $x(t)$ or the output $y(t)$;
- $x(t)$ and $y(t)$ are not linearly related;
- There is a poor choice of time window function or insufficient frequency resolution;
- There is a time delay between the two signals $x(t)$ and $y(t)$ comparable to the length of the recording.

The coherence function was measured for all the horizontal and vertical grid positions and the results are shown in the remainder of this section. The correlation values obtained are always less than 1 which indicates the presence of random noise in the measurements. The values of correlation are very close to 1 for the majority of the modes that were measured, except in the modes below the fundamental resonance of the room, where the correlation values obtained are small when the receiver is not located close to the source. A low value of coherence indicates that the measured output was affected by noise and was not linearly related to the input signal.

The other three possible causes of $\gamma^2 < 1$ are ruled out. The input and output signals are expected to be linearly related as the system under measurement is expected to be a linear time invariant (LTI) system. The possible effect of poor choice of frequency analyser settings discounted because values of coherence very close to 1

were obtained and the settings were kept constant throughout the entirety of the measurements. The length of the recordings was set to 4 s which is much larger than the time delay to be expected between the input and output signals which should be a maximum of 6 ms, considering acoustic propagation over a 2 m distance between the excitation point and microphone.

The coherence contour plots obtained (Figures 6.21 - 6.25) generally show values very close to 1, which indicates that the transfer function measurements are valid. However, low coherence values were obtained in some areas of the contour plots corresponding to the resonance peaks below the fundamental frequency of the room, indicating that the sound radiation from the plate was very weak in these areas and therefore the response at the microphones was dominated by random noise.

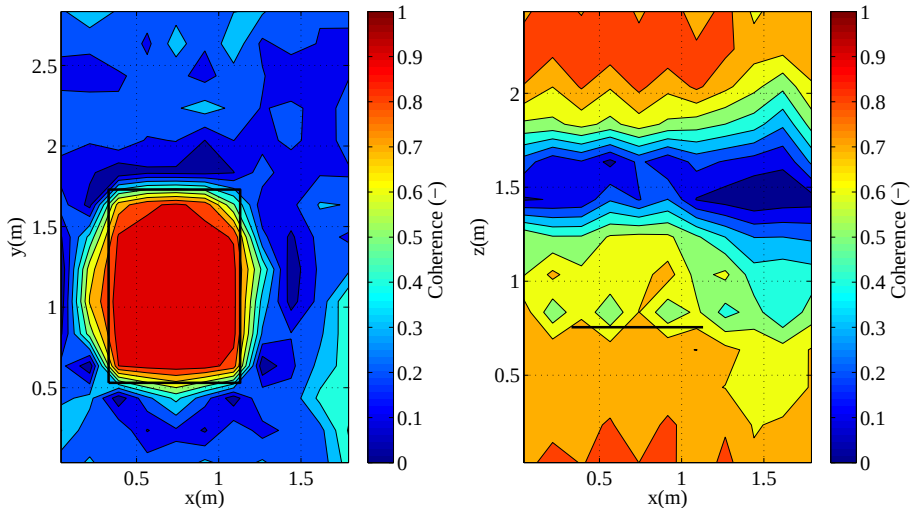

Horizontal grid (27 Hz)

Vertical grid (27 Hz)

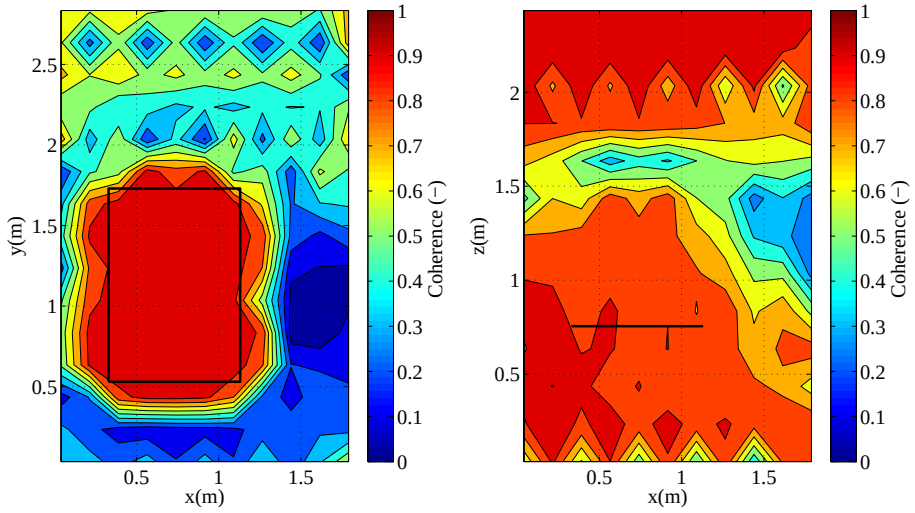

Horizontal grid (48 Hz)

Vertical grid (48 Hz)

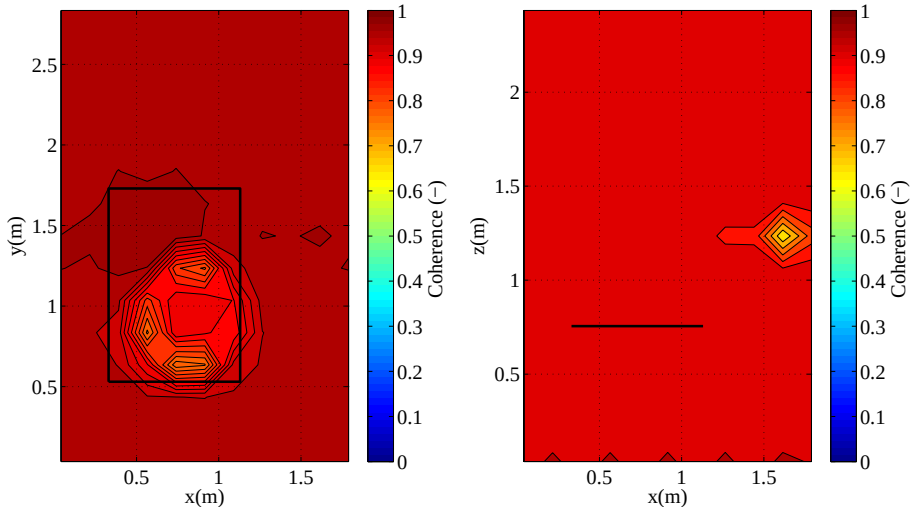

Horizontal grid (68 Hz)

Vertical grid (68 Hz)

Figure 6.21: Coherence function contours measured at resonance frequencies.

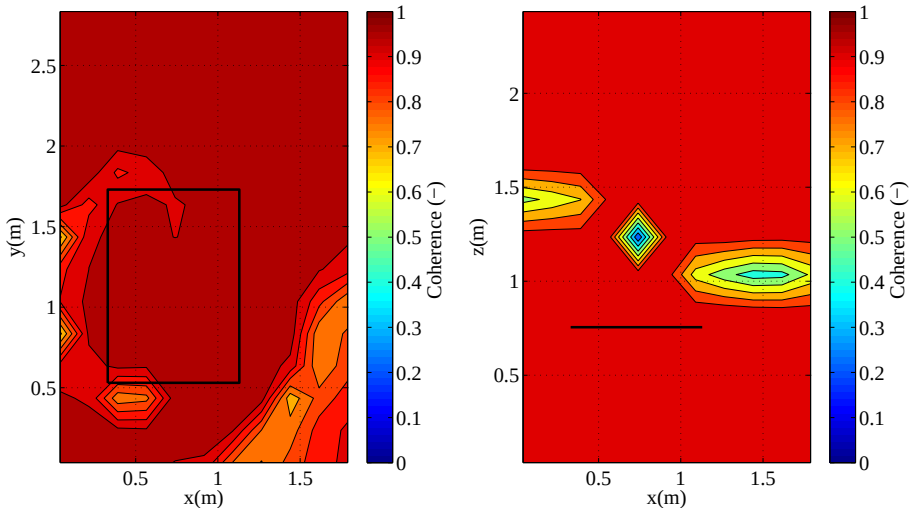

Horizontal grid (82 Hz)

Vertical grid (82 Hz)

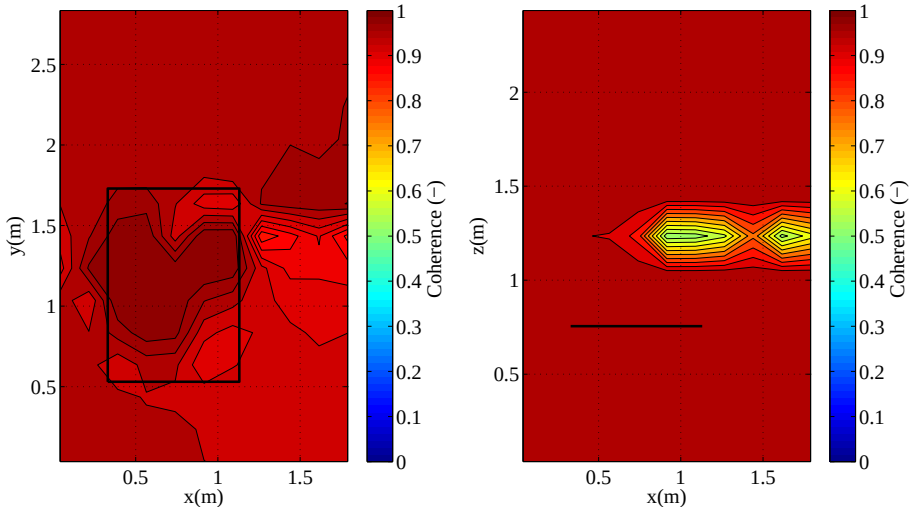

Horizontal grid (92 Hz)

Vertical grid (91 Hz)

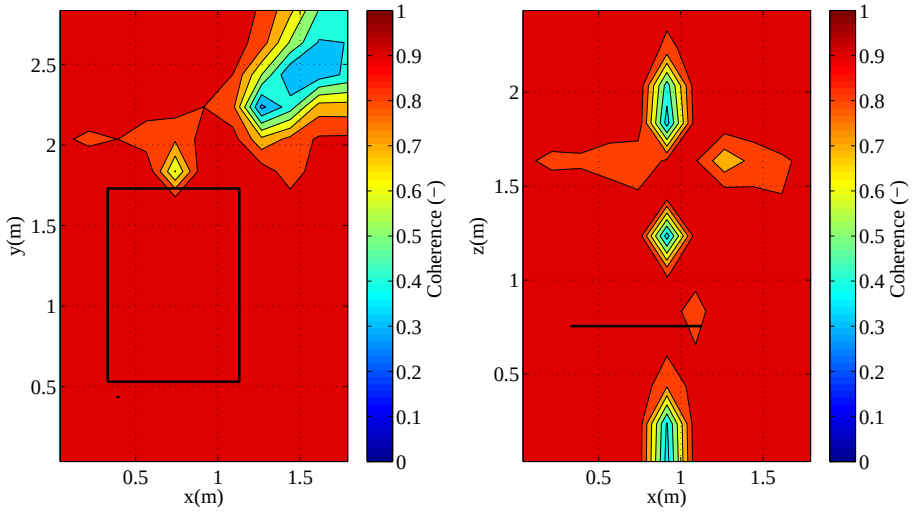

Horizontal grid (104 Hz)

Vertical grid (104 Hz)

Figure 6.22: Coherence function contours measured at resonance frequencies.

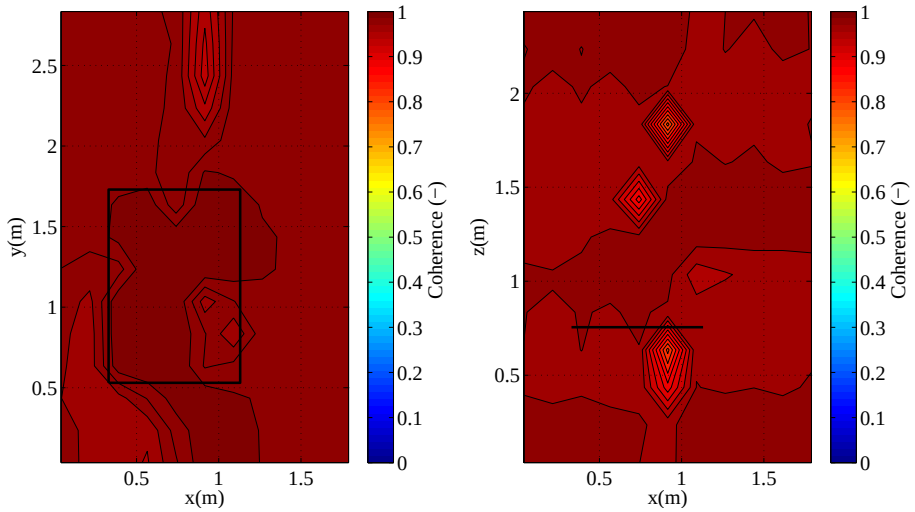

Horizontal grid (116 Hz) Vertical grid (116 Hz)

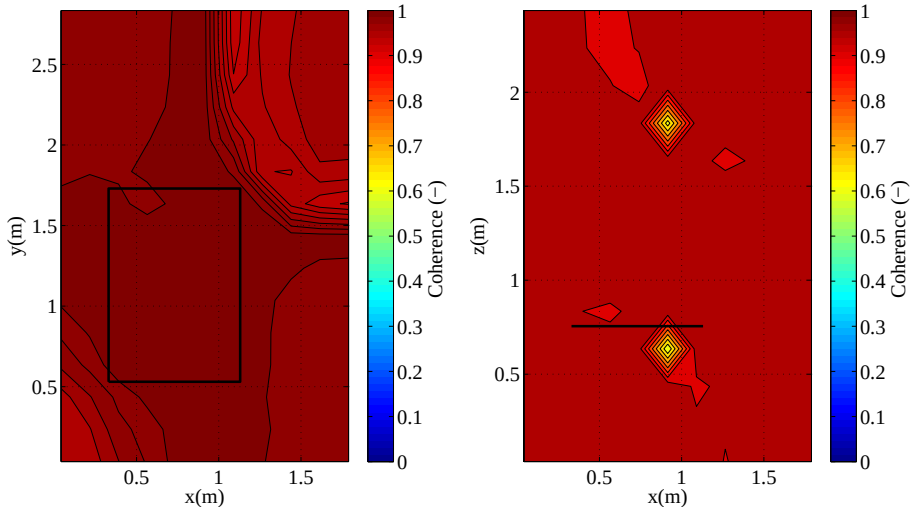

Horizontal grid (131 Hz) Vertical grid (131 Hz)

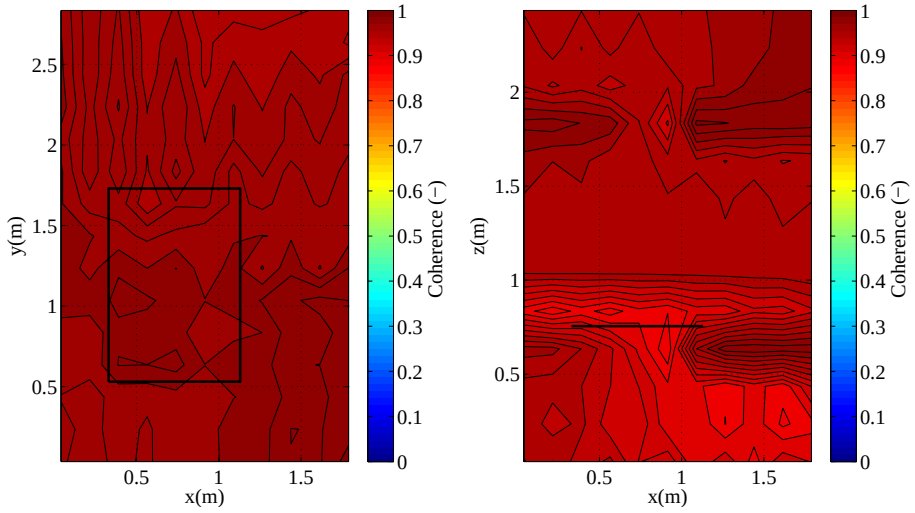

Horizontal grid (133 Hz) Vertical grid (133 Hz)

Figure 6.23: Coherence function contours measured at resonance frequencies.

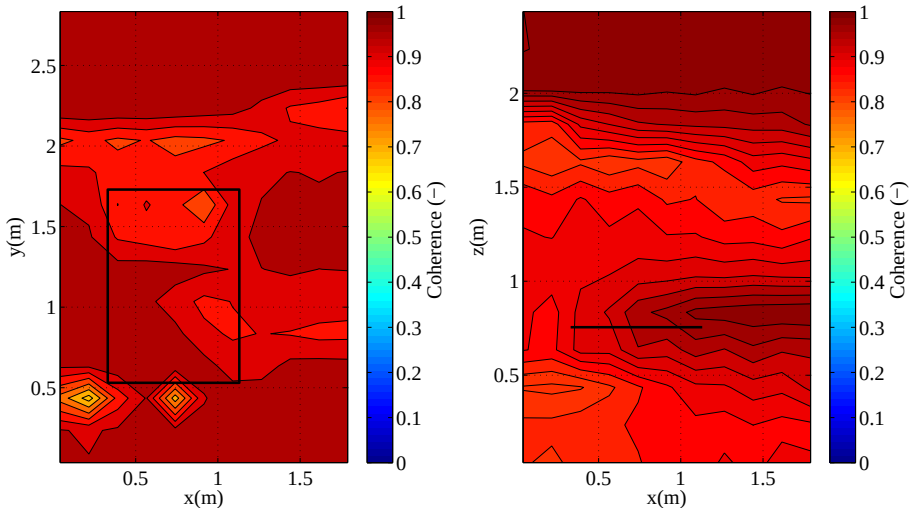

Horizontal grid (139 Hz)

Vertical grid (139 Hz)

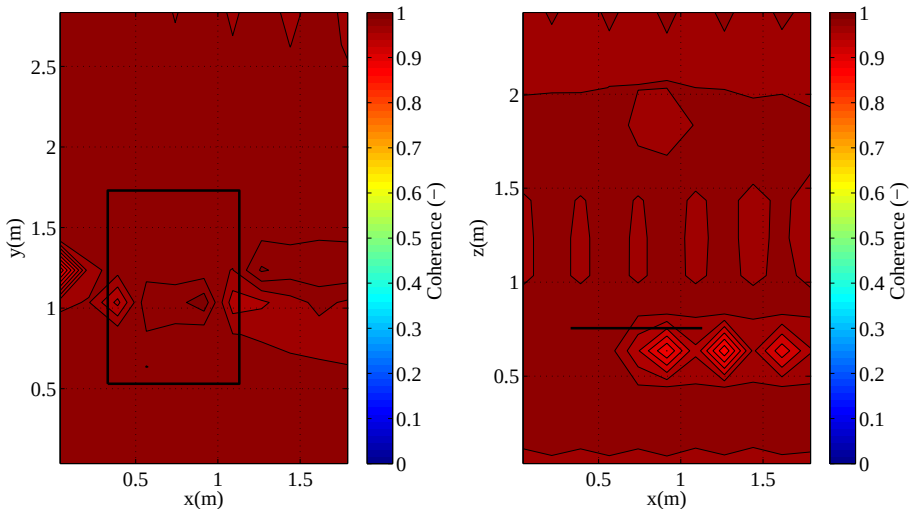

Horizontal grid (148 Hz)

Vertical grid (148 Hz)

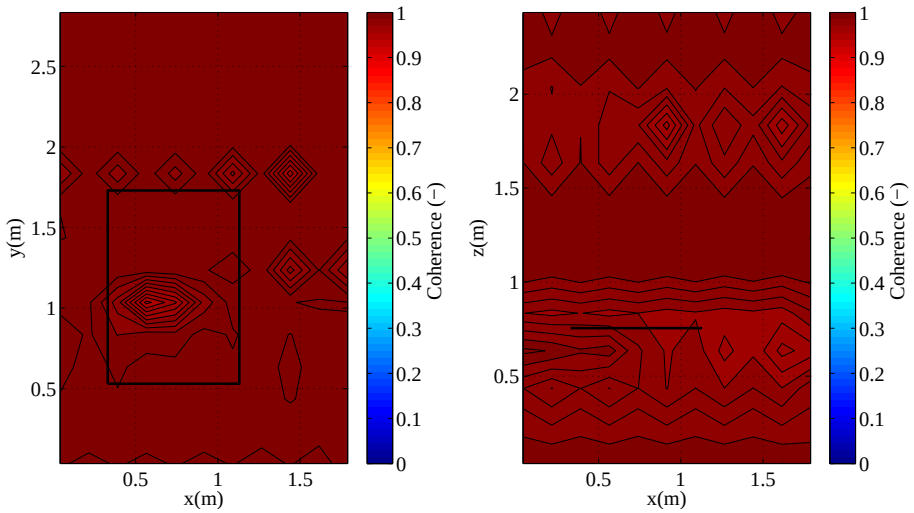

Horizontal grid (150 Hz)

Vertical grid (150 Hz)

Figure 6.24: Coherence function contours measured at resonance frequencies.

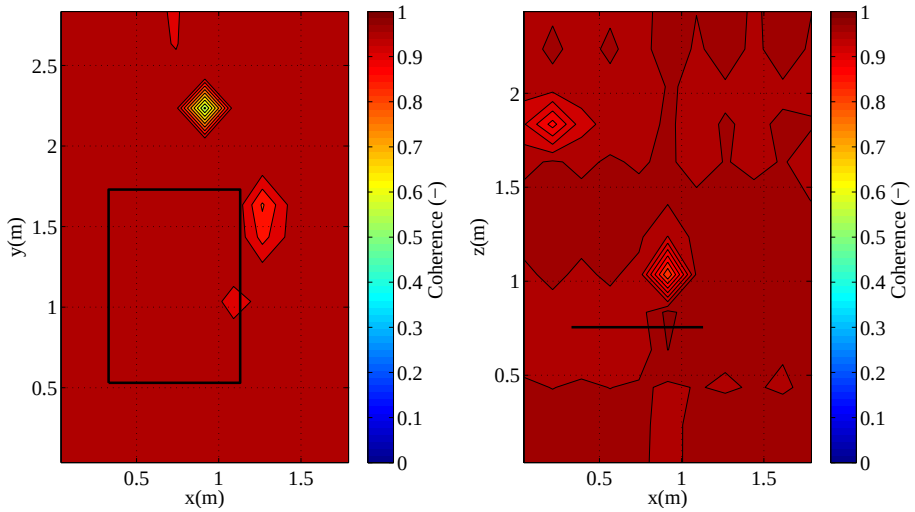

Horizontal grid (166 Hz)

Vertical grid (166 Hz)

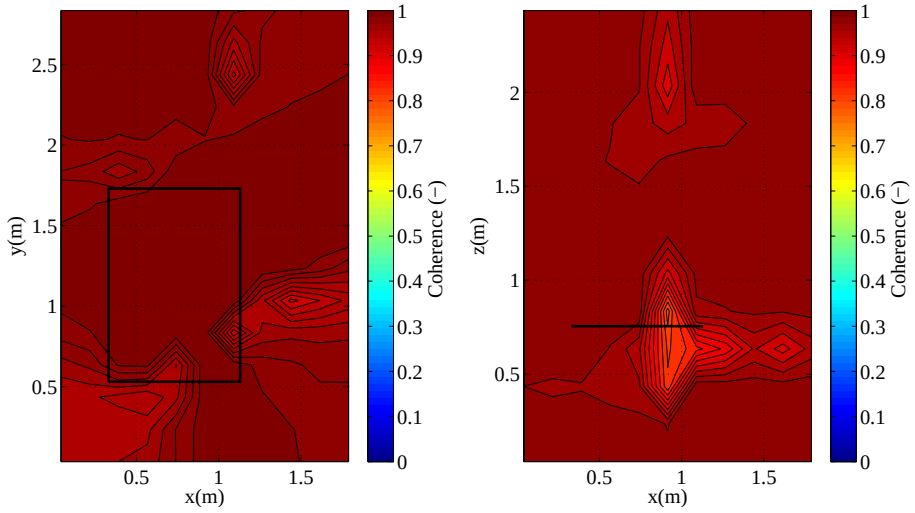

Horizontal grid (177 Hz)

Vertical grid (177 Hz)

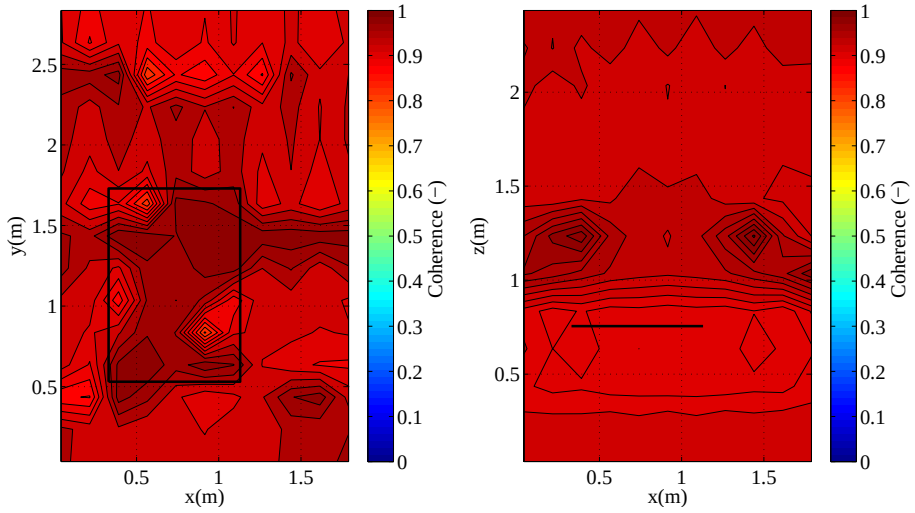

Horizontal grid (193 Hz)

Vertical grid (193 Hz)

Figure 6.25: Coherence function contours measured at resonance frequencies.

6.6 Conclusions

This chapter described the experimental validation of the vibroacoustic FDTD model for a mechanically point-excited aluminium plate radiating into a small reverberation chamber. The effects of numerical dispersion in the FDTD model were found to be negligible when comparing the FDTD resonance peaks with the analytical solution for an acoustic enclosure and for a simply supported plate.

The results of the FDTD predictions were compared to the measured driving-point mobilities of the plate and transfer functions of pressure-to-force inside the small reverberation chamber. The close agreement between FDTD and measurements validates both the scaling approach and the simplified boundary approach to modelling the interface between air and the plate that were proposed and implemented in FDTD. It was possible to obtain these numerical results using an ordinary desktop computer due to the computational advantages enabled by the simplified boundary and scaling approaches.

The vibroacoustic FDTD results for the aluminium plate radiating inside the small reverberation chamber were experimentally validated in terms of pressure-to-force transfer functions taken at several positions along a horizontal and a vertical measurement grid. The validity of the transfer function measurements was confirmed by a set of coherence grid measurements. Close agreement between measured and FDTD pressure-to-force transfer function contour plots was obtained, including for the two resonance peaks obtained below the fundamental acoustic mode of the room.

7 Conclusions

In this thesis, new approaches to acoustic and vibroacoustic modelling with FDTD at low-frequencies have been described and experimentally validated.

For acoustic modelling of a space containing a porous panel with air on both sides, the porous material has been incorporated into FDTD using a Rayleigh model as proposed by Suzuki et al. However, to accurately reproduce the low-frequency sound field, a Moving Frame Model (MFM) was introduced to account for motion of the porous panel. The MFM assumes lumped mass behaviour of the porous panel which is coupled to the FDTD update equations that incorporate the Rayleigh model. Experimental validation used a small reverberant room under three different conditions: (1) empty room, (2) with a mineral fibre panel partially dividing the room, and (3) with a mineral fibre panel completely dividing the room. This confirmed that for two spaces that are completely subdivided by a porous panel, the MFM can account for a spring-mass-spring resonance which results in a peak in the response below the fundamental frequency of the room. Close agreement was obtained between experimental results and FDTD incorporating the MFM; this validates the models as well as implementation of the loudspeaker as a hard velocity source.

The vibroacoustic modelling focused on the prediction of the vibration of a thin elastic plate undergoing point excitation and radiating into an acoustic cavity. To achieve this, two new modelling approaches were introduced: scaling procedures to significantly reduce computation times and a simplified boundary approach to simplify the implementation of the solid-air boundaries. In comparison with room acoustic simulations, it can be computationally expensive to run a vibroacoustic model with a fine spatial resolution because wavespeeds for structure-borne sound are relatively high. The scaling approach was proposed and validated to overcome this problem. Modifications to the geometry and physical properties are used to preserve the dynamic characteristics of the model whilst allowing much larger time

steps. This reduces the total number of iterations necessary to complete the simulation and significantly reduces computation times. In addition, it was shown that the scaling approach can be applied to more complex problems that involve more than one geometrically parallel thin plate and more than one acoustic cavity. An alternative approach to model the boundaries between the air and the solid medium, the simplified boundary approach, is also proposed and implemented in FDTD to improve computational efficiency and allowing for simpler implementation. Both modelling approaches proposed were experimentally validated by the agreement between FDTD and measurements. This confirms the validity of implementing a thin plate undergoing bending wave motion as a three-dimensional solid that can support multiple wave types. The general finding from the comparison of measured and predicted pressure-to-force transfer functions is that FDTD is capable of predicting the spatial variation of sound pressure in close agreement with measured data. In the frequency range below the lowest room mode, the close agreement between FDTD and measurements shows the existence of large variations in sound pressure level. This confirms the importance of validated vibroacoustic models to predict sound fields inside acoustic cavities in the low-frequency range.

7.1 Suggestions for future work

Future work on acoustic FDTD modelling of porous materials could be extended to deal with materials covered by a thin layer of fabric. This would be useful to the automotive industry for modelling low-frequency sound fields in car cabins as many car seats have a thin protective cover layer.

Future work on vibroacoustic FDTD modelling could consider whether it is computationally advantageous and feasible to apply the scaling approach to orthogonally-arranged plates, i.e. two plates forming an L-junction or to a set of six plates forming a rectangular cavity. The mathematical derivation of the numerical dispersion characteristics of the vibroacoustic FDTD scheme described in this thesis upon which the

scaling approach is based could also be carried out in future work. It would also be of interest to assess whether it is feasible to apply the scaling approach to situations where these sets of orthogonal plates were mechanically connected, instead of being simply supported. The development of a scaling approach that could be applied for a vibroacoustic rectangular cavity problem would be of particular interest for engineering fields such as building acoustics, where it is necessary to predict both direct and flanking transmission between rooms.

References

[1] K. S. Yee, "Numerical solution of the initial boundary value problems involving maxwell's equations in isotropic media," *IEEEE transactions on Antennas and Propagation*, vol. 14, no. 3, pp. 302–307, 1966.

[2] K. Kunz and R. Luebbers, *Finite Difference Time Domain Method for Electromagnetics*. Boca Raton: CRC press, 1993.

[3] J. D. Poorter and D. Botteldooren, "Acoustical finite-difference time-domain simulations of subwavelength geometries," *The Journal of the Acoustical Society of America*, vol. 104, pp. 1171–1177, 1998.

[4] S. Sakamoto, H. Nagatomo, A. Ushiyama, and H. Tachibana, "Calculation of impulse responses and acoustic parameters in a hall by the finite-difference time-domain method," *Acoust. Sci. Tech.*, vol. 29, no. 4, pp. 256–265, 2008.

[5] B. CottÃĺ, P. Blanc-Benon, C. Bogey, and F. Poisson, "Time-domain impedance boundary conditions for simulations of outdoor sound propagation," *AIAA Journal*, vol. 47, no. 10, 2009.

[6] T. Renterghem, D. Botteldooren, and K.Verheyen, "Road traffic noise shielding by vegetation belts of limited depth," *Journal of Sound and Vibration*, vol. 331, pp. 2404–2425, 2012.

[7] K. Kim and J. M. Lees, "Volcanic Vent Geometry and Infrasonic Radiation via FDTD Modeling," *AGU Fall Meeting Abstracts*, Dec. 2010.

[8] Q. H. Liu and B. K. Sinha, "A 3d cylindrical PML/FDTD method for elastic waves in fluid-filled pressurized boreholes in triaxially stressed formations," *Geophysics*, vol. 68, no. 5, pp. 1731–1743, 2003.

[9] B. K. Sinha, E. Şimşek, and Q.-H. Liu, "Elastic-wave propagation in deviated wells in anisotropic formations," *Geophysics*, vol. 71, no. 6, pp. D191–D202, 2006.

[10] C. Schroeder, W. Scott, and G. Larson, "Elastic waves interacting with buried land mines: a study using the FDTD method," *Transactions on Geodesic and Remote Sensing*, vol. 40, no. 6, pp. 1405–1415, 2002.

[11] I. M. Hallaj and R. O. Cleveland, "Fdtd simulation of finite-amplitude pressure and temperature fields for biomedical ultrasound," *The Journal of the Acoustical Society of America*, vol. 105, no. 5, pp. L7–L12, 1999.

[12] G. Pinton, J.-F. Aubry, M. Fink, and M. Tanter, "Effects of nonlinear ultrasound propagation on high intensity brain therapy," *Medical Physics*, vol. 38, no. 3, pp. 1207–1216, 2011.

[13] P. Moczo., J. O.A.Robertsson, and L. Eisner, "The finite-difference time-domain method for modeling of seismic wave propagation," *Advances in Geophysics*, vol. 48, no. 5, pp. 421–516, 2007.

[14] P. Moczo, J. Kristek, and M. Gális, *The Finite-Difference Modelling of Earthquake Motions: Waves and Ruptures*. Cambridge: Cambridge university Press, first ed., 2014.

[15] T. Okamoto, H. Takenaka, T. Nakamura, and T. Aoki, "Large-scale simulation of seismic-wave propagation of the 2011 hoku-oki m9 earthquake," in *Proceedings of the International Symposium on Engineering Lessons Learned from the 2011 Great East Japan Earthquake*, March 2012.

[16] T. Yokota, S. Sakamoto, and H. Tachibana, "Visualization of sound propagation and scattering in rooms," *Acoust. Sci. Tech.*, vol. 23, no. 1, pp. 40–46, 2002.

[17] P. Dias, J. Madeira, and B. S. Santos, "Teaching 3d modelling and visualization using vtk," *Comput. Graph.*, vol. 32, pp. 363–370, 2008.

[18] D. Botteldooren, "Finite-difference time-domain simulation of low-frequency room acoustics problems," *The Journal of the Acoustical Society of America*, vol. 98, pp. 3302–3308, 1995.

[19] A. Celestinos and S. B. Nielsen, "Low-frequency loudspeaker-room simulation using finite differences in the time domain - part 1: Analysis*," *Journal of the*

Audio Engineering Society, vol. 56, no. 10, pp. 772–786, 2008.

[20] A. Southern, D. Murphy, G. Campos, and P. Dias, "Finite difference room acoustic modelling on a general purpose graphics processing unit," in *Audio Engineering Society Convention 128*, May 2010.

[21] E. J.Shaughnessy, I. Katz, and J. Schaffer, *Introduction to fluid mechanics*. New York: Oxford University Press, 2005.

[22] R. J. Craik, *Sound transmission through Buildings using Statistical Energy Analysis*. England: Gower Publishing Limited, 1996.

[23] L. Gilles, S. Hagness, and L. Vaźquez, "Comparison between staggered and unstaggered finite-difference time-domain grids for few-cycle temporal optical soliton propagation," *Journal of Computational Physics*, vol. 161, pp. 379–400, 2000.

[24] H. Suzuki, A. Omoto, and K. Fujiwara, "Treatment of boundary conditions by finite difference time domain method," *Acoust. Sci. Tech.*, vol. 28, no. 1, pp. 16–26, 2007.

[25] D. Sullivan, *Electromagnetic Simulation Using the FDTD Method*. New York: IEEE press, 2000.

[26] J. D. Hoffman and S. Frankel, *Numerical Methods for Engineers and Scientists*. Basel: Marcel Dekker, Inc., second ed., 2001.

[27] K. Kowalczyk and M. van Walstijn, "Room acoustics simulation using 3-d compact explicit FDTD schemes," *IEEE Transactions on Audio, Speech, and Language Processing*, vol. 19, no. 1, pp. 34–46, 2011.

[28] J. Simpson and A. Taflove, "Efficient modeling of impulsive ELF antipodal propagation about the earth sphere using an optimized two-dimensional geodesic FDTD grid," *IEEE Antennas and Wireless Propagation Letters*, vol. 3, pp. 215–218, 2004.

[29] D. Botteldooren, "Acoustical finite-difference time-domain simulation in a

quasi-cartesian grid," *The Journal of the Acoustical Society of America*, vol. 95, pp. 2313–2319, 1994.

[30] W. Yu and R. Mittra, "A conformal FDTD algorithm for modeling perfectly conducting objects with curved-shaped surfaces and edges," *Microwave and Optical Technology Letters*, vol. 27, no. 2, pp. 136–138, 2000.

[31] J. Tolan and J. Schneider, "Locally conformal method for acoustic finite-difference time-domain modeling of rigid surfaces," *Journal of the Acoustical Society of America*, vol. 114, no. 5, pp. 2575–2581, 2003.

[32] B. Hamilton and S. Bilbao, "Hexagonal vs. rectilinear grids for explicit finite difference schemes for the two-dimensional wave equation," in *Proceedings of Meetings on Acoustics ICA 2013*, vol. 19, June 2013.

[33] W. M. Henk Kaarle Versteeg, *An introduction to computational fluid dynamics - The finite volume method*. Essex: Pearson Prentice Hall, second ed., 2007.

[34] S. W. Staker, C. L. Holloway, A. U. Bhobe, and M. Piket-May, "Alternating-direction implicit (ADI) formulation of the finite-difference time-domain (FDTD) method: Algorithm and material dispersion implementation," *IEEE Transactions on Electromagnetic Compatibility*, vol. 45, no. 2, pp. 156–166, 2003.

[35] A. Taflove and S. Hagness, *Computational Electrodynamics*. Boston: Artech House, third ed., 2005.

[36] Y. Sendo, H. Kudo, T. Kashiwa, and T. Ohtani, "The FDTD(2,4) method for highly accurate analysis in three-dimensional space," *Electr. Commun. Jpn.*, vol. 86, no. 11, pp. 30–36, 2003.

[37] Q. H. Liu, "The pseudospectral time-domain (PSTD) algorithm for acoustic waves in absorptive media," *ieee transactions on ultrasonics, ferroelectrics, and frequency control*, vol. 45, no. 4, pp. 1044–1055, 1998.

[38] Q. H. Liu, "Large-scale simulations of electromagnetic and acoustic measurements using the pseudospectral time-domain (PSTD) algorithm," *IEEE trans-*

actions on Geoscience and Remote sensing, vol. 37, no. 2, pp. 917–926, 1999.

[39] D. Champeney, *Fourier transforms and their physical applications*. London: Academic press, 1973.

[40] J. Schneider, "Implementation of transparent sources embedded in acoustic finite-difference time-domain grids," *The Journal of the Acoustical Society of America*, vol. 103, pp. 136–142, 1998.

[41] R. Janaswamy and Y. Liu, "An unstaggered colocated finite-difference scheme for solving time-domain maxwell's equations in curvilinear coordinates," *IEEE Transactions on Antennas and Propagation*, vol. 45, no. 11, pp. 1584–1591, 1997.

[42] A. V. Londersele, D. D. Zutter, and D. V. Ginste, "A collocated 3-D HIE-FDTD scheme with PML," *IEEE Microwave and Wireless Components Letters*, vol. 27, no. 7, pp. 609–611, 2017.

[43] Y. Liu, "Fourier analysis of numerical algorithms for the maxwell equations," *Journal of Computational Physics*, vol. 124, pp. 396–416, 1996.

[44] J. Berenger, "A perfectly matched layer for the absorption of electromagnetic waves," *J. Comput. Phys.*, vol. 114, pp. 185–200, 1994.

[45] Q.-H. Liu and J. Tao, "The perfectly matched layer for acoustic waves in absorptive media," *Journal of the Acoustical Society of America*, vol. 102, no. 4, pp. 2072–2082, 1997.

[46] D. B. Davidson, *Computational Electromagnetics for RF and Microwave Engineering*. Madrid: Cambridge University Press, 2005.

[47] F. Zheng and Z. Chen, "A finite-difference time-domain method without the courant stability conditions," *IEEE Microwave and Guided Wave Letters*, vol. 9, no. 11, pp. 441–443, 1999.

[48] W. Yu, X. Yang, Y. Liu, and R. Mittra, *Electromagnetic Simulation Techniques Based on the FDTD Method*. New Jersey: John Wiley & Sons, 2009.

[49] L. Zhou, F. Yang, R. Long, F. Yan, W. Han, and M. Gao, "A hybrid method of higher-order FDTD and subgridding technique," *IEEE Antennas and Wireless Propagation Letters*, vol. 15, pp. 1261–1264, 2016.

[50] P. Nelson and S. Elliot, *Active Control of Sound*. San Diego: Academic press, 1992.

[51] T. Rossing, *Springer Handbook of Acoustics*. New York: Springer-Verlag, 2007.

[52] F. Fahy, *Sound and structural vibration - Radiation, Transmission and Response*. San Diego: Academic Press, 1985.

[53] M. Kleiner, *Acoustics and Audio Technology*. Fort Lauderdale: J. Ross Publishing, third ed., 2012.

[54] L. Kinsler, A. Frey, A. Coppens, and J. Sanders, *Fundamentals of Acoustics*. Weinheim: John Wiley & sons, Inc., fourth ed., 2000.

[55] J. Borwick, *Loudspeaker and Headphone Handbook*. Johannesburg: Focal press, third ed., 2001.

[56] H. Kuttruff, *Room Acoustics*. London: Spon press, fourth ed., 2000.

[57] C. Hopkins, *Sound Insulation*. Amsterdam: Elsevier, 2007.

[58] D. Bies and C. Hansen, *Engineering Noise Control - Theory and Practice*. London: Spon Press, third ed., 2003.

[59] J. Escolano, F. Jacobsen, and J. Lópes, "An efficient realization of frequency dependent boundary conditions in an acoustic finite-difference time-domain model," *J. Sound Vib.*, vol. 316, pp. 234–247, 2008.

[60] M. A. Biot, "Theory of propagation of elastic waves in a fluid-saturated porous solid. i. low-frequency range," *The Journal of the Acoustical Society of America*, vol. 28, no. 2, pp. 168–178, 1956.

[61] M. Delany and E. Bazley, "Acoustical properties of fibrous absorbent materials," *Applied Acoustics*, vol. 3, pp. 105–116, 1970.

[62] J. Allard and N. Atalla, *Propagation of Sound in Porous Media.* Chichester: John Wiley and Sons, second ed., 2009.

[63] T. J. Cox and P. D'Antonio, *Acoustic Absorbers and Diffusers.* London: Taylor & Francis, second ed., 2009.

[64] L. Beranek and I. Vér, *Noise and Vibration Control Engineering - Principles and applications.* Toronto: John Wiley & sons, 1992.

[65] N. Ferreira and C. Hopkins, "Using finite-difference time-domain methods with a Rayleigh approach to model low-frequency sound fields in small spaces subdivided by porous materials," *Acoust. Sci. Tech.*, vol. 34, no. 5, pp. 332–341, 2013.

[66] L. Beranek, "Acoustical properties of homogeneus, isotropic rigid tiles and flexible blankets," *The Journal of the Acoustical Society of America*, vol. 19, pp. 556–568, 1947.

[67] P. Moczo, J. O. A. Robertsson, and L. Eisner, *The Finite-Difference Time-Domain Method for Modeling of Seismic Wave Propagation.* Elsevier - Academic Press, 2007.

[68] M. Toyoda and D. Takahashi, "Prediction for architectural structure-borne sound by the finite-difference time-domain method," *Acoust. Sci. Tech.*, vol. 30, no. 4, pp. 265–276, 2009.

[69] W. Zhang, Y. Shen, and L. Zhao, "Three-dimensional anisotropic seismic wave modelling in spherical coordinates by a collocated-grid finite-difference method," *Geophysical Journal International*, vol. 188, pp. 1359–1381, 2012.

[70] F. D. Hastings, J. B. Schneider, and S. L. Broschat, "Application of the perfectly matched layer (PML) absorbing boundary condition to elastic wave propagation," *Journal of the Acoustical Society of America*, vol. 100, no. 5, pp. 3061–3069, 1996.

[71] M. Toyoda, H. Miyazaki, T. Shiba, A. Tanaka, and D. Takahashi, "Finite-difference time-domain method for heterogeneous orthotropic media with damp-

ing," *Acoust. Sci. Tech.*, vol. 33, no. 2, pp. 77–85, 2012.

[72] Y. Fung, *A first Course in Continuous Mechanics*. Englewood Cliffs: Prentice-Hall, 1969.

[73] L. Cremer, M. Henckl, and E. Ungar, *Structure-borne sound using a plate model*. Berlin: Springer-Verlag, second ed., 1973.

[74] D. Bland, *The Theory of Linear Viscoelasticity*. Oxford: Pergamon Press, 1960.

[75] S. Tan, *Calculus: Early Transcendentals*. Belmont: Cengage Learning, Inc., 2010.

[76] L. Boltzmann, "Zur theorie der elastischen nachwirkung," *Poggendor fs Annalen*, vol. 7, p. 624, 1876.

[77] J. Robertsson, J. Blanch, and W. Symes, "Viscoelastic finite-difference modeling," *Geophysics*, vol. 59, no. 9, pp. 1444–1456, 1994.

[78] T. Asakura, T. Ishizuka, T. Miyajima, M. Toyoda, and S. Sakamoto, "Finite-difference time-domain analysis of structure-borne sound using a plate model," *Acoust. Sci. Tech.*, vol. 34, no. 1, pp. 48–51, 2013.

[79] A. Leissa, *Vibration of Plates*. Acoustical Society of America, 1993.

[80] T. Asakura and S. Sakamoto, "Finite-difference time-domain analysis of sound insulation performance of wall systems," *Build. Acoust.*, vol. 16, no. 3, pp. 267–281, 2009.

[81] M. Toyoda, D. Takahashi, and Y. Kawai, "Averaged material parameters and boundary conditions for the vibroacoustic finite-difference time-domain method with a nonuniform mesh," *Acoust. Sci. Tech.*, vol. 33, no. 4, pp. 273–276, 2012.

[82] T. Kurose, K. Tsuruta, C. Totsuji, and H. Totsuji, "Dtd simulations of acoustic waves in two-dimensional phononic crystals using parallel computer," *Memoirs of the Faculty of Engineering, Okayama University*, vol. 43, pp. 16–21, 2009.

[83] C. Fackler, J. Botts, and N. Xiang, "Parallelized finite difference time domain

room acoustic simulation," *The Journal of the Acoustical Society of America*, vol. 132, p. 1880, 2012.

[84] T. Asakura and S. Sakamoto, "Improvement of sound insulation of doors or windows by absorption treatment inside the peripheral gaps," *Acoust. Sci. Tech.*, vol. 34, no. 4, pp. 241–252, 2013.

[85] T. Asakura, T. Ishizuka, T. Miyajima, M. Toyoda, and S. Sakamoto, "Finite-difference time-domain analysis of structure-borne sound using a plate model based on the kirchhoff-love plate theory," *Acoust. Sci. Tech.*, vol. 35, no. 3, pp. 127–138, 2014.

[86] T. Asakura, T. Ishizuka, T. Miyajima, M. Toyoda, and S. Sakamoto, "Prediction of low frequency structure-borne sound in concrete structures using the finite-difference time-domain method," *The Journal of the Acoustical Society of America*, vol. 136, no. 3, pp. 1085–1100, 2014.

[87] T. Asakura, T. Ishizuka, T. Miyajima, and M. Toyoda, "Finite-difference time-domain analysis of the vibration characteristics of a beam-plate structure using a dimension-reduced model," *Appl. Acoust.*, vol. 92, pp. 75–85, 2015.

[88] G. B. Warburton, "The vibration of rectangular plates," *Proceedings of the institute of Mechanical Engineering*, vol. 168, pp. 371–384, 1954.

[89] F. Fahy and J. Walker, *Advanced Applications in Acoustics, Noise and Vibration*. London: Spoon Press, first ed., 2004.

[90] J. Yin and C. Hopkins, "Prediction of high-frequency vibration transmission across coupled, periodic ribbed plates by incorporating tunneling mechanisms," *The Journal of the Acoustical Society of America*, vol. 133, no. 4, pp. 2069–2081, 2013.

[91] S. K. Olesen, "Low frequency room simulation using finite difference equations," in *102nd Audio Engineering Society Convention*, March 1997.

[92] R. Randall, *Frequency Analysis*. Denmark: Bruel & Kjaer, third ed., 1987.

[93] A. Chaigne and C. Lambourg, "Time-domain simulation of damped impacted plates. i. theory and experiments," *The Journal of the Acoustical Society of America*, vol. 109, no. 4, pp. 1422–1432, 2001.

[94] K. F. Riley, M. P. Hobson, and S. J. Bence, *Mathematical Methods for Physics and Engineering*. São Paulo: Cambridge University Press, third ed., 2006.

[95] P. W. Williams, *Numerical Computation*. London: Thomas Nelson and Sons Ltd, first ed., 1972.

[96] D. J. Ewins, *Modal Testing*. Research Studies Press, second ed., 2000.

[97] R. Perera, A. Ruiz, and C. Manzano, "Performance assessment of multicriteria damage identification genetic algorithms," *Computers and Structures*, vol. 87, pp. 120–127, 2009.

Appendix I - Mathematical symbols and operators

This appendix defines mathematical operators and symbols used in Chapters 2 and 3. The material included in this appendix is entirely based on published literature [79, 94].

7.1.1 Forward difference operator

The forward difference operator of a scalar field f at a position (i, j, k) along the x-direction is defined as:

$$D_x f^n|_{i,j,k} = \frac{f^n|_{i+1,j,k} - f^n|_{i,j,k}}{\Delta x}$$

along the y-direction:

$$D_y f^n|_{i,j,k} = \frac{f^n|_{i,j+1,k} - f^n|_{i,j,k}}{\Delta y}$$

along the z-direction:

$$D_z f^n|_{i,j,k} = \frac{f^n|_{i,j,k+1} - f^n|_{i,j,k}}{\Delta z}$$

7.1.2 Divergence

The divergence of a vector field $f_i = (f_x, f_y, f_z)$ is denoted by ∇ and defined by:

$$\nabla \cdot f_i = \frac{\partial f_x}{\partial x} + \frac{\partial f_y}{\partial y} + \frac{\partial f_z}{\partial z}$$

7.1.3 Fourier transform

The symbol $\mathcal{F}$ denotes the Fourier transform. The Fourier transform establishes an equivalence between the time domain and the frequency domain [39]:

$$p(t) \overset{\mathcal{F}}{\longleftrightarrow} \tilde{P}(\omega)$$

and is defined by [94]:

$$\widetilde{P}(\omega) = \mathcal{F}\left\{p(t)\right\} = \frac{1}{\sqrt{2\pi}} \int_{\infty}^{\infty} p(t) e^{-\mathbf{i}\omega t} dt$$

where $\widetilde{P}(\omega)$ is a complex function of frequency known as the 'spectral function'. Conversely $\mathcal{F}^{-1}$ denotes the inverse Fourier transform and is denoted by:

$$p(t) = \mathcal{F}^{-1}\left\{\widetilde{P}(\omega)\right\} = \frac{1}{\sqrt{2\pi}} \int_{\infty}^{\infty} \widetilde{P}(\omega) e^{\mathbf{i}\omega t} d\omega$$

Other physical variables related by the Fourier transform include the spatial position and corresponding wave number. For example the a spatial distribution of pressure $p(x)$ yields the following Fourier transform, also known as the 'wavenumber transform' [52]:

$$\widetilde{P}(k_x) = \frac{1}{\sqrt{2\pi}} \int_{\infty}^{\infty} p(x) e^{-\mathbf{i}k_x x} dx$$

and the inverse

$$p(x) = \frac{1}{\sqrt{2\pi}} \int_{\infty}^{\infty} \widetilde{P}(k_x) e^{\mathbf{i}k_x x} dk_x$$

7.1.4 Gradient

The gradient of a multi-variable function $f(x_1, x_2, ..., x_n)$ is denoted by ∇ and defined by:

$$\nabla f = \frac{\partial f}{\partial x_1}\hat{\boldsymbol{e_1}} + ... + \frac{\partial f}{\partial x_n}\hat{\boldsymbol{e_n}}$$

7.1.5 Kronecker delta

The Kronecker delta δ_{ij} is defined by:

$$\begin{cases} \delta_{ij} = 1 & \text{if} \quad i = j \\ \delta_{ij} = 1 & \text{otherwise} \end{cases}$$

where i and j are integers.

7.1.6 Laplacian

In Cartesian coordinates, the Laplacian operator over a scalar filed ψ is defined by:

$$\nabla^2\psi = \frac{\partial^2\psi}{\partial x^2} + \frac{\partial^2\psi}{\partial y^2} + \frac{\partial^2\psi}{\partial z^2}$$

7.1.7 Orthogonal functions

Two polynomials $p_i(x)$ and $p_j(x)$ are orthogonal with respect to a weight function $w(x)$ if the following condition is verified over an interval $x_1 < x < x_2$ [95]:

$$\int_{x_1}^{x_2} p_i(x)p_j(x)w(x) = 0$$

for $i \neq j$ and $w(x) > 0$.

In addition, if, the following is verified to be true

$$\int_{x_1}^{x_2} p_i^2(x) w(x) = 1$$

for all i, then the polynomials $p_i(x)$ form an orthonormal set.

Appendix II - A comparison of isolated aluminium plate mode shapes obtained from NMM and FDTD using MTMAC

This appendix contains an assessment of the validity of the general three-dimensional FDTD method for simulating thin plate bending wave motion. It compares the results obtained for the isolated aluminium plate using FDTD and analytical bending wave theory for thin plates [73].

The analytical approach uses a Normal Mode Model (NMM) to calculate the eigenfrequencies (equation 3.57) and the mode shapes of a simply-supported plate given by [73]:

$$\psi_X = sin(\frac{n_x \pi x}{L_x}) sin(\frac{n_y \pi y}{L_y})$$

The Modal Assurance Criterion (MAC) can be used to assess the spatial correlation between FDTD and analytical mode shapes, and is given by [96]:

$$MAC(X,Y) = \frac{\left|\{\psi_X\}^T \{\psi_Y\}\right|^2}{\left(\{\psi_X\}^T \{\psi_X\}\right)\left(\{\psi_Y\}^T \{\psi_Y\}\right)}$$

where ψ_X and ψ_Y are the modal shapes associated with modes X and Y.

However, the MAC does not account for any differences in the predicted eigenfrequencies; hence a comparison is carried out using the Modified Total Modal Assurance Criterion (MTMAC). This is based on the spatial correlation between corresponding FDTD and analytical mode shapes as well as the difference in their eigenfrequencies. MTMAC is defined by [97]:

$$MTMAC(X,Y) = \frac{MAC(X,Y)}{1 + \left| \frac{\omega_{\psi_X}^2 - \omega_{\psi_Y}^2}{\omega_{\psi_X}^2 + \omega_{\psi_Y}^2} \right|}$$

where ω_{ψ_X} and ω_{ψ_Y} are the eigenfrequencies at which the corresponding modes occur.

For the simply supported aluminium plate considered in this thesis, the MTMAC values obtained for the comparison of the first six modes (up to 200Hz) from FDTD and the analytical model are shown in Figure 7.1.

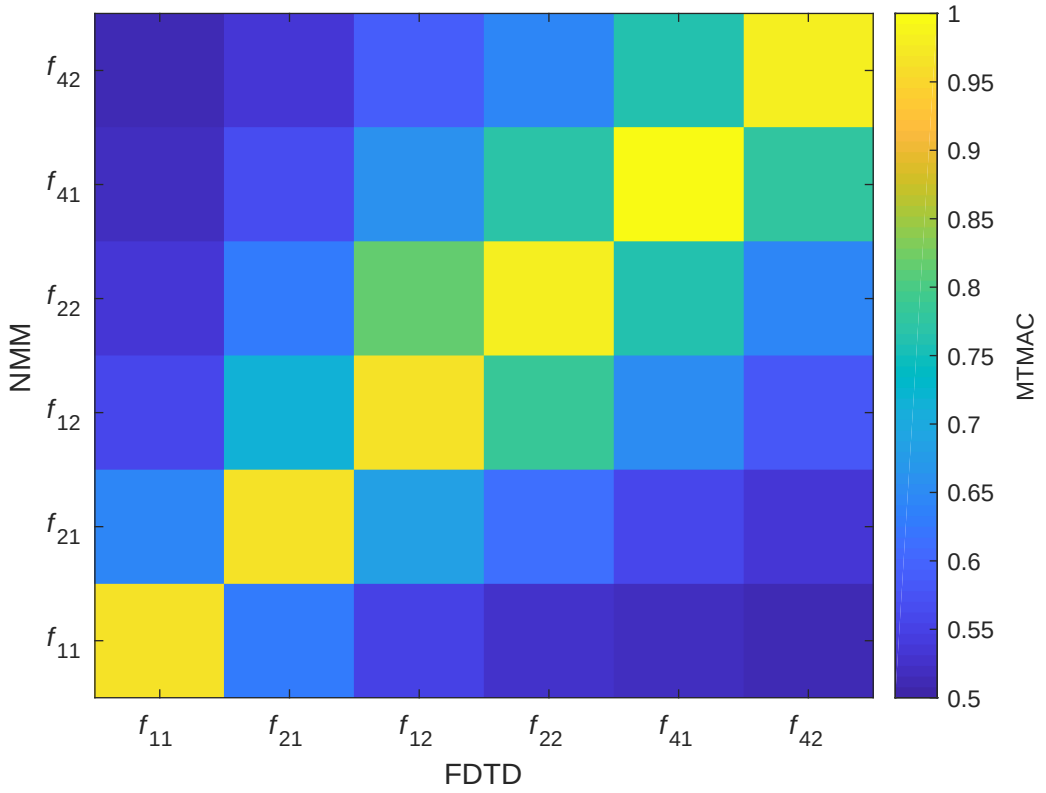

Figure 7.1: MTMAC values for the first six modes of the aluminium plate using eigenfrequencies and mode shapes determined from FDTD and an analytical model for thin plate bending wave theory.

Figure 7.1 shows that the MTMAC values are close to unity on the leading diagonal (i.e. highly correlated), with low values on the off-diagonal elements. The correlation pattern obtained between FDTD and the analytical model is similar to that which exists when the analytical model is compared with itself. This confirms that the

results obtained using the general three-dimensional FDTD method are equivalent to those of the analytical model which describes thin plate bending wave motion.

Appendix III - Basic FDTD source code

The following FDTD source code is written in Python and simulates two acoustic impulse sources that occur simultaneously in 2D space. The output of this simulation is shown in Figure 2.4. The code attempts to be clear and readable rather than computationally efficient.

```
import numpy as np
import matplotlib.pyplot as plt

################    DEFINE VARIABLES    ###############

c = 343 # speed of sound
rho = 1.2 # air density
k = 1 / (rho*(c**2)) # compressibility modulus

DimX = 140 # number of elements along the x-direction
DimY = 140 # number of elements along the y-direction
Niteration = 57 # number of iterations
dx = 1 # spatial resolution along the x direction
dy = 1 # spatial resolution along the y direction
dt = 1 / (c*( 1/(dx**2) + 1/(dy**2) )**0.5) # time resolution (Courant condition)

# Pre-allocate pressure and velocity field variables #
P = np.zeros( (DimX,DimY) )
Vx = np.zeros( (DimX,DimY) )
Vy = np.zeros( (DimX,DimY) )

################    DEFINE SOURCE FUNCTION    ###############

# pre-allocate memory for the source function #
source = np.zeros( Niteration )

# Define source constants #
sigma = 0.01
to = 0.02
```

```
# Define source function ( derivative of the Gaussian pulse ) #
for N in range(0,Niteration):
    t = N * dt # Calculate the value of time
    source[N] = (1e-3)*((t - to)/sigma**3)*np.exp(-((t - to)**2)/(2*(sigma**2)))

################    MAIN FDTD LOOP    ###############
for N in range(0,Niteration):
    t = N * dt # Calculate the value of time
    ######### Update pressures ###########
    for i in range(1,DimX-1):
        for j in range(1,DimY-1):
            if ( (i == 60) and (j == 60) ):
                # Source excitation (derivative of the Gaussian pulse):
                P[i,j] = source[N]
            elif ( (i == 85) and (j == 85) ):
                # Another source:
                P[i,j] = source[N]
            else: # Pressure update equation:
                P[i,j] = P[i,j] - (1/k) * dt * ( ((Vx[i+1,j] - Vx[i,j])/(dx))
+   ((Vy[i,j+1] - Vy[i,j])/(dy)))
    ######### Update velocities ###########
    for i in range(1,DimX):
        for j in range(1,DimY):
            Vx[i,j] = Vx[i,j] - (1/rho) * dt / dx * (P[i,j] - P[i-1,j])
            Vy[i,j] = Vy[i,j] - (1/rho) * dt / dy * (P[i,j] - P[i,j-1])

################    PLOTTING    ###############

plt.pcolormesh(P, cmap=plt.cm.RdYlGn)
plt.clim(-1.5, 1.5)
plt.xlabel('x (m)')
plt.ylabel('y (m)')
bar = plt.colorbar()
bar.set_label('Pressure (Pa)', rotation=90)
plt.show()
```

Appendix IV - Frequency characteristics of the damping coefficients

This appendix documents the results of a numerical investigation into the damping characteristics of each of the damping coefficients β, χ and γ. Several simulations were carried out using different values for the β, χ and γ coefficients and the corresponding loss factors were calculated.

The 0.05m thick plate used in the numerical investigation is simply supported and has dimensions of 1.2m x 0.70m. The material properties correspond (arbitrary choice) to medium density fiberboard (ρ=760 kg/m^3, c_{L} = 2560 m/s and ν = 0.3.).

Figure 7.2 shows the calculated loss factors as a function of frequency using different sets of values for the damping coefficients:

The results indicate that the damping coefficient β results in a loss factor that is inversely proportional to frequency, whereas χ and γ result in similar frequency characteristics, i.e. a linear increase with frequency. When all the loss factors β, χ and γ are considered simultaneously, the results show that the loss factor obtained follows a frequency-dependent loss factor [71] similar to Rayleigh damping. Since the loss factor profile of χ and γ are very similar, this numerical investigation suggests that, in principle, one of these damping coefficients can be set to zero without any loss of generality in the overall frequency dependence of the loss factor profile.

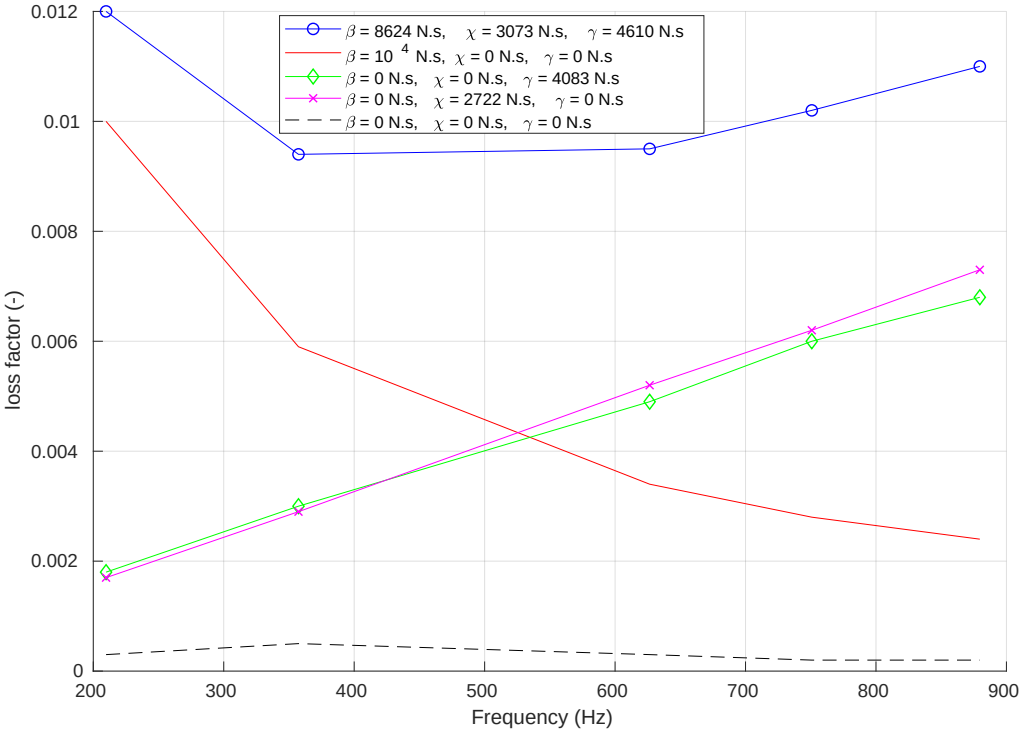

Figure 7.2: Frequency characteristics of the damping coefficients